Bralower, T.J., Premoli Silva, I., Malone, M.J., et al., 2002
Proceedings of the Ocean Drilling Program, Initial Reports Volume 198

3. Site 1207[1]

Shipboard Scientific Party[2]

PRINCIPAL RESULTS

Background

Site 1207 is the northernmost site in the Shatsky transect, lying some 5° north of the sites on the Southern High. The site is located in lower bathyal (3103 m) water depth close to the most elevated, central part of the Northern High of Shatsky Rise. The paleodepth history of this site is not well known, but subsidence was likely rapid in the interval immediately after its formation in the Valanginian (135 Ma), then slowed considerably. Paleoreconstructions suggest that the site was formed and remained in equatorial latitudes for the first 50 m.y. of its history.

The Northern High has not been drilled before; thus, the stratigraphy was unknown prior to drilling Site 1207. The sedimentary section at Site 1207 is ~1200 m thick. Seismic profiles show a generally horizontal stratigraphy, with several prominent reflectors. Drilling objectives were to recover a Paleogene and Cretaceous section to investigate climate change during an interval of long-term global warmth. Correlation with reflectors on the Southern High defined by Sliter and Brown (1993) was tentative. The most prominent reflectors on the Southern High, reflectors R1 of Cenomanian–Coniacian age and R2 of Barremian–Aptian age, are apparent on seismic profiles. The drilling strategy was to core through R2 in a first hole using the advanced piston corer/extended core barrel (APC/XCB), to core a second APC hole to refusal, and then to core a hole using the rotary core barrel (RCB) through R2. Finally, a full suite of logs was to be collected through the whole sequence.

A 622.5-m upper Barremian to Holocene section was penetrated at Site 1207. Recovery was excellent in the upper Campanian to Holocene section, but poor in the upper Barremian to lower Campanian, where chert horizons were extremely common. Results show a surprisingly

[1]Examples of how to reference the whole or part of this volume.
[2]Shipboard Scientific Party addresses.

Ms 198IR-103

different sedimentary sequence than the one previously documented at Deep Sea Drilling Project (DSDP) and Ocean Drilling Program (ODP) sites on the Southern High of Shatsky Rise. The Paleogene and uppermost Cretaceous sequence likely is missing as a result of major early Neogene slumping and erosion (Fig. **F1;** see also lines 5A and 5B in Figure **F7**, p. 13, in Klaus and Sager, this volume). Thus, we were unable to achieve our Paleogene objectives at this site. The middle Miocene to Pliocene section, on the other hand, is expanded (161 m thick), apparently complete, and composed of nannofossil ooze with diatoms that also contain planktonic foraminifers and radiolarians (Fig. **F2**). The section contains prominent carbonate cycles that appear to record orbital climate fluctuations. The section should provide a valuable biochronology as well as important information on the nature of ocean circulation changes.

At the opposite end of the stratigraphic column, a horizon of highly carbonaceous (up to 34.7 wt% organic carbon [C_{org}]) lower Aptian claystone that correlates to the global Oceanic Anoxic Event (OAE1a), including the Selli level of the southern Alps and Apennines of Italy, was recovered. Organic matter in these horizons is exceptionally well preserved. Organic geochemical, stable isotopic, and paleontological analyses of this C_{org}-rich interval will help constrain the environmental changes during OAE1a in the Pacific Ocean. Drilling at Site 1207 was impeded by the presence of chert throughout the lower Campanian to Barremian section. Drilling and logging at Site 1207 revealed important information about the nature and stratigraphy of this chert that will help develop strategies to improve recovery in such chalk/chert sequences.

Unique Neogene Section

Upper Miocene to Holocene sediments (lithologic Subunit IA) recovered at Site 1207 contain common to abundant diatoms (between 10% and 40%), a far higher proportion than in contemporaneous units from sites on the Southern High of Shatsky Rise. At Southern High Site 305, the relative proportion of diatoms is 5%–15% in the Miocene to Holocene section, but it decreases rapidly at the unconformity between the upper Miocene and the upper Oligocene (Larson, Moberly, et al., 1975). Diatoms were described as rare in samples from Sites 47 and 577 (Koizumi, 1975; Koizumi and Tanimura, 1985). Approximately 5° of latitude separates Site 1207 from the previously drilled sites on the Southern High, and it is feasible that this distance is associated with a significant change in oceanographic regime.

The abundance of diatoms in lithologic Subunit IA (0–131.3 meters below seafloor [mbsf]) sediments suggests that surface waters over Site 1207 were moderately to highly productive from the late Miocene to the Holocene. Alternatively, high biosiliceous production at Site 1207 may be an effect of local topographic upwelling. This option is not appealing given the absence of significant diatom concentration in sediments on the Southern High. More likely, the abundance of diatoms at Site 1207 reflects a component of productive subarctic surface waters over the site in the late Neogene. The relative proportion of diatoms is considerably lower in Subunit IB (131.5–162.5 mbsf) sediments, likely as a result of lower surface water productivity in the early middle to early late Miocene. The abundance of *Discoaster,* a nannoplankton genus thought to thrive in oligotrophic waters (e.g., Chepstow-Lusty et al., 1989) appears to be antithetical to the proportion of diatoms in the Neogene section.

F1. Interpretation of seismic reflection profile, Site 1207, p. 53.

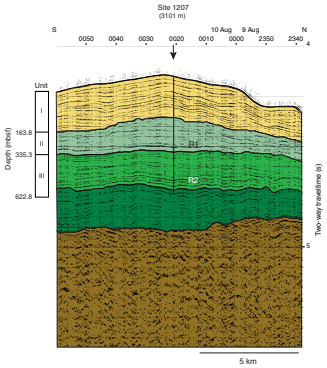

F2. Coring results, Hole 1207A, p. 54.

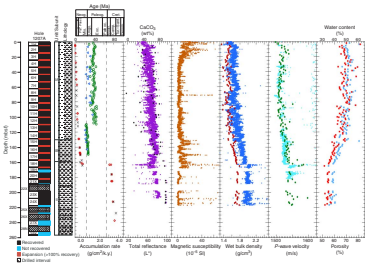

One of the most prominent features of the Neogene section at Site 1207 is the decimeter-scale lithologic cycles in Cores 198-1207A-1H to 18H between dominantly darker green-gray horizons and lighter tan-gray-white horizons. These cycles show significant changes in the relative percentage of diatoms (see **"Lithostratigraphy,"** p. 53, in "Specialty Syntheses" in the "Leg Summary" chapter) and marked differences in the nature of carbonate preservation. Reconstructions suggest that the site was above the calcite compensation depth (CCD) after at least the early Pliocene but close to this level in the Miocene (Rea et al., 1995); thus, the cycles could represent variations in dissolution as a result of changes in the depth of the lysocline. Variation in biosiliceous production may also be responsible for the cycles.

Today, Site 1207 lies in a subtropical water mass toward the north of the range of the warm water Kuroshio Extension Current. To the north of the site lies a significant front, a transition region between subtropical and subarctic water masses. Transition zone waters are derived from off the coast of northern Japan, where the cold, nutrient-rich Oyashio Current mixes with the warm, nutrient-poor Kuroshio Current. These waters move eastward across the Pacific in the West Wind Drift at a latitude of 40°–42°N. The location of Site 1207 is highly sensitive to past climatic variations because of its proximity to the transition zone.

Significant oceanographic changes occurred during the Neogene that had profound effects on circulation and distribution of water masses in the Pacific Ocean; these changes appear to be reflected in the sedimentary record at Site 1207. An event at 14.5 Ma has been associated with the formation of the East Antarctica Ice Sheet (Kennett et al., 1985); another event at 11 Ma is related to the closure of the Indo-Pacific seaway (Romine and Lombari, 1985). These events led to a steepening of temperature gradients and intensification of North Pacific gyral circulation including the ancestral Kuroshio Current. The modified circulation resulted in the development of a distinct North Pacific transitional water mass, separated from the northern subpolar region, and the northward displacement of temperate organisms. The development of distinct water masses in the North Pacific combined with long-term cooling may also be responsible for the marked facies change between lithologic Subunits IB and IA that corresponds to a sharp increase in biosiliceous material in sediments at ~9 Ma.

Koizumi (1985) correlated fluctuations in Pliocene–Pleistocene diatom communities at DSDP Sites 579 and 580 in the abyssal plain northwest of Shatsky Rise to climatic fluctuations that caused variation in the amount of subarctic waters at these sites. In colder intervals of the late Miocene to Pleistocene, Site 1207 may have been within the transition zone between the subtropical water mass and the subarctic water mass (Fig. **F3**), even though the site was well to the south of its current location (32°N at 10 Ma) (R. Larson, pers. comm., 2001). Thus, fluctuations in the proportion of diatoms, which are more abundant in subarctic than subtropical waters, may reflect latitudinal shifts in the position of the transition zone.

Shipboard biostratigraphic data suggest that nannofossils have suffered a greater amount of dissolution in greenish layers that are enriched in diatoms; preservation is considerably better in the white-gray ooze layers that have fewer diatoms. If the greenish layers correspond to cool intervals as argued above, then the pattern of preservation is opposite to that of most sites in the Pacific (e.g., Farrell and Prell, 1991; Zahn et al., 1991). A body of evidence suggests that during glacial stages intermediate deepwaters were produced in the Pacific and that these

F3. Changes in ocean circulation that led to cycles in upper Miocene to Holocene section, p. 56.

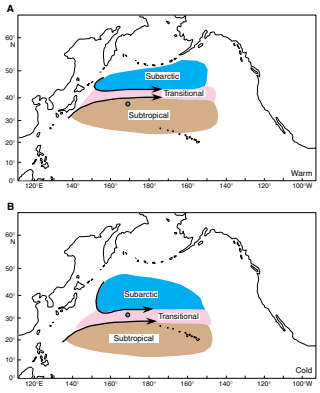

young, nutrient-poor waters caused little dissolution close to their source. An opposite pattern was noted at Site 882 on Emperor Seamount by Haug et al. (1995), who argued that the upwelling of nutrient- and CO_2-rich waters during glacial stages increased carbonate dissolution. Microfossils suggest a similar mechanism for dissolution patterns in the upper Miocene to Pleistocene at Site 1207.

A significant peak in opal accumulation rates occurs between 3.2 and 2.75 Ma at other sites from the northern Pacific (Haug et al., 1995; Maslin et al., 1995). The origin of this peak and subsequent decline is uncertain, but the base of this peak corresponds to the beginning of long-term global cooling that culminated in Northern Hemisphere glaciation, and the top of the peak corresponds to the rapid advance of Northern Hemisphere glaciers. Although qualitative in nature, a sharp rise in the abundance of diatoms occurs in the middle of Core 198-1207A-6H and continues up to the lower part of Core 198-1207A-3H. The age model indicates that this interval corresponds approximately to the 3.2- to 2.75-Ma period.

Origin of the 60-m.y. Hiatus

One of the surprises of drilling at Site 1207 was a major unconformity between the middle Miocene and upper Campanian. This hiatus represents ~60 m.y. of stratigraphic record. The unconformity lies at the base of a 3.3-m interval of zeolitic nannofossil clay (lithologic Subunit IC; 162.5–163.8 mbsf), at the center of which are a 5-cm Mn nodule and a few chert nodules. The interval has common micronodules of phosphate, volcanic glass, and grains of quartz, feldspar, and heavy minerals, as well as authigenic phillipsite crystals. Microfossils of Campanian and Miocene ages are mixed throughout the clay interval, possibly because of drilling disturbance. Very rare Paleogene nannofossils and foraminifers were observed in a few samples from this interval.

The age of the event(s) that caused the unconformity is difficult to interpret from the fossil record. The most likely age is an interval prior to the middle Miocene (16 Ma), the age of immediately overlying sediments. The presence of a Mn crust and micronodules, chert nodules, and zeolite minerals suggests an extended interval of seafloor exposure. A mixture of nannofossils of Campanian and Miocene ages suggests winnowing of underlying units after the hiatus. Paleogene microfossils hint at the presence of some intermediate section before removal during the hiatus interval.

Major unconformities are also found at Sites 49 and 50 near the base of the southwestern flank of the Southern High (4282 and 4487 m, respectively) (Table T1). At these sites, Pleistocene ooze directly overlies uppermost Jurassic or lowermost Cretaceous chalk. At Site 306 on the southern flank of the Southern High, Pleistocene sediments directly overlie those of Albian age. All of these sites are located on significant slopes; thus, it is likely that unconformities were produced by the removal of sediments by mass wasting. The unconformities at Sites 49 and 50 are characterized by zeolitic clay, common phillipsite, and Mn-coated rock fragments, chert, and ash pebbles. The core with mixed Albian and Quaternary at Site 306 contains Mn nodules and chert fragments.

Several possibilities exist for the origin of the major unconformity at Site 1207. A number of prominent hiatuses in the deep sea are caused by changes in the CCD resulting from shifts of carbonate deposition to shallow-water environments coincident with sea-level rise (e.g., Loutit

T1. Locations, depths, maximum ages, and ages of major unconformities, p. 116.

et al., 1988) or changes in deepwater circulation that increases the age of a water mass at a particular location. Although the subsidence history of Site 1207 is undetermined at the current time, and the history of the CCD in the Pacific is still somewhat uncertain, available information (Thierstein, 1979; Rea et al., 1995) suggests that the CCD was substantially deeper than the current depth of Site 1207 in early Miocene to late Eocene times (Rea et al., 1995). The curve of Rea et al. (1995) for the northwest Pacific indicates that Site 1207 was likely near or slightly below the CCD at some point in the Maastrichtian–middle Eocene. However, the sediment record on the Southern High suggests that the CCD history for Shatsky Rise is different from the history for the northwest Pacific developed by Rea et al. (1995). Indeed, a separate study (Thierstein, 1979) shows that the current depth of Site 1207 was substantially above the Pacific CCD in the Campanian–Maastrichtian. Given that the site must have been shallower than its current depth throughout the Campanian to Miocene interval, it is unlikely that dissolution is responsible for the unconformity.

A second possible mechanism for the unconformity is that sediments were removed from the top of the Northern High during one or a series of erosion, slumping, or mass wasting events. Seismic line TN037-5A shows an interval of disturbed, diagonal reflectors with thicknesses ranging to 100 m as far as 10 km to the north and south of Site 1207. These disturbed horizons may represent beds truncated by erosion or slumping (Fig. F4).

The depth and age distribution of Neogene deep-sea hiatuses have been studied in detail by Keller and Barron (1987). These authors found a prominent hiatus between 15 and 16 Ma in CN4, which corresponds to the minimum age of the major unconformity at Site 1207. Keller and Barron (1987) also observed that hiatuses in the depth range of Site 1207 are concentrated on plateaus, rises, and seamounts and suggested that they were most likely due to slumping events.

Site 1207 lies between basement highs to the east and west. The unconformity lies substantially below the level of the highs. Thus it is possible that this paleotrough served as a north-south conduit for bottom-water flow from the Cretaceous to the early Neogene. This flow may have steepened and undercut the sediments leading to slumping on the north and south of the present summit. In fact, a prominent canyon, which may have been produced by mass wasting, lies just to the north of Site 1207. Erosion would have been efficient while sedimentation rates were lower in the middle Miocene, but once productivity and, hence, sedimentation rates increased in the late Miocene, a sediment drape was established over the paleotrough.

In summary, results from Site 1207 show a drastically different sequence than anywhere on the Southern High of Shatsky Rise. Available seismic profiles suggest that sediments of Paleogene and latest Cretaceous age are not present on the Northern High as opposed to the Southern High, where these units are widespread. Conversely, the Miocene–Holocene section on Northern High is relatively expanded, whereas this sequence is thin or absent on the Southern High.

Early Aptian Oceanic Anoxic Event

A major highlight of Site 1207 is the recovery of a 45-cm-thick, dark brown, finely laminated C_{org}-rich claystone of early Aptian age in lithologic Unit III (335.3–622.8 mbsf). The presence of lamination indicates dysoxic or anoxic conditions at the seafloor for the duration of the

F4. Hypothesized sequence of events that produced major Campanian–Miocene unconformity, Northern High of Shatsky Rise, p. 57.

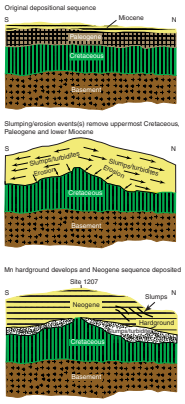

event. Organic carbon contents are extremely high (up to 34.7 wt%); characterization of this organic matter indicates it is algal and bacterial in origin. Gamma ray logging data suggest that an additional 50 cm of claystone was not recovered. Biostratigraphy indicates that this distinct horizon was deposited during OAE1a (Schlanger and Jenkyns, 1976; Bralower et al., 1993).

C_{org}-rich horizons of OAE1a age are also found at Sites 305 on Southern High, Shatsky Rise, 463 Mid-Pacific Mountains, and 866 (Resolution Guyot) (Sliter, 1989; Jenkyns, 1995). Only Sites 463 and 866 have decent recovery. The Site 1207 record extends the latitudinal and depth transect of this event in the Pacific Ocean. At Site 463 (2525-m water depth), carbonaceous limestones with up to 7.6 wt% C_{org} are associated with volcanic ash. At Site 866 (1373-m water depth), thin C_{org}-rich (14.2 wt%) claystones are found in a sequence of shallow-water carbonates. Organic matter characterization, including stable carbon isotope analysis indicate that the C_{org} in both sites is of algal marine origin (Dean et al., 1981; Baudin et al., 1995), similar to that at Site 1207.

Detailed microfossil biostratigraphic studies (Sliter, 1989; Bralower et al., 1994; Erba, 1994) have demonstrated that Site 463 C_{org}-rich horizons correlate exactly with carbonaceous units of early Aptian age known as the Niveau Goguel in southeastern France (Bréhéret, 1988), the Livello Selli type-level in central Italy (Coccioni et al., 1987), and the Livello Selli equivalents from the Italian and Swiss Alps, Sicily, DSDP Site 641 in the eastern North Atlantic, and northern Mexico (i.e., Weissert and Lini, 1991; Bralower et al., 1994; Erba, 1994; Menegatti et al., 1998; Erba et al., 1999; Bralower et al., 1999).

OAE1a is associated with abrupt changes in calcareous nannofossil assemblages, especially among a rock-forming group known as the nannoconids, which decline sharply in abundance just prior of the onset of the event (Erba, 1994). Other robust nannofossil taxa radiate and increase in size (Tremolada and Erba, 2002). Diversity and abundance of planktonic foraminifers decline rapidly prior to OAE1a. Planktonic foraminifers are absent at the base of the event as a result of dissolution then fluctuate from rare to few and from low to moderate diversity through the rest of the event. When present, taxa are mainly adapted to the poor oxygen contents in the upper water column (Magniez-Jannin, 1998; Premoli Silva et al., 1999). Radiolarians are abundant throughout but exhibit a marked compositional change at the beginning of the event (Premoli Silva et al., 1999).

The early Aptian event is marked by a distinctive carbon isotopic profile consisting of a ~2‰–3‰ negative shift at the base of the event followed by a ~4‰–5‰ increase. The pronounced negative excursion has been recognized at Site 866 on Resolution Guyot (Jenkyns, 1995), the southern Alps of Italy (Menegatti et al., 1998; Erba et al., 1999), the Isle of Wight (Gröcke et al., 1999), and northern Mexico (Bralower et al., 1999).

Early Aptian C_{org}-rich units that correlate to OAE1a have been found in a limited number of locations compared to the Cenomanian–Turonian Oceanic Anoxic Event (OAE2). This has led to some uncertainty as to whether the event was global in scale. Recovery of the early Aptian C_{org}-rich horizon at Site 1207 provides additional evidence that OAE1a was a global event. The record of OAE1a at Site 1207 is more complete than any other deep-sea record except possibly Site 463. The C_{org} contents are exceedingly high, and the burial depth is relatively shallow (565.5 mbsf). Hence, the organic geochemical records should be nearly

pristine. These and biotic records should provide key information on the environmental changes that occurred during the anoxic event.

Chert

Chert is a fundamental part of the Cretaceous stratigraphic section on Shatsky Rise. Unfortunately, little was known about the distribution and nature of chert. For example, it was unclear whether these units are nodular or layered or whether they are distributed randomly through the section or in individual zones.

The occurrence of chert in the Shatsky Rise section is thought to reflect its path across the equatorial divergence, where high productivity led to accumulation of opaline siliceous microfossils in the sediment. As the sediment was subsequently buried, this opal was progressively transformed to quartz. The stratigraphic distribution of chert in the sediment may yield important information about the width and strength of the equatorial divergence and whether this productivity varied in a predictable fashion (i.e., on orbital timescales); chert morphology may provide indications of the nature of the diagenetic process.

The uppermost chert horizon at Site 1207 lies in upper Campanian sediments at 76 Ma. Common chert is found from the lower Campanian (79–80 Ma) to the base of the hole (lithologic Units II and III; 163.8–335.3 and 335.3–622.8 mbsf, respectively). Assuming the reconstruction of R. Larson (pers. comm., 2001), these data suggest that the equatorial divergence was significantly wider than today, ranging to ~15° north of the equator. The presence of chert throughout the section indicates that the site remained within the equatorial divergence from the Aptian up to the early Campanian. In fact, the reconstructed path predicts that the site remained within the divergence for at least the first 60 m.y. of its history.

Anecdotal drilling information and logging data show that chert levels are extremely close together for the entire lower Campanian to upper Barremian section. Formation MicroScanner (FMS) data indicate that the cherts are generally finely layered as opposed to nodular and that most layers are <10 cm thick. However, interbedded soft sediment layers are <1 m thick and most often under 30 cm. These interbeds are mainly composed of ooze or soft chalk down to the Aptian, suggesting that the burial depths were never much greater than those at present. The softness of these interbeds exacerbated recovery efforts in the mid- and Upper Cretaceous interval.

BACKGROUND AND OBJECTIVES

Site 1207 is located in lower bathyal (3103 m) water depth close to the most elevated, central part of the Northern High of Shatsky Rise. According to the reconstruction of Nakanishi et al. (1989), basement underlying the site was formed in Magnetochron CM14 in the early Valanginian (~135 Ma). The site is located on seismic line TN037-5A (see Fig. **F1**).

Site 1207 is the northernmost in the Shatsky transect, some 5° north of the Southern High. Plate reconstructions suggest that this site exited the equatorial high-productivity zone ~5 m.y. before the Southern High (R. Larson, pers. comm., 2001), and thus the uppermost chert horizon should lie in an older part of the stratigraphic section. The paleodepth of this site is ~1200 m in the early Maastrichtian based on the estimate

of Barrera et al. (1997) for Site 305. Application of subsidence curves for normal oceanic crust (e.g., Sclater et al., 1971) yields a depth of ~500 m in the mid-Cretaceous and close to sea level at the time that the Northern High was formed. However, the site probably subsided rapidly initially, then followed a less steep curve than typical crust (e.g., McNutt et al., 1990).

The Northern High has not been drilled before; thus, the stratigraphy was unknown prior to our drilling of Site 1207. The ages of reflectors and the major seismic units cannot be correlated with the Southern High with any degree of certainty. Site 1207 drilling was designed to provide knowledge of the stratigraphy of the Northern High as well as correlation of units and reflectors with the Central and Southern Highs. The sedimentary section at Site 1207 is moderately thick (Fig. **F1**), ~1200 m, assuming velocity estimates from Site 305 and a tentative correlation of units. Tentative predrilling correlation with the Southern High seismic units of Sliter and Brown (1993) suggested a thick seismic Unit 5 (pre-Aptian) that is characterized by discontinuous reflectors, relatively thick Units 4 (Aptian–Turonian) and 3 (Turonian–Maastrichtian), with intervals marked by prominent reflectors separated from intervals with generally continuous, but weak reflectors. Seismic Units 2 and 1 (Neogene) at Site 1207 are relatively thin and show diffuse reflectors. These seismic data suggest that the Cretaceous section at Site 1207 is relatively expanded.

Site 1207 represents the northernmost site of the Leg 198 latitudinal transect and lies in the middle of the depth transect. Combined with the other sites in the transect, Site 1207 sediments will be used to:

1. Reconstruct changes in the properties of surface and deep waters through the Cretaceous and Paleogene. This will help to constrain the character and stability of intermediate- and deep-water circulation, vertical and latitudinal/thermal gradients, and basin fractionation during ancient intervals of extreme warmth.
2. Understand the significance of unconformities in the Shatsky Rise section and determine whether they are related to local or regional changes in ocean circulation (currents) or changes in carbonate production (i.e., CCD variations).
3. Determine long-term changes in biotic communities and how they relate to oceanographic and climatic evolution. In particular, we will monitor changes in the relative abundances of truly tropical and high-latitude planktonic foraminifers, nannoplankton, diatoms, and radiolarian species through time as well as planktonic and benthic (benthic foraminifers and ostracods) indicators for productivity variations.
4. Shed light on the origin of transient climatic events such as the mid-Cretaceous Oceanic Anoxic Events (OAEs) and determine the nature of chemical (i.e. CCD, nutrients, and oxygenation) and physical oceanographic changes (temperature gradients) during these events.
5. Understand water column stratification during mid-Cretaceous OAEs as well as obtain complete records of organic-rich sediments suitable for detailed paleontological and geochemical investigations. These data will allow us to more fully determine the response of marine biotas to abrupt environmental changes and to constrain changes in carbon and nutrient cycling during the OAEs.

6. Determine the timing of the equatorial crossing of Shatsky Rise as well as variations in the intensity of upwelling in this region through time by using the age of chert in the sedimentary section.
7. Determine the paleoceanographic factors controlling the origin and nature of orbital cycles in the Site 1207 sedimentary section.
8. Determine changes in the intensity of atmospheric circulation through time and how they relate to climate deterioration by using the Neogene section at Site 1207, which should contain an excellent clay mineral record.

OPERATIONS

Leg 198 officially began at 1100 hr on 27 August 2001 with passage of the first line ashore in Yokohama, Japan, ending Leg 197 ~19 hr early. At 0930 hr on 31 August, after 4 days of port call activities, the last line was released and the ship maneuvered into the harbor.

Transit from Yokohama to Site 1207

The transit to the first site was initially slowed by the presence of Typhoon Wutip, which was forecast to cross over Site 1207 about the same time as our full-speed arrival projection. To maintain a safe distance from the storm, we kept the correct course but at reduced speed for the first several days of the transit. As the typhoon increased speed and began moving to the northeast of the site, we increased our speed accordingly. Overall, the 1158-nmi, 5.2-day transit was accomplished at an average speed of 9.2 knots (kt). Upon arriving at the coordinates for the site, the thrusters and hydrophones were lowered at 1730 hr on 5 September, followed by deployment of a positioning beacon.

Hole 1207A

Once the vessel settled on location, an APC/XCB/motor-driven core barrel (MDCB) outer barrel assembly was assembled and the MDCB system was deck tested prior to deployment of the APC. After two unsuccessful attempts at obtaining a mudline core, a 4.82-m core was retrieved at 1225 hr on 6 September, initiating Hole 1207A. With the bit positioned at a depth of 3107 meters below rig floor (mbrf), the mudline core indicated a seafloor depth of 3111.7 mbrf, or 3000.7 meters below sea level (mbsl).

Piston coring advanced to 181.8 mbsf, with recovery averaging 103% (Table T2). Cores 3H through 18H were oriented. The advance-by-recovery technique was used for Cores 19H and 20H. Piston coring was terminated when these two successive cores failed to fully stroke, impeded by chert layers. We then switched to the XCB system.

T2. Coring summary, p. 117.

The first XCB core (Core 21X) was advanced 6.7 m, with good recovery (101%) until encountering a chert layer, which destroyed a soft formation XCB cutting shoe. A second XCB core barrel was deployed, equipped with a hard formation cutting shoe; however, only minimal advancement (0.1 m) was achieved after 1 hr of rotating time, no recovery, and the destruction of the hard formation shoe. An XCB center bit was then deployed to drill through the chert, advancing to a depth of 197.9 mbsf. Three successive cores were then cut (Cores 23X through 25X); the first two recovered 100% and 99%, respectively. Core 25X ad-

vanced only 2.0 m in 75 min rotating time with no recovery. The XCB center bit was deployed for a second time to drill through the chert. Another XCB core was attempted; however, Core 26X advanced only 2.0 m, recovering only a few chert fragments (5% recovery). The center bit was deployed for a third time to drill through a chert layer to a depth of 237.3 mbsf. Core 27X advanced 6.4 m recovering a few pieces of chert (1% recovery). The center bit was deployed for a fourth time to clean up the hole and hopefully clear any remnant carbide cutters and debris from the previously used XCB cutting shoe. Prior to recovering the center bit, a 30-barrel (bbl) mud sweep was pumped to aid in flushing any debris from the hole.

We then switched to the MDCB system in an attempt to increase recovery. Upon retrieval of MDCB Core 28N (5% recovery), drilling personnel observed that the core barrel had been heavily scoured. In addition to the scouring on the core barrel, the crown of the diamond bit was severely damaged. These observations suggested that either the MDCB bit had been in contact with a primary bit cone or that there was debris in the hole. Because of the doubt about the condition of the primary bit and hole, additional MDCB coring was suspended. A final XCB core was attempted with only 0.2 m advanced in 35 min. With no recovery in this core and concerns about bit and hole conditions, we decided to terminate coring in Hole 1207A at 256.6 mbsf in favor of RCB coring in Hole 1207B. Overall, the XCB was deployed for eight cores, with an average recovery of 71.1%. The drill string was retrieved, clearing the rotary table at 0015 hr on 9 September, ending Hole 1207A.

Hole 1207B

After retrieving the drill string, an RCB bottom-hole assembly (BHA) with a center bit assembly was deployed, and Hole 1207B was spudded at 1115 hr on 9 September. Approximately 4.25 hr was spent drilling the hole down to a depth of 157.0 mbsf and recovering the RCB center bit assembly. An RCB core barrel was deployed, and RCB coring advanced to a depth of 622.8 mbsf, taking 49 cores. As anticipated, recovery was poor through an interval of closely spaced chert layers interbedded with ooze. Coring parameters were varied continuously in an attempt to boost recovery. In addition, several core catcher configurations were also used, including flapper core catchers. Beginning with Core 40R, a combination of flapper core catcher and no core liner was used to minimize or eliminate jamming. Although somewhat unorthodox for coring in sedimentary strata, recovery did improve over the last 96.3 m. Improved recovery also coincided with increased lithification of the interbedded carbonate layers, so it is difficult to attribute improved recovery solely to coring without liners. Overall, recovery in Hole 1207B averaged 12.9%.

Coring was terminated when the depth objective was attained, and the hole was swept with 40 bbl of drilling mud, followed by a wiper trip to 159.9 mbsf. No overpull or drag was noted. During the return trip to bottom, 40 m of soft fill was noted and circulated out of the hole. Another 40-bbl mud sweep was conducted, and the bit was released. The hole was then displaced with 217 bbl of logging mud, and the pipe was tripped back and positioned at 126.4 mbsf in preparation for logging.

The first logging run was made with the triple combination (triple combo) tool suite (see **"Downhole Measurements,"** p. 27, in the "Explanatory Notes" chapter for details on the logging tools and see **"Downhole Measurements,"** p. 40, for further details on the logging

operations), which was deployed to a depth of ~621 mbsf, or within 1.5 m of total depth. A second pass with this tool suite failed to pass ~379 mbsf.

The second logging run included two passes with the FMS-sonic tool string. Both passes with this tool suite were also halted at a depth of ~379 mbsf. The third and final logging run was made with the geologic high-resolution magnetic tool (GHMT) tool suite and reached a depth of ~367 mbsf.

After completion of the logging operations, the drill string was retrieved, clearing the seafloor at 1715 hr on 13 September and ending Site 1207. Upon recovery of the beacon and retraction of the thrusters and hydrophones, the ship began the transit to Site 1208.

LITHOSTRATIGRAPHY

Description of Lithologic Units

The 622.8 m of sediment cored in two holes at Site 1207 consists largely of nannofossil ooze, clayey nannofossil ooze, chalk, limestone, and chert. Minor components throughout the sequence include foraminifers, diatoms, and radiolarians. Other minor to trace components include pyrite and silicoflagellates. Volcanic glass is a disseminated trace component and is concentrated in a few discrete ash layers in the Neogene portion of the sequence. The Neogene is characterized by pronounced color/lithologic cycles on a decimeter scale. A major unconformity/condensed interval representing the lower Miocene, Paleogene, and Maastrichtian consists of manganese oxides and clays. Chert layers are common in the lower Campanian through upper Barremian portion of the sequence. As a result of the interbedded chert, ooze, and chalk through much of the Cretaceous, recovery was poor and consisted primarily of chert (Table T3). Recovery improved somewhat near the bottom of the hole as the result of the predominance of limestone and coring without a core liner in place in the core barrel.

T3. Downhole variation in colors of recovered chert, Hole 1207B, p. 119.

The sequence has been subdivided into three major lithologic units. Unit I extends from 0 to 163.8 mbsf (Hole 1207A), the apparent base of the unconformity (middle Miocene over Campanian). Unit I consists primarily of nannofossil ooze interbedded with clayey nannofossil ooze or nannofossil ooze with diatoms. These variations are expressed as decimeter scale light–dark color cycles. Unit II begins at the base of the short condensed interval and/or hiatus at 163.8 mbsf (Hole 1207A) representing the early Miocene, Paleogene, and Maastrichtian and extends from there to 335.3 mbsf (Hole 1207B), encompassing the Campanian to Turonian. It consists of mottled to homogeneous nannofossil ooze and chalk with interbedded chert or chert nodules. Unit III consists of Cenomanian(?) through Barremian nannofossil limestone and chert, including a 45-cm-thick layer of dark C_{org}-rich mudstone in the lower Aptian. The exact placement of the Unit II/III boundary is difficult because of the low core recovery. Downhole logs also do not show any abrupt increase in bulk density in this interval. The color of recovered chert (Table T3) changes gradually downhole, but the transition from reddish hues to dominantly gray hues occurs near the Unit II/Unit III contact in the Turonian.

Leg 198 was the first to employ the digital imaging system, which at Site 1207 worked very well. Virtually immediate access to good digital images and the color reflectance data from the Minolta 2002 System

provides a powerful way to illustrate lithologic trends and events at high resolution. Carbonate data were obtained for calibration of smear slide estimates (see "Carbonate and Organic Carbon," p. 27, in "Organic Geochemistry") (Fig. F5), and some X-ray diffraction (XRD) data were also collected and main X-ray peaks identified (Table T4).

Lithologic Unit I

Intervals: 198-1207A-1H-1, 0 cm, to 18H-5, 102 cm, and 198-1207B-1R-1 through 1R-CC
Depths: 0 to 163.8 mbsf in Hole 1207A and 157.0–166.5 mbsf in Hole 1207B
Age: Holocene to middle Miocene

Subunit IA

Unit I has been subdivided into three subunits (Fig. F6). Subunit IA extends from 0 to 131.3 mbsf (Hole 1207A). It consists of alternating nannofossil ooze with diatoms, radiolarians, and clay in varying amounts (Fig. F7) and diatom/radiolarian or clayey nannofossil ooze, and is characterized by relatively low red/blue (680 nm/420 nm) ratios in color reflectance (Fig. F5). Periodic lithologic variations are expressed as decimeter-scale light–dark color cycles ranging in wavelength from 80 to 150 cm (Figs. F8, F9, F10). The thinner (30–50 cm) dark beds range from greenish gray (5G 6/1) to light greenish gray (5G 8/1) in color, whereas the thicker (~50–100 cm) light beds range from light olive gray (5GY 6/1) to light gray (N7). Color reflectance indicates that the cycle amplitudes are most pronounced in the upper part of the Pleistocene (Fig. F5). The contacts between the interbeds tend to be gradational from dark to light at the top, and sharp from light to dark at the bottom, overprinted by bioturbation (Figs. F9, F10).

Millimeter-scale pyrite laminae and blebs (Fig. F11) are common throughout this unit. Dark gray and green millimeter-scale "diagenetic" bands and laminae (Fig. F12) are randomly distributed, although they tend to be more frequent in the light intervals and around some lithologic contacts. Disseminated volcanic glass and discrete centimeter-thick ash bands are most frequent in the Pleistocene.

Common sedimentary structures include burrows and indistinct mottling. Bioturbation is rare to moderate throughout Unit I. This interval was recovered by the APC, and there is no indication of deformation by drilling. We noted a distinct scour surface at interval 198-1207A-12H-5, 77–79 cm. The contact occurs in a scoured light band overlain by a dark band and ash bed (Fig. F13).

Subunit IB

Subunit IB extends from 131.3 to 162.5 mbsf (Sections 198-1207A-15H-2 through 18H-5) and consists primarily of yellowish gray (5Y 8/1) to very pale orange (10YR 8/2) nannofossil ooze. The transition from Subunit IA is marked by a significant increase in the overall reflectance as well as in bulk density and a distinct color change from green-gray hues above to orange hues below. Carbonate content increases downhole in this unit (Fig. F5) to Core 198-1207A-17H (Fig. F14) in which clay content increases. Although radiolarians occur in this interval, siliceous microfossils generally are less abundant than in Subunit IA. The nannofossil ooze in Subunit IB is stiffer than the more siliceous nannofossil ooze above, and smear slides reveal signs of incipient dissolution and cementation of carbonate in the comparatively high carbonate

F5. Core recovery, lithologic units, age with biostratigraphic zonations, color reflectance, and percent carbonate, Hole 1207A, p. 58.

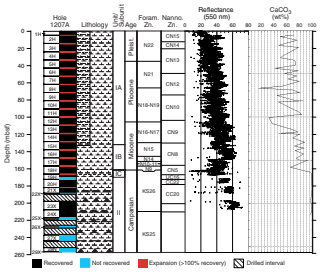

T4. Results of XRD analyses, p. 120.

F6. Core recovery, lithologic units, and age with corresponding biostratigraphic zonations, p. 59.

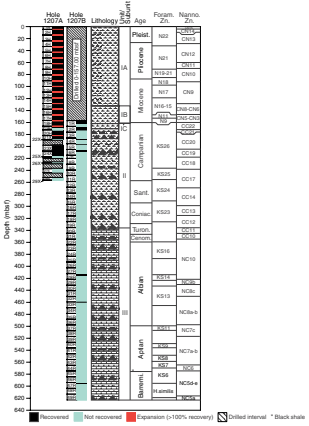

F7. Estimates of biosiliceous material, Hole 1207A, p. 60.

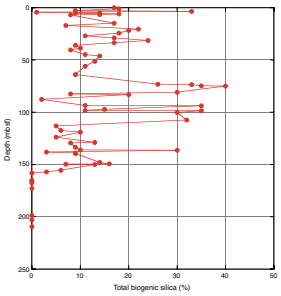

content oozes. Volcanic glass is generally a trace constituent. Burrows are common to abundant throughout Subunit IB, with *Zoophycos* as the only recognizable trace fossil (Fig. F15).

Subunit IC

Subunit IC is a thin interval of dark grayish brown (10YR 4/2) to light brownish gray (10YR 6/2) nannofossil clay with zeolites and manganese micronodules (Fig. F16) that extends from 162.5 to 163.8 mbsf and was recovered only in Hole 1207A (interval 198-1207A-18H-5, 25–102 cm). We attempted to recore this interval in Hole 1207B but failed to recover it. This subunit encompasses a major unconformity between the middle Miocene and the Campanian. The dark clay interval above the unconformity includes a 5-cm-thick Mn crust. Several dark brown chert nodules are present in the interval below the Mn crust. Twinned crystals of phillipsite (Fig. F17) are common. The base of the clay-rich and Mn micronodule-rich zone is intensely bioturbated and includes burrow fills of light-colored nannofossil ooze (Fig. F16). Early middle Miocene and rare Paleogene calcareous nannofossils were found below the Mn nodule layer to the base of the dark clay layer, indicating a highly condensed zone (see "Biostratigraphy," p. 18). Manganite and todorokite were identified as Mn-bearing minerals in XRD traces from this interval (Table T4).

Lithologic Unit II

Intervals: 198-1207A-18H-5, 102 cm, through 29N-CC and 198-1207B-2R-1, 0 cm, through 19R-1, 17 cm
Depths: 163.8–256.4 mbsf in Hole 1207A and 166.5–335.3 mbsf in Hole 1207B
Age: upper Campanian to lower Turonian

Unit II in Site 1207 consists primarily of dusky yellow-brown (10YR 4/2) to very pale orange (10YR 8/2) to grayish orange (10YR 7/4) nannofossil ooze with chert, that was fragmented and broken during drilling, in the lower part. There are decimeter-scale cycles in color as above, but they are shorter in wavelength (20–50 cm) and have much more subtle color transitions. Common sedimentary structures include faint burrows and mottles. Bioturbation is rare to moderate throughout Unit II. Intervals of relatively chert-free ooze are characterized by good recovery (essentially 100%), whereas recovery was poor or nonexistent in cherty intervals. Rotary coring in Hole 1207B resulted in lower recovery and more core disturbance.

Lithologic Unit III

Interval: 198-1207B-20R-1, 0 cm, through 49R-1, 39 cm
Depth: 335.3–603.5 mbsf
Age: lower Turonian to upper Barremian

Lithologic Unit III consists predominantly of light gray (N7) to greenish gray (5GY 6/1) limestone and chert of varying color from pale red (10R 6/3) to olive black (5Y 2/1) (Table T3). The top of Unit III is defined on the basis of the change from friable chalk to limestone, but this designation is rather arbitrary because we recovered very little chalk. In fact, little of this sequence was recovered, except for that below ~555 mbsf. There is a general trend in chert color downhole from reddish hues near

F8. Percent total color reflectance and percent carbonate, Hole 1207A, p. 61.

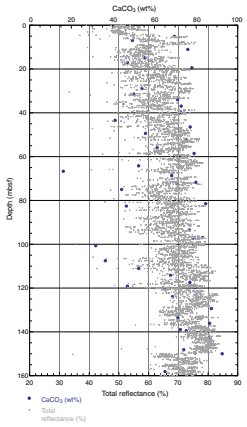

F9. Composite digital photograph, color reflectance, and bulk density, Core 198-1207A-2H, p. 62.

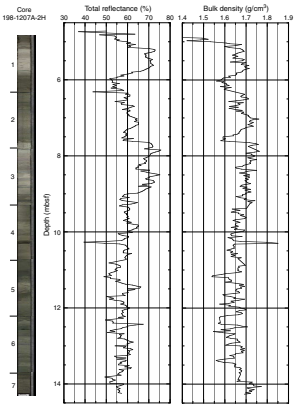

F10. Composite digital photograph, color reflectance, and bulk density, Core 198-1207A-5H, p. 63.

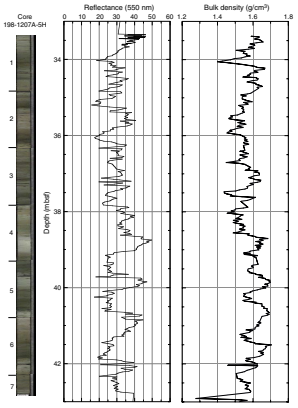

the top of Unit III to gray and black near the base (Table T3). Chert fragments often have inclusions and/or coatings of porcellanite. Although we did not recover intact bedding relationships, the FMS downhole log (see "FMS Image Logs and Cherts," p. 43, in "Downhole Measurements") indicates that many of the chert horizons are relatively thin bedded (10 cm) over much of the sequence but very closely spaced.

An interesting sequence of lower Aptian dark greenish gray (5GY 5/1) limestones was recovered in Section 198-1207B-43R-1. The limestones are highly bioturbated but intercalated with several thin (1–5 cm thick) beds of silt- and sand-sized material. These thin beds have sharp, erosive basal contacts and are only slightly bioturbated. Cross-lamination was observed in one bed. The silt- and sand-sized grains consist of pyritized radiolarians and, possibly, altered volcanic glass. These characteristics suggest possible episodic traction currents.

A spectacular aspect of the recovered interval is that of ~45-cm of dark-colored, C_{org}-rich claystone (interval 198-1207B-44R-1, 60–105 cm; Fig. F13) in the lower Aptian. Shipboard analyses indicate C_{org} contents ranging between 1.7 and 34.7 wt% (Fig. F18). This claystone is finely laminated throughout, although the lamination is very faint. Intervals of radiolarian silt occur at the base and in the upper part of the claystone. Contacts with units above and below were not recovered, but the interval recovered is intact. This unit is the apparent equivalent of the Livello Selli in Italy and other similar units worldwide that represent the deposits of so-called OAE1a (e.g. Sliter, 1989; Bralower et al., 1994).

The limestones in the lower Aptian and Barremian of Unit III are typically highly bioturbated and contain pyritized radiolarians and small nodules of pyrite. Compactional flattening of burrows is common, giving the appearance of streaks and laminae of darker color (typically shades of gray). *Planolites* was the only trace fossil identified. Chert is generally recovered as 1- to 5-cm-thick fragments with colors ranging from dark brownish red (10R 3/4) to grayish green (10G 4/2) and dark gray (N3) to black (N1) (Table T3). Some of the cherts are grainy and appear to represent chertified radiolarites, whereas others clearly represent silicification of limestones.

Thin Section Descriptions

Several thin sections were prepared from selected lithologies recovered at Site 1207 (see "Site 1207 Thin Sections," p. 78). A thin section of the manganese crust in Section 198-1207A-18H-5 at 44–47 cm is mostly composed of isotropic Fe-Mn minerals but in some areas shows fine-scale structures, including microstromatolitic banding and columns (Fig. F19). Locally, spherulitic clusters of zoned phillipsite crystals are included within the opaque groundmass that constitutes the majority of the Fe-Mn crust (Fig. F19).

The remainder of the thin sections were selected to document the nature of lithified sediments within the Cretaceous section. Most of the recovery in the pre-Campanian section consisted only of fragments of chert with adhering porcellanite and chalk. The nannofossil chalk, partly silicified nannofossil chalk (porcellanite) and chert, all contain varying amounts of foraminifers and radiolarians (see "Site 1207 Thin Sections," p. 78). Chert fragments in Campanian soupy ooze (Fig. F20) represent the first lithified sediment in the Cretaceous section. Minor chalk/limestone intervals show some silica cementation (Fig. F21). The transitions between chalk, porcellanite, and chert are illustrated in Figures F22, F23, F24, and F25. All phases of silica were noted. Opal occurs

F11. Visible pyrite blebs, p. 64.

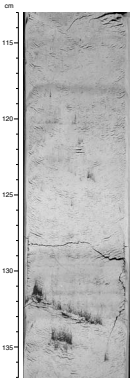

F12. Diagenetic laminae, light to dark cyclicity, mottled fabric, and pyrite blebs, p. 65.

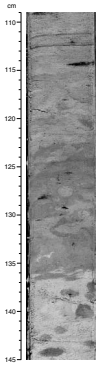

F13. Scour surface overlain by dark greenish gray volcanic ash, p. 66.

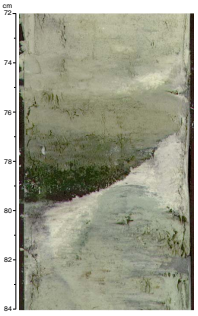

as unaltered radiolarian tests and as opaline cements, locally with lepisphere textures. The chalcedony and microquartz occur as replacements of radiolarian and foraminiferal tests and nannofossils, as well as pore-filling cements within microfossils and the matrix.

Interpretation

Sedimentation

Unit I

Sediment of Unit I was deposited under oxic conditions as indicated by its homogeneous to highly bioturbated nature. There is evidence of variations in productivity and/or carbonate dissolution in the prominent carbonate cycles that characterize most of the unit. The darker-colored intervals generally contain higher amounts of very well preserved biosiliceous material and probably represent intervals of higher surface water productivity. It is also possible that these intervals represent periods of higher carbonate dissolution. Based on average sedimentation rates of 18.4 m/my over the last 8 m.y. (see Fig. **F32**), the cycle frequency appears to be similar to that of glacial–interglacial cycles, with the dark beds representing glacials and the light beds representing interglacials. A preliminary analysis of the frequency of the dark–light cycles using color reflectance data (Fig. **F26**) suggests that the dominant period of the cycles corresponds to obliquity (41 k.y.) for the period from 0.6 to 2.5 Ma. The cold-water nature of the nannofossil assemblages (see **"Neogene,"** p. 18, in "Calcareous Nannofossils," in "Biostratigraphy") in the dark layers suggests that they represent "glacial" intervals, which in the Quaternary Pacific Ocean, were generally times of higher productivity with lower rates of carbonate dissolution. Thus, the prominent color and compositional cycles are similar to those observed elsewhere in the North Pacific (Haug et al., 1995). This character developed in Core 198-1207A-15H (Fig. **F14**) at a depth of ~132 mbsf (late Miocene; ~8.3 Ma) and continued through the Pleistocene. Peaks in abundance of biosiliceous material based on smear slide determinations (Fig. **F7**) occur at depths of 25–35 mbsf (latest Pliocene), 65–75 mbsf (early Pliocene), and 95–110 mbsf (latest Miocene–early Pliocene). These intervals are marked by significant decreases in bulk density that indicate zones of higher porosity because of the relatively low compressibility of biosiliceous-rich sediment (e.g. Core 198-1207A-5H; Fig. **F10**). The large changes in bulk density over intervals of a few meters give rise to prominent reflectors in the seismic reflection profiles over the site, creating a highly reflective Neogene–Quaternary sequence.

Below 132 mbsf (Subunit IB), the sediment is more oxidized, characterized by shades of pale orange and gray orange and an increase in the red/blue reflectance ratios. The carbonate content increases, giving rise to higher bulk density (Core 198-1207A-15H; Fig. **F27**), although biosiliceous material is present to a depth of 156 mbsf. Cyclic dark and light intervals are present from 132 to 156 mbsf, but the average thickness of the cycles is less than those found above 132 mbsf. The average sedimentation rate of Subunit IB is <2 m/m.y., which, when taken with the sediment composition, suggests that the oxidized character is a product of lower surface water productivity and slower sediment accumulation.

The character of seismic reflection profiles over the Northern High of Shatsky Rise suggests that the Neogene–Quaternary sequence is a drift deposit in which there is a systematic change in the thickness of that seismic unit (see **"Background and Objectives,"** p. 7). However, there

F14. Composite digital photograph, color reflectance, and bulk density, Core 198-1207A-17H, p. 67.

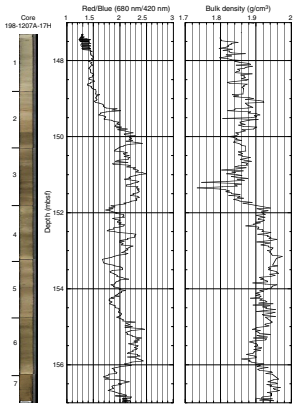

F15. *Zoophycos* burrows, p. 68.

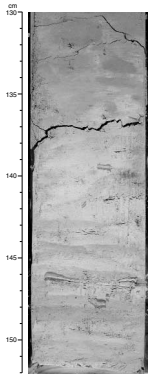

F16. Composite digital photograph, color reflectance, and bulk density, Core 198-1207A-18H, p. 69.

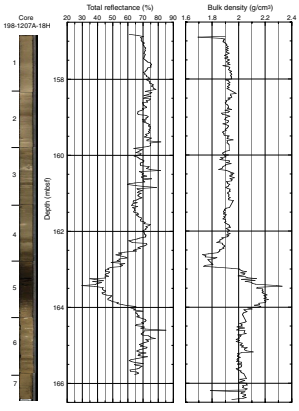

is no direct evidence in the cores for influence of deep currents sweeping the top of the North High during the Miocene–Pleistocene. We did not observe any winnowed, coarse-grained layers or laminae suggesting traction currents. Sharp contacts, several of which could be attributed to current erosion, were observed in several cores, most notably Core 198-1207A-5H (Fig. F13); however, there is no evidence of missing time at that level based on preliminary biostratigraphy. A sharp contact at the top of a dark layer in Core 198-1207A-17H (Fig. F14), at ~150 mbsf, may represent an unconformity or highly condensed interval based on several missing planktonic foraminiferal zones (N15 over N11). However, there is no obvious erosional feature in this interval, and carbonate contents remain relatively high (Fig. F5), although there is a concentration of sand-sized mineral grains and larger discoasters near the contact.

The character of Subunit IC suggests an unconformity and/or condensed zone that caps the Cretaceous sequence and is, in turn, overlain by Miocene strata. A manganese crust formed near the top of the contact, probably as the result of episodic or long-term seafloor exposure. It is not clear whether this interval represents several episodes of sedimentation followed by sediment removal by currents or a single episode of slumping followed by short-term exposure. Seismic reflection profiles to the north and south of the drill site exhibit somewhat chaotic reflections below the reflector that is interpreted as representing the top of the Cretaceous. Reflectors representing Upper Cretaceous horizons terminate against the overlying unconformity in all directions away from the site, suggesting an erosional origin for the unconformity. Unit I reflectors appear to onlap the unconformity to the east and west of Site 1207.

Unit II

It is possible that the undermining of the flanks of Shatsky Rise occurred as the result of a prolonged rise in the lysocline and CCD during the post-Maastrichtian, causing slumping of these units. However, the overburden on the Upper Cretaceous does not appear to have been too thick at any time as indicated by the unlithified oozes. It is more likely, however, that the unconformity represents one or more periods of erosion by strong bottom currents sweeping over the top of the rise. Away from Site 1207, the seismic reflection records indicate considerable truncation of underlying reflectors in the upper Cretaceous sequence against the reflector that represents the unconformity surface (Fig. F1). The downcutting appears to be greatest on the flanks of the Northern High.

Relatively pure nannofossil oozes and interbedded cherts indicate pelagic sedimentation on the northern part of Shatsky Rise during the Late Cretaceous as it moved northward on the Pacific plate away from a broad equatorial belt of high productivity. The input of biosiliceous material waned in the Campanian as indicated by the absence of chert layers in the upper Campanian oozes.

Unit III

A highlight of coring is the recovery of a 45-cm-thick dark brown, finely laminated, C_{org}-rich claystone of early Aptian age (Section 198-1207B-44R-1) (Fig. F18). This bed records deposition and preservation of C_{org} during part of OAE1a. The fine laminations suggest that anaerobic conditions prevailed at or above the seafloor on the Northern High of Shatsky Rise, which was located ~5°N at 120 Ma (see **"Background**

F17. Concentrations of tan/brown phillipsite crystals from the Miocene condensed zone, p. 70.

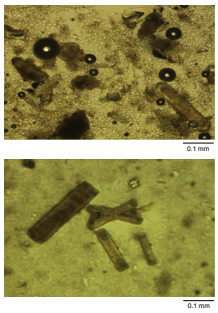

F18. Lower Aptian "Selli" level, a C_{org}-rich claystone, with total reflectance and organic carbon determinations, p. 71.

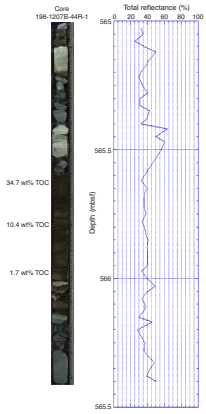

F19. Manganese crust from the Miocene condensed section, p. 72.

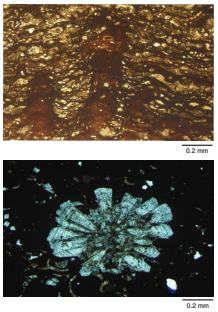

and Objectives," p. 7), the approximate time of OAE1a. It is possible that an expanded oxygen-minimum zone that developed within the equatorial divergence impinged on Shatsky Rise. The paleodepth of this part of Shatsky Rise was most likely shallower than 3 km at that time. Similar C_{org}-rich layers were recovered elsewhere in the Pacific Ocean at Site 463, on the Mid-Pacific Mountains, nearly 20° south of Site 1207, but possibly still within an expanded equatorial belt of high productivity. Moderate to abundant bioturbation throughout the remainder of the recovered section suggests oxygenated conditions prevailed during deposition.

In Section 198-1207B-43R-1, several thin (1–5 cm) layers of silt- and sand-sized material are interbedded with greenish gray (5GY 5/1) limestones. These layers have sharp, erosive basal contacts and a suggestion of cross-lamination. They contain altered glass, pyritized radiolarians, and other grains that appear to have been winnowed and transported by traction currents. These features might suggest that Shatsky Rise was swept by bottom currents during the Aptian following OAE1a.

Diagenesis

Unit I

Sediment of Unit I is unlithified but has experienced some compaction with depth, on the basis of trends in bulk density (see Fig. F45). The major feature of Unit I is its dominant green gray color and the relative abundance of pyrite. The low redox conditions probably result from a combination of relatively high productivity in surface waters and consequent high C_{org} flux to the seafloor with initial preservation under high average sediment accumulation rates. The sulfate concentration in interstitial waters decreases, and alkalinity increases somewhat downcore through Unit I (see Fig. F41), indicating that sulfate reduction has occurred as indicated by the observation of pyrite blebs and laminae in the sediments (Fig. F18). The low redox conditions and pyrite formation is accompanied by a pronounced decrease downhole in bulk magnetic susceptibility (Fig. F44) and magnetic intensity (Fig. F28), probably as a result of the dissolution of magnetic minerals. Another interesting redox-related feature is the common green to dark gray laminae and bands (Fig. F13) that have been termed "diagenetic laminae." These probably represent sites of precipitation of reduced iron that has migrated from darker, clay-rich intervals into lighter-colored, less clay-rich intervals. They usually occur within a few centimeters of the contact between intervals of darker and lighter colors. Such diagenetic laminae are also seen locally as halos around dark-colored burrows.

Unit II

Another intriguing aspect of diagenesis is the lack of cementation/lithification of nannofossil ooze of Late Cretaceous age. One would expect that the diagenetic potential in these oozes is relatively high because of the abundance of well-preserved calcareous nannofossils in them. The lack of lithification suggests that burial depths were never much greater than at present. This could be explained by frequent slumping and or current erosion of sediment deposited between the Campanian and middle Miocene. Although cementation did not occur to any great extent, rhombohedral micritic carbonate grains were observed in smear slides of the Campanian oozes. The presence of chert interbeds up to 10 cm thick indicates an active driver for silica diagenesis in the absence of significant carbonate diagenesis.

F20. Rim of chert fragment recovered within soupy white Campanian ooze, p. 73.

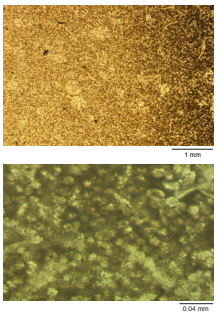

F21. Turonian nannofossil limestone/chalk with radiolarians, p. 74.

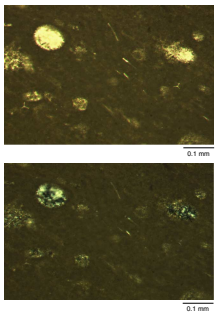

F22. Transition from nannofossil chalk to porcellanite to calcareous chert, p. 75.

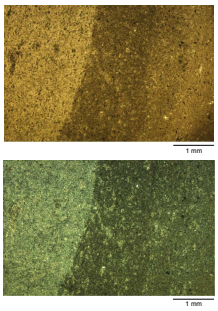

F23. Fragment of dark reddish foraminifer-radiolarian chert/porcellanite, Albian section, p. 76.

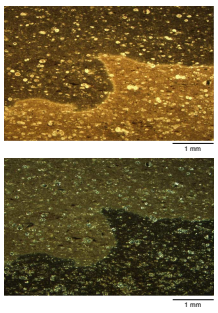

Unit III

The top of this unit marks the change to limestone. Strongly flattened burrows in much of the recovered limestone below 550 mbsf indicate considerable compaction prior to cementation. The gray to green colors and common pyrite and pyritized radiolarians indicate that low redox conditions prevailed after deposition.

BIOSTRATIGRAPHY

An apparently continuous upper Miocene to Pleistocene section of siliceous nannofossil ooze and nannofossil ooze was cored with the APC at Hole 1207A based on calcareous plankton biostratigraphy. An unconformity in Section 198-1207A-17H-2, 107 cm, separates the upper Miocene and middle Miocene and is marked by a sharp color change. A thin interval of middle Miocene nannofossil ooze (interval 198-1207A-17H-2, 107 cm, to 18H-5, 43 cm) overlies a 59-cm-thick condensed lower Miocene section containing reworked Paleogene and Cretaceous nannofossils. This condensed interval consists of darker-colored nannofossil clay capped by a manganese crust in interval 198-1207A-18H-5, 43–102 cm. An unconformity spanning nearly 60 m.y. is present at the bioturbated contact between dark yellow-brown lower Miocene nannofossil clay and dusky yellow-brown Campanian nannofossil ooze at 102 cm in Section 198-1207A-18H-5. The mid-Campanian to Barremian section cored at Site 1207 appears to be biostratigraphically complete.

All core catcher samples were examined, and additional samples were used to refine datums and zonal boundaries. Calcareous nannofossils are generally abundant and moderately to well preserved in Neogene and Cretaceous sediments of Holes 1207A and 1207B. Despite poor recovery in the Cretaceous section, diverse nannofossil assemblages were recovered in almost all intervals, from small sediment chips or from chalk/limestone scraped off chert pieces. In general, Neogene planktonic foraminifers are also moderately to well preserved, but foraminiferal abundances are relatively low because of selective dissolution and fragmentation. Foraminiferal abundance shows an inverse relationship to siliceous microfossil abundance. Moderately well preserved planktonic foraminiferal assemblages occur where calcareous ooze or chalk was recovered.

Studies of benthic foraminifers were conducted on selected core catcher samples. Benthic foraminifers are generally well preserved but rare or few in abundance. The >250-µm size fraction was examined for the Neogene samples, and the >125-µm size fraction was examined for the Cretaceous samples.

Calcareous Nannofossils

Neogene

The Neogene section ranges from lower Miocene (Subzone CN1b–Zone CN3) to upper Pleistocene (CN15) and appears to be relatively complete, at least within the biostratigraphic resolution achieved shipboard (Table T5). Nannofossils are abundant throughout, and preservation is moderate to good but deteriorates in the lower to middle Miocene nannofossil ooze. A number of short hiatuses may be present in the lower to middle Miocene interval. Most of the zones of Okada and Bukry (1980) were recognized, but division at subzonal level was not al-

F24. Zoned chert nodule from an Aptian section, p. 77.

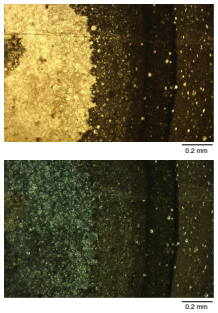

F25. Higher magnification view of contact between chert and porcellanite, p. 78.

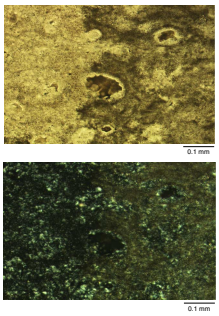

F26. Detrended color reflectance vs. age for the Pliocene–Pleistocene, with superimposed predicted angle of obliquity, p. 79.

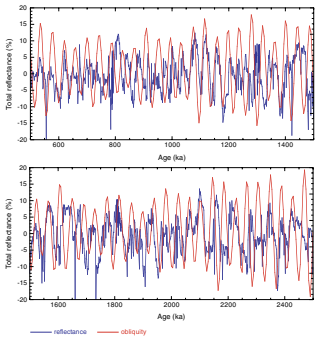

ways possible. In particular, the rarity or absence of sphenoliths and the rarity of discoasters prevented the recognition of a number of zones and subzones. The rarity of these two important nannolith groups suggests a common paleoenvironmental cause, the most likely being enhanced surface water productivity and cooler temperatures as supported by planktonic foraminiferal assemblages. Such conditions would have supported high abundances of r-selected noelaerhabdacean coccoliths, such as *Reticulofenestra, Gephyrocapsa,* and *Emiliania,* and excluded or reduced k-selected nannoliths, such as the discoasters and sphenoliths.

The thick Pliocene–Pleistocene section was subdivided using the standard Okada and Bukry (1980) markers; however, because the discoasters are rare throughout, their last occurrence (LO) should be viewed with caution. We were not able to identify the Pleistocene *Gephyrocapsa* subzonal events (first occurrence [FO] *Gephyrocapsa caribbeanica* and *Gephyrocapsa parallela*) due to difficulties in discerning these two taxa from other species of *Gephyrocapsa* and *Reticulofenestra* that were present in the assemblages. Notably *Reticulofenestra asanoi* (Section 198-1207A-2H-CC) and small reticulofenestrids were particularly abundant. The former taxon has a short range across the CN13/CN14 boundary.

The middle to upper Miocene section was divided using datums based on species of *Catinaster, Discoaster,* and *Amaurolithus,* but the subzonal marker species *Amaurolithus amplificus* was not observed and the ranges of *Discoaster kugleri, Discoaster hamatus,* and *Discoaster loeblichii* could not be satisfactorily resolved due to inconsistent ranges and poor preservation. The LO of the genus *Amaurolithus* was recorded at an anomalously low stratigraphic level relative to the FOs of *Discoaster asymmetricus* and *Ceratolithus rugosus,* and it plots off the age-depth line (Fig. **F32**). Rare *Amaurolithus* specimens may have been overlooked due to the abundance of siliceous material, which has similar birefringence and relief.

The oldest Neogene section is difficult to date and subdivide due to the absence of the sphenoliths, which are used to define the top and bottom of Zone CN2 and the bottom of Zone CN5. The exception was Sample 198-1207A-18H-4, 45–46 cm, which yields common *Sphenolithus heteromorphus* (Zone CN3–CN4). Samples below this level are tentatively dated as Subzone CN1b–Zone CN3, based on the exceptional abundance of *Discoaster deflandrei* (acme top within Zone CN3; Young, 1998) and the absence of older, robust taxa, such as *Cyclicargolithus abisectus, Reticulofenestra bisecta,* and *Zygrhablithus bijugatus,* which have LOs in Subzone CN1a and lower Subzone CN1b. The lowermost Miocene assemblage was observed in Sample 198-1207A-18H-5, 126 cm, just below the major color change within a clearly bioturbated interval and, notably, 83 cm below the prominent manganese crust. Our interpretation of the mixed zone is that the Campanian/Miocene boundary lies at the color change in Section 198-1207A-18H-5, 102 cm. The lowermost 60 cm of Miocene sediment contains prevalent Cretaceous (Campanian) reworking, which decreases upward from the color change. Consistent but rare Paleogene reworking was also encountered in an interval from 198-1207A-18H, 50 to 102 cm, consisting of late Paleocene–early Eocene taxa such as *Discoaster multiradiatus* and *Tribrachiatus orthostylus.*

Cretaceous

The Cretaceous section ranges from upper Campanian (Zone CC22) to Barremian (Subzones NC5d and NC5e) and appears to be complete, at least within the biostratigraphic resolution achieved shipboard. Nanno-

F27. Composite digital photograph, color reflectance, and bulk density, Core 198-1207A-15H, p. 80.

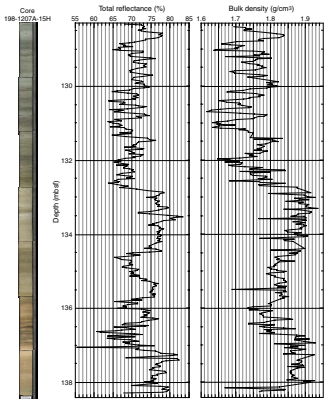

T5. Calcareous nannofossil datums, ages, and depths, p. 121.

fossils are generally abundant but variable in preservation. Overgrowth is prevalent in the Barremian and Turonian to Campanian intervals; good to pristine preservation was encountered in the Aptian and Albian.

A near-complete succession of nannofossil zones was recognized, and those that were not identified are most probably absent as a result of biogeographic and preservational factors or poor core recovery rather than incomplete stratigraphy. Many of the Sissingh (1977) CC Zones were recognized in the Upper Cretaceous section (Table T5). The relatively common and consistent occurrence of the *Aspidolithus parcus* coccoliths and *Ceratolithoides* and *Uniplanarius* nannoliths in the upper part of the Upper Cretaceous section allowed confident subdivision of the Campanian, and the youngest Cretaceous assemblages were placed in Zone CC22/Subzone UC15d (lower upper Campanian). Zones CC14 to CC19 could not be completely subdivided as a result of the absence of the holococcolith marker species of *Lucianorhabdus* and *Calculites,* the nannolith *Marthasterites furcatus,* and the coccolith *Reinhardtites anthophorus*. The latter two species are notoriously unreliable markers, and their absence is not entirely surprising. Holococcoliths are known to display shelf affinities (e.g., Burnett, 1998), which may explain their absence at this oceanic site. In addition, this interval yields the poorest preservation of the entire hole, and absences may be due to dissolution.

Zones NC6 to NC10 are all present, but the subzonal markers *Conusphaera rothii* and *Micrantholithus hoschulzii* were absent, almost certainly because of biogeographic exclusion, and we were unable to divide the *Hayesites irregularis-albiensis* plexus, thus missing the *Hayesites albiensis* datum. Subzone NC9a was not recognized as the FOs of *Eiffellithus monechiae* and *Axopodorhabdus albianus* corresponded to the same sample (198-1207B-29R-CC).

The age of the oldest sediments is problematic because of the lack of low-latitude datums in the Barremian interval. The age is given as Subzones NC5d and NC5e, based on the absence of *Hayesites irregularis* (FO in Sample 198-1207B-44R-CC) and absence of *Calcicalathina oblongata* (LO at 126.9 Ma). Inference of the latter datum is highly suspect because *C. oblongata* is rarely encountered outside the Tethyan biogeographic region. However, the presence of *Assipetra terebrodentarius* (FO mid–Subzone NC5c, close to the Barremian/Hauterivian boundary) in the deepest sample (198-1207B-49R-CC) provides a secondary datum that supports the Barremian age determination. The organic-rich horizon recovered in Core 198-1207B-44R lies within Zone NC6, between the FO of *Eprolithus floralis* (198-1207B-43R-CC) and the FO of *Hayesites irregularis* (44R-CC), strongly supporting the correlation of this interval with OAE1a.

Planktonic Foraminifers

Neogene

Planktonic foraminiferal abundance generally is low in the Neogene of Hole 1207A. Relatively low abundances of whole, moderately to well-preserved specimens of foraminifers and high abundances of foraminiferal fragments show that differential dissolution has modified the assemblages, particularly in the Pliocene–Pleistocene part of the section. Dissolution of planktonic foraminifers is likely to be at least partially responsible for the observed abundance of radiolarians and benthic organisms in the >63-µm sediment assemblages.

Temperate water species dominate many of the Neogene planktonic foraminiferal assemblages of Hole 1207A. The abundance of cool water taxa is the consequence of differential dissolution of the less heavily calcified and more porous tropical-subtropical species, as well as strong seasonality and/or high productivity. The abundance of the upwelling-indicator species *Globigerina bulloides,* together with an abundance of diatoms, radiolarians, and a healthy benthic fauna consisting of benthic foraminifers, echinoderms, ostracodes, and sponges, suggest that (seasonal) productivity was high at this site during much of the Pliocene and Pleistocene. Productivity may have also varied cyclically as suggested by the pronounced decimeter-scale color/lithologic cycles observed in lithologic Unit I (see **"Lithostratigraphy,"** p. 11). For example, dark-colored bands of siliceous nannofossil ooze in Samples 198-1207A-5H-1, 80–82 cm, and 5H-CC contain relatively few planktonic foraminifers and an abundance of the mat-forming diatom genus *Thalassiothrix,* whereas the white band in Sample 198-1207A-5H-4, 80–82 cm, contains a very similar assemblage of planktonic foraminifers but with very few diatoms and few radiolarians.

Common Pliocene–Pleistocene taxa include *Globigerina bulloides, Globorotalia inflata, Globorotalia crassaformis, Globorotalia puncticulata, Globoconella conomiozea, Neogloboquadrina dutertrei,* and *Neogloboquadrina pachyderma* (dextral). Persistent late Miocene taxa include *Orbulina universa, Neogloboquadrina acostaensis, Sphaeroidinellopsis seminulina,* and *Globoturborotalita nepenthes*. In general, species of the genus *Globigerinoides* are rare but persistent through the Neogene. No species of the tropical, dissolution-resistant *Pulleniatina* were observed. A 15- to 20-m-thick interval of the lower Pliocene (Sections 198-1207A-9H-4 to 11H-1), in particular, is marked by a low diversity assemblage dominated by *G. puncticulata, G. conomiozea,* and *S. seminulina*.

Many biostratigraphically useful tropical-subtropical taxa occur sporadically or in low abundances, including *Sphaeroidinella dehiscens, Globorotalia menardii, Globorotalia tumida, Globorotalia plesiotumida, Globorotalia merotumida,* and *Paragloborotalia mayeri* (Table **T6**). As a consequence, secondary marker taxa are used to make biostratigraphic assignments and/or confirm zonal assignments based on rare or sporadic primary marker taxa. For example, the FO of *G. crassaformis,* FO *G. puncticulata,* FO *G. conomiozea,* and the LO of *Globoturborotalita nepenthes* are used to delineate positions within Zone N19; the FOs of *Globorotalia margaritae, Globoconella cibaoensis,* and *Globigerinoides conglobatus* are useful within Zone N17.

T6. Planktonic foraminiferal datums, ages, and depths, p. 122.

A sharp lithologic break in Section 198-1207A-17H-2 marks an unconformity of ~2.5–3.5 m.y. that spans planktonic foraminiferal Zones N15 (upper Miocene) to lower N12 or upper N11 (middle Miocene). Reworked Late Cretaceous planktonic foraminifers occur sporadically in the middle Miocene sediments (Sections 198-1207A-17H-4 to 18H-4) below this unconformity. *Fohsella peripheroacuta, Fohsella peripheroronda, Globorotalia praemenardii, Globorotalia miozea, Orbulina universa,* and *Globoquadrina dehiscens* are characteristic taxa of middle Miocene Zones N9–N11 in Hole 1207A. Sample 198-1207A-18H-4, 78–80 cm, is assigned to Zone N9 based on the co-occurrence of *O. universa, Praeorbulina glomerosa,* and *Globigerinatella insueta* in the absence of *F. peripheroacuta.*

Cretaceous

Few small-sized Cretaceous planktonic foraminifers including *Heterohelix* spp., *Hedbergella holmdelensis,* and schackoinids, together with rare Miocene taxa, occur in Sections 198-1207A-18H-5 and 18H-6 below the

horizon with manganese nodules. The underlying Cretaceous assemblages (Sample 198-1207A-19H-1, 26–28 cm, to 21X-3, 26–28 cm, and Core 198-1207B-2R) are characterized by the absence of age-diagnostic taxa and are dominated by small-sized heterohelicids, hedbergellids, globigerinelloidids, and juvenile globotruncanids. A moderately well preserved mid-Campanian assemblage occurs in Sections 198-1207A-21X-3 through 23X-CC and 198-1207B-3R-CC through 9R-CC (Table T6). *Globotruncana arca, Globotruncana orientalis, Globotruncanita elevata, Globotruncanita atlantica,* and *Globotruncanita stuartiformis* are common in the large size fraction (>250 µm), whereas *Hedbergella holmdelensis, Globigerinelloides messinae, Globigerinelloides ultramicrus, Heterohelix globulosa, Heterohelix dentata,* and *Heterohelix planata* dominate the small size fractions (45–250 µm). Few specimens of *Schackoina cenomana* and *Schackoina multispinata* are also present. Based on the presence of *G. atlantica,* this latter interval is assigned to the mid-Campanian *Globotruncana ventricosa* Zone (KS26). The lower Campanian *Globotruncanita elevata* Zone (KS25) is recorded at the bottom of Hole 1207A (Sample 198-1207A-24X-CC) based on the absence of *G. atlantica* and presence of common *G. elevata.*

In the remainder of the Cretaceous sequence, planktonic foraminifers could only be collected in a few cores because the very low recovery was dominated by chert fragments with rare carbonates. Consequently, few biozones are recognized. The biostratigraphic resolution based on planktonic foraminifers may improve with the study of indurated lithologies in thin section. Sample 198-1207B-18R-CC, 37–39 cm, yielded a few specimens of *Hedbergella holmdelensis* and rare specimens of the long-ranging *Hedbergella planispira* and *G. ultramicrus.* Because *H. holmdelensis* seems to appear in the *Dicarinella concavata* Zone (KS23), this assemblage is probably not older than Coniacian.

Few *Rotalipora appenninica, Ticinella madecassiana,* and *Praeglobotruncana delrioensis* are recorded from Cores 198-1207B-22R through 24R, indicating correlation of this stratigraphic interval to the upper Albian *R. appenninica* Zone (KS16). The presence of *Biticinella breggiensis* together with rare to few *Ticinella praeticinensis, Ticinella roberti, T. madecassiana, Globigerinelloides bentonensis,* and *Hedbergella delrioensis* in Sample 198-1207B-28R-CC, 11–16 cm, in the absence of *Ticinella subticinensis,* indicates the *T. praeticinensis* Subzone of the *Biticinella breggiensis* Zone (KS14) of early late Albian age. Samples 198-1207B-30R-CC and 33R-1, 103–104 cm, contain *Ticinella primula, Ticinella raynaudi, T. roberti, Hedbergella rischi,* and *H. planispira.* These two levels are assigned to the middle Albian *Ticinella primula* Zone (KS13) based on the presence of *T. primula* and the absence of *B. breggiensis.*

Rare *Globigerinelloides barri, Globigerinelloides blowi, Globigerinelloides aptiense,* and "*Hedbergella delrioensis*" are recorded in Sample 198-1207B-40R-CC, 15–17 cm. This level is assigned to the upper Aptian *Globigerinelloides algerianus* Zone (KS9) based on the presence of *G. barri,* whose range closely overlaps with that of the nominate taxon (Sigal, 1977). The presence of *"H. delrioensis"* and *G. blowi,* which both first occur in Sample 198-1207B-43R-CC, 20–21 cm, may indicate the *G. blowi* Zone (KS6). In the oldest sample studied (Sample 198-1207B-47R-3, 79–81 cm), the presence of *Clavihedbergella eocretacea, Clavihedbergella semielongata, Hedbergella sigali, Hedbergella similis,* and *Gubkinella graysonensis* indicates the *Hedbergella similis–Hedbergella kuznetsovae* Zone of Barremian age according to Coccioni and Premoli Silva (1994).

Thin Section Analysis

Planktonic foraminifers have been studied in a number of thin sections cut from indurated Cretaceous sedimentary rocks, mainly chert and porcellanite. Planktonic foraminiferal abundance and preservation vary from sample to sample depending on the degree of rock silicification. Planktonic foraminifers may become visible with crossed nicols or brightfield or both. Calcitic foraminiferal tests are frequently preserved and often recrystallized. The calcitic wall rarely is replaced by silica, but frequently both types of preservation occur in the same sample.

The biostratigraphy of certain intervals can be constrained, and some biozones were recognized. The distribution of planktonic foraminifers identified in thin section is shown in Table T7 along with abundance estimates of benthic foraminifers, radiolarians, and other fossil groups.

T7. Distribution of Cretaceous planktonic foraminifers in indurated lithologies, p. 123.

The occurrence of *Dicarinella asymetrica* in Sample 198-1207B-15R-CC, 12–15 cm, identifies the base of the nominal zone (KS24) of Santonian age. The top of the zone, which lies very close to the Santonian/Campanian boundary, corresponds to the disappearance level of the marginotruncanids in Sample 198-1207A-28N-1, 3–4 cm.

Core 198-1207B-16R is attributed to the *D. concavata* Zone (KS23) of Coniacian age, based on the presence of the nominal species. The *D. concavata* Zone is extended to include Sample 198-1207B-18R-CC, 14–15 cm, which yields common whiteinellids, along with *Globigerinelloides bollii, Hedbergella flandrini, Marginotruncana coronata*, and *Marginotruncana tarfayaensis*. The occurrence of the latter taxon supports this zonal assignment, as *M. tarfayaensis* is known to appear just prior to the base of the *D. concavata* Zone close to the base of the upper Turonian.

Core 198-1207B-37R is assigned to the latest Aptian *Ticinella bejaouaensis* Zone (KS11) based on the presence of the nominal species along with *Hedbergella trocoidea* and a possible *Planomalina cheniourensis*. The occurrence of *Globigerinelloides ferreolensis,* together with rare *Hedbergella trocoidea, "H. delrioensis,"* and *G. aptiense*, indicates that the assemblage from Sample 198-1207B-42R-CC, 40–41 cm, may correlate to the late Aptian *G. ferreolensis* Zone (KS8) or possibly to the *Globigerinelloides algerianus* Zone (KS9).

The oldest foraminiferal fauna observed in thin section from Hole 1207B occurs in Sample 198-1207B-46R-1, 96–98 cm, and is assigned to the *Globigerinelloides blowi* Zone (KS6) of late Barremian age.

Benthic Foraminifers

Neogene

In Sample 198-1207A-1H-CC, ~50% of the benthic foraminifers belong to spinose uvigerinids such as *Uvigerina hispida* and *Uvigerina hispidocostata* (Table T8). Other characteristic components are *Cibicidoides wuellerstorfi, Melonis sphaeroides, Pyrgo lucernula,* and *Pyrgo murrhina*. *Melonis sphaeroides* represents more than 30% of the assemblage in Sample 198-1207A-4H-CC. Other important components are *Pyrgo lucernula, P. murrhina, Oridorsalis umbonatus, U. hispida,* and *Eggerella bradyi*. In Sample 198-1207A-6H-CC, the assemblage is characterized by abundant *C. wuellerstorfi, P. lucernula, P. murrhina,* and *U. hispida*.

T8. Neogene benthic foraminifers, p. 124.

The main components of benthic foraminifers in Sample 198-1207A-8H-CC are *C. wuellerstorfi*, gyroidinoids, *Pullenia bulloides, Oridorsalis umbonatus, Pyrgo lucernula,* and *P. murrhina,* along with agglutinated forms such as *Eggerella bradyi, Haplophragmoides* spp., and *Karreriella bradyi*.

Sample 198-1207A-11H-CC contains well-preserved and diverse benthic foraminifers. The assemblage is mainly composed of *Gyroidinoides neosoldanii, Gyroidinoides girardanus, O. umbonatus, P. bulloides, P. lucernula, P. murrhina, Stilostomella abyssorum, U. hispida, U. hispidocostata, Haplophragmoides* spp., and *K. bradyi*. Smaller numbers of *Cibicidoides cicatricosus, Cibicidoides incrassatus,* and *Cibicidoides subhaidingeri* are also included. Sample 198-1207A-12H-CC of late Miocene age is characterized by such taxa as *O. umbonatus, G. girardanus, Nonion* spp., *P. bulloides, P. lucernula, P. murrhina,* and *E. bradyi*. In Sample 198-1207A-15H-CC, benthic foraminifers show moderate preservation and low abundance. The most common taxa in this sample are *O. umbonatus* and *S. abyssorum*. *P. lucernula* and *P. murrhina,* the dominant species in overlying samples, are markedly less abundant.

The middle Miocene Sample 198-1207A-17H-CC contains common, well-preserved benthic foraminifers. The main taxa are *Anomalinoides globulosus, C. wuellerstorfi, C. subhaidingeri, O. umbonatus, P. bulloides,* and *Stilostomella subspinosa*. Sample 198-1207B-1R-CC yields few moderately preserved benthic foraminifers, including *A. globulosus, Pullenia bulloides, S. abyssorum,* and *S. subspinosa*.

Neogene benthic foraminifers indicate upper abyssal paleowater depths (2000–3000 m) (Woodruff, 1985; van Morkoven et al., 1986) at Site 1207.

Cretaceous

In the interval representing the early to middle Campanian (Samples 198-1207A-18H-CC through 23X-CC and 198-1207B-2R-CC through 6R-CC), benthic foraminifers show moderate to good preservation but are rare to few in abundance (Table **T9**). Calcareous trochospiral benthic taxa (*Conorbinoides hillebrandti, Nuttallides truempyi, O. umbonatus, Osangularia plummerae,* and gyroidinoids), *Dentalina* spp., and *Lenticulina* spp. generally characterize the assemblage, although *Gaudryina pyramidata* is absent in the lower Campanian. Most specimens are small (125–250 µm).

T9. Cretaceous benthic foraminifers, p. 125.

Sample 198-1207B-9R-CC contains benthic foraminiferal components similar to those observed higher in the Campanian, except for the absence of *O. umbonatus*. Because of the presence of chert and poor recovery, no useful core catcher samples were available from Sample 198-1207B-10R-CC through 21R-CC. In Samples 198-1207B-22R-CC and 24R-CC, benthic foraminifers are poor to moderately preserved and rare to few in abundance. Most specimens are small (125–250 µm). Calcareous trochospiral forms such as *Gavelinella* sp., *Gyroidinoides globosus, Gyroidinoides infracretaceus, Hanzawaia ammophila, Protosangularia albiana,* and *Protosangularia cenomaniana,* along with *Serovaina lobulata, Dentalina* spp., *Lenticulina* spp., *Saracenaria* spp., *Spiroplectammina excolata,* and *Pseudoclavulina globulifera* characterize the benthic assemblage.

Samples 198-1207B-28R-CC, 30R-CC, and 33R-1, 103–104 cm, are middle to late Albian in age. The samples are characterized by calcareous trochospiral such as *H. ammophila, P. albiana, P. cenomaniana, Serovaina lobulata, G. infracretaceus,* and agglutinated taxa (*Pseudoclavulina globulifera, Remesella* sp., *Dorothia* spp., and *Gaudryina dividens*). Test preservation is poor to moderate and abundance is few. Almost all specimens are small (125–250 µm).

In the Aptian to Barremian interval, useful benthic foraminifers are found in only two core catcher samples (198-1207B-43R-CC and 47R-CC). Sample 198-1207B-43R-CC contains poorly preserved but abun-

dant benthic foraminifers. The main components are quite different from those observed upsection and are dominated by nodosariids, unilocular forms, and *G. dividens*. In Sample 198-1207B-47R-CC, benthic foraminifers show poor preservation but high abundance. The assemblage is represented by *Dentalina* spp., *Lenticulina* spp., *Oolina* spp., *Pyrulina* spp., and abundant *Marssonella* sp.

Benthic foraminiferal evidence suggests a deepening upward trend from upper lower bathyal (~1000–1500 m water depth) in the Barremian–Aptian to upper abyssal depths (~2000–3000 m) by Campanian time.

PALEOMAGNETISM

All archive halves of core sections from Hole 1207A that did not show a large degree of drilling-related deformation were measured on the shipboard pass-through magnetometer. Of the top 21 cores from Hole 1207A, only Core 198-1207A-19H was excluded owing to drilling disturbance. Measurements were also made on the least disturbed sections from the RCB cores from Hole 1207B: Cores 198-1207B-1R through 3R. Natural remanent magnetization (NRM) was measured for each core section, followed by two to four steps of alternating-field (AF) demagnetization up to a maximum peak field of 20 mT. The maximum peak field was set at this level in order not to compromise the archive sections for possible shore-based (u-channel) studies. Magnetization intensities of NRM and magnetization intensities after AF demagnetization at peak fields of 20 mT are in the 10^{-1}–10^{-2} A/m range near the seafloor but fall to 10^{-3}–10^{-4} A/m at 30 mbsf (Fig. **F28**). This decrease may be the result of diagenetic reduction of remanence-carrying magnetite in the upper part of the sedimentary section. The plot of magnetic remanence intensity vs. depth shows several oscillations between 30 and 100 mbsf, probably indicating variation in the amount or preservation of magnetic minerals. These variations are mimicked by the curve of iron content vs. depth (see **"Inorganic Geochemistry,"** p. 33).

In those parts of the record where the remanence intensity is slightly higher (above ~5×10^{-4} A/m at the 20-mT AF demagnetization step), it is possible to interpret the 20-mT AF demagnetized inclination and declination values in terms of polarity zones. In regions of low magnetization intensity, however, the record is uninterpretable. The cores provide a clear record of C1n (Brunhes Chron), C1r.1n (Jaramillo Subchron), and C2n (Olduvai Subchron) in the upper 30 mbsf (Fig. **F29**). Below this depth, however, the record is compromised by low remanence intensities, which average about one order of magnitude above the noise level of the shipboard magnetometer (the noise level of the magnetometer corresponds to a magnetization intensity of ~3×10^{-5} A/m). We tentatively interpret a thick reverse polarity interval at 100–110 mbsf as C3r (base of the Gilbert Chron) and a thick normal polarity zone at 141–152 mbsf as C5n (Fig. **F29**). Other polarity zones are shown in Figure **F29** but are uncertain because the polarity zone pattern is nonunique owing to intervals of uninterpretable polarity or erratic directions (colored gray in the figure) and at least one significant unconformity (interpreted from biostratigraphic data to be at the base of C5n). Shore-based studies should allow the polarity record for Hole 1207A to be refined.

An age-depth curve for the upper 150 mbsf (Fig. **F30**) implies a mean interval sedimentation rate of 14–21 m/m.y. for the last 7 m.y. Prior to 7 Ma, the mean interval sedimentation rate is only ~5 m/m.y. This age-

F28. Archive-half magnetization intensities after AF demagnetization at peak fields of 20 mT, Hole 1207A, p. 81.

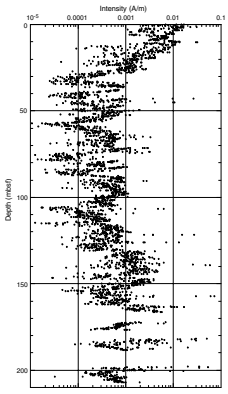

F29. Inclination after AF demagnetization at peak fields of 20mT, Hole 1207A, p. 82.

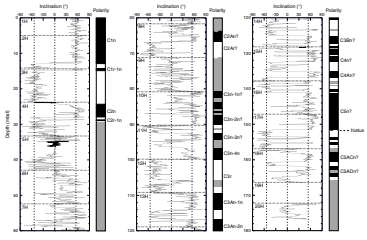

F30. Age-depth curve derived from magnetic stratigraphy, p. 83.

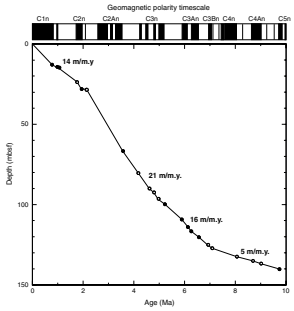

depth curve agrees well with biostratigraphic datums, but this is partly because of the use of biostratigraphic datums to aid interpretation of polarity zones in the polarity record. The figure shows that only a few polarity chron interpretations are considered robust (solid circles).

Measurements from Cores 198-1207B-1R through 3R show a stable magnetization component with mean magnetization intensity after AF demagnetization at peak fields of 20 mT of ~5×10^{-4} A/m. Normal polarity magnetizations are consistent with deposition in the late Campanian, during C33n or C32n. One short, 30-cm reversed interval was found in Section 198-1207B-2R-4.

SEDIMENTATION AND ACCUMULATION RATES

Changes in sedimentation rate in Holes 1207A and 1207B are illustrated in a plot of calcareous microfossil datum ages (first and last occurrences) vs. depth (Fig. F31). These rates rely on major calcareous nannofossil and planktonic foraminiferal datums presented in Tables T5 and T6. A hiatus of nearly 60 m.y. separates the Neogene and Cretaceous sediments at Site 1207. An expanded view of the Neogene (Fig. F32) shows that the lower middle Miocene is condensed (~0.5 m/m.y.), followed by increasing rates of sedimentation: 4.3 m/m.y. in the upper middle Miocene, 8.5 m/m.y. in the upper Miocene, and 18.4 m/m.y. in the uppermost Miocene–Pleistocene interval. The Barremian–Campanian part of the section (Fig. F33) accumulated at a nearly constant rate of ~8.7 m/m.y.

Mass accumulation rates for the bulk sediment, carbonate, and noncarbonate fractions were calculated using dry bulk density (see "Index Properties," p. 40, in "Physical Properties") and carbonate concentration (see "Organic Geochemistry," p. 27) data through two linear sedimentation rate segments in the Neogene. Two segments are defined: (1) 0 to 107.41 mbsf (uppermost Miocene–Pleistocene) and (2) 107.41 to 150.00 mbsf (upper Miocene). These segments were chosen to reflect the major changes in sedimentation rate shown in Figure F32. Because of poor recovery through chert-rich intervals, it was not possible to calculate reliable mass accumulation rates for the Cretaceous section recovered at Site 1207.

Bulk sediment accumulation rates for the upper Miocene section average 0.8 g/cm²/k.y., and average carbonate and noncarbonate fraction accumulation rates are 0.6 and 0.2 g/cm²/k.y., respectively. Both bulk sediment and carbonate accumulation rates decrease gradually through late Miocene time (9.7–5.8 Ma). The average accumulation rate of the noncarbonate fraction remains uniform. A significant increase in accumulation rates coincides with the increase in sedimentation rates at 107.41 mbsf (5.82 Ma). Uppermost Miocene–Pleistocene bulk sediment accumulation rates average 1.4 g/cm²/k.y. Average accumulation rates for the carbonate and noncarbonate fractions during the same time period are 0.9 and 0.5 g/cm²/k.y., respectively. Although, on average, bulk accumulation rates remained relatively constant during latest Miocene to Pleistocene time, there were significant changes in the relative rates at which carbonate and noncarbonate fractions accumulated (Fig. F34). Overall, the decrease of carbonate accumulation rate is balanced by an increase of noncarbonate material, reflecting the increase in abundance of ash and siliceous microfossils, especially in the Pliocene–Pleistocene section (see "Lithostratigraphy," p. 11).

F31. Age-depth plot of calcareous nannofossils and planktonic foraminiferal datums, p. 84.

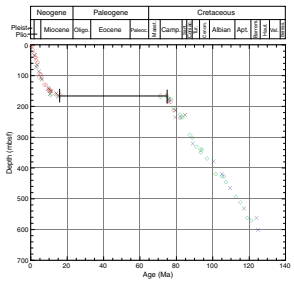

F32. Age-depth plot of Neogene calcareous nannofossil and planktonic foraminiferal datums, Hole 1207A, p. 85.

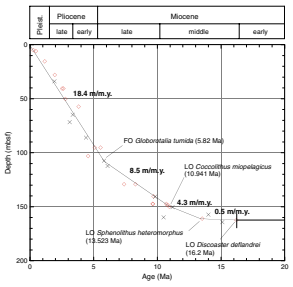

F33. Age-depth plot of Cretaceous calcareous nannofossil and planktonic datums, p. 86.

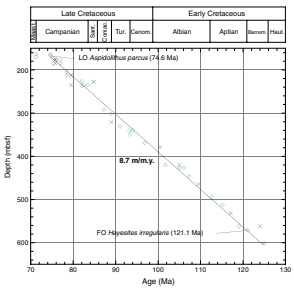

F34. Mass accumulation rates vs. depth and age for the Neogene, Hole 1207A, p. 87.

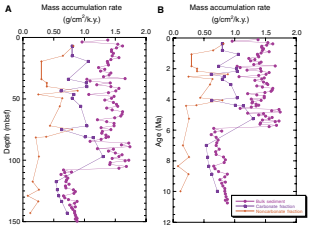

ORGANIC GEOCHEMISTRY

Volatile Hydrocarbons

Headspace gas analysis was conducted as part of the standard protocol required for shipboard safety and pollution prevention monitoring. A total of 23 cores from Hole 1207A were evaluated (Table T10). The concentrations of CH_4 were extremely low (≤3 µL/L [ppmv]); no hydrocarbon gases higher than C_1 were detected. The downhole profile of CH_4 concentration in Hole 1207A shows a subsurface maximum in gas concentrations (Fig. F35), which is perhaps attributable to methanogenic bacterial activity in the near subsurface, albeit at levels barely above background. This interpretation is consistent with the occurrence of maximum sulfate concentrations at shallower depths (see "Alkalinity, Sulfate, Ammonium, Phosphate, Manganese, and Iron," p. 34, in "Inorganic Geochemistry"). Two samples from Hole 1207B were analyzed. The first was taken from the Campanian section (Core 198-1207B-6R), where the CH_4 concentration matched those from comparable depths in Hole 1207A, and the second was taken from a disturbed Albian core (Core 198-1207B-28R). The highest CH_4 concentrations for the site were observed in this latter sample, though they remain at trace levels (4.5 µL/L).

T10. Concentrations of CH_4 in headspace gas, p. 126.

F35. CH_4 and sulfate profiles, p. 88.

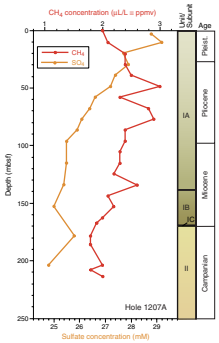

Carbonate and Organic Carbon

Carbonate determinations by coulometry were made for a total of 73 samples from Hole 1207A and Hole 1207B (Table T11). Samples were selected to provide a measure of the carbonate content within different units and to assess the influence of carbonate content on color reflectance. The values for carbonate range from 16 to 87 wt% (Table T11) within Subunit IA, reflecting variations in the proportions of siliceous and calcareous microfossils. The lowest value was an interval enriched in silica. The carbonate content profile shows alternating values downcore (Fig. F36). The variations observed are primarily an artifact of the dominant criterion for sample selection, namely the choice of intervals that are representative of extremes in color and lithology. However, some of the variations in these sediment properties likely are related to climatic fluctuations induced by orbital cycles. Carbonate contents are high (mean = 97.2 wt%) and show little variability in the Campanian calcareous oozes (Unit II).

Elemental concentrations of C, H, N, and S were measured (Table T12) for three samples from the carbonaceous interval correlated to the early Aptian OAE1a, hereafter described as upper, middle, and lower. Remarkably, the uppermost layer of the recovered interval of the black shale (upper; Sample 198-1207B-44R-1, 60–61 cm; 565.60 mbsf) contains 34.7 wt% organic carbon. A second sample from the central portion of the carbonaceous interval (middle; Sample 198-1207B-44R-1, 76–77 cm) contains 10.4 wt% organic carbon, and the base of the recovered interval (lower; Sample 198-1207B-44R-1, 103–104 cm) was determined to be 1.7 wt% organic carbon. However, these isolated values are indicators of the range of organic carbon values; they do not imply progressive enrichment through the section, especially given the inherent variability of C_{org}-rich horizons at other sites in the Pacific (Table T13). In addition, logging data from Site 1207 (Fig. F43) suggests that the actual thickness of the OAE1a horizon may be more than twice the

T11. Carbonate contents, Holes 1207A and 1207B, p. 127.

F36. Downhole profiles of carbonate content and organic carbon contents, p. 89.

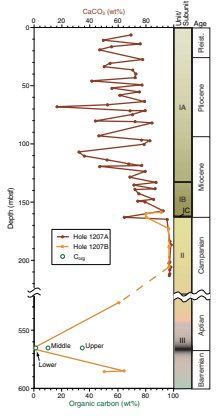

T12. Results from CNSH analysis, OAE1a samples, p. 128.

T13. Organic carbon and Rock-Eval pyrolysis results, p. 129.

interval recovered. The S content of the upper C_{org}-rich layer was also exceptionally high (10.6 wt%) (Table T12). Smear slide analysis shows that this sample contains abundant pyrite, although some of the sulfur exists in the form of organo-sulfur compounds (see below).

The C/N values for the lower, middle, and upper samples of the OAE1a are 16.2, 22.3, and 25.0, respectively (Table T12). In contemporary environments, high C/N ratios (>20–25) tend to reflect land-derived organic matter (Meyers, 1994), but C_{org}-rich horizons are exceptions to this tenet. Many mid-Cretaceous black shales (e.g., Meyers et al., 1984; Meyers, 1987) and Neogene or Quaternary sapropels (Meyers and Doose, 1999; Nijenhuis and de Lange, 2000) yield high C/N values that lie in the range typically indicative of terrestrial organic matter. Yet these units contain only minor contributions of material from land plants; visually, they are composed predominantly of amorphous organic matter derived from marine algae and bacteria. Consequently, the C/N ratios seem somewhat anomalous, which suggests that either the characteristics of the source organic matter are unusual and/or nitrogen cycling in these horizons may be radically different from the norm. Exceptional preservation of algal organic matter may reduce recycling of its nitrogen contents within the water column, thereby decreasing C/N ratios (Meyers and Doose, 1999). Perhaps the survival of cell walls that are rich in lipids and aliphatic biopolymers, like sheaths, significantly enhances C_{org} contents, without similarly increasing nitrogen content. C/N ratios would also be modified by preferential removal of nitrogen-rich organic compounds during anaerobic degradation of organic matter (Nijenhuis and de Lange, 2000). Moreover, nitrogen isotope profiles for Toarcian black shales provide evidence of partial denitrification in environments in which C_{org}-rich intervals are deposited (Jenkyns et al., 2001), and one might speculate that N-limitation led to higher C/N ratios. The recognition of high C/N ratios (31 to 590) in kerogens from the Archean and early Proterozoic (Beaumont and Robert, 1999) further confirms that the cycling of nitrogen behaves differently in anaerobic systems.

Rock-Eval Pyrolysis

Rock-Eval investigations focused on samples from the early Aptian OAE1a to assess the origin of their kerogen. The hydrogen index (HI) and oxygen index (OI) values for the three samples generally are similar, despite the vast differences in their C_{org} contents (Table T13). The high HI and extremely low OI values confirm that Type I organic matter is dominant in all the samples (Fig. F37) (Tissot et al., 1974) and indicate that they are composed of organic matter of algal and bacterial origins. In addition, the relatively low T_{max} values attest to the thermal immaturity of these samples.

F37. Oxygen and hydrogen indices, p. 90.

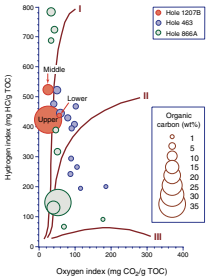

Assessment of Extractable Hydrocarbons

The hydrocarbons in the lower, middle, and upper samples (198-1207B-44R-1, 103–104 cm; 44R-1, 76–77 cm; and 44R-1, 60–61 cm) from the lower Aptian OAE1a horizon were extracted to enable exploration of their biomarker compositions. The information obtained provides evidence of the biological sources and thermal maturity of the organic matter and of the likely depositional environment. The procedure followed the methodology described in "Organic Geochemistry,"

p. 18, in the "Explanatory Notes" chapter. In addition, gas chromatography–mass spectrometry (GC-MS) was used to examine the biomarker composition of a CH_2Cl_2 eluate from the silica separation step of the middle sample consisting primarily of ketones.

The color of the extracts reflected their C_{org} contents. In particular, the color of the upper horizon extract was intense for such a small sample size. Also, during sample preparation by chromatographic separation, a pronounced pink coloration was evident in the polar (CH_2Cl_2) eluant, suggesting a significant porphyrin content. The hexane-soluble constituents, primarily consisting of aliphatic hydrocarbons, were analyzed by GC-MS and were identified from responses at specific target intervals in individual ion chromatograms and from their mass spectra. All of these components are well documented as components of mid-Cretaceous black shales (e.g., Barnes et al., 1979; Brassell et al., 1980, 1986; Rullkötter et al., 1984, 1987; Farrimond et al., 1986, 1990; Simoneit, 1986). Consideration of the principal characteristics of the samples (Table **T14**) and their relative abundances of biomarker components (Table **T15**) enables assessment and interpretation of aspects of the depositional environment of OAE1a.

Source of Organic Matter and Depositional Paleoenvironment

The extractable hydrocarbons are dominated by biomarkers of algal and bacterial origin, primarily short chain *n*-alkanes, and suites of polycyclic steroid and hopanoid hydrocarbons (Figs. **F38, F39;** Tables **T15, T16**). The abundance of n-C_{17} and the presence of branched alkanes, complemented by occurrences of methylhopanes, provide convincing evidence for contributions from cyanobacteria, especially in the lower sample. The steroids and hopanoids are derived from eukaryotic algae and bacteria, respectively (Table **T15**), although the absence of 4-methyl steroidal hydrocarbons suggests that dinoflagellates (Brassell and Eglinton, 1983; Robinson et al., 1984; Summons et al., 1987) were sparse among the plankton community. The only indication of allochthonous materials is the trace amounts of C_{25+} *n*-alkanes with pronounced odd/even preference that likely reflect inputs of vascular plant waxes borne by eolian dust (Simoneit, 1978; Zafiriou et al., 1985; Gagosian and Peltzer, 1986; Gagosian et al., 1987). The prevalence and character of bacterial components is consistent with the existence of a microbial mat, perhaps akin to those of the sulfur-oxidizing bacteria *Thioploca* in benthic settings (Williams and Reimers, 1983; McCaffrey et al., 1989; Ferdelman et al., 1997). Similarly, the organo-sulfur species, notably phytenyl thiophenes (Rullkötter et al., 1984; Brassell et al., 1986; ten Haven et al., 1990), confirm diagenetic incorporation of sulfur into organic moieties. The pristane/phytane ratios are less than unity (Table **T14**), which is typical of sediments associated with anaerobic systems (Didyk et al., 1978). In contrast, the presence of various ketones (Table **T15**) provides circumstantial evidence for oxidation of precursor lipids (Simoneit, 1973) or food web processes within the water column. However, steroidal ketones can also be biosynthetic products (Gagosian et al., 1982; Brassell and Eglinton, 1983; Robinson et al., 1984; Brassell et al., 1987) and consequently cannot provide conclusive, independent evidence of oxygenation levels in the water column or underlying sediments. In fact, the presence of lamination combined with

T14. Dominant biomarkers and compound ratios, p. 130.

T15. Biomarker carbon number ranges and relative abundances, p. 131.

F38. GC-MS trace of aliphatic hydrocarbons (base of lower Aptian), p. 91.

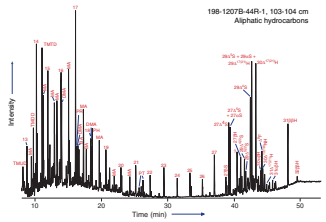

F39. GC-MS trace of aliphatic hydrocarbons (top of lower Aptian), p. 92.

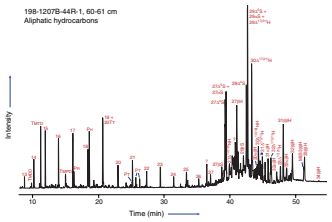

T16. Biomarker component identities, p. 133.

the extremely high C_{org} contents is compelling evidence of anaerobic bottom water conditions.

Stratigraphic Variations in Biomarkers

The major variation in the biomarker signatures related to planktonic sources of organic matter is the evidence for more substantial cyanobacterial contributions in the lower sample. There are also subtle differences among the samples in their distribution of bacterial markers, reflecting either a hierarchical community or temporal changes in the planktonic or benthic bacterial populations. The hopanoid composition of the upper sample, combined with the extraordinary C_{org} and S preservation (Table T12), is consistent with the development of a microbial mat. By contrast, the steroidal distributions are remarkably uniform, suggesting little change in eukaryotic algal populations during OAE1a.

Summary

The catalog of biomarkers identified includes no significant constituents that do not originate from bacterial and/or algal sources (Table T15). Thus, the hydrocarbon composition of the intervals is consistent with the results from Rock-Eval pyrolysis that indicate algal and bacterial origins for the organic matter.

Organic-Rich Aptian Strata from the Mid-Pacific

Aptian organic-rich horizons have been recovered from several sites in the Pacific, including another site on Shatsky Rise (Site 305) (Table T13). Few detailed analyses of the organic geochemistry of these horizons have been performed. However, the availability of measurements of C_{org} contents combined with limited Rock-Eval data enables comparisons with results from shipboard analyses of the Aptian organic-rich interval from Site 1207. In the absence of carbon isotopic data, perhaps the best comparative measure is the modified van Krevelen diagram used to diagnose Rock-Eval data (Fig. F37), preferably complemented by biomarker compositions.

The C_{org} contents of Aptian samples from Site 1207 span the range associated with other organic-rich units. The high value of 34.7 wt% is comparable to that reported for the uppermost horizon of the expansive Aptian interval at Site 866, which contained 34.5 wt% C_{org} (Table T13). However, the organic-rich intervals at Site 866 show a disparate range of HI and OI indices that reflects the variable sources and/or degree of oxidation of organic matter in these shallow-water deposits. Several samples from Site 866 reveal affinities with terrestrial organic matter (i.e., OI > HI), whereas others appear to resemble the characteristics representative of algal kerogens, especially those from lacustrine systems. Moreover, inspection of published chromatograms (Baudin et al., 1995) reveals substantial differences between the aliphatic hydrocarbon distributions at Site 866 and Site 1207. It is difficult to properly compare the two sets of data in the absence of published identification of individual components within the chromatograms of Site 866 samples, although it is apparent that their *n*-alkane profiles are markedly different from those at Site 1207. Similarly, the comparative distributions of polycyclic aliphatic hydrocarbons, especially steranes and hopanes, ap-

pear to show significant disparities, based on simple efforts at peak identification by matching gas chromatography (GC) retention times.

Despite these discrepancies, there is one sample from Site 866 (143-866A-88R-1, 56–58 cm) (Table T13) that possesses Rock-Eval characteristics (Fig. F37) comparable to those from Site 1207 samples. Unfortunately, the absence of a published chromatogram for this sample precludes comparison of biomarker data. However, it lies within OAE1a recognized by the negative $\delta^{13}C$ excursion for carbonate that occurs immediately below Core 143-866A-188R (Jenkyns, 1995). Consequently, it suggests that there may be some uniformity in the organic matter associated with the early Aptian OAE1a event, which might imply conditions that exerted controls on the character of primary production and biomass.

A more extensive correlation between the HI and OI indices from the Site 1207 samples exists with samples from Site 463 that possess C_{org} contents exceeding 2.5 wt%. Other intervals at Site 463 with lower organic carbon contents tend to possess lower HI and higher OI indices. Poor resolution of individual components in the published chromatogram of the lower Aptian samples from this site (Samples 62-463-70-6, 29–35, and 39–42 cm) (Dean et al., 1981) hampers comparisons of biomarker compositions. Also, the assignments of C_{33} and C_{35} *n*-alkanes, based solely on GC retention time, appear erroneous. The same compounds are reported in Albian Sample 62-465A-38-1, 142–150 cm (Dean et al., 1981), but GC-MS analysis of a comparable Albian sample (from Section 62-465A-38-3) failed to detect them (Comet et al., 1981). Consequently, these peaks more likely correspond to hopanes, akin to those recognized at Site 1207. Reinterpretation of the identities of *n*-alkanes implies that these higher plant markers are absent and thereby eliminates the sole biomarker evidence for terrestrial organic matter in the lower Aptian at Site 463. Thus, algal/bacterial organic matter is dominant in the lower Aptian of both Sites 463 and 1207. Further comparison of their biomarker compositions is merited, and it seems pertinent to focus on Section 62-463-70-6 for two reasons. First, the Rock-Eval data for the C_{org}-rich sample from Sample 62-463-70-6, 39–42 cm (Table T13), are directly comparable to those from Site 1207, which place them adjacent on the van Krevelen diagram (Fig. F37). Second, this sample has a $\delta^{13}C_{org}$ of –27.7‰, which is the most negative value, albeit within a limited data set, from the lower Aptian at Site 463. Analysis of Sample 62-317A-16-2, 131–134 cm, from the Aptian at Site 317 presents a different picture. It has high C_{org} (24.7 wt%) (Table T13) and S contents (12.7 wt%), and the $\delta^{13}C$ value of its kerogen is –21.6‰ (Simoneit and Stuermer, 1982). Prominent among its biomarkers are the C_{31} *n*-alkane and 17b(H),21b(H)-homohopane, but it possesses a low relative abundance of pristine and phytane (PR/PH = 0.8) and no steroidal components. These biomarker characteristics, which have few parallels among the other lower Aptian samples, are indicative of deposition in a productive lagoon (Simoneit and Stuermer, 1982).

In summary, there is a consistency in Rock-Eval characteristics among specific intervals within the lower Aptian at Sites 463, 866, and 1207, whereas the biomarker characteristics for Site 317 appear anomalous. Further correlation among these sites awaits comprehensive evaluation by combining carbon isotopic profiles and detailed biomarker analysis in a high-resolution sample set.

Depositional Scenarios for OAE1a

The biomarker results have yielded perhaps the most informative indication of the depositional conditions of the early Aptian OAE1a event at Site 1207, namely evidence for cyanobacterial contributions from the occurrence of diagnostic branched alkanes in the lower sample. Recognition of the cyanobacterial contributions requires explanation. Are these diagnostic biomarkers observed because of enhanced preservation that effectively captured a molecular profile of the characteristics of oceanic phytoplankton typical of that time? Or does the evidence for cyanobacteria reflect their occurrence as biological harbingers of the conditions that triggered formation of the organic-rich intervals? Given the prominence of these biomarkers in the lower layer, it seems likely that the occurrence of cyanobacteria may be related to temporal variations in primary productivity associated with the early Aptian event. Perhaps ocean biomass and plankton populations changed in association with the advent of C_{org}-rich sediment deposition and then evolved further once environmental conditions conducive to the sequestration of organic matter were established and stabilized. A prominent role for cyanobacteria among plankton might suggest that nitrate was limiting. Evidence for water mass denitrification in the early Toarcian OAE (Jenkyns et al., 2001) demonstrates the critical controls on productivity exerted by nitrogen cycling and could help to explain the anomalously low C/N ratios for these C_{org}-rich intervals. Invocation of a phase of enhanced cyanobacterial production during OAE1a may also reflect a response to Fe availability that both triggers and stimulates increased phytoplankton production (Leckie et al., in press). Moreover, cyanobacterial lipids are depleted in ^{13}C relative to their biomass (Sakata et al., 1997), and enhanced production and preservation of their hydrocarbon moieties therefore could potentially enhance the negative excursion in $\delta^{13}C_{org}$ associated with OAE1a (Menegatti et al., 1998; Bralower et al., 1999).

The subsequent changes in biomarkers that are manifested in the molecular stratigraphic records reflect evolving plankton communities, culminating in a population that seems to have included algae with colonial or mat affinities. Perhaps the last vestige of the early Aptian event sustained benthic microbial mats that enhanced the exceptional preservation of organic matter.

The extraordinary sequestration of organic matter (up to 34.7 wt%), even by comparison with other organic-rich intervals within the mid-Cretaceous, reflects a perturbation of the ocean-climate system that radically changed the processes controlling biogeochemical cycling. The profound effect on plankton productivity is recorded by exceptional preservation of organic matter from algal and bacterial sources, aided by anaerobic conditions. Progressive trends in phytoplankton populations survive in their molecular legacies, notably the indication of contributions from cyanobacteria within this OAE. Reconstruction of temporal changes in plankton communities and depositional conditions can be accomplished by elucidation of paleontological assemblages, isotopic C and N profiles and excursions, and evaluation of molecular signatures. These combined approaches offer complementary lines of evidence that can describe the biological response to this upheaval in carbon cycling and help define its cause.

INORGANIC GEOCHEMISTRY

Interstitial Water Chemistry

A total of 17 interstitial water samples were collected at Site 1207: 16 from Hole 1207A at depths ranging from 2.95 to 203.80 mbsf and 1 from Hole 1207B at 208.5 mbsf. This report includes data from Hole 1207A only; the sample recovered from Hole 1207B was too severely disturbed to provide reliable geochemical information. Details of analytical methods are provided in "Inorganic Geochemistry," p. 21, in the "Explanatory Notes" chapter. Filtered (0.45 µm) samples were analyzed for pH, salinity, chlorinity (Cl^-), alkalinity, sulfate (SO_4^{2-}), phosphate (HPO_4^{2-}), ammonium (NH_4^+), silica ($Si(OH)_4$), boron (H_3BO_3), iron (Fe^{2+}), manganese (Mn^{2+}), and major cations (Na^+, K^+, Mg^{2+}, Ca^{2+}, Li^+, Sr^{2+}, and Ba^{2+}). A compilation of data is provided in Table T17. Cited values for average seawater composition are from Millero and Sohn (1992) and Broecker and Peng (1982); values for North Pacific Deep Water (NPDW) composition are from Rea et al. (1993).

T17. Results of geochemical analyses, Hole 1207A, p. 134.

The pore water samples span the range of sediments in lithologic Unit I (0–162.50 mbsf) and extend into lithologic Unit II (162.5–335.3 mbsf). The major lithologic trends that affect pore water geochemistry include a transition from nannofossil ooze with diatoms and siliceous clayey nannofossil ooze to nannofossil clay just above the boundary between lithologic Units I and II (see "Lithologic Unit I," p. 12, in "Lithostratigraphy"). Volcanic ash, typically concentrated in discrete layers, is common throughout lithologic Unit I. Abundant zeolites (i.e., phillipsite) and manganese micronodules occur within the lowermost portion of Unit I. Chert is common below this depth.

pH, Salinity, Chlorinity, and Sodium

In Hole 1207A, the pH of pore waters ranged from 7.17 to 7.43, with the minimum value at 39.25 mbsf and a mean value of 7.33 ± 0.06 (1 σ). All values are lower than the average seawater value of 8.1. The relatively narrow range of values reflects the buffering capacity of the carbonate-dominated sediment. Salinity was uniform throughout the profile, with an average value of 35.0 ± 0.25 g/kg.

In Hole 1207A, Cl^- concentrations range from a low of 547 mM at 10.75 mbsf to a high of 566 mM at 58.25 mbsf (Fig. F40B). The Cl^- concentration in the shallowest sample (2.75 mbsf) is slightly higher than the Pacific Ocean Deep Water (PODW) value of 554 mM. Below the minimum value at 10.75 mbsf, Cl^- concentrations exhibit a gradual increase to a maximum value of 566 mM at 58.25 mbsf. Below this depth, concentrations fluctuate around a mean value of 561 mM. The broad downcore fluctuations in Cl^- may reflect the ongoing adjustment of the pore water Cl^- concentrations to variations in mean ocean salinity, which has generally increased over the past few million years in response to increasing continental ice volume (McDuff, 1985).

F40. Sodium and chloride profiles, p. 93.

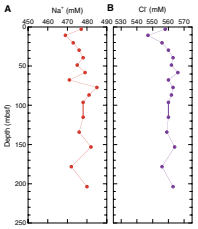

Sodium (Na^+) concentrations, calculated by charge balance (see Broecker and Peng, 1982), range from a low of 469 mM at 10.75 mbsf to a high of 485 mM at 77.25 mbsf (Fig. F40A), with average concentrations (477 ± 4 mM) slightly higher than that of average seawater (470 mM). The broad trend of increasing concentrations to ~58 mbsf below the minimum value at 10.75 mbsf is similar to that observed in the Cl^- data and may reflect the salinity changes discussed above. The cause of

significant variation in Na^+ below this depth is unclear but may be related to the alteration of volcanic ash in lithologic Unit I and zeolites in Subunit IC (see "Lithostratigraphy," p. 11).

Alkalinity, Sulfate, Ammonium, Phosphate, Manganese, and Iron

Although alkalinity variations in the interstitial waters of Hole 1207A are minor, a distinct downcore trend is evident. Alkalinity increases steadily from 3.09 mM at 2.75 mbsf to 4.32 mM at 96.25 mbsf. Below 96.25 mbsf, alkalinity values remain relatively uniform, averaging 4.18 ± 0.12 mM (Fig. F41A). The shape of the downcore trend indicates that the highest rate of alkalinity production, generated mostly as bicarbonate ion (HCO_3^-) at the measured pH, is occurring within the upper ~90 m of the profile. This interpretation is supported by the sulfate (SO_4^{2-}) profile, which shows a decrease from near the average seawater value of 28 mM to 25.5 mM over the same depth interval (Fig. F41B). SO_4^{2-} reduction is reflected in the sediments by the presence of pyrite in lithologic Unit I (see "Lithologic Unit I," p. 12, in "Lithostratigraphy"). The uniformity of the alkalinity and SO_4^{2-} values below ~90 mbsf suggests the absence of significant alkalinity production via SO_4^{2-} reduction in the lower part of the pore water profile.

Ammonium (NH_4^+) and phosphate (HPO_4^{2-}) in pore waters in the upper parts of sequences dominated by biogenic sediments are produced largely through the decomposition of organic matter (Gieskes, 1983). NH_4^+ and HPO_4^{2-} concentrations are low throughout Hole 1207A, with values of 79–220 µM and 0.5–5.0 µM, respectively (Fig. F41E, F41F). Although more variable, the first ~100 m of the NH_4^+ profile is similar to that of alkalinity. This similarity suggests that NH_4^+ is being produced through the anaerobic reduction of organic matter. NH_4^+ concentrations generally decrease below this depth, suggesting that no NH_4^+ is being produced in the lower part of the profile. This interpretation is consistent with the uniformity of the alkalinity and SO_4^{2-} profiles below ~90 mbsf. Fluctuations in the NH_4^+ profile between ~50 and 100 mbsf may reflect the irregular addition of NH_4^+ to the pore water system as a result of the leaching and weathering of the abundant silicic volcanic material in lithologic Unit I (see "Lithologic Unit I," p. 12, in "Lithostratigraphy"). HPO_4^{2-} concentrations are highest in the shallowest interstitial water sample (5.0 µM) and decrease sharply to a value of 1.3 µM at 29.75 mbsf. Below this depth, HPO_4^{2-} concentrations show a gradual downcore decrease to a minimum value of 0.5 µM at the bottom of the profile (Fig. F41E). This broad trend is interrupted by a brief excursion to a concentration of 2.9 µM at 39.25 mbsf. The very low levels of dissolved HPO_4^{2-} below the uppermost pore water sample likely reflect the effective adsorption of any phosphate produced via organic matter degradation onto the surfaces of the carbonate sediment (Walter and Burton, 1986). As indicated above, the alkalinity and SO_4^{2-} profiles suggest that rates of organic matter degradation are low in the sediments of lithologic Units I and II.

Iron (Fe^{2+}) profiles show significant variation downcore, with concentrations ranging from 0.1 to 35.4 µM (Fig. F41D). The overall trend is toward decreasing concentration with increasing depth. Variations in the Fe^{2+} profile are attributed to the proximity of iron sources, such as volcanic ash to areas of sulfate reduction and pyrite precipitation in

F41. Alkalinity, sulfate, manganese, iron, phosphate, and ammonium profiles, p. 94.

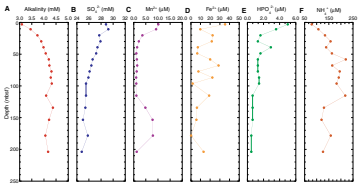

lithologic Unit I (see "Lithologic Unit I," p. 12, in "Lithostratigraphy"). The lowest observed concentration of dissolved Fe^{2+}, 0.1 µM at 178.25 mbsf, may reflect the formation of the manganese micronodules that occur in lithologic Subunit IC. The overall trend of decreasing Fe^{2+} concentrations is related to the absence of volcanic debris, the major Fe^{2+} source, below ~162 mbsf and reflects diffusion between sites of high and low Fe^{2+} concentrations.

Pore water manganese (Mn^{2+}) concentrations decrease from 10.0 µM in the shallowest sample to a minimum of 1 µM at 48.75 mbsf. Concentrations remain uniformly low to 134.25 mbsf, increase to 7.9 µM between 153.25 and 178.25 mbsf, and decrease to 1.2 µM at the base of the profile (Fig. F41C). Elevated Mn^{2+} concentrations in the two shallowest samples suggest that the degradation of organic matter is sufficient to deplete oxygen in the upper part of the sediment column, above the depth at which the sulfate and alkalinity profiles indicate that SO_4^{2-} reduction occurs. The sharp decrease to low and uniform concentrations between 48.75 and 134.25 mbsf suggests that a manganese carbonate phase may be forming within this interval. The requisite reducing conditions in the sediment column are consistent with the occurrence of pyrite and may be reflected in the low red/blue (680/420 nm) ratios in color reflectance through this interval (see "Lithostratigraphy," p. 11). The excursion to higher Mn^{2+} concentrations in the lower part of the pore water profile centers on lithologic Subunit IC, which encompasses a major unconformity between the middle Miocene and the Campanian. The unconformity surface is characterized by the presence of a 5-cm-thick manganese oxide crust; the interval contains abundant manganese oxide micronodules (see "Subunit IC," p. 13, in "Lithostratigraphy"). The sediment below the unconformity is described as yellowish brown to pale yellowish brown with relatively high red/blue (680/420 nm) ratios in color reflectance (see "Lithologic Unit II," p. 13, in "Lithostratigraphy"). These features suggest that the sediment column remained relatively oxic during deposition. By contrast, the sediments above the unconformity appear to have been less oxidizing, and perhaps mildly reducing, at shallow depths during deposition. Accumulation of Miocene sediments atop the unconformity led to the development of redox conditions within the Campanian deposits, which ultimately became reducing enough to support the dissolution of manganese oxides associated with the unconformity surface. This interpretation is consistent with the SO_4^{2-} profile through this interval, which suggest that redox conditions in sediments below the unconformity are now reducing. The progressive dissolution of manganese oxides led to the development of a diffusion gradient between high concentrations associated with the unconformity surface and low concentrations in the pore waters of overlying sediments.

Potassium, Silica, and Lithium

Potassium (K^+) concentrations decrease gradually downcore in Hole 1207A from a maximum of 12.2 mM in the shallowest sample (2.75 mbsf) to values approaching that of average seawater (10.2 mM) in the deepest sample at 203.80 mbsf (Fig. F42A). Elevated concentrations correspond to the distribution of volcanic ash and pumice in the upper ~160 m of the hole (see "Lithostratigraphy," p. 11), suggesting that the major source for K^+ in the pore water is glass-rich, silicic volcanic material. K^+ is liberated from the solid phase via leaching and weather-

F42. Potassium, silica, and lithium profiles, p. 95.

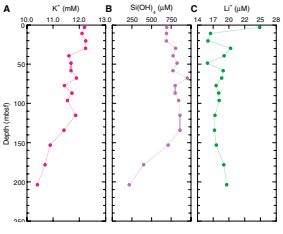

ing reactions that produce clays (i.e., smectite). The downcore decrease in K^+ likely reflects a diminishing source of volcanic ash and pumice, diffusion toward greater depths, and possible exchange with basaltic basement.

The dissolved silica, $Si(OH)_4$, concentrations throughout the upper ~150 m of Hole 1207A (765 ± 126 µM) are distinctly higher than in the overlying water (NPDW value = 160 µM). Below ~150 mbsf, values decrease to a minimum of 216 µM at 203.8 mbsf (Fig. **F42B**). High $Si(OH)_4$ concentrations in the upper part of the hole are interpreted to reflect the leaching and weathering of volcanic ash and pumice in lithologic Unit I. $Si(OH)_4$ concentrations likely approaching saturation levels in the pore waters of lithologic Unit I have allowed for excellent preservation (based on analysis of smear slides) of the abundant siliceous microfossils that occur throughout this interval. Lower pore water $Si(OH)_4$ concentrations correspond to the appearance of chert in the sediment column. A significant removal of $Si(OH)_4$ from pore waters may be induced by the recrystallization of opal-A to opal-CT (e.g., Baker, 1986) or quartz (e.g., Gieskes, 1981).

Lithium (Li^+) concentrations decrease abruptly from a value approaching that of modern seawater (27 µM) in the shallowest sample (2.75 mbsf), to relatively uniform values at greater depths that fluctuate around a mean of 17.7 ± 1.2 µM (Fig. **F42C**). The observed depletion may reflect uptake by clay minerals forming through the weathering of volcanic material and possibly zeolites (Gieskes, 1981), which occur in the lower 3 m of lithologic Unit I (see **"Lithologic Unit I,"** p. 12, in "Lithostratigraphy").

Calcium, Magnesium, Strontium, Boron, and Barium

Concentrations of calcium (Ca^{2+}) and magnesium (Mg^{2+}) are similar to that of average seawater at the top of the pore water profile and show an antithetical relationship downcore (Fig. **F43A, F43B**). Ca^{2+} concentrations increase slightly downcore from 10.4 mM in the upper part of the profile to 11–12 mM, whereas Mg^{2+} concentrations decrease from 53.8 to 51.5 mM. The most likely influences on the relative abundances of Ca^{2+} and Mg^{2+} in pore waters at Site 1207 include calcium carbonate dissolution, weathering reactions involving volcanic ash in lithologic Unit I, and weathering reactions involving the volcanic basement. Each of these processes serves to create a source of Ca^{2+} and a sink for Mg^{2+}. The alteration of volcanic ash typically releases Ca^{2+} to solution while sequestering Mg^{2+}in alteration products such as magnesian smectites or sepiolite (McDuff and Gieskes, 1976; Lawrence and Gieskes, 1981). No shipboard data are available to determine the influence of such weathering processes on the pore water profile at Site 1207.

Strontium (Sr^{2+}) concentrations show a gradual increase from values similar to that of average seawater at 86 µM in the shallowest sample at 2.75 mbsf to 258 µM at 153.25 mbsf (Fig. **F43C**). Below this depth, Sr^{2+} concentrations decrease to 233 µM at the bottom of the profile (203.80 mbsf). The dominant influence on the Sr^{2+} profile is likely carbonate dissolution and/or recrystallization (Baker et al., 1982). This interpretation is supported by smear slide observations (see **"Lithostratigraphy,"** p. 11) and by increasing Sr/Ca ratios with increasing depth (Fig. **F43C**). If weathering of relatively calcium-enriched volcanic ash was a major contributor to Sr^{2+} levels in the pore fluids, Sr/Ca ratios would be expected to decrease. Generally, low Sr^{2+} concentrations suggest that little

F43. Calcium, magnesium, strontium, barium, and boron profiles, p. 96.

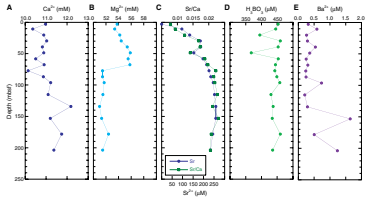

alteration of carbonate is occurring relative to most other pelagic sites (Baker et al., 1982).

Boron, generated mostly as borate, H_3BO_3, at the measured pH levels, shows little downcore variation (Fig. F43D), with average concentrations (438 ± 25 µM) slightly higher than that of average seawater (416 µM). These concentrations and the lack of variability in the profile suggest that boron may not be involved in the sediment–pore water interactions discussed above. Average Ba^{2+} concentrations in interstitial waters of Hole 1207A are extremely low (0.5 ± 0.4 µM) but consistently higher than that of average seawater (0.1 µM). Ba^{2+} concentrations vary significantly with depth, trending toward higher values near the base of the profile (Fig. F43E). Possible sources of Ba^{2+} in the sediments of Site 1207 include skeletal debris and volcanic ash, which may be undergoing leaching and/or dissolution (see above), and $BaSO_4$, which may be undergoing dissolution as a consequence of sulfate reduction.

PHYSICAL PROPERTIES

Physical properties at Site 1207 were measured on both whole-round sections and discrete samples from split-core sections. Whole-round measurements included the continuous determination of magnetic susceptibility, gamma ray attenuation (GRA) bulk density, compressional *P*-wave velocity, and natural gamma radiation, using the multisensor track (MST) as well as discrete measurements of thermal conductivity. Discrete compressional *P*-wave velocity was measured at a frequency of at least one measurement per split-core section in both Holes 1207A and 1207B. Index properties were measured on discrete samples from split-core sections at a frequency of one measurement per section throughout Hole 1207A and on Cores 198-1207B-4R through 6R.

MST Measurements

All core sections from Holes 1207A and 1207B were routinely measured on the MST for magnetic susceptibility and GRA density at 2.5-cm intervals (Figs. F44, F45). MST *P*-wave velocity was routinely measured at 2.5-cm intervals in all Hole 1207A APC cores (Fig. F46) but was not measured for any XCB, MDCB, or RCB cores, because of the poor contact between the sediment and core liner. During the collection of *P*-wave data, it was noted that erroneous values were being recorded by the MST *P*-wave logger (PWL) (e.g., Fig. F46A). Subsequently, these anomalies were traced to a faulty transducer, which was replaced following the completion of MST data collection from the Site 1207 cores. Consequently, archived MST *P*-wave data from Hole 1207A should be used with extreme caution. Natural gamma radiation was measured routinely on the MST at 30-cm intervals and then at 10-cm intervals in some Cretaceous cores (Fig. F47). All collected MST data are archived in the ODP Janus database.

Magnetic susceptibility data (Fig. F44) are generally higher in magnitude in the uppermost 20 m of the Site 1207 sedimentary column, compared to the relatively lower values evident from 20 to 130 mbsf (these depth intervals are located within lithologic Subunit IA; see "Lithologic Unit I," p. 12, in "Lithostratigraphy". Such a change in magnetic susceptibility values is probably related to the oxidation state of iron in these sediments, as pyrite is commonly found in sediments in the interval below 20 mbsf (see "Lithologic Unit I," p. 12, in "Lithostratigra-

F44. MST magnetic susceptibility vs. depth, Holes 1207A and 1207B, p. 97.

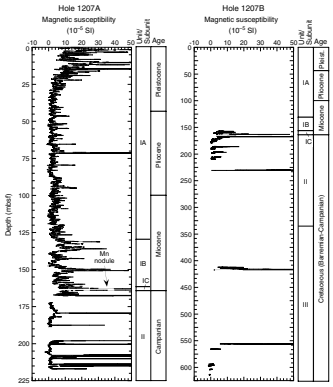

F45. MST GRA bulk density vs. depth, Holes 1207A and 1207B, p. 98.

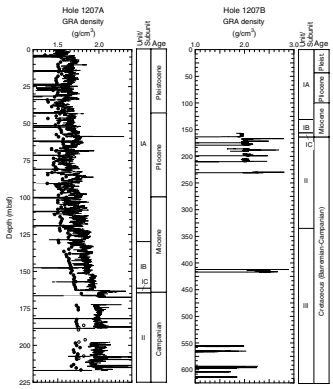

F46. MST *P*-wave velocity vs. depth, Hole 1207A, p. 99.

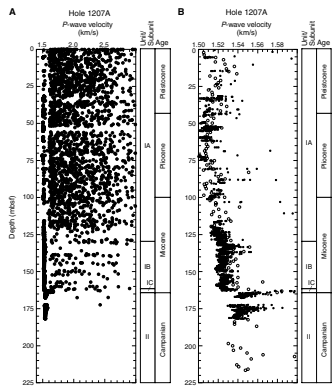

phy"), reflecting reduced conditions. Furthermore, the low magnetic susceptibility values in the lower sedimentary interval resulted in the collection of weak magnetic inclination data from these sediments (see **"Paleomagnetism,"** p. 25). Peaks in magnetic susceptibility in lithologic Subunit IA may correlate with distinct ash layers (see **"Lithologic Unit I,"** p. 12, in "Lithostratigraphy"). In the Pleistocene–Pliocene section, an excellent correlation is observed between magnetic susceptibility data and color reflectance measurements, the latter primarily the total reflectance value (L*) and the 550-nm wavelength (see **"Lithologic Unit I,"** p. 12, in "Lithostratigraphy"). Both magnetic susceptibility and color reflectance data in this interval reveal a pronounced cyclicity, which may be useful in identifying astronomically controlled depositional processes. Magnetic susceptibility values are higher in lithologic Subunit IB, relative to values between 20 and 130 mbsf in Subunit IA, with a peak value in Subunit IC delimiting the ferromanganese nodule (see **"Lithologic Unit I,"** p. 12, in "Lithostratigraphy") recovered close to the Campanian–Miocene unconformity (see **"Biostratigraphy,"** p. 18) at ~163 mbsf. Magnetic susceptibility values are generally close to background values in lithologic Unit II (Campanian) and do not exhibit any consistent downhole variation.

MST GRA bulk density data exhibit a general downhole increase in magnitude (Fig. **F45**), resulting from sediment compaction and dewatering processes with increased overburden pressure. In addition to the overall downhole trend, GRA bulk density data also show distinct variations that relate to lithologic changes at several distinct horizons (see **"Lithostratigraphy,"** p. 11). GRA bulk density values exhibit a change in magnitude at ~130 mbsf, across the boundary between lithologic Subunits IA and IB. Cyclical variation in GRA bulk density values, similar to that evident in magnetic susceptibility (see above) and color data, is also found within Pleistocene–Miocene lithologic Subunit IA. A further increase in the GRA bulk density values occurs at ~165 mbsf, the boundary between lithologic Subunit IC and Unit II, and correlates with the Campanian–Miocene unconformity (see **"Biostratigraphy,"** p. 18). However, GRA bulk density values are consistently higher than the discrete wet bulk density measurements (Table **T18**) throughout Hole 1207A. These overestimated GRA bulk density values can be explained by the relatively high carbonate content, porosity, and moisture content of sediments; the calibration procedure for the MST GRA sensor is optimized for mixed-lithology sediments. Consequently, the GRA method overestimates the density in carbonate-rich sediments of all lithologic units and is most pronounced in Unit II because this unit has the highest carbonate contents (see **"Lithostratigraphy,"** p. 11, and **"Inorganic Geochemistry,"** p. 33).

MST *P*-wave velocities were recorded at 2.5-cm intervals in Hole 1207A sections to a depth of ~182 mbsf (Fig. **F46**). Despite many obviously high *P*-wave velocities recorded by the MST PWL, a general trend to higher velocities with increased depth in the sediment column can be discerned from values lying between 1500 and 1600 m/s. MST *P*-wave velocities also exhibit a stepped increase in magnitude at ~165 mbsf, across the boundary between lithologic Subunit IC and Unit II that represents the Campanian–Miocene unconformity (see **"Biostratigraphy,"** p. 18) at Site 1207. The magnitude of the reliable MST PWL values also compare well with the discrete measurements of *P*-wave velocity (Table **T19;** Fig. **F48**), as illustrated in the right-hand plot of Figure **F46.**

F47. MST natural gamma radiation vs. depth, Holes 1207A and 1207B, p. 100.

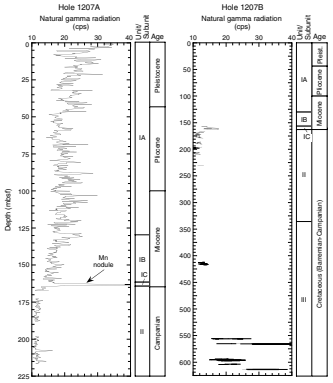

T18. Discrete index properties measurements, p. 135.

T19. Discrete measurements of *P*-wave velocity, p. 138.

F48. *P*-wave velocities from discrete samples vs. depth, Holes 1207A and 1207B, p. 101.

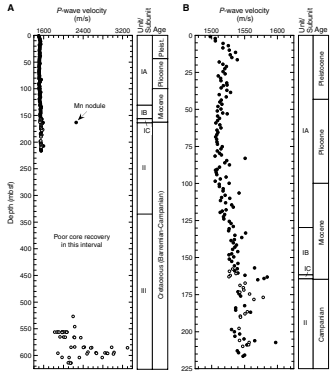

Natural gamma radiation data were collected using the MST for Hole 1207A cores at 30-cm intervals and at 10-cm intervals in some cores of Cretaceous age recovered from Hole 1207B (Fig. F47). In the upper 225 m of Hole 1207A, natural gamma radiation generally decreases downhole, with a marked peak value highlighting the presence of the Mn nodule (see "Lithologic Unit I," p. 12, in "Lithostratigraphy") at ~163 mbsf, close to the Campanian–Miocene unconformity (see "Biostratigraphy," p. 18). Natural gamma radiation also exhibits cyclical variation in the Pleistocene–Miocene sediments of lithologic Subunits IA, IB, and IC. Within lithologic Unit II (Campanian), natural gamma radiation values are considerably lower in magnitude and approach background values, compared to those data from higher in the stratigraphic section. At the base of Hole 1207B, in lithologic Unit III, natural gamma radiation increases to values comparable to those in lithologic Subunit IA.

P-Wave Velocity

Discrete measurements of compressional *P*-wave velocity were obtained on Site 1207 split-core sections using the modified Hamilton Frame (PWS3) velocimeter. These data are listed in Table T19 and illustrated in Figure F48. Data were collected at a routine sampling frequency of one measurement per section, with additional measurements made on a single Mn nodule, and chert and black-shale sediments. The *P*-wave velocity values measured for the cherts range from 4322.4 to 5842.5 m/s (mean *P*-wave velocity = 5306.7 m/s). The Mn nodule (see "Lithologic Unit I," p. 12, in "Lithostratigraphy") recovered proximal to the Campanian–Miocene unconformity (see "Biostratigraphy," p. 18) had a *P*-wave velocity of 2257.5 m/s. The *P*-wave velocity data obtained for chert samples are not plotted in Figure F48 because of their higher magnitude relative to proximal sediments and the limitations of axis scaling. Velocities vary between ~1500 m/s in the soft surface sediments and ~1600 m/s in the more consolidated sediments found in Hole 1207A. Discrete *P*-wave measurements show an increase in velocity with depth, between 0 and ~225 mbsf, which is similar to that evident in the reliable data obtained with the MST PWL (see the caveat detailed in "MST Measurements," p. 37). The magnitude of discrete Hamilton frame velocimeter and useful MST PWL determined *P*-wave velocities are comparable. The lack of evidence for early diagenetic cementation near the seafloor, as shown by high-percentage porosity in the interval 0–225 mbsf (Fig. F49), suggests that increasing *P*-wave velocity with depth in the upper 225 m of the sedimentary column is primarily the consequence of compaction and pore fluid expulsion. An increase in discrete *P*-wave velocities through this stratigraphic interval broadly correlates with an increase in the magnitude of discrete bulk density values (Fig. F50). *P*-wave values then increase to ~1800–3050 m/s in the lithified sediments recovered at the base of Hole 1207B. *P*-wave velocities recorded for the deepest sediments recovered in Hole 1207B exhibit significant variability in magnitude and are dependent on the lithology (excluding chert) of the sampled sediment (see "Lithologic Unit I," p. 12, in "Lithostratigraphy").

Thermal Conductivity

Thermal conductivity data from Site 1207, obtained using the TK04, are listed in Table T20 and shown in Figure F51. Measurements were made on Sections 1, 3, and 5 of each core from Hole 1207A, and on Sec-

F49. Water content relative to bulk sediment and solid phase, porosity, and void ratio vs. depth, Holes 1207A and 1207B, p. 102.

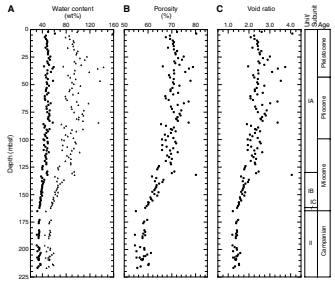

F50. Discrete measurements of *P*-wave velocities vs. discrete wet bulk density measurements, Hole 1207A, p. 103.

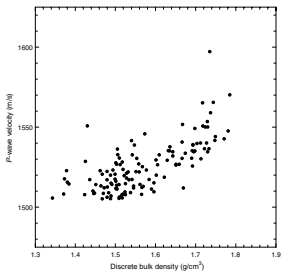

T20. Discrete measurements of thermal conductivity, p. 140.

F51. Whole-core thermal conductivity vs. depth, Holes 1207A and 1207B, p. 104.

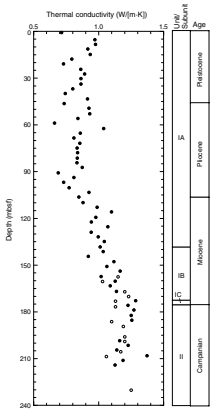

tions 1, 3, and 5 of Cores 198-1207B-1R through 6R, 9R, and 28R. Average thermal conductivity for the 79 data points is 1.01 W/(m·K), with a standard deviation of 0.18. Site 1207 thermal conductivity values also exhibit a general increase in magnitude with depth below seafloor, increasing from ~0.85 W/(m·K) near the seafloor to ~1.20 W/(m·K) at ~210 mbsf. The downhole increase in thermal conductivity values broadly correlates with a decrease in porosity (see values in Table T18 and also Fig. F49) with increased sediment burial depth (Fig. F52), as would be expected from increased sediment consolidation at greater depths.

F52. Whole-core thermal conductivity vs. discrete measurements of porosity, Hole 1207A, p. 105.

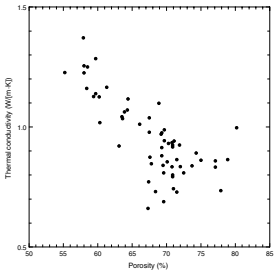

F53. Wet bulk, dry, and grain density vs. depth, Holes 1207A and 1207B, p. 106.

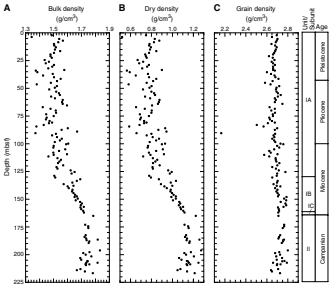

Index Properties

Index properties were determined only for discrete samples from Hole 1207A and Cores 198-1207B-4R through 6R. These data are listed in Table T18 and shown in Figures F49 and F53. Index properties primarily reflect progressive sediment compaction and fluid expulsion with depth in the sediment column, but also indicate changes in sediment composition as defined by lithologic units and subunits (see "Lithostratigraphy," p. 11). Bulk and dry density increase slightly in magnitude between the seafloor and ~125 mbsf, within lithologic Subunit IA. The greatest increase in bulk and dry density at Site 1207 occurs within lithologic Subunit IB, between ~125 and ~160 mbsf, and values then remain approximately constant to ~225 mbsf through lithologic Subunit IC and Unit II. By comparison, grain density exhibits a small downhole increase in magnitude and does not change at the boundary between lithologic units. Water content, porosity, and void ratio all exhibit a general downhole decrease in magnitude in lithologic Unit I (Pleistocene–Miocene), between the seafloor and ~160 mbsf. No further significant downhole decrease in these properties occurs within lithologic Unit II (Campanian). The lack of any sharp transition in water content, porosity, and void ratio between lithologic Units I and II suggests that the Campanian sediments may not have been overlain by a significant thickness of sediments older than those currently of Miocene age.

Summary

Physical properties data at Site 1207 show variation with depth below seafloor that suggests progressive compaction and fluid expulsion are the dominant controlling factors. Offsets in certain physical properties data, such as GRA bulk density, indicate that the dominant properties are also influenced by lithologic changes.

DOWNHOLE MEASUREMENTS

Operations

Downhole measurements in Hole 1207B were made after completion of RCB coring to a total depth of 622.8 mbsf. Prior to logging, Hole 1207B was reamed, flushed of debris, and filled with 40 bbl of sepiolite mud. No tight spots were encountered during the reaming, and 40 m of soft fill was removed from the bottom of the hole. Three tool strings were run: the triple combo, the FMS-Sonic, and the GHMT (see "Wireline Logging," p. 27, in "Downhole Measurements," in the "Explana-

tory Notes" chapter; also see Fig. F8, p. 53, and Table T7, p. 62, both in the "Explanatory Notes" chapter). The triple combo tool string (porosity, density, resistivity, and natural gamma radiation) was successfully lowered to 622 mbsf, within 1 m of the total hole depth, and logged up to the base of the pipe at 125.5 mbsf (Fig. F54). This logging run encountered a bridge at 173 mbsf but was able to pass through it, and no further bridges were encountered. The tools provided continuous and high-quality log data. The borehole diameter ranged from 10 in at the base of the hole, increasing to a maximum of 18 in toward the top of the logged section. The hole contained ledges that formed at the hard chert layers, with the relatively soft ooze in between preferentially washed away. After the main pass of this tool string, it was lowered down the hole again, but could not pass below 383 mbsf. The hole was logged from this point to the pipe with the Lamont-Doherty Earth Observatory multisensor gamma tool (MGT). The other tools in the tool string (the Schlumberger tools) had to be switched off during MGT logging.

The FMS-sonic logging tool string (microresistivity, seismic velocity, and natural gamma radiation) was lowered to 380 mbsf, where a bridge that had been encountered during the previous run prevented access to the lower reaches of the hole. Two passes of the dipole shear sonic imager tool were run in the monopole compressional and dipole shear data acquisition modes, the first with a medium frequency source, and the second with a low frequency source more suited to low-velocity formations.

The third logging tool string was the GHMT (magnetic field, magnetic susceptibility, and natural gamma radiation), which logged two passes from 370 and 355 mbsf to the base of the pipe. Unfortunately, a malfunction in the tool resulted in a collection of only partially useful logs. The symptom of the total magnetic field log was that it alternated between field values of ~32000 and 43000 nT, when it should have had only small variations around an average value of ~43000 nT. The susceptibility log has the same pattern as the core measurements in the interval of overlap, but its baseline is offset from zero (to ~500 ppm), and the log displays large negative peaks, both of which are very difficult to explain in terms of the known susceptibility of the sediments.

The wireline depth to seafloor was determined from the step increase in gamma ray values at the sediment water interface to be at 3110.5 mbrf; the driller's mudline depth used for establishing core depth was 3111.7 mbrf.

Logging Units

Hole 1207B was divided into six units on the basis of the logs (Figs. F55, F56).

Logging Unit 1: Base of Pipe (125 mbsf) to 164 mbsf

Unit 1 is characterized by higher gamma radiation values than the underlying units and uniformly low resistivities. At its base is a peak in gamma radiation, density, resistivity, and photoelectric absorption factor, which corresponds to the Campanian–Miocene unconformity and manganese nodule layer.

F54. Summary of logging runs, Hole 1207B, p. 107.

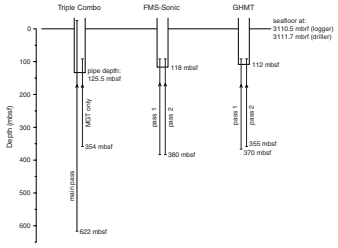

F55. Geophysical logs and equivalent core physical properties measurements, Hole 1207B, p. 108.

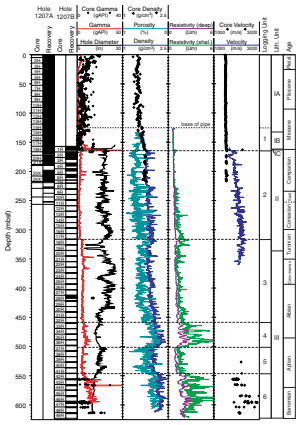

F56. Geochemical logs, Hole 1207B, p. 109.

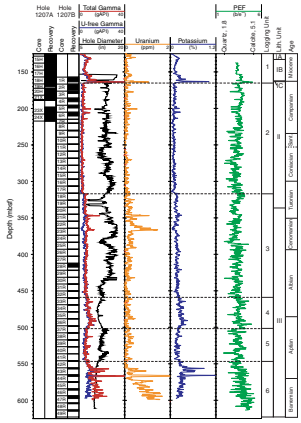

Logging Unit 2: 164–316 mbsf

Unit 2 is characterized by generally low gamma radiation values. The FMS images show that there are numerous layered cherts present in this interval (see "FMS Image Logs and Cherts," p. 43), increasing in frequency down the unit.

Logging Unit 3: 316–458 mbsf

The top of this unit is distinguished by a downhole stepped increase in gamma radiation values, indicating perhaps more terrestrial material in this unit relative to the one above.

Logging Unit 4: 458–502 mbsf

This unit is characterized by relatively higher gamma ray values, high densities and high resistivity values. There are five major peaks in density and resistivity within the unit, indicating well-lithified sediment or closely spaced chert layers.

Logging Unit 5: 502–547 mbsf

Unit 5 has similar log characteristics to Unit 3. It has relatively low gamma radiation and density values.

Logging Unit 6: 547 mbsf to the Base of Hole (622 mbsf)

Unit 6 is characterized by the highest gamma ray values in the logged section, caused mostly by uranium. Resistivity and density values are high, again indicating well-lithified sediment. This unit contains a 1.2-m-thick gamma radiation peak, which is associated with a C_{org}-rich black shale recovered in the lower Aptian part of the section.

Black Shales

The lower Aptian black shale recovered in Core 198-1207B-44R is clearly represented in the logs by a large peak in gamma radiation at 566 mbsf (Fig. F57). Uranium is the main contributor to the gamma radiation peak; uranium peaks are often associated with black shales because the uranium is adsorbed by the organic matter in the shale. The black shale is also apparent in other logs as low density values because of the low density of organic matter and as high porosity values because the porosity tool detects the amount of hydrogen in the formation, which is usually a good indicator of pore water content but is present here also in the organic matter.

The shale is ~1.2 m thick, according to the uranium, porosity, and density logs. The peak value in uranium occurs toward the top of the black shale interval. Approximately 40 cm of shale was recovered; thus, it appears that about two-thirds of the interval was not recovered.

The total C_{org} content can be estimated from the density log. The result is only approximate because we assume that the shale and the background sediments have the same porosity and adopt values for some densities (e.g., of the organic matter) that are not well constrained. Following Rider (1996), we used the following three equations to find that the organic matter content is 23.3 wt% by volume and 17.7 wt% by mass. If the mass percent carbon in the organic matter is 85

F57. Gamma radiation, density, and porosity logs around the OAE1a black shale interval, p. 110.

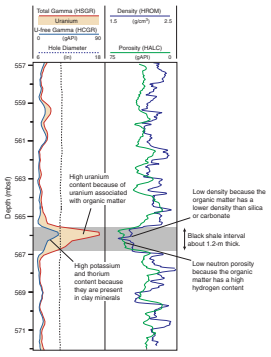

wt%, then there is an average of 15 wt% TOC in the black shale at 566 mbsf, which is approximately the average of TOC measured by Rock-Eval pyrolysis (see "Carbonate and Organic Carbon," p. 27, in "Organic Geochemistry").

$$\Phi_{fl} = \frac{\rho_{ma} - \rho_{bk}}{\rho_{ma} - \rho_{fl}}, \quad (1)$$

$$\Phi_{om} = \frac{\rho_{ma} - \rho_{bs}}{\rho_{ma} - \rho_{om}}, \text{ and} \quad (2)$$

$$TOC\% = \frac{0.85 \times \rho_{om} \times \Phi_{om}}{\rho_{om}(\Phi_{om}) + \rho_{ma}(1 - \Phi_{om} - \Phi_{fl})} \times 100\%, \quad (3)$$

where,

ρ_{bk} = 23 g/cm³ = density of background sediment (from density log),
ρ_{bs} = 1.88 g/cm³ = density of black shale interval (from density log),
ρ_{om} = 1.2 g/cm³ = density of organic matter (assumed),
ρ_{ma} = 2.7 g/cm³ = density of matrix (grain density),
ρ_{fl} = 1.05 g/cm³ = density of seawater,
ϕ_{fl} = water-filled porosity, and
ϕ_{om} = volume fraction of organic matter.

There are no other gamma radiation peaks of the same magnitude in the Cretaceous section at Hole 1207B. There are some smaller peaks, notably at 556 and 560 mbsf just above the main event and at 367 and 346 mbsf. The gamma radiation peak at 346 mbsf (Fig. F58) appears to be at or very close to the Cenomanian/Turonian boundary, which corresponds to a prominent oceanwide anoxic event that led to deposition of C_{org}-rich units globally. This peak might then represent a minor black shale at this site. However, hardgrounds also often have an associated uranium peak, and it is also possible that the peak represents a period of nondeposition. The thickness of this peak is ~60 cm, based on the high-resolution gamma radiation log of the MGT, and the amplitude is six times less than the peak at 566 mbsf (1.1 ppm compared with 6.4 ppm uranium). Unfortunately, uranium content is not usually a good quantitative guide to the organic matter content of the sediment.

FMS Image Logs and Cherts

Hole 1207B has very low core recovery from 217 mbsf to the total depth; most cores in this interval contain only pieces of chert. The FMS image logs, available from 148–380 mbsf, show a series of highly resistive thin beds alternating with lower resistivity layers (resistive beds appear light in the FMS image, and conductive beds appear dark) (Fig. F59). We attribute this layering to hard chert layers within soft ooze and chalk. The frequency of cherts increases downhole, reaching a maximum at 320 mbsf. The form of the cherts was predominantly layered (present in the images of all four of the FMS pads), rather than nodular (present in only one or two pad images at a particular depth).

The locations and thicknesses of the cherts were taken from the FMS images (Fig. F60). The dynamic image is better than the static image for this task because the color contrast over short intervals is enhanced. The chert layers also form small ledges in the hole, as shown by the reduction in hole diameter in the caliper logs (Fig. F59). The chert per-

F58. Comparison of gamma radiation logs around Cenomian/Turonian boundary, p. 111.

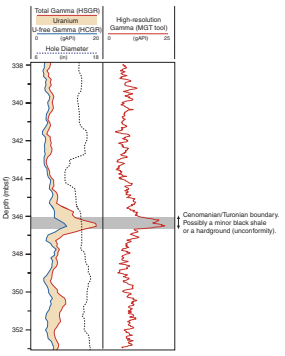

F59. Layered cherts as resistive bands across four pads, p. 112.

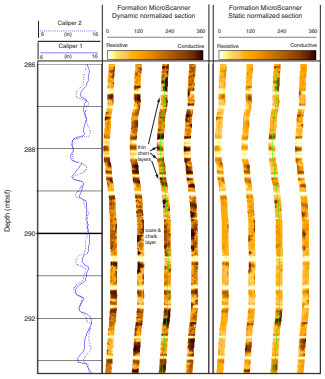

F60. Chert distribution, thickness, and percentage, Hole 1207B, p. 113.

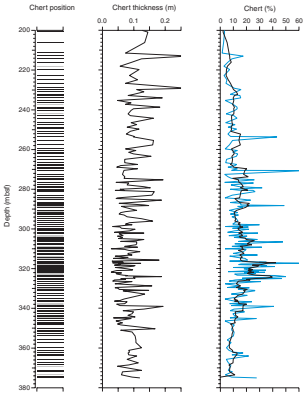

centage for each chert/ooze alternation was calculated and is also presented in Figure F60.

The total count of chert layers is 214 layers between 200 and 380 mbsf, with the highest frequency being between 316 and 326 mbsf. The thickness ranges from 3 to 20 cm, with an average thickness of 8.8 cm.

Low core recovery in chalk-chert sequences has been the subject of much discussion (Keene, 1975). However, little information is available on the form, thickness, and distribution of chert layers. The logging data from this site provide an important basis for further discussions of core recovery in chalk/chert and ooze/chert alternating sequences.

Synthetic Seismogram

We constructed a synthetic seismogram for Site 1207 using downhole and core physical properties measurements to date the various reflectors on the seismic section and to place the notable horizons identified in the core in their two-dimensional setting. Nearly continuous velocity and density measurements from the Hole 1207A cores were available to 217 mbsf. We used the Hamilton Frame (PWS3) velocities (see **"*P*-Wave Velocities,"** p. 39, in "Physical Properties") because they are typically more reliable than the MST *P*-wave values, and the MST GRA bulk densities (see **"MST Measurements,"** p. 37, in "Physical Properties"). Densities lower than 1.4 g/cm³ were removed from the data set because they typically result from section-end and void effects. For the downhole logs, velocity data were available from 120 to 360 mbsf, and density data were available from 125 to 612 mbsf. To complete the velocity profile, we calibrated the logarithm of the resistivity (medium induction phasor-processed resistivity [IMPH]) to the velocity measurements using a linear least-squares fit:

$$\text{Velocity} = 2.139 + (1.675 \times \log_{10} \text{IMPH}).$$

We found that the velocity log contained occasional bad values that caused spurious reflections in the synthetic seismogram, so we used the velocity derived from resistivity (a more robust measurement) for the whole interval (130–620 mbsf).

The synthetic seismogram was calculated using the IESX software by Schlumberger GeoQuest (Fig. F61), using the standard method described by Rider (1996), among others. The velocity and density data were converted from depth to two-way traveltime (TWT) using the interval velocities. Impedance (velocity × density) was calculated, and the impedance contrast between successive layers gave the reflection coefficient series. The source wavelet (–90° phase, extracted from the 20 seismic traces surrounding the hole location) was convolved with the reflection coefficient series to give the synthetic seismogram. The synthetic seismogram was stretched and squeezed slightly to line up the synthetic reflections with those in the seismic section to give the final version shown in Figures F61 and F62.

F61. Synthetic seismogram, Hole 1207B, p. 114.

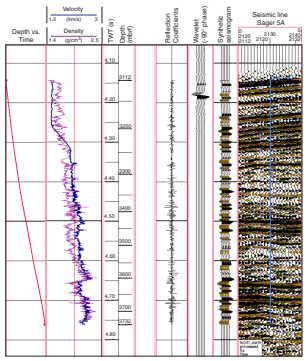

F62. Synthetic seismogram, seismic line Sager 5A, p. 115.

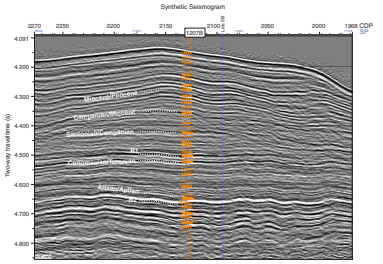

REFERENCES

Aquino Neto, F.R., Restle, A., Connan, J., Albrecht, P., and Ourisson, G., 1982. Novel tricyclic terpanes (C_{19}, C_{20}) in sediments and petroleums. *Tetrahedron Lett.,* 23:2027–2030.

Baker, P.A., 1986. Pore-water chemistry of carbonate-rich sediments, Lord Howe Rise, Southwest Pacific Ocean. *In* Kennett, J.P., von der Borch, C.C., et al., *Init. Repts. DSDP,* 90 (Pt. 2): Washington (U.S. Govt. Printing Office), 1249–1256.

Baker, P.A., Gieskes, J.M., and Elderfield, H., 1982. Diagenesis of carbonates in deep-sea sediments—evidence from Sr^{2+}/Ca^{2+} ratios and interstitial dissolved Sr^{2+} data. *J. Sediment. Petrol.,* 52:71–82.

Barnes, P.J., Brassell, S.C., Comet, P., Eglinton, G., McEvoy, J., Maxwell, J.R., Wardroper, A.M.K., and Volkman, J.K., 1979. Preliminary lipid analysis of core sections 18, 24, and 30 from Hole 402A. *In* Montadert, L., Roberts, D.G., et al., *Init. Repts. DSDP,* 48: Washington (U.S. Govt. Printing Office), 965–976.

Barrera, E., Savin, S.M., Thomas, E., and Jones, C.E., 1997. Evidence for thermohaline-circulation reversals controlled by sea level change in the latest Cretaceous. *Geology,* 25:715–718.

Baudin, F., Deconinck, J.-F., Sachsenhofer, R.F., Strasser, A., and Arnaud, H., 1995. Organic geochemistry and clay mineralogy of Lower Cretaceous sediments from Allison and Resolution guyots (Sites 865 and 866), Mid-Pacific Mountains. *In* Winterer, E.L., Sager, W.W., Firth, J.V., and Sinton, J.M. (Eds.), *Proc. ODP, Sci. Results,* 143: College Station, TX (Ocean Drilling Program), 173–196.

Beaumont, V., and Robert, F., 1999. Nitrogen isotope ratios of kerogens in Precambrian cherts; a record of the evolution of atmosphere chemistry? *Precambrian Res.,* 96:63–82.

Bralower, T.J., Arthur, M.A., Leckie, R.M., Sliter, W.V., Allard, D.J., and Schlanger, S.O., 1994. Timing and paleoceanography of oceanic dysoxia/anoxia in the Late Barremian to Early Aptian. *Palaios,* 9:335–369.

Bralower, T.J., CoBabe, E., Clement, B., Sliter, W.V., Osburne, C., and Longoria, J., 1999. The record of global change in mid-Cretaceous (Barremian–Albian) sections from the Sierra Madre, northeasterm Mexico. *In* Huber, B.T., Bralower, T.J., and Leckie, R.M. (Eds.), *J. Foraminiferal Res.,* 29:418–437.

Bralower, T.J., Sliter, W.V., Arthur, M.A., Leckie, R.M., Allard, D.J., and Schlanger, S.O., 1993. Dysoxic/anoxic episodes in the Aptian-Albian (Early Cretaceous). *In* Pringle, M.S., Sager, W.W., Sliter, M.V., and Stein, S. (Eds.), *The Mesozoic Pacific: Geology, Tectonics, and Volcanism*. Geophys. Monogr., Am. Geophys. Union, 77:5–37.

Brassell, S.C., 1984. Aliphatic hydrocarbons of a Cretaceous black shale and its adjacent green claystone from the southern Angola Basin. Deep Sea Drilling Project, Leg 75. *In* Hay, W.W., Sibuet, J.C., et al., *Init. Repts. DSDP,* 75 (Pt. 2): Washington (U.S. Govt. Printing Office), 1019–1030.

Brassell, S.C., Comet, P.A., Eglinton, G., Isaacson, P.J., McEvoy, J., Maxwell, J.R., Thomson, I.D., Tibbetts, P.J., and Volkman, J.K., 1980. The origin and fate of lipids in the Japan Trench. *In* Douglas, A.G., and Maxwell, J.R. (Eds.), *Advances in Organic Geochemistry 1979:* Oxford (Pergamon Press), 375–392.

Brassell, S.C., and Eglinton, G., 1983. Steroids and triterpenoids in deep-sea sediments as environmental and diagenetic indicators. *In* Bjorøy, M. (Ed.), *Advances in Organic Geochemistry 1981:* Chichester (Wiley), 684–697.

Brassell, S.C., Eglinton, G., and Howell, V.J., 1987. Palaeoenvironmental assessment for marine organic-rich sediments using molecular organic geochemistry. *In* Brooks, J., and Fleet, A.J. (Eds.), *Marine Petroleum Source Rocks*. Spec. Publ.—Geol. Soc. London, 26:79–98.

Brassell, S.C., Eglinton, G., and Maxwell, J.R., 1983. The geochemistry of terpenoids and steroids. *Biochem. Soc. Trans.,* 11:575–586.

Brassell, S.C., Eglinton, G., Maxwell, J.R., and Philp, R.P., 1978. Natural background of alkanes in the aquatic environment. *In* Hutzinger, O., van Lelyveld, L.H., and Zoeteman, B.C.J. (Eds.), *Aquatic Pollutants: Transformation and Biological Effects:* Oxford (Pergamon Press), 69–86.

Brassell, S.C., Lewis, C.A., de Leeuw, J.W., de Lange, F., and Sinninghe Damsté, J.S., 1986. Isoprenoid thiophenes: novel diagenetic products in sediments? *Nature,* 320:160–162.

Brassell, S.C., McEvoy, J., Hoffmann, C.F., Lamb, N.A., Peakman, T.M., and Maxwell, J.R., 1984. Isomerization, rearrangement and aromatisation of steroids in distinguishing early stages of diagenesis. *In* Schenck, P.A., de Leeuw, J.W., and Lijmbach, G.W.M. (Eds.), *Advances in Organic Geochemistry 1983:* Oxford (Pergamon Press), 11–23.

Brassell, S.C., Wardroper, A.M.K., Thomson, I.D., Maxwell, J.R., and Eglinton, G., 1981. Specific acyclic isoprenoids as biological markers of methanogenic bacteria in marine sediments. *Nature,* 290:693–696.

Bréhéret, J.G., 1988. Episodes de sédimentation riches en matière organique dans les marnes bleues d'âge Aptien et Albien de la partie pélagique du bassin vocontien. *Bull. Geol. Soc. Fr.,* 8:349–356.

Broecker, W.S., and Peng, T.-H., 1982. *Tracers in the Sea:* Palisades, NY (Lamont-Doherty Geol. Observ.).

Burnett, J.A., 1998. Upper Cretaceous. *In* Bown, P.R. (Ed.), *Calcareous Nannofossil Biostratigraphy:* London (Chapman and Hall), 132–199.

Cameron, D.H., 1976. Carbon and carbonate analyses, Leg 33. *In* Schlanger, S.O., Jackson, E.D., et al., *Init. Repts. DSDP,* 33: Washington (U.S. Govt. Printing Office), 959–963.

Cande, S.C., and Kent, D.V., 1995. Revised calibration of the geomagnetic polarity time scale for the Late Cretaceous and Cenozoic. *J. Geophys. Res.,* 100:6093–6095.

Chepstow-Lusty, A., Backman, J., and Shackleton, N.J., 1989. Comparison of upper Pliocene *Discoaster* abundance variations from North Atlantic Sites 552, 607, 658, 659, and 662: further evidence for marine plankton responding to orbital forcing. *In* Ruddiman, W.F., Sarnthein, M., et al., *Proc. ODP, Sci. Results,* 108: College Station, TX (Ocean Drilling Program), 121–141.

Coccioni, A., Nesci, O., Tramontana, M., Wezel, F.C., and Moretti, E., 1987. Descrizione di un livello-guida "radiolaritico-bituminoso-ittiolitico" alla base delle marne a fucoidi nell'Apennino umbro-marchigiano. *Boll. Soc. Geol. Ital.,* 106:183–192.

Coccioni, R., and Premoli Silva, I., 1994. Planktonic foraminifera from the Lower Cretaceous of Rio Argos sections (southern Spain) and biostratigraphic implications. *Cretaceous Res.,* 15:645–687.

Comet, P.A., McEvoy, J., Brassell, S.C., Eglinton, G., Maxwell, J.R., and Thomson, I.D., 1981. Lipids of an Upper Albian limestone, Deep Sea Drilling Project Site 465, Section 465A-38-3. *In* Thiede, J., Vallier, T.L., et al., *Init. Repts. DSDP,* 62: Washington (U.S. Govt. Printing Office), 923–937.

Dachs, J., Bayona, J.M., Fowler, S.W., Miquel, J.C., and Albaiges, J., 1998. Evidence for cyanobacterial inputs and heterotrophic alteration of lipids in sinking particles in the Alboran Sea (SW Mediterranean). *Mar. Chem.,* 60:189–201.

Dastillung, M., Albrecht, P., and Ourisson, G., 1980. Aliphatic and polycyclic ketones in sediments. C_{27}–C_{35} ketones and aldehydes of the hopane series. *J. Chem. Res.,* 5:(*M*)2325–2352; (*S*)166–167.

Dean, W.E., 1981. Calcium carbonate and organic carbon in samples from Deep Sea Drilling Project Sites 463, 464, 465, and 466. *In* Thiede, J., Vallier, T.L., et al., *Init. Repts. DSDP,* 62: Washington (U.S. Govt. Printing Office), 869–876.

Dean, W.E., Claypool, G.E., and Thiede, J., 1981. Origin of organic-carbon-rich Mid-Cretaceous limestones, Mid-Pacific Mountains and southern Hess Rise. *In* Thiede, J., Vallier, T.L., et al., *Init. Repts. DSDP,* 62: Washington (U.S. Govt. Printing Office), 877–890.

Didyk, B.M., Simoneit, B.R.T., Brassell, S.C., and Eglinton, G., 1978. Organic geochemical indicators of palaeoenvironmental conditions of sedimentation. *Nature,* 272:216–222.

Edmunds, K.L.H., Brassell, S.C., and Eglinton, G., 1980. The short-term diagenetic fate of 5a-cholestan-3b-ol: *in situ* radiolabelled incubations in algal mats. *In* Douglas, A.G., and Maxwell, J.R. (Eds.), *Advances in Organic Geochemistry 1979:* Oxford (Pergamon Press), 427–434.

Eglinton, G., and Hamilton, R.J., 1963. The distribution of alkanes. *In* Swain, T. (Ed.), *Chemical Plant Taxonomy:* London (Academic Press), 187–208.

Erba, E., 1994. Nannofossils and superplumes: the early Aptian "nannoconids crisis." *Paleoceanography,* 9:483–501.

Erba, E., Channell, J.E.T., Claps, M., Jones, C., Larson, R., Opdyke, B., Premoli Silva, I., Riva, A., Salvini, G., and Torricelli, S., 1999. Integrated stratigraphy of the Cismon APTICORE (southern Alps, Italy): a "reference section" for the Barremian–Aptian interval at low latitudes. *J. Foraminiferal Res.,* 29:371–391.

Farrell, J.W., and Prell, W.L., 1991. Pacific $CaCO_3$ preservation and $\delta^{18}O$ since 4 Ma: paleoceanic and paleoclimatic implications. *Paleoceanography,* 6:485–498.

Farrimond, P., Eglinton, G., and Brassell, S.C., 1986. Geolipids of black shales and claystones in Cretaceous and Jurassic sediment sequences from the North American Basin. *In* Summerhayes, C.P., and Shackleton, N.J. (Eds.), *North Atlantic Palaeoceanography.* Spec. Publ.—Geol. Soc. London, 21:347–360.

Farrimond, P., Eglinton, G., Brassell, S.C., and Jenkyns, H.C., 1990. The Cenomanian/Turonian anoxic event in Europe: an organic geochemical study. *Mar. Pet. Geol.,* 7:75–89.

Ferdelman, T.G., Lee, C., Pantoja, S., Harder, J., Bebout, B.M., and Fossing, H., 1997. Sulfate reduction and methanogenesis in a *Thioploca*-dominated sediment off the coast of Chile. *Geochim. Cosmochim. Acta,* 61:3065–3079.

Gagosian, R.B., and Peltzer, E.T., 1986. The importance of atmospheric input of terrestrial organic material to deep sea sediments. *In* Leythaeuser, D., and Rullkötter, J. (Eds.), *Advances in Organic Geochemistry 1985:* Oxford (Pergamon Press), 897–903.

Gagosian, R.B., Peltzer, E.T., and Merrill, J.T., 1987. Long-range transport of terrestrially derived lipids in aerosols from the south Pacific. *Nature,* 325:800–803.

Gagosian, R.B., and Smith, S.O., 1979. Steroid ketones in surface sediments from the south-west African Shelf. *Nature,* 277:287–289.

Gagosian, R.B., Smith, S.O., and Nigrelli, G.E., 1982. Vertical transport of steroid alcohols and ketones measured in a sediment trap experiment in the equatorial Atlantic Ocean. *Geochim. Cosmochim. Acta,* 46:1163–1172.

Gelpi, E., Schneider, H., Mann, J., and Oró, J., 1970. Hydrocarbons of geochemical significance in microscopic algae. *Phytochemistry,* 9:603–612.

Gieskes, J.M., 1981. Deep-sea drilling interstitial water studies: implications for chemical alteration of the oceanic crust, layers I and II. *In* Warme, J.E., Douglas, R.G., and Winterer, E.L. (Eds.), *The Deep Sea Drilling Project: A Decade of Progress*. Spec. Publ.—Soc. Econ. Paleontol. Mineral., 32:149–167.

————, 1983. The chemistry of interstitial waters of deep-sea sediments: interpretation of deep-sea drilling data. *In* Riley, J.P., and Chester, R. (Eds.), *Chemical Oceanography* (Vol. 8): London (Academic), 221–269.

Goossens, H., de Leeuw, J.W., Schenck, P.A., and Brassell, S.C., 1984. Tocopherols as likely precursors of pristane in ancient sediment and crude oils. *Nature,* 312:440–442.

Greiner, A.Ch., Spyckerelle, C., and Albrecht, P., 1976. Aromatic hydrocarbons from geological sources: I. New naturally occurring phenanthrene and chrysene derivatives. *Tetrahedron,* 32:257–260.

Greiner, A.Ch., Spyckerelle, C., Albrecht, P., and Ourisson, G., 1977. Aromatic hydrocarbons from geological sources: V. Mono and diaromatic hopane derivatives. *J. Chem. Res.,* (M):3829–3871; (S):334–335.

Gröcke, D.R., Hesselbo, S.P., and Jenkyns, H.C., 1999. Carbon-isotope composition of Lower Cretaceous fossil wood: ocean-atmosphere chemistry and relation to sea-level change. *Geology,* 27:155–158.

Han, J., McCarthy, E.D., Calvin, M., and Benn, M.H., 1968. Hydrocarbon constituents of the blue-green algae, *Nostoc muscorum, Anacystis nidulans, Phormidium luridum* and *Chlorogloea fritschii*. *J. Chem Soc. C,* 2785–2791.

Haug, G.H., Maslin, M.A., Sarnthein, M., Stax, R., and Tiedemann, R., 1995. Evolution of northwest Pacific sedimentation patterns since 6 Ma (Site 882). *In* Rea, D.K., Basov, I.A., Scholl, D.W., and Allan, J.F. (Eds.), *Proc. ODP, Sci. Results,* 145: College Station, TX (Ocean Drilling Program), 293–314.

Howard, D.L., Simoneit, B.R.T., and Chapman, D.J., 1984. Triterpenoids from lipids of *Rhodomicrobium vannielli*. *Arch. Microbiol.,* 137:200–204.

Hussler, G., and Albrecht, P., 1983. C_{27}-C_{29} monoaromatic anthrasteroid hydrocarbons in Cretaceous black shales. *Nature,* 304:262–263.

Hussler, G., Chappe, B., Wehrung, P., and Albrecht, P., 1981. C_{27}–C_{29} ring A monoaromatic steroids in Cretaceous black shales. *Nature,* 294:556–558.

Jackson, E.D., and Schlanger, S.O., 1976. Regional synthesis, Line Islands chain, and Manahiki Plateau, Central Pacific Ocean, DSDP Leg 33. *In* Schlanger, S.O., Jackson, E.D., et al. (Eds.), *Init. Repts. DSDP* 33: Washington (U.S. Govt. Printing Office), 915–927.

Jenkyns, H.C., 1995. Carbon-isotope stratigraphy and paleoceanographic significance of the Lower Cretaceous shallow-water carbonates of Resolution Guyot, Mid-Pacific Mountains. *In* Winterer, E.L., Sager, W.W., Firth, J.V., and Sinton, J.M. (Eds.), *Proc. ODP, Sci. Results,* 143: College Station, TX (Ocean Drilling Program), 99–104.

Jenkyns, H.C., Gröcke, D.R., and Hesselbo, S.P., 2001. Nitrogen-isotope evidence for water mass denitrification during the Early Toarcian (Jurassic) Oceanic Anoxic Event. *Paleoceanography,* 16:593–603.

Keene, J.B., 1975. Cherts and porcellanites from the North Pacific DSDP, Leg 32. *In* Larson, R.L., Moberly, R., et al. *Init. Repts. DSDP,* 32: Washington (U.S. Govt. Printing Office), 429–507.

Keller, G., and Barron, J.A., 1987. Paleodepth distribution of Neogene deep-sea hiatuses. *Paleoceanography,* 2:697–713.

Kenig, F., Sinninghe Damsté, J.S., de Leeuw, J.W., and Huc, A.Y., 1995. Occurrence and origin of mono-, di- and trimethylalkanes in modern and Holocene cyanobacterial mats from Abu Dhabi, United Arab Emirates. *Geochim. Cosmochim. Acta,* 59:2999–3015.

Kennett, J.P., Keller, G., and Srinivasan, M.S., 1985. Miocene planktonic foraminiferal biogeography and paleoceanographic development of the Indo-Pacific region. *In* Kennett, J.P. (Ed.), *The Miocene Ocean: Paleoceanography and Biogeography.* Mem.—Geol. Soc. Am., 163:197–236.

Koizumi, I., 1975. Neogene diatoms from the northwestern Pacific Ocean, Deep Sea Drilling Project. *In* Larson, R.L., Moberly, R., et al., *Init. Repts. DSDP,* 32: Washington (U.S. Govt. Printing Office), 865–889.

Koizumi, I., and Tanimura, Y., 1985. Neogene diatom biostratigraphy of the middle latitude western North Pacific, Deep Sea Drilling Project Leg 86. *In* Heath, G.R., Burckle, L.H., et al., *Init. Repts. DSDP,* 86: Washington (U.S. Govt. Printing Office), 269–300.

Köster, J., Volkman, J.K., Rullkötter, J., Scolz-Böttcher, B.M., Reithmeir, J., and Fisher, U., 1999. Mono-, di- and trimethyl-branched alkanes in cultures of the filamentous cyanobacterium *Calothrix scopulorum*. *Org. Geochem.,* 30:1367–1379.

Larson, R.L., Moberly, R., et al., 1975. *Init. Repts. DSDP,* 32: Washington (U.S. Govt. Printing Office).

Laskar, J., 1990. Chaotic motion of the solar system: numerical estimate of chaotic zones. *Icarus,* 88:266–291.

Lawrence, J.R., and Gieskes, J.M., 1981. Constraints on water transport and alteration in the oceanic crust from isotopic composition of pore water. *J. Geophys. Res.,* 86:7924–7934.

Leckie, R.M., Bralower, T., Cashman, R., in press. Oceanic anoxic events and plankton evolution: biotic response to tectonic forcing during the mid-Cretaceous. *Paleoceanography.*

Loutit, T.S., Hardenbol, J., Vail, P.R., and Baum, G.R., 1988. Condensed sections: the key to age determination and correlation of continental margin sequences. *In* Wilgus, C.K., Hastings, B.S., Ross, C.A., Posamentier, H.W., Van Wagoner, J., and Kendall, C.G.St.C. (Eds.), *Sea-Level Changes: An Integrated Approach.* Spec. Publ.—Soc. Econ. Paleontol. Mineral., 42:183–213.

Mackenzie, A.S., Brassell, S.C., Eglinton, G., and Maxwell, J.R., 1982. Chemical fossils: the geological fate of steroids. *Science,* 217:491–504.

Magniez-Jannin, F., 1998. L'élongation des loges chez les foraminifères panctoniques du Crétacé inférieur: une adaptation à la sous-oxygénation des eaux?. *Comptes Rendues de l'Académie des Sciences* (Serie II): *Sciences de la Terre et des Planetes:* Montrouge (Gauthier-Villars), 326:207–213.

Maslin, M.A., Haug, G.H., Sarnthein, M., Tiedemann, R., Erlenkeuser, H., and Stax, R., 1995. Northwest Pacific Site 882: the initiation of Northern Hemisphere glaciation. *In* Rea, D.K., Basov, I.A., Scholl, D.W., and Allan, J.F. (Eds.), *Proc. ODP, Sci. Results,* 145: College Station, TX (Ocean Drilling Program), 315–329.

McCaffrey, M.A., Farrington, J.W., and Repeta, D.J., 1989. Geochemical implications of the lipid composition of *Thioploca* spp. from the Peru upwelling region, 15°S. *Org. Geochem.,* 14:61–68.

McDuff, R.E., 1985. The chemistry of interstitial waters, Deep Sea Drilling Project Leg 86. *In* Heath, G.R., Burckle, L.H., et al., *Init. Repts. DSDP,* 86: Washington (U.S. Govt. Printing Office), 675–687.

McDuff, R.E., and Gieskes, J.M., 1976. Calcium and magnesium profiles in DSDP interstitial waters: diffusion or reaction? *Earth Planet. Sci. Lett.,* 33:1–10.

McNutt, M.K., Winterer, E.L., Sager, W.W., Natland, J.H., and Ito, G., 1990. The Darwin Rise: a Cretaceous superswell? *Geophys. Res. Lett.,* 17:1101–1104.

Mélières, F., Deroo, G., and Herbin, J.-P., 1981. Organic-matter-rich and hypersiliceous Aptian sediments from western Mid-Pacific Mountains, Deep Sea Drilling Project Leg 62. *In* Thiede, J., Vallier, T.L., et al., *Init. Repts. DSDP,* 62: Washington (U.S. Govt. Printing Office), 903–915.

Menegatti, A.P., Weissert, H., Brown, R.S., Tyson, R.V., Farrimond, P., Strasser, A., and Caron, M., 1998. High resolution $\delta^{13}C$ stratigraphy through the early Aptian "Livello Selli" of the Alpine Tethys. *Paleoceanography,* 13:530–545.

Meunier-Christmann, C., Albrecht, P., Brassell, S.C., ten Haven, H.L., van der Linden, B., Rullkötter, J., and Trendel, J.M. 1991. Occurrence of dammar-13(17)-enes in sediments: indications for a yet unrecognized microbial constituent. *Geochim. Cosmochim. Acta,* 55:3475–3483.

Meyers, P.A., 1987. Organic-carbon content of sediments and rocks from Deep Sea Drilling Project Sites 603, 604, and 605, western margin of the North Atlantic. *In* van Hinte, J.E., Wise, S.W., Jr., et al., *Init. Repts. DSDP,* 93 (Pt. 2): Washington (U.S. Govt. Printing Office), 1187–1194.

————, 1994. Preservation of elemental and isotopic source identification of sedimentary organic matter. *Chem. Geol.,* 144:289–302.

Meyers, P.A., Brassell, S.C., and Huc, A.Y., 1984. Geochemistry of organic carbon in South Atlantic Sediments from DSDP Leg 75. *In* Hay, W.W., Sibuet, J.-C., et al., *Init. Repts. DSDP,* 75 (Pt. 2): Washington (U.S. Govt. Printing Office), 967–981.

Meyers, P.A., and Doose, H., 1999. Sources, preservation, and thermal maturity of organic matter in Pliocene–Pleistocene organic-carbon–rich sediments of the western Mediterranean Sea. *In* Zahn, R., Comas, M.C., and Klaus, A. (Eds.), *Proc. ODP, Sci. Results,* 161: College Station, TX (Ocean Drilling Program), 383–390.

Millero, F.J., and Sohn, M.L., 1992. *Chemical Oceanography:* Boca Raton (CRC Press).

Moldowan, J.M., Fago, F.J., Lee, C.Y., Jacobson, S.R., Watt, D.S., Nacer-Eddine, S., Jeganathan, A., and Young, D.C., 1990. Sedimentary 24-*n*-propylcholestanes, molecular fossils diagnostic of marine algae. *Science,* 247:309–312.

Nakanishi, M., Tamaki, K., and Kobayashi, K., 1989. Mesozoic magnetic anomaly lineations and seafloor spreading history of the Northwestern Pacific. *J. Geophys. Res.,* 94:15437–15462.

Nijenhuis, I.A., and de Lange, G.J., 2000. Geochemical constraints on Pliocene sapropel formation in the eastern Mediterranean. *Mar. Geol.,* 163:41–63.

Okada, H., and Bukry, D., 1980. Supplementary modification and introduction of code numbers to the low-latitude coccolith biostratigraphic zonation. *Mar. Micropaleontol.,* 5:321–325.

Ourisson, G., Albrecht, P., and Rohmer, M., 1979. The hopanoids: paleochemistry and biochemistry of a group of natural products. *Pure Appl. Chem.,* 51:709–729.

Ourisson, G., Rohmer, M., and Poralla, K., 1987. Microbial lipids betrayed by their fossils. *Microbiol. Sci.,* 4:52–57.

Peakman, T.M., Farrimond, P., Brassell, S.C., and Maxwell, J.R., 1986. De-A-steroids in immature marine shales. *In* Leythaeuser, D., and Rullkötter, J. (Eds.), *Advances in Organic Geochemistry 1985:* Oxford (Pergamon Press), 779–789.

Peakman, T.M., and Maxwell, J.R. 1988. Early diagenetic pathways of steroid alkenes. *In* Mattavelli, L., and Novelli, L. (Eds.), *Advances in Organic Geochemistry 1987:* Oxford (Pergamon Press), 583–592.

Philp, R.P., Brown, S., Calvin, M., Brassell, S.C., and Eglinton G., 1978. Hydrocarbon and fatty acid distributions in recently deposited algal mats at Laguna Guerrero, Baja California. *In* Krumbein, W.E., (Ed.), *Environmental Biogeochemistry and Geomicrobiology* (Vol. 1): *The Aquatic Environment:* Ann Arbor (Ann Arbor Science), 255–270.

Premoli Silva, I., Erba, E., Salvini, G., Locatelli, C., and Verga, D., 1999. Biotic changes in Cretaceous oceanic anoxic events of the Tethys. *J. Foraminiferal Res.,* 29:352–370.

Rea, D.K., Basov, I.A., Janecek, T.R., Palmer-Julson, A., et al., 1993. *Proc. ODP, Init. Repts.,* 145: College Station, TX (Ocean Drilling Program).

Rea, D.K., Basov, I.A., Krissek, L.A., and the Leg 145 Scientific Party, 1995. Scientific results of drilling the North Pacific transect. *In* Rea, D.K., Basov, I.A., Scholl, D.W., and Allan, J.F. (Eds.), *Proc. ODP, Sci. Results,* 145: College Station, TX (Ocean Drilling Program), 577–596.

Rider, M., 1996. *The Geological Interpretation of Well Logs* (2nd ed.): Caithness (Whittles Publishing).

Robinson, N., Eglinton, G., Brassell, S.C., and Cranwell, P.A., 1984. Dinoflagellate origin for sedimentary 4α-methylsteroids and 5α(H)-stanols. *Nature,* 308:439–441.

Rohmer, M., Bisseret, P., and Neunlist, S., 1992. The hopanoids, prokaryotic triterpenoids and precursors of ubiquitous molecular fossils. *In* Moldowan, J.M., Albrecht, P., and Philp, R.P., *Biological Markers in Sediments and Petroleum:* Englewood Cliffs, NJ (Prentice Hall), 1–17.

Rohmer, M., Bouvier-Nave, P., and Ourisson, G., 1984. Distribution of hopanoid triterpenes in prokaryotes. *J. Genet. Microbiol.,* 130:1137–1150.

Romine, K., and Lombari, G., 1985. Evolution of Pacific circulation in the Miocene: radiolarian evidence from DSDP Site 289. *In* Kennett, J.P. (Ed.), *The Miocene Ocean: Paleoceanography and Biogeography.* Mem.—Geol. Soc. Am., 163:273–290.

Rullkötter, J., Mukhopadhyay, P.K., and Welte, D.H., 1984. Geochemistry and petrography of organic matter in sediments from Hole 530A, Angola Basin, and Hole 532, Walvis Ridge, Deep Sea Drilling Project. *In* Hay, W.W., Sibuet, J.-C., et al., *Init. Repts. DSDP,* 75 (Pt. 2), Washington (U.S. Govt. Printing Office), 1069–1087.

————, 1987. Geochemistry and petrography of organic matter from Deep Sea Drilling Project Site 603, lower continental rise off Cape Hatteras. *In* van Hinte, J.E., Wise, S.W., Jr., et al., *Init. Repts. DSDP,* 93 (Pt. 2): Washington (U.S. Govt. Printing Office), 1163–1176.

Rullkötter, J., and Welte, D.H., 1983. Maturation of organic matter in areas of high heat flow: A study of sediments from DSDP Leg 63, offshore California, and Leg 64, Gulf of California. *In* Bjorøy, M., et al. (Eds.), *Advances in Organic Geochemistry 1981:* Chichester (Wiley), 438–448.

Sakata, S., Hayes, J.M., McTaggart, A.R., Evans, R.A., Leckone, K.J., and Togasaki, R.K., 1997. Carbon isotopic fractionation associated with lipid biosynthesis by a cyanobacterium: relevance for interpretation of biomarker records. *Geochim. Cosmochim. Acta,* 61:5379–5389.

Schlanger, S.O., and Jenkyns, H.C., 1976. Cretaceous oceanic anoxic events: causes and consequences. *Geol. Mijnbouw,* 55:179–184.

Sclater, J.G., Anderson, R.N., and Bell, M.L., 1971. Elevation of ridges and evolution of the central Eastern Pacific. *J. Geophys. Res.,* 76:7888–7915.

Shiea, J., Brassell, S.C., and Ward, D.M., 1990. Mid-chain branched mono- and dimethyl alkanes in hot spring cyanobacterial mats: a direct biogenic source for branched alkanes in ancient sediments? *Org. Geochem.,* 15:223–231.

Shipboard Scientific Party, 1975. Site 305: Shatsky Rise. *In* Larson, R.L., Moberly, R., et al., *Init. Repts. DSDP,* 32: Washington (U.S. Govt. Printing Office), 75–158.

Sigal, J., 1977. Essai de zonation du Crétacé méditerranéen à l'aide des foraminifères planctoniques. *Geol. Mediterr.,* 4:99–108.

Simoneit, B.R., 1973. Identification of isoprenoidal ketones in Deep Sea Drilling Project core samples and their geochemical significance. *In* Burns, R.E., Andrews, J.E., et al., (Eds.) *Init. Repts. DSDP,* 21: Washington (U.S. Govt. Printing Office), 909–923.

Simoneit, B.R.T., 1986. Biomarker geochemistry of black shales from Cretaceous oceans—an overview. *Mar. Geol.,* 70:9–41.

————, 1978. The organic chemistry of marine sediments. *In* Riley, J.P., and Chester, R. (Eds.), *Chemical Oceanography* (2nd ed.) (Vol. 7): New York (Academic Press), 233–311.

Simoneit, B.R.T., and Stuermer, D.H., 1982. Organic geochemical indicators for sources of organic matter and paleoenvironmental conditions in Cretaceous oceans. *In* Schlanger, S.O., and Cita, M.B. (Eds.), *Nature and Origin of Cretaceous Carbon-Rich Facies:* New York (Academic Press), 145–163.

Sinninghe-Damsté, J.S., Ripstra W.I.C., de Leeuw, J.W., and Schenck, P.A., 1988. Origin of organic sulphur compounds and sulphur-containing high molecular weight substances in sediments and immature crude oils. *In* Mattavelli, L., and Novelli, L. (Eds.), *Advances in Organic Geochemistry 1987:* Oxford (Pergamon Press), 593–606.

Sinninghe Damsté, J.S., Rijpstra, W.I.C., Kock-van Dalen, A.C., De Leeuw, J.W., and Schenck, P.A., 1989. Quenching of labile functionalized lipids by inorganic sulphur species: evidence for the formation of sedimentary organic sulfur compounds at the early stages of diagenesis. *Geochim. Cosmochim. Acta,* 53:1343–1355.

Sissingh, W., 1977. Biostratigraphy of Cretaceous calcareous nannoplankton. *Geol. Mijnbouw,* 56:37–65.

Sliter, W.V., 1989. Aptian anoxia in the Pacific Basin. *Geology,* 17:909–912.

Sliter, W.V., and Brown, G.R., 1993. Shatsky Rise: seismic stratigraphy and sedimentary record of Pacific paleoceanography since the Early Cretaceous. *In* Natland, J.H., Storms, M.A., et al., *Proc. ODP, Sci. Results,* 132: College Station, TX, (Ocean Drilling Program), 3–13.

Summons, R.E., and Jahnke, J.L., 1990. Identification of the methylhopanes in sediments and petroleums. *Geochim. Cosmochim. Acta,* 54:247–251.

Summons, R.E., Volkman, J.K., and Boreham, C.J., 1987. Dinosterane and other steroidal hydrocarbons of dinoflagellate origin in sediments and petroleum. *Geochim. Cosmochim. Acta,* 51:3075–3082.

ten Haven, H.L., Littke, R., Rullkötter, J., Stein, R., and Welte, D.H., 1990. Accumulation rates and composition of organic matter in late Cenozoic sediments underlying the active upwelling area off Peru. *In* Suess, E., von Huene, R., et al., *Proc. ODP, Sci. Results,* 112: College Station, TX (Ocean Drilling Program), 591–606.

Thierstein, H.R., 1979. Paleoceanographic implications of organic carbon and carbonate distribution in Mesozoic deep sea sediments. *In* Talwani, M., Hay, W., and Ryan, W.B.F. (Eds.), *Deep Drilling Results in the Atlantic Ocean.* Am. Geophys. Union, Maurice Ewing Ser., 3:249–274.

Tissot, B., Durand, B., Espitalié, J., and Combaz, A., 1974. Influence of the nature and diagenesis of organic matter in the formation of petroleum. *AAPG Bull.,* 58:499–506.

Tremolada, F., and Erba, E., 2002. Morphometric analysis of Aptian *Assipetra infracretacea* and *Rucinolithus terebrodentarius* nannoliths: implications for taxonomy, biostratigraphy, and paleoceanography. *Mar. Micropaleo,* 44:77–92.

van Morkhoven, F.P.C.M., Berggren, W.A., and Edwards, A.S., 1986. Cenozoic cosmopolitan deep-water benthic foraminifera. *Bull. Cent. Rech. Explor.—Prod. Elf-Aquitaine,* 11.

Volkman, J.K., 1986. A review of sterol markers for marine and terrigenous organic matter. *Org. Geochem.,* 9: 83–99.

Volkman, J.K., and Maxwell, J.R., 1986. Acyclic isoprenoids as biological markers. *In* Johns, R.B. (Ed.), *Biological Markers in the Sedimentary Record:* New York (Elsevier), 1–42.

Walter, L.M., and Burton, E.A., 1986. The effect of orthophosphate on carbonate mineral dissolution rates in seawater. *Chem. Geol.,* 56:313–323.

Weissert, H., and Lini, A., 1991. Ice age interludes during the time of Cretaceous greenhouse climate? *In* Müller, D.W., McKenzie, J.A., and Weissert, H. (Eds.), *Controversies in Modern Geology: Evolution of Geological Theories in Sedimentology, Earth History and Tectonics:* New York (Academic Press), 173–191.

Williams, L.A., and Reimers, C., 1983. Role of bacterial mats in oxygen-deficient marine basins and coastal upwelling regimes; preliminary report. *Geology,* 11:267–269.

Woodruff, F., 1985. Changes in Miocene deep-sea foraminiferal distribution in the Pacific Ocean: relationship to paleoceanography. In Kennett, J.P. (Ed.), *The Miocene Ocean: Paleoceanography and Biogeography.* Mem.—Geol. Soc. Am., 163:131–175.

Young, J.R., 1998. Neogene. *In* Bown, P.R. (Ed.), *Calcareous Nannofossil Biostratigraphy:* London (Chapman and Hall), 225–265.

Zafiriou, O.C., Gagosian, R.B., Peltzer, E.T., Alford, J.B., and Loder, T., 1985. Air-to-sea fluxes of lipids at Enewetak Atoll. *J. Geophys. Res.,* 90:2409–2433.

Zahn, R., Rushdi, A., Pisias, N.G., Bornhold, B.D., Blaise, B., and Karlin, R., 1991. Carbonate deposition and benthic $\delta^{13}C$ in the subarctic Pacific: implications for changes of the oceanic carbonate system during the past 750,000 years. *Earth Planet. Sci. Lett.,* 103:116–132.

Figure F1. Interpretation of seismic reflection profile across Site 1207. Mustard = middle Miocene to Holocene, light green = Campanian–Turonian, medium green = Cenomanian to Aptian, dark green = Barremian to Valanginian. Eroded or slumped layers are seen on north and south ends of the Campanian–Turonian unit. Numbers across the figures are shotpoints. R = reflector. For details on the borehole depth to traveltime conversion, see **"Depth-Traveltime Conversion,"** p. 26, in "Physical Properties" in the "Explanatory Notes" chapter.

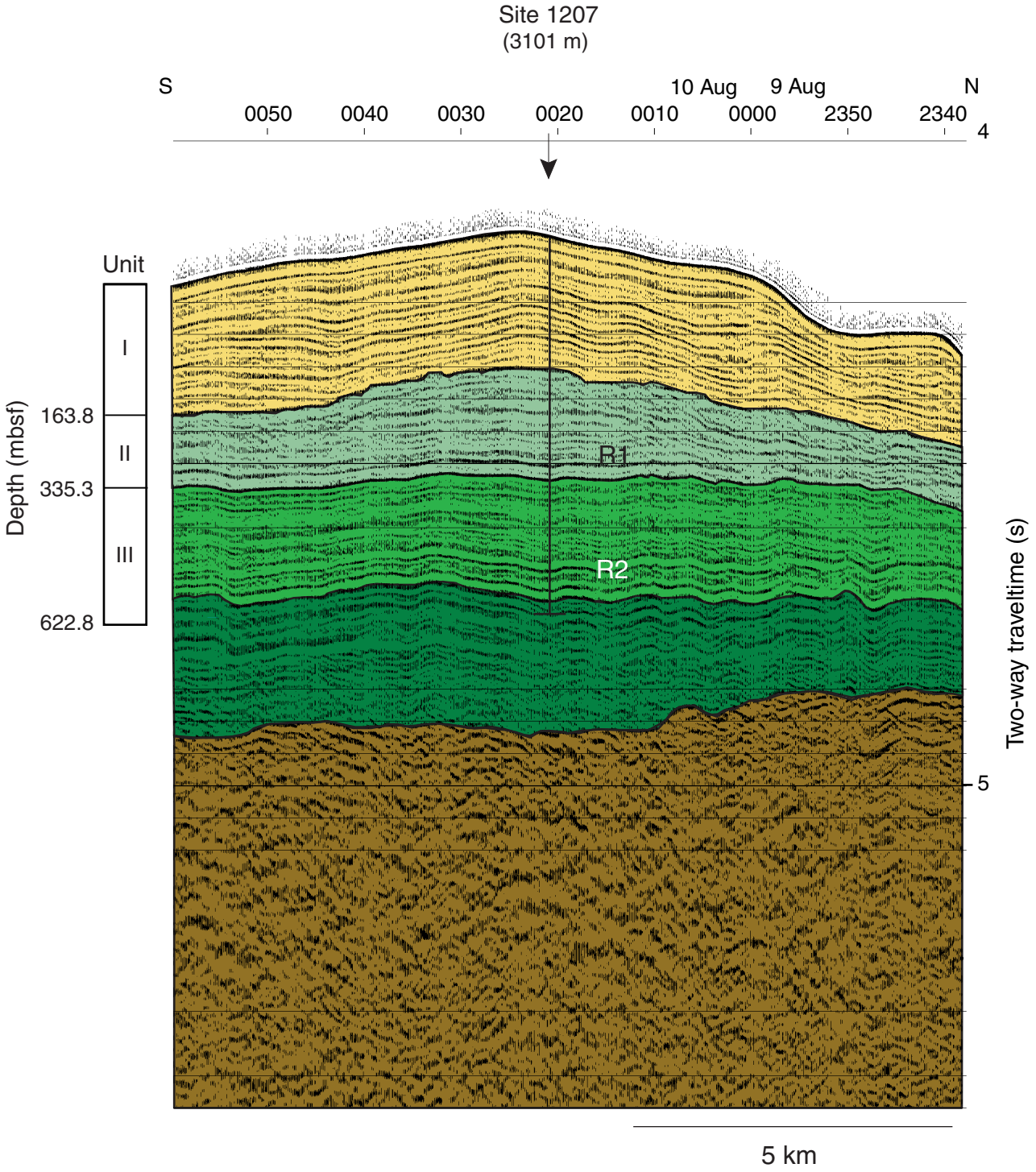

Figure F2. Summary diagram of coring results for Hole 1207A plotted on the meters below seafloor (mbsf) scale. Maximum penetration measured with the drill pipe was 256.6 mbsf. The core recovery column is a graphic representation of the cored and recovered intervals for this hole. Large gaps in core recovery (<100% nominal recovery) near the base of the hole are primarily the result of coring problems that arose when chert was encountered. The graphic lithology column presents the major sediment types and defined lithologic units. The depth-age model is represented by calcareous nannofossil (red diamonds) and planktonic foraminiferal (black crosses) datum levels; dashed lines represent the Cretaceous/Tertiary and Oligocene/Miocene boundaries. Mass accumulation rates were calculated for total sediment (green open circles) and carbonate only (blue triangles). The color reflectance lightness parameter (L*) (purple points) was measured every 2.5 cm, and the percentage calcium carbonate ($CaCO_3$) values are shown for comparison. Multisensor track (MST) magnetic susceptibility (brown points) and GRA wet bulk density (dark blue points) were measured every 2.5 cm, and index properties wet bulk density measurements (red circles) were completed on average once per section. MST *P*-wave velocity (light blue points) was determined every 2.5 cm, and discrete *P*-wave measurements (green circles) averaged at least one per section for comparison. Index properties determinations of porosity (blue squares) and percentage water content (red circles) were completed once per section on average. The accurate correction factor for the raw instrument magnetic susceptibility values is 0.68×10^{-5}. (**Figure shown on next page.**)

Figure F2 (continued). (Caption shown on previous page.)

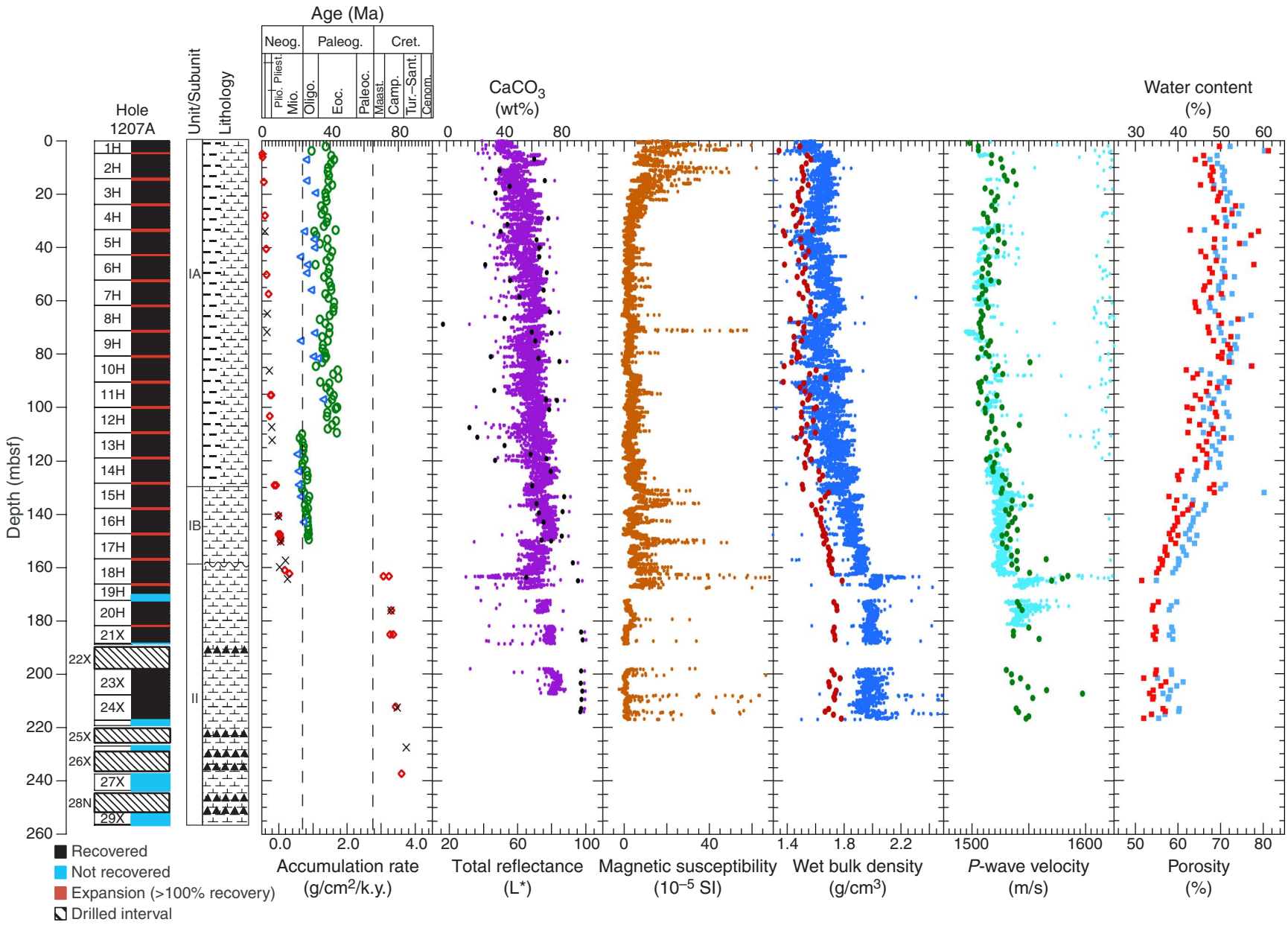

Figure F3. Changes in ocean circulation that led to cycles in upper Miocene to Holocene section. **A.** Circulation during warm/light cycle member. **B.** Circulation during cold/dark cycle member. Circle = location of Site 1207.

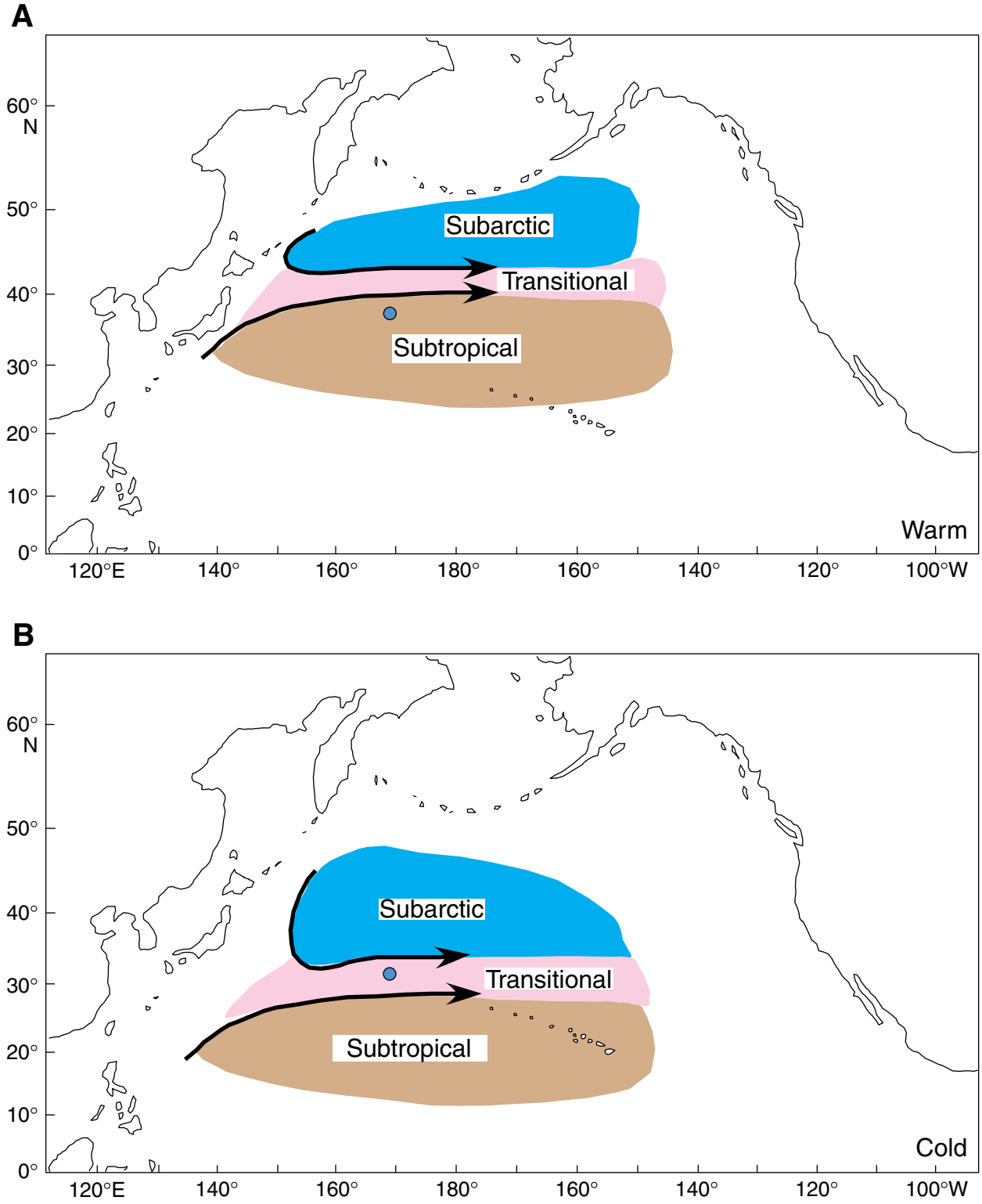

Figure F4. Hypothesized sequence of events that produced major Campanian–Miocene unconformity on the Northern High of Shatsky Rise.

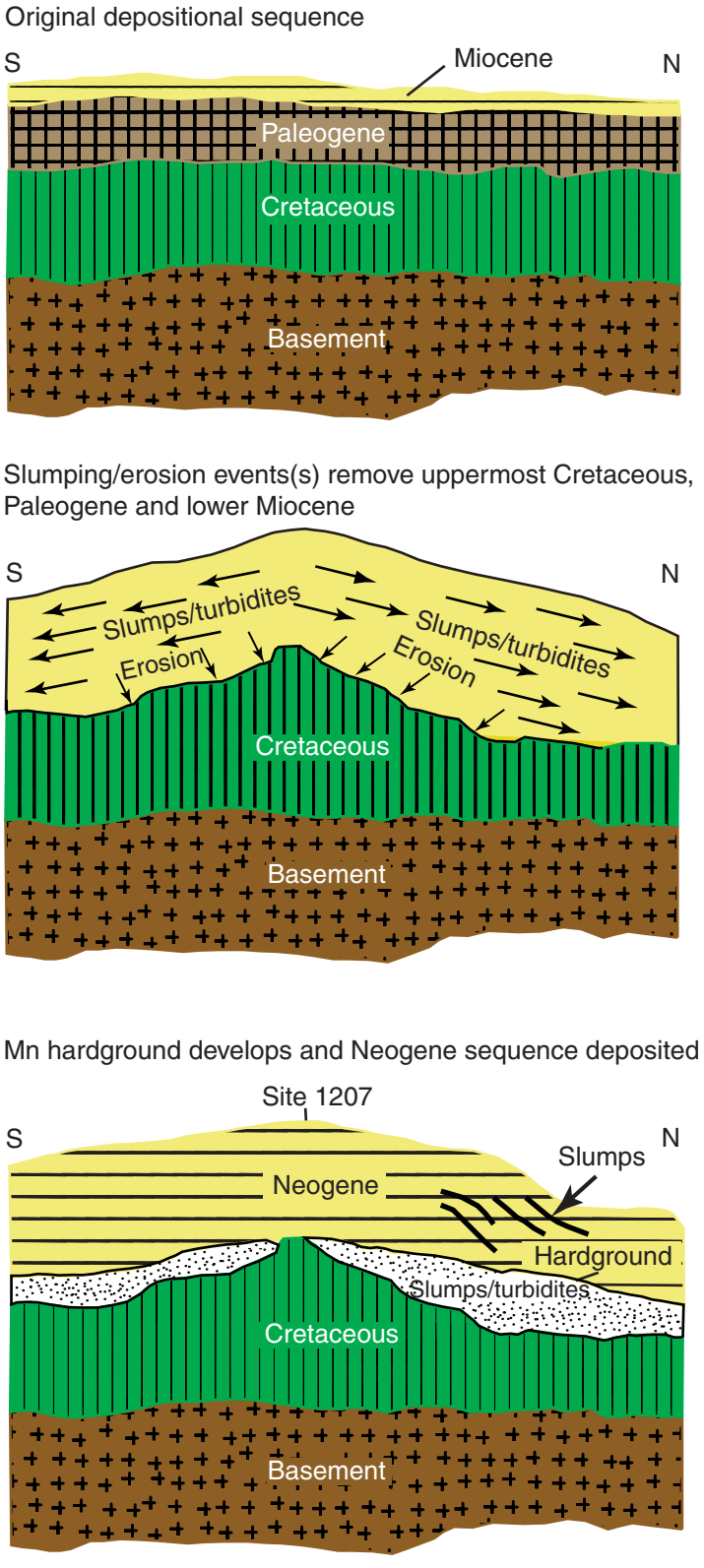

Figure F5. Core recovery, lithology, lithologic units, age with corresponding biostratigraphic zonations, color reflectance (at 550 nm), and percent carbonate for Hole 1207A. Depth is shown on the far left. Reflectance and percent carbonate data both illustrate the lithologic transition downcore from a greenish colored, less oxidized clayey nannofossil ooze to a lighter-colored, more oxidized nannofossil ooze. The prominent spike in the reflectance data coincides with a substantial hiatus or condensed interval between Campanian- and mid-Miocene–age sediment. Foram. zn. = foraminiferal zone, nanno. zn. = nannofossil zone.

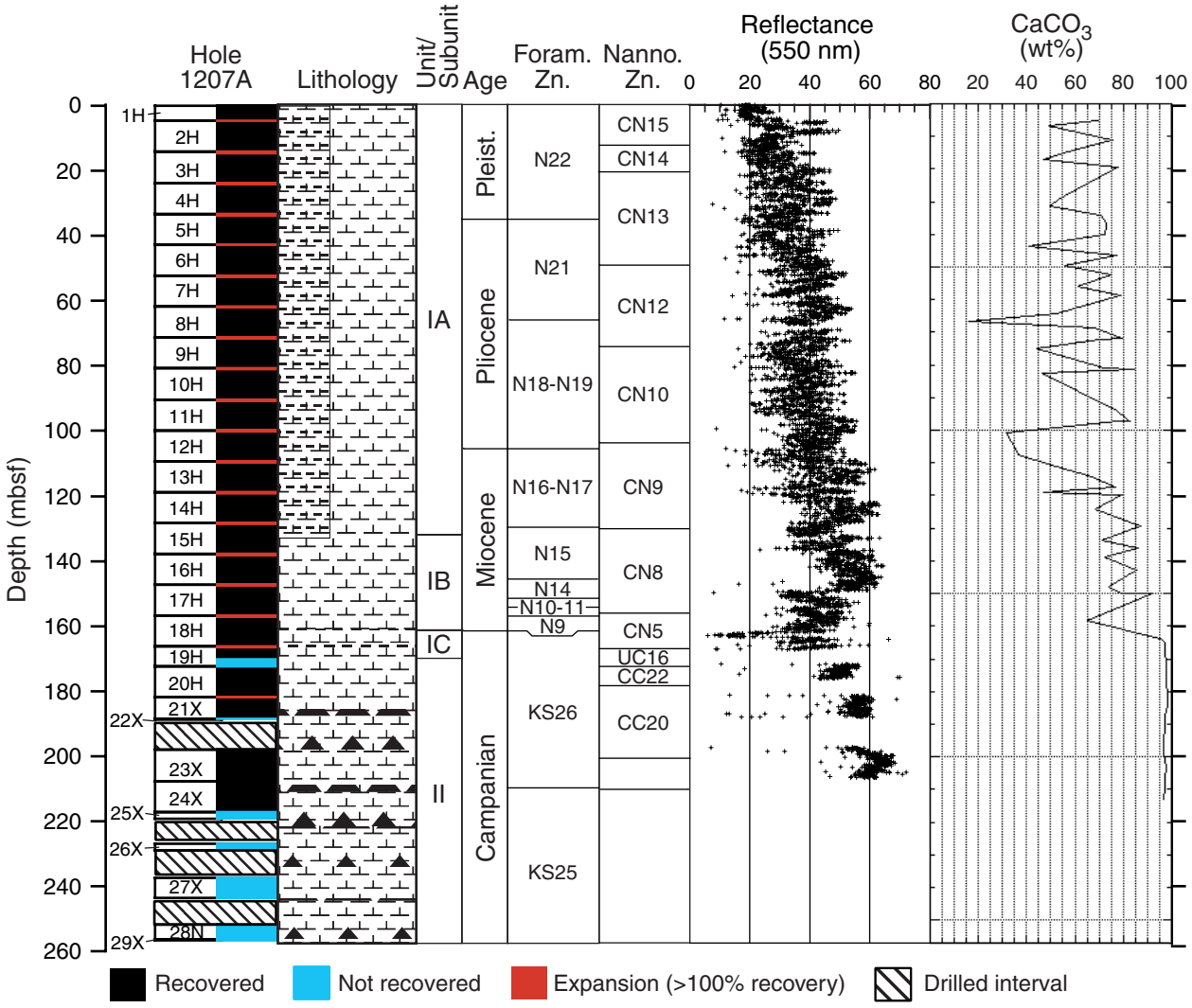

Figure F6. Core recovery, lithology, lithologic units, and age with corresponding biostratigraphic zonations for Site 1207. Foram. zn. = foraminiferal zone, nanno. zn. = nannofossil zone.

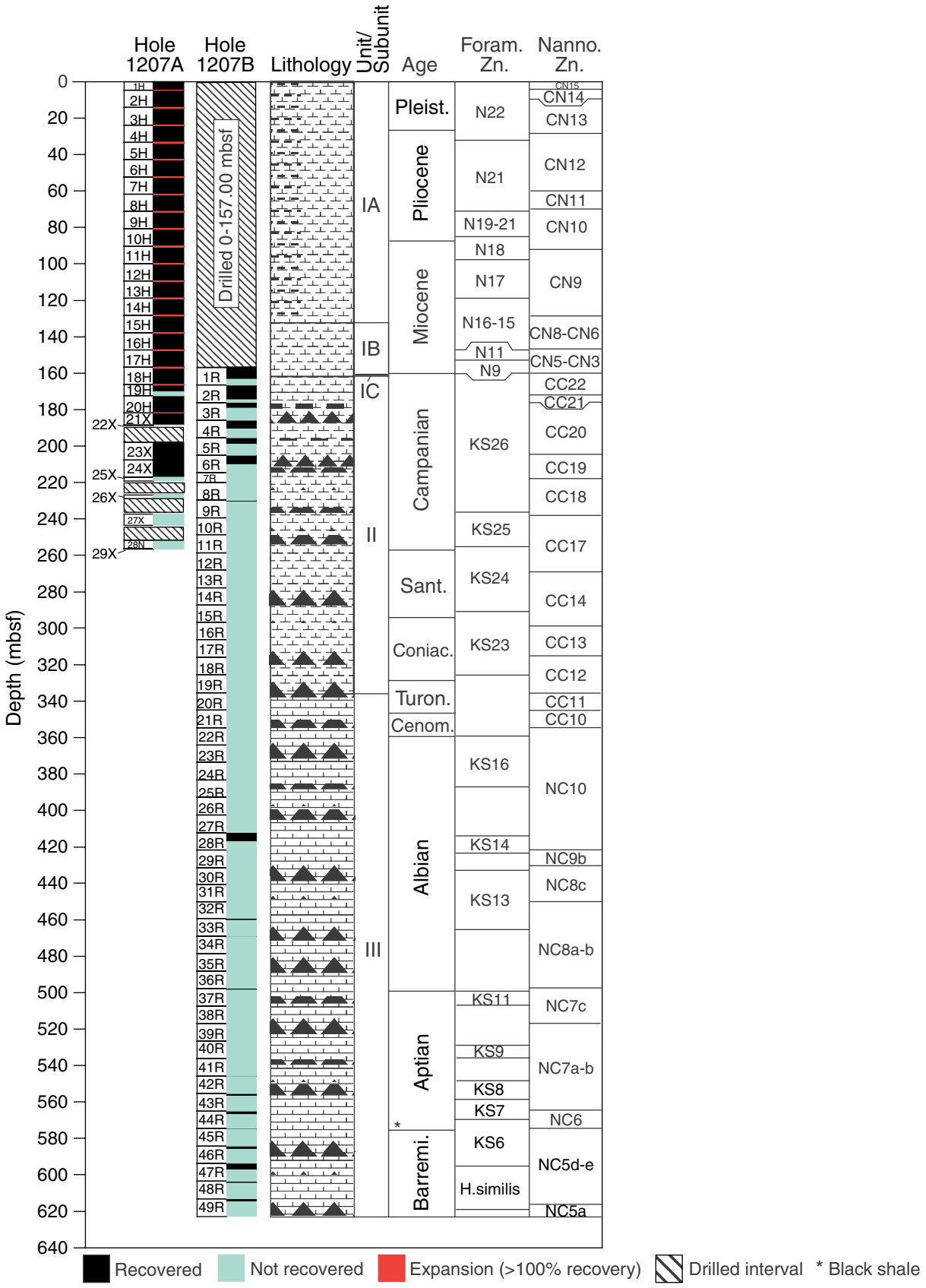

Figure F7. Estimates of biosiliceous material from Hole 1207A smear slides. Biogenic silica is generally greater in Subunit IA than in Subunit IB and is a rare component of the soft sediment in Unit II.

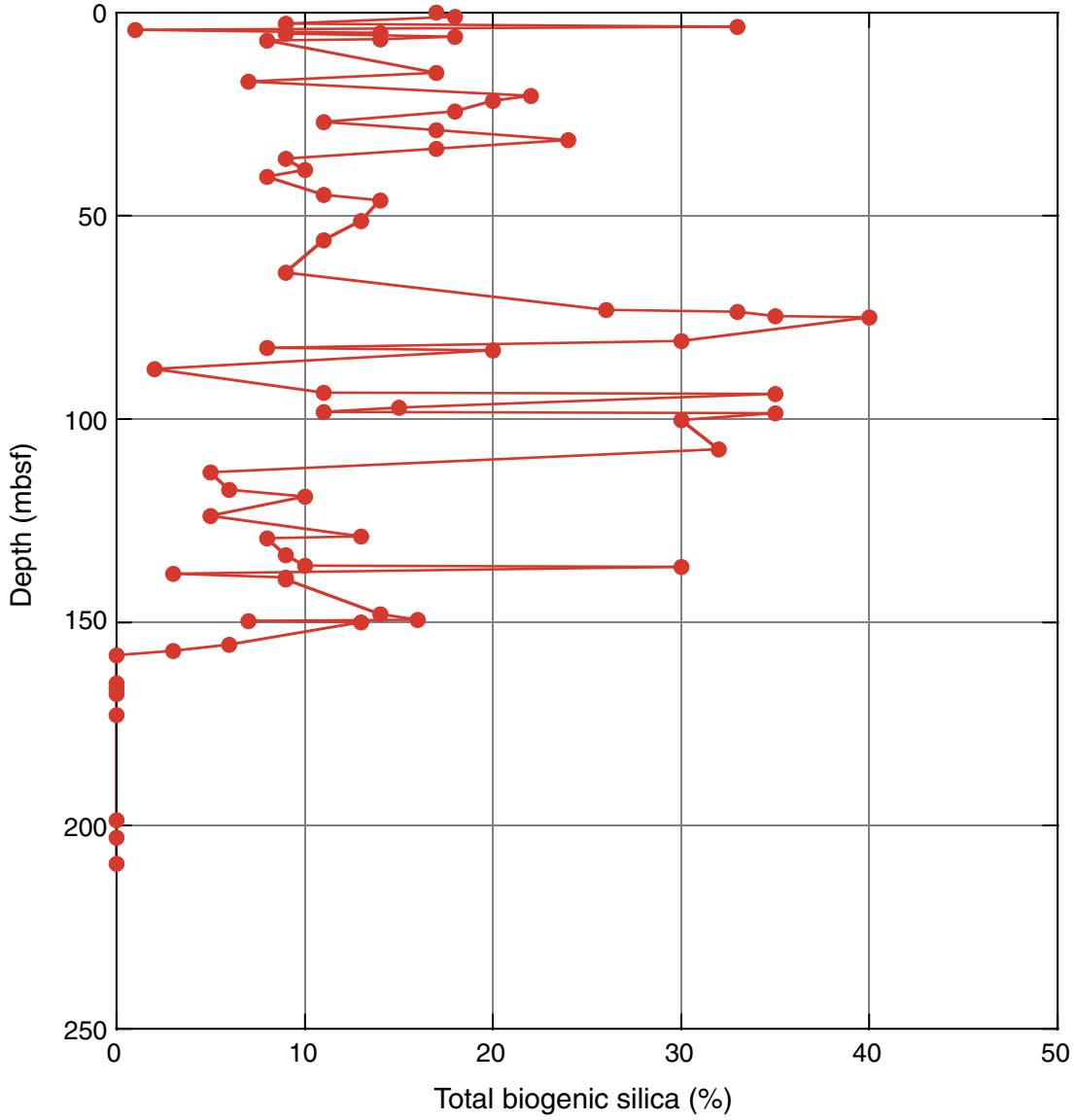

Figure F8. Percent total color reflectance and percent carbonate for Hole 1207A are superimposed to demonstrate a direct relationship between carbonate and reflectance.

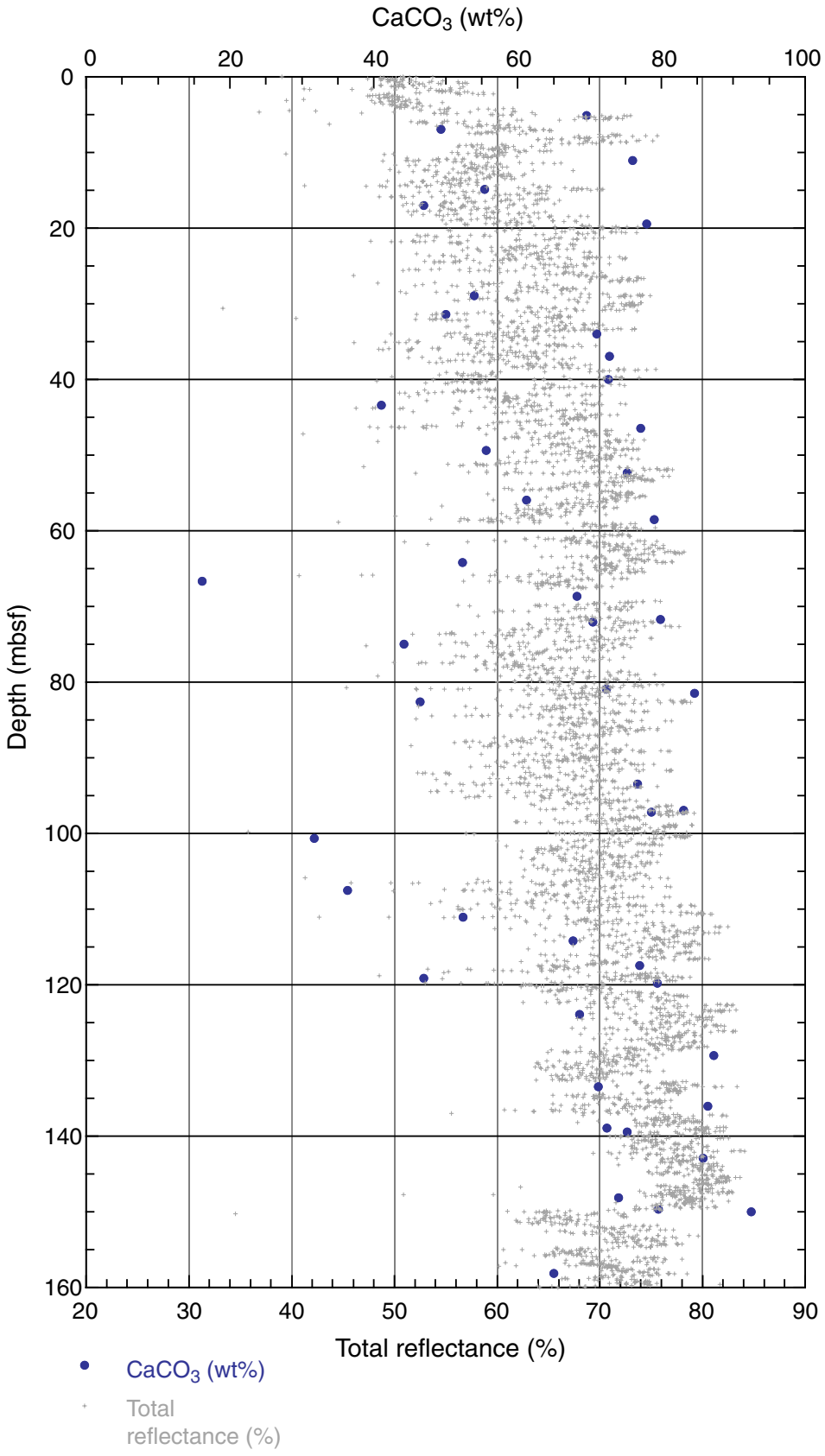

Figure F9. Composite digital photograph, color reflectance, and bulk density for Core 198-1207A-2H. This core is late Pleistocene in age.

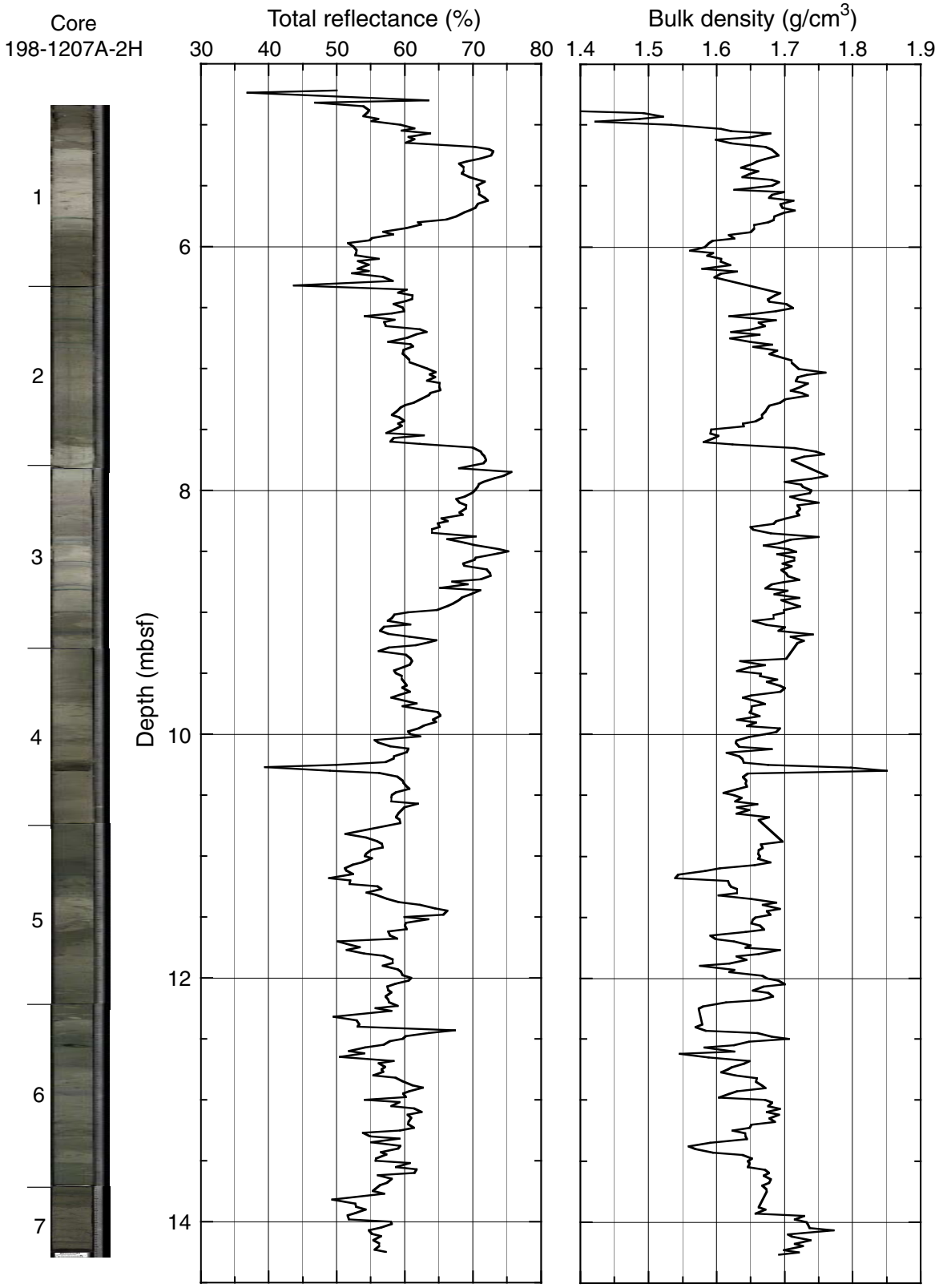

Figure F10. Composite digital photograph, color reflectance, and bulk density for Core 198-1207A-5H. This core is late Pliocene in age.

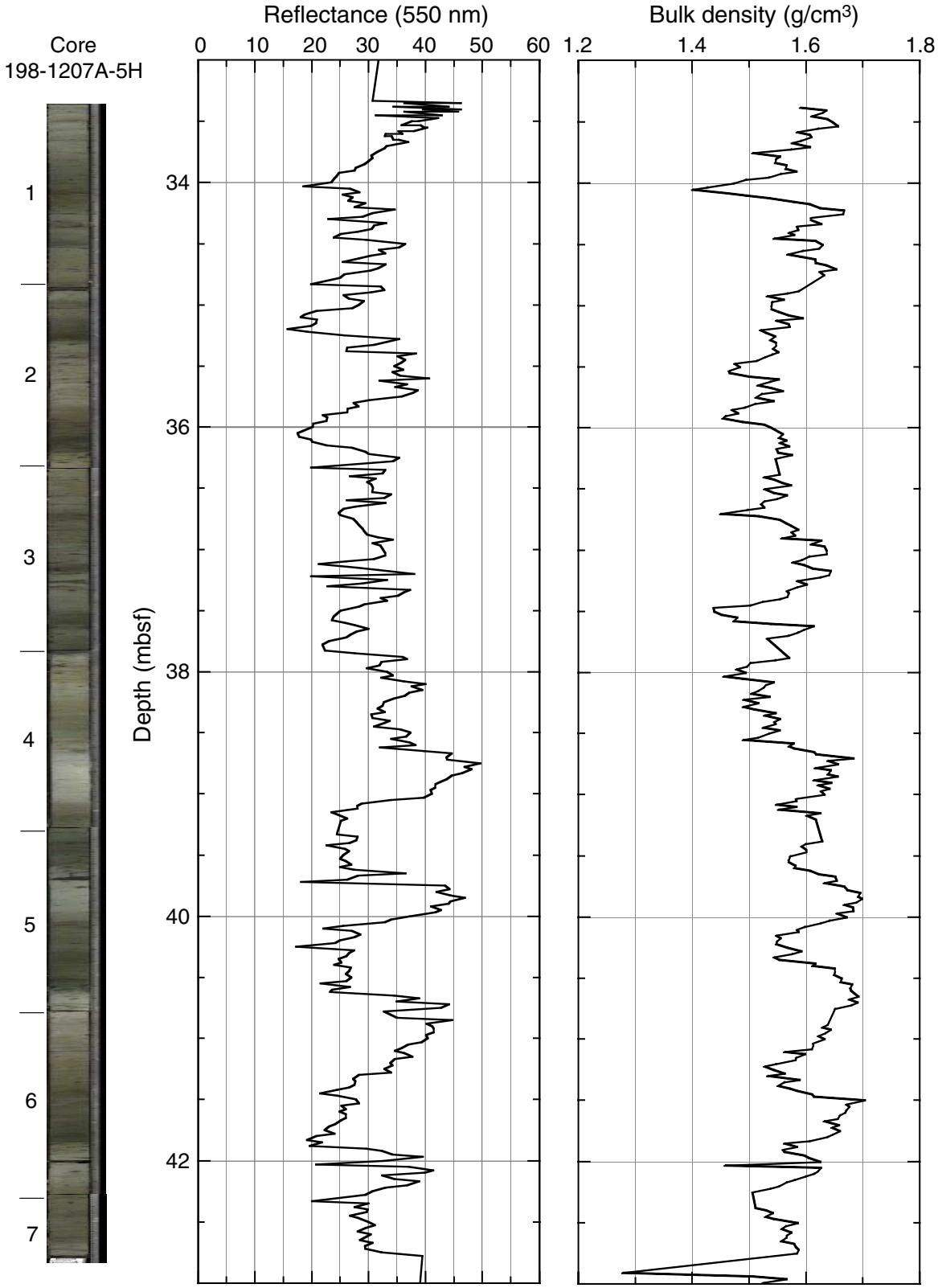

Figure F11. Close-up photograph of pyrite blebs visible between 131 and 135 cm (interval 198-1207A-8H-5, 113–137 cm).

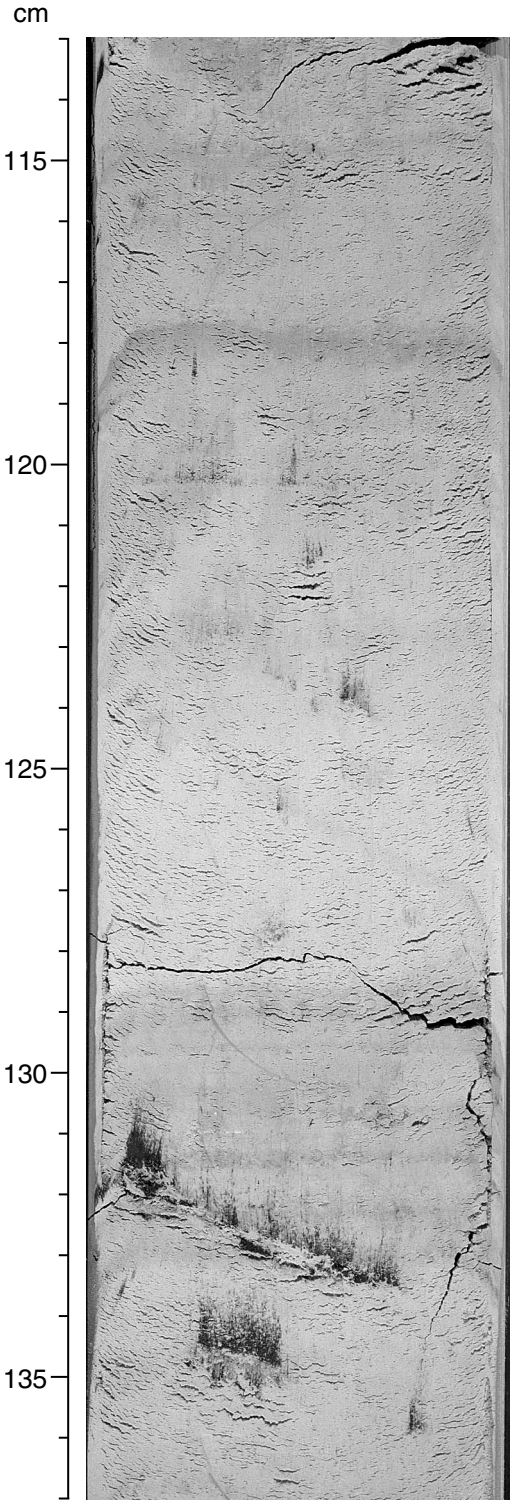

Figure F12. Close-up photograph of diagenetic laminae, which can be observed between 111.5 and 113 cm (interval 198-1207A-5H-2. 109–145 cm). Light to dark cyclicity of the sediment, mottled fabric, and blebs of pyrite are also visible in this photograph.

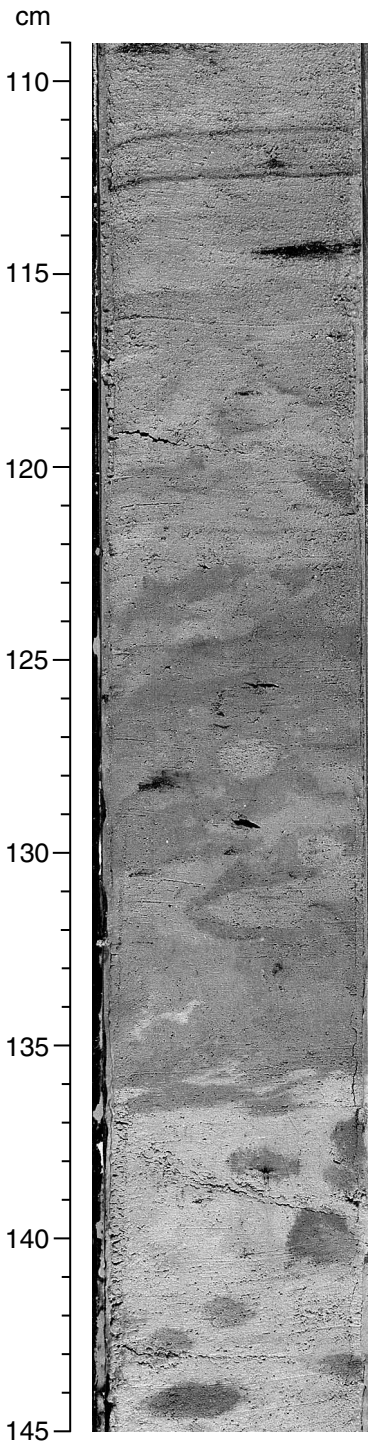

Figure F13. Close-up digital photograph showing a scour surface overlain by a dark greenish gray volcanic ash (interval 198-1207A-12H-5, 72–84 cm).

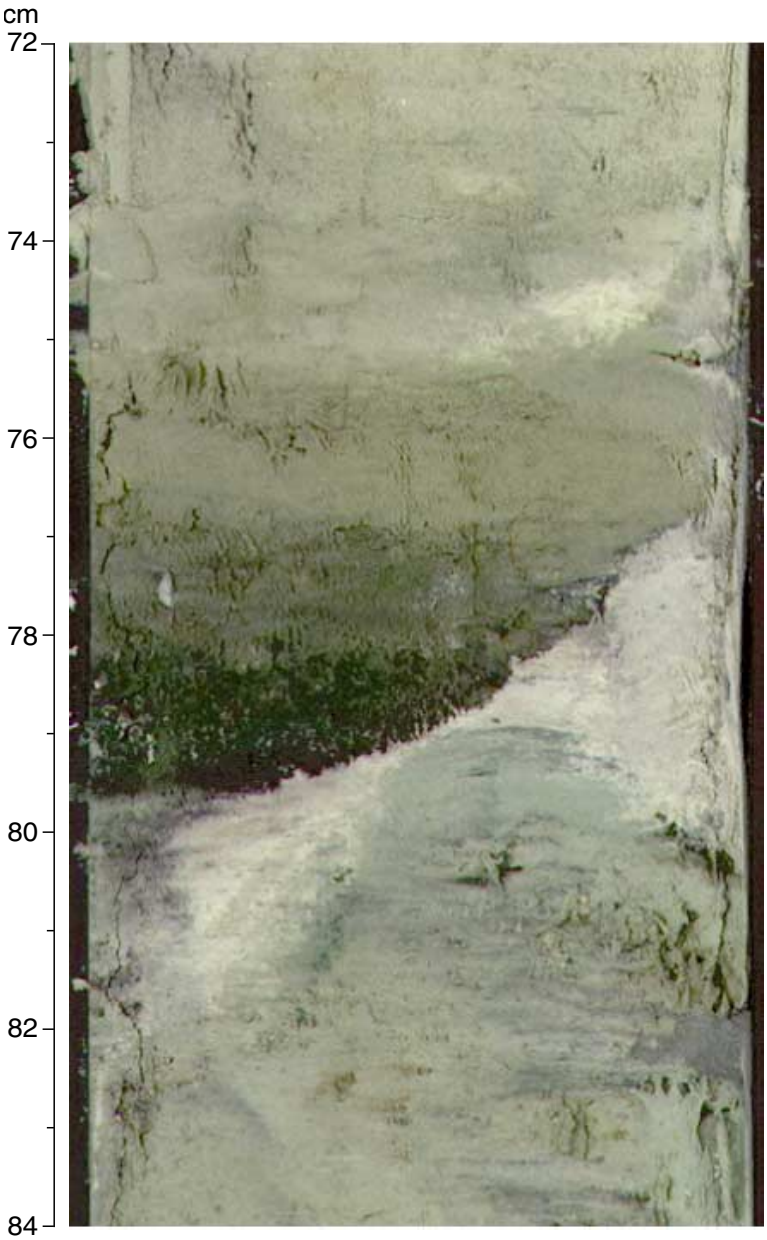

Figure F14. Composite digital photograph, color reflectance, and bulk density for Core 198-1207A-17H. This core is middle Miocene in age.

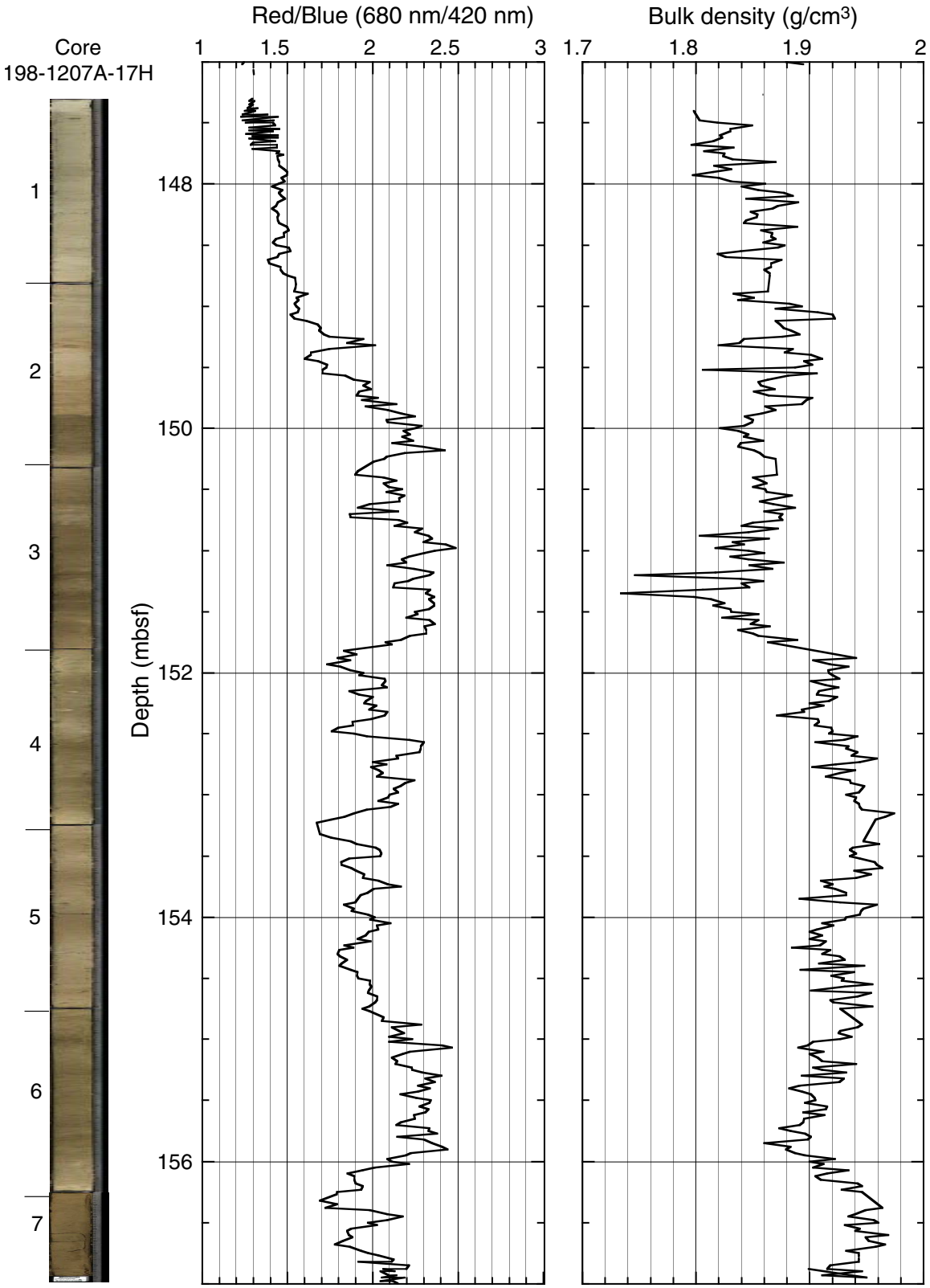

Figure F15. Close-up photograph of faint *Zoophycos* burrows (interval 198-1207A-10H-6, 130–152 cm).

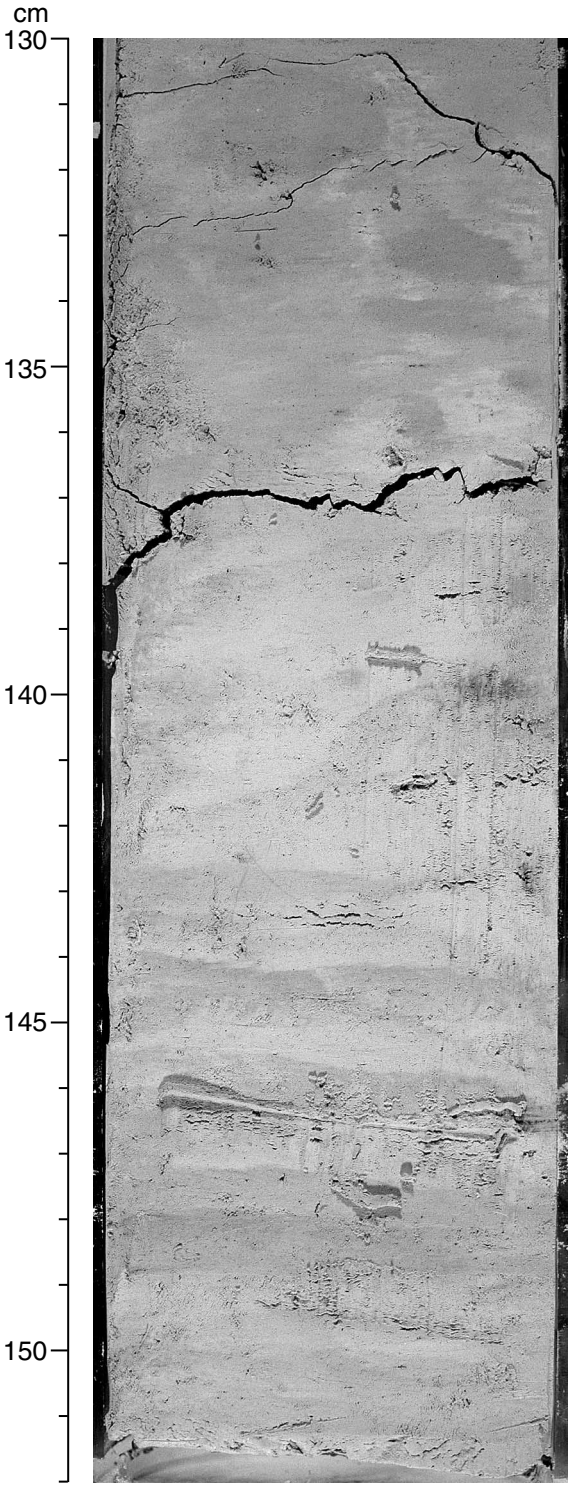

Figure F16. Composite digital photograph, color reflectance, and bulk density for Core 198-1207A-18H. This core is Campanian to middle Miocene in age.

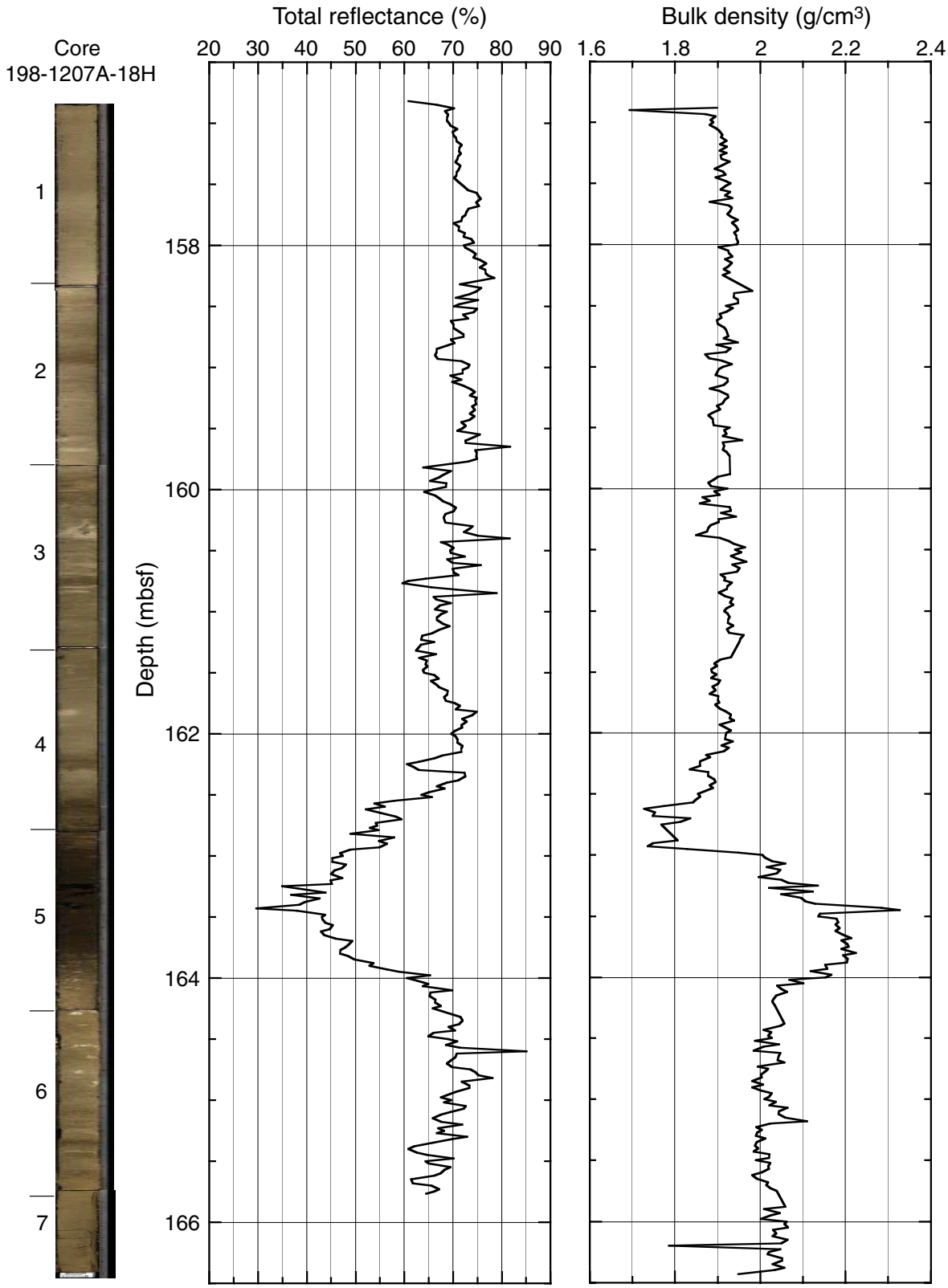

Figure F17. Smear slide photomicrographs of Samples 198-1207B-18H-5, 90–91 cm (top), and 18H-5, 50–51 cm (bottom), from the Miocene condensed zone showing concentrations of tan/brown phillipsite crystals. These exhibit zoning and twinning (x-shaped crystal cluster in lower view). Note the fish tooth in the upper center of the top view. Both views are under plane-polarized light.

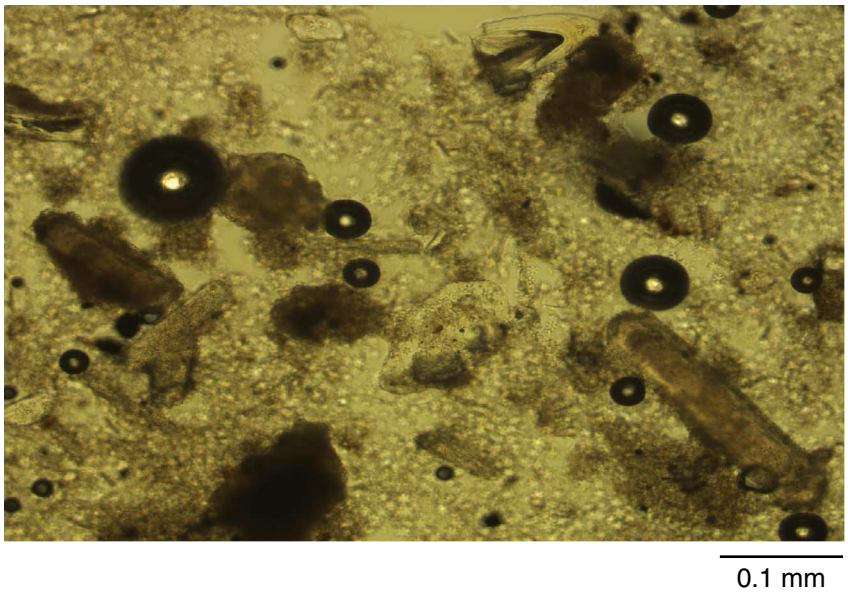

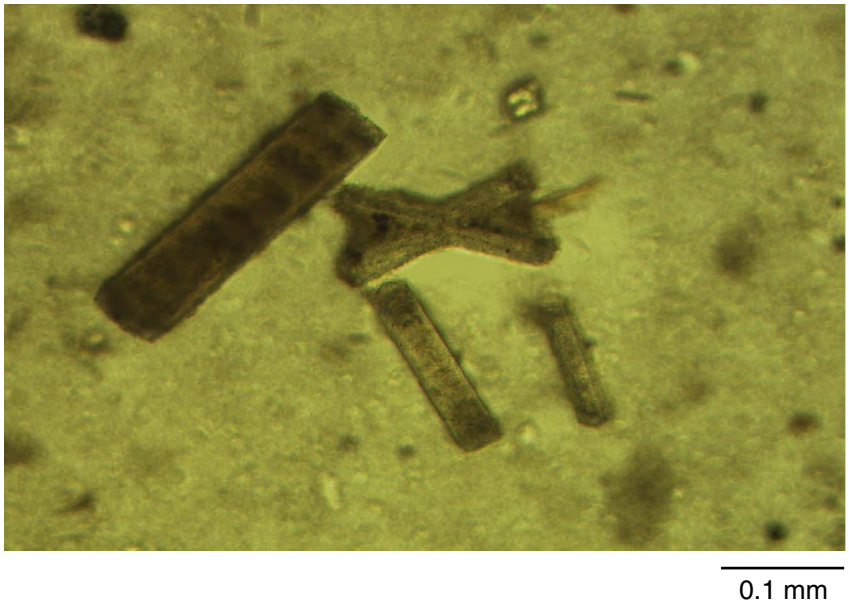

Figure F18. Composite digital photograph of Core 198-1207B-44R-1 showing the lower Aptian OAE1a level, a C_{org}-rich claystone. Total reflectance is illustrated, along with values of three shipboard organic carbon determinations. TOC = total organic carbon.

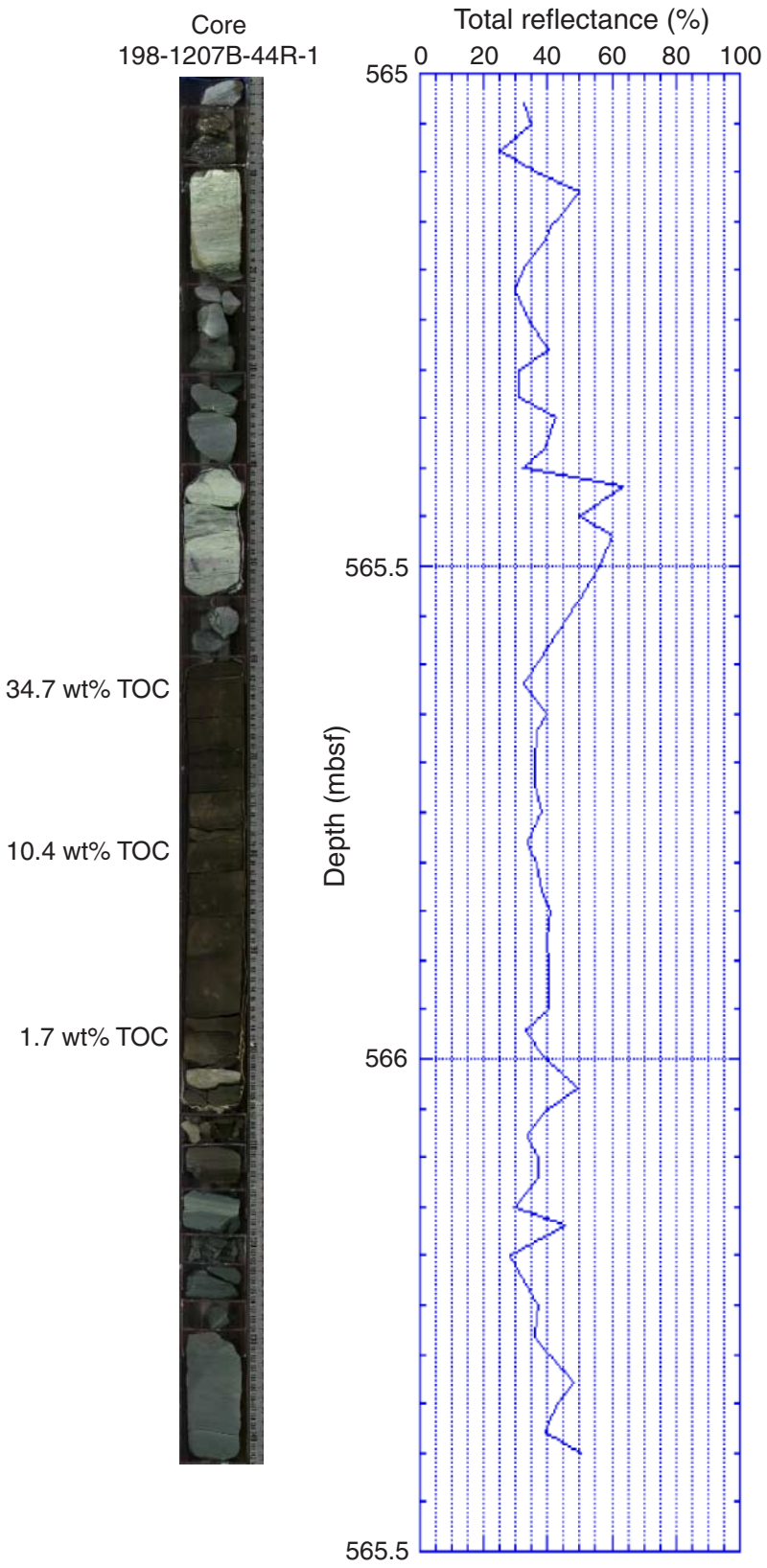

Figure F19. Thin section photomicrographs of a manganese crust from the Miocene condensed section (Sample 198-1207A-18H-5, 44–47 cm). The upper view is of microstromatolitic lamination and columnal structures that were likely products of microbial growth on the seafloor. Light patches are microfossils, now largely replaced by Fe-Mn oxide minerals, which were concentrated in the topographic lows between Fe-Mn oxide columns as the crust developed. The lower view is more representative of the thin section, which is mostly composed of opaque Fe-Mn oxides, but here is shown with a spherulitic cluster of zoned phillipsite crystals. Both views are under plane-polarized light.

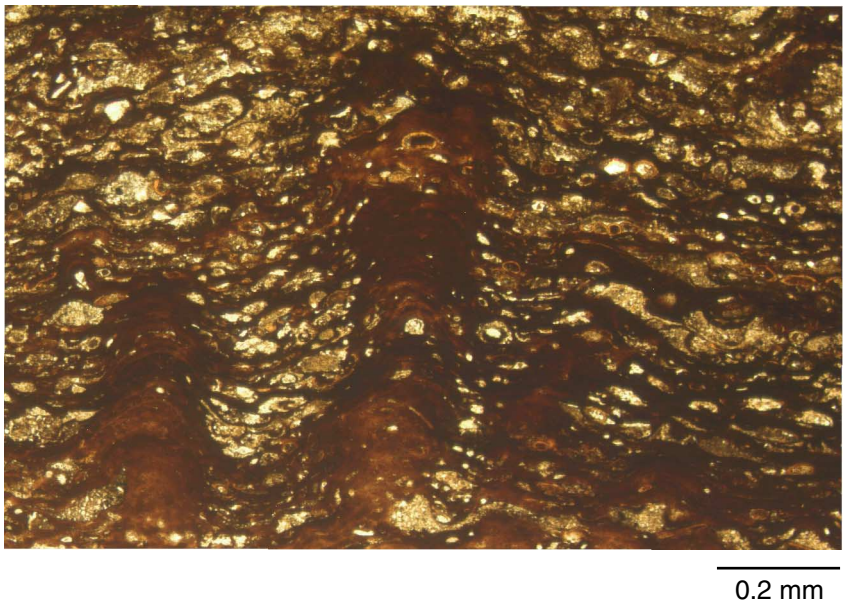

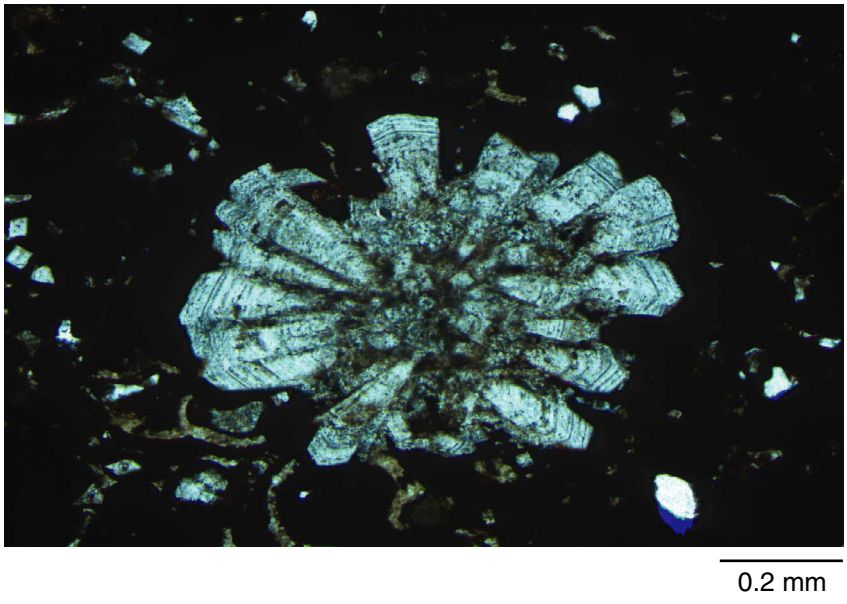

Figure F20. Thin section photomicrographs of the rim of a chert fragment recovered within soupy white Campanian ooze (Sample 198-1207A-24X-5, 4–5 cm). The speckled appearance is due to circular white blebs of microquartz embedded within a tan opal matrix/cement. Under crossed nicols (not shown here) the white circular features exhibit some birefringence, whereas the surrounding tan "cement" is isotropic. At higher magnification (lower view), some of the blebs exhibit "doughnut" shapes, suggesting that they may be silicified coccoliths. The percent of opaline groundmass is high (~50%), similar to the porosity estimates for surrounding unconsolidated nannofossil ooze. Note the presence of a silicified foraminifer (chambers in center) and thin quartz lenses of uncertain origin. Both views are under plane-polarized light.

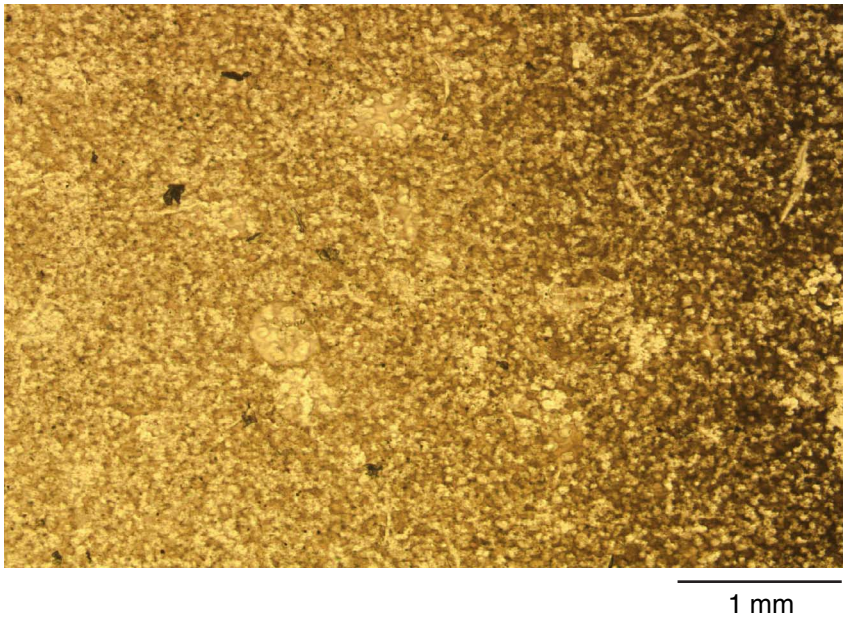

Figure F21. Thin section photomicrographs of a Turonian nannofossil limestone/chalk with radiolarians (Sample 198-1207B-18R-CC, 10–11 cm). Opaline tests of radiolarians have been recrystallized and filled with chalcedony and microquartz. Small tripartite and thin white rods are radiolarian spicules/spines. The chalk/limestone matrix looks relatively pristine with no authigenic quartz. The upper view is under plane-polarized light, whereas the lower view is with nicols crossed.

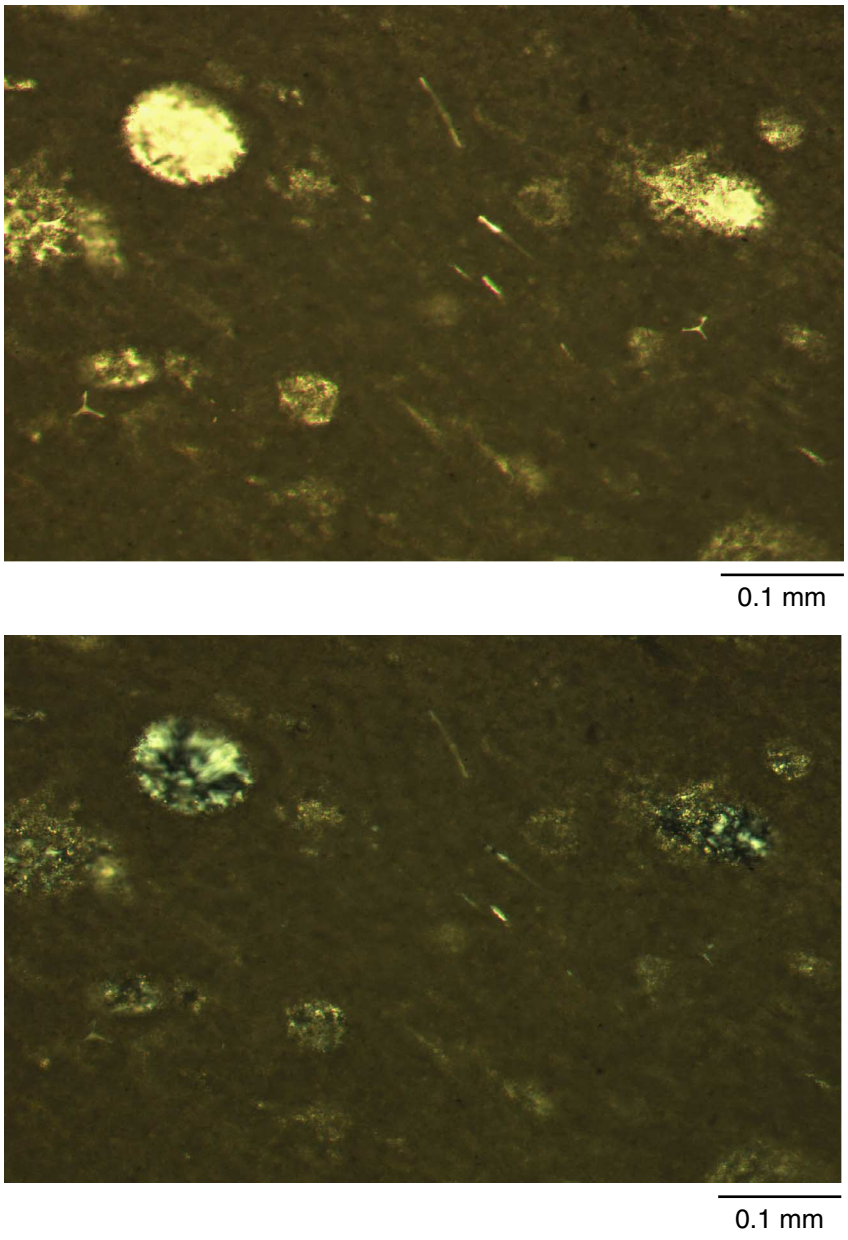

Figure F22. Thin section photomicrographs of the Coniacian section (Sample 198-1207B-14R-CC, 15–21 cm). The transition from nannofossil chalk on the right to porcellanite to calcareous chert on the left is pictured here. Some isotropic, tan opal was noted in the matrix of the porcellanite. The upper view is under plane-polarized light, whereas the lower view is with nicols crossed.

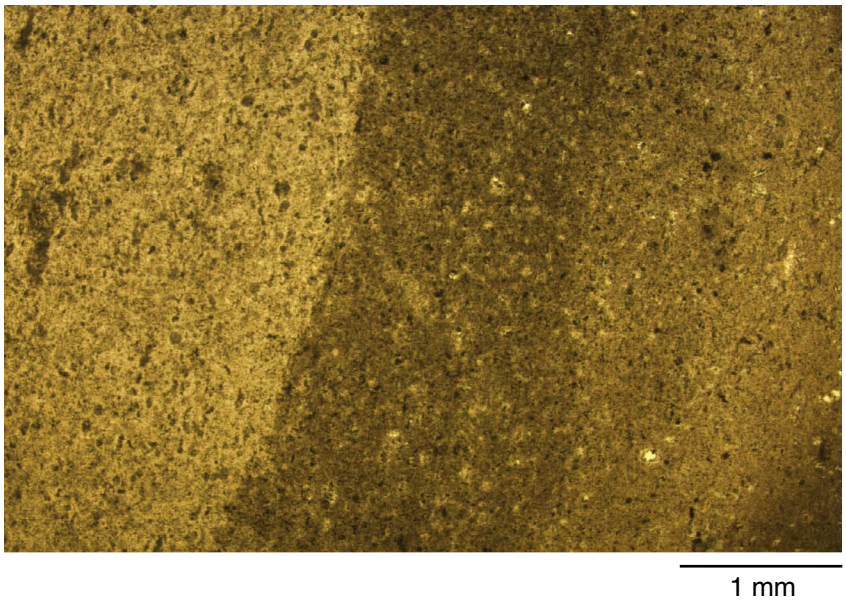

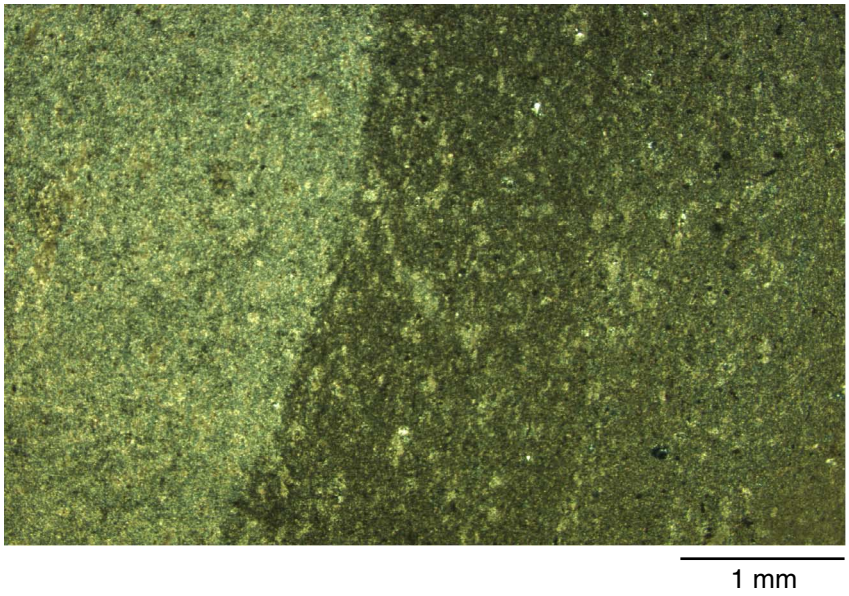

Figure F23. Thin section photomicrographs of a fragment of dark reddish foraminifer-radiolarian chert/porcellanite taken from the Albian section (Sample 198-1207B-33R-CC, 80–82 cm). There is an abrupt, but irregular, front between silicified (lower) and unsilicified (upper) parts of the sample. Note the many foraminifers filled by tan and colorless (chalcedony/microquartz) cements. The tan cement is interpreted as once having been opal, but it is now birefringent (lower view) recrystallized quartz. Foraminifers are locally partly to wholly replaced by silica. The upper view is under plane-polarized light, whereas the lower view is with nicols crossed.

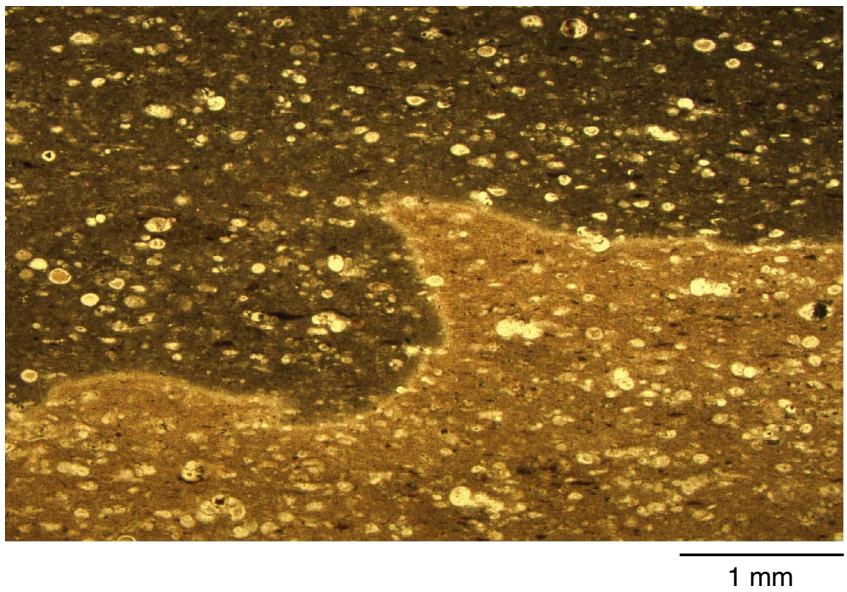

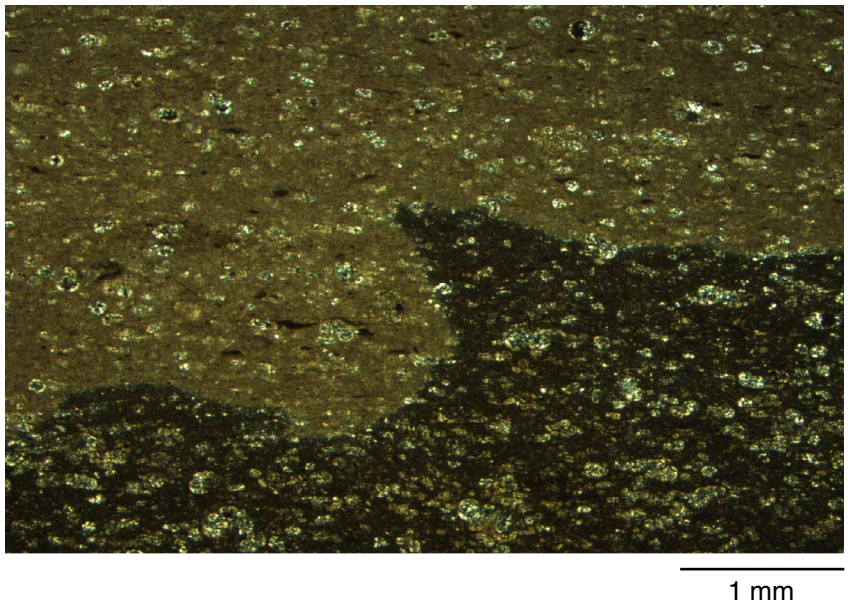

Figure F24. Thin section photomicrographs of a zoned chert nodule from the Aptian section (Sample 198-1207B-37R-CC, 25–27 cm). This cross-sectional view shows that silicification was localized in a burrow filling where radiolarians (and porosity) were concentrated prior to alteration. The dark zone intervening between chert on the left and chalk on the far right consists of porcellanite with higher concentrations of opaque minerals, essentially a reaction front. The upper view is under plane-polarized light, whereas the lower view is with nicols crossed.

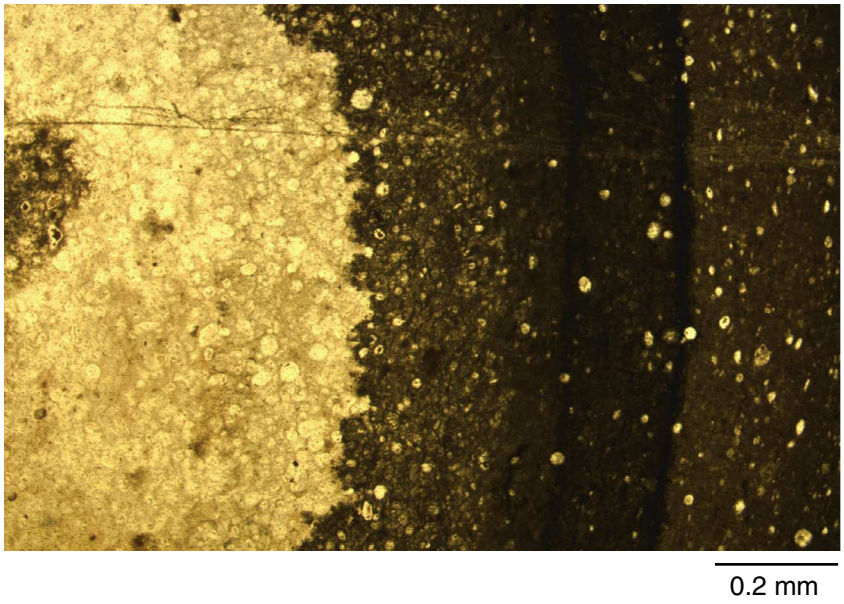

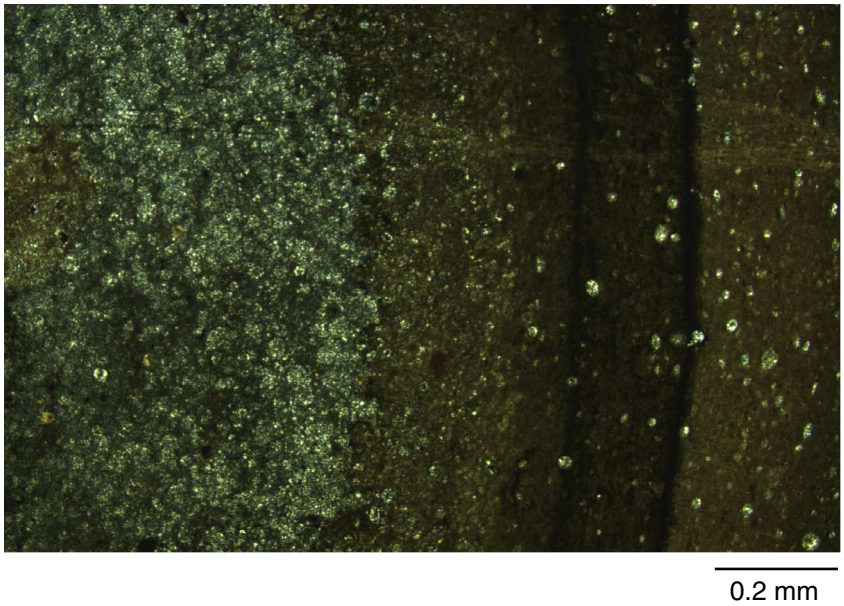

Figure F25. Thin section photomicrographs of a zoned chert nodule from the Aptian section (Sample 198-1207B-37R-CC, 25–27 cm). This is a higher magnification view of the contact between chert (left) and porcellanite (right). Radiolarians are filled with tan, isotropic opal. Note how carbonate and other impurities in the porcellanite groundmass help define tests of radiolarians and how these tests become "ghosts" in the chertified portion of the sample. The upper view is under plane-polarized light, whereas the lower view is with nicols crossed.

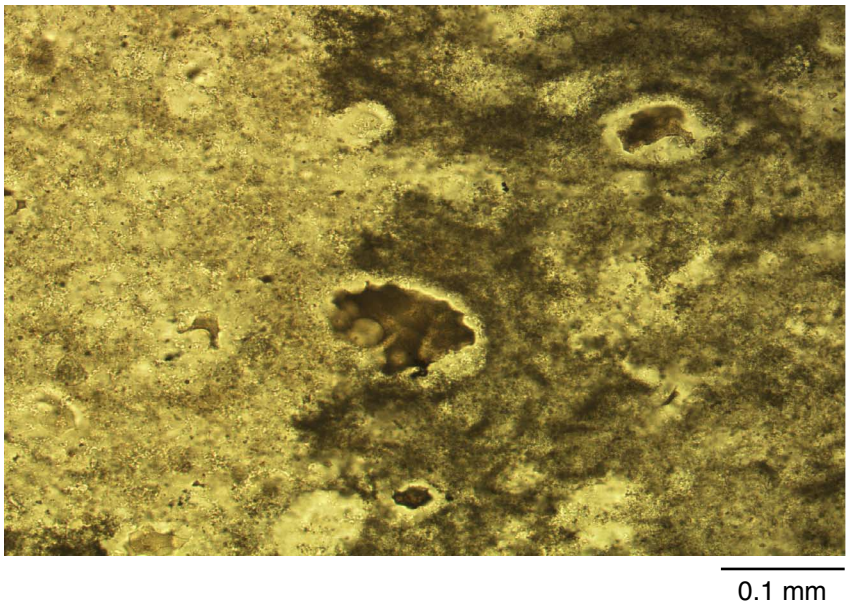

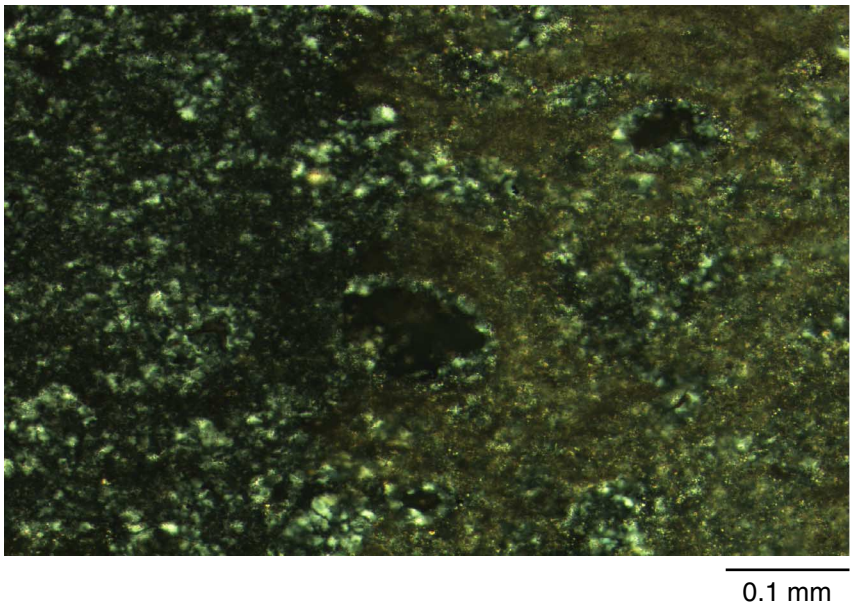

Figure F26. Plots of detrended color reflectance vs. age for the Pliocene–Pleistocene (0.6–2.5 Ma) with superimposed predicted angle of obliquity (data from Laskar, 1990) for the same interval. Color reflectance was detrended by taking a curve of mean reflectance and subtracting the point-to-point deviation of reflectance from it. Reflectance values were collected at 2.5-cm intervals, which is ~1 sample/1.5 k.y. on average for the interval selected. Note the approximate correspondence between the two curves, suggesting that obliquity drove the observed cyclicity.

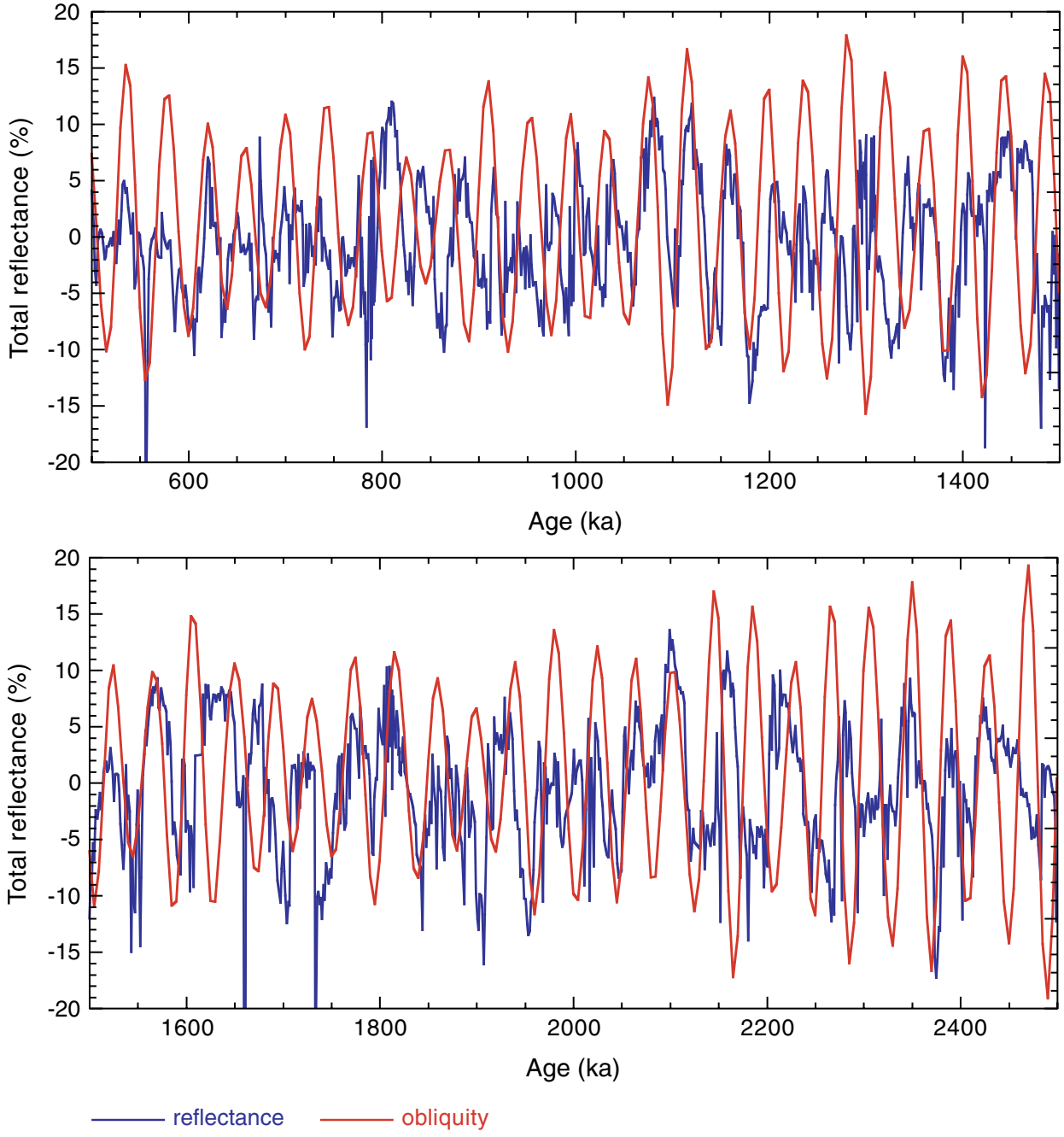

Figure F27. Composite digital photograph, color reflectance, and bulk density, Core 198-1207A-15H. This core is late Miocene in age.

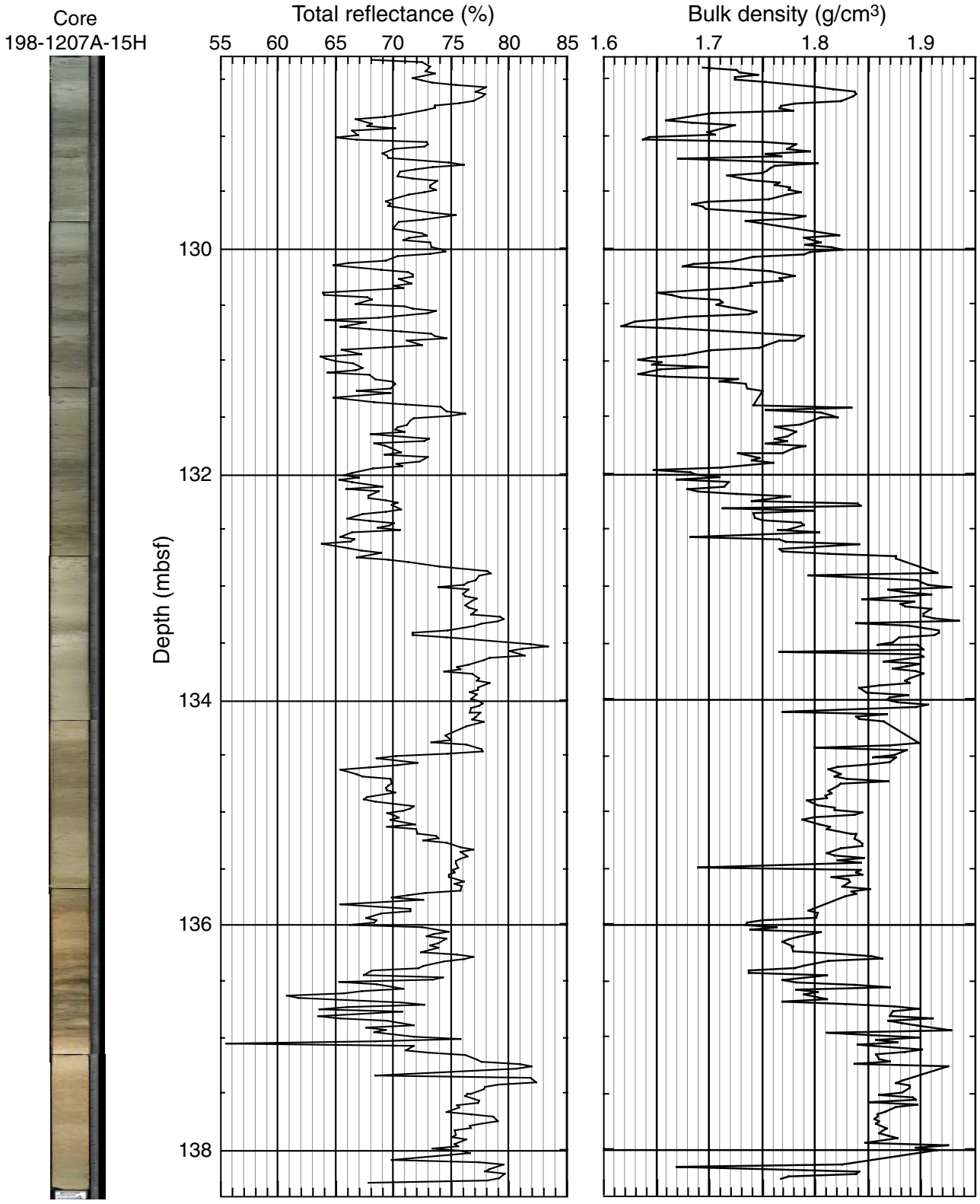

Figure F28. Hole 1207A archive-half magnetization intensities after AF demagnetization at peak fields of 20 mT as measured with the shipboard pass-through magnetometer.

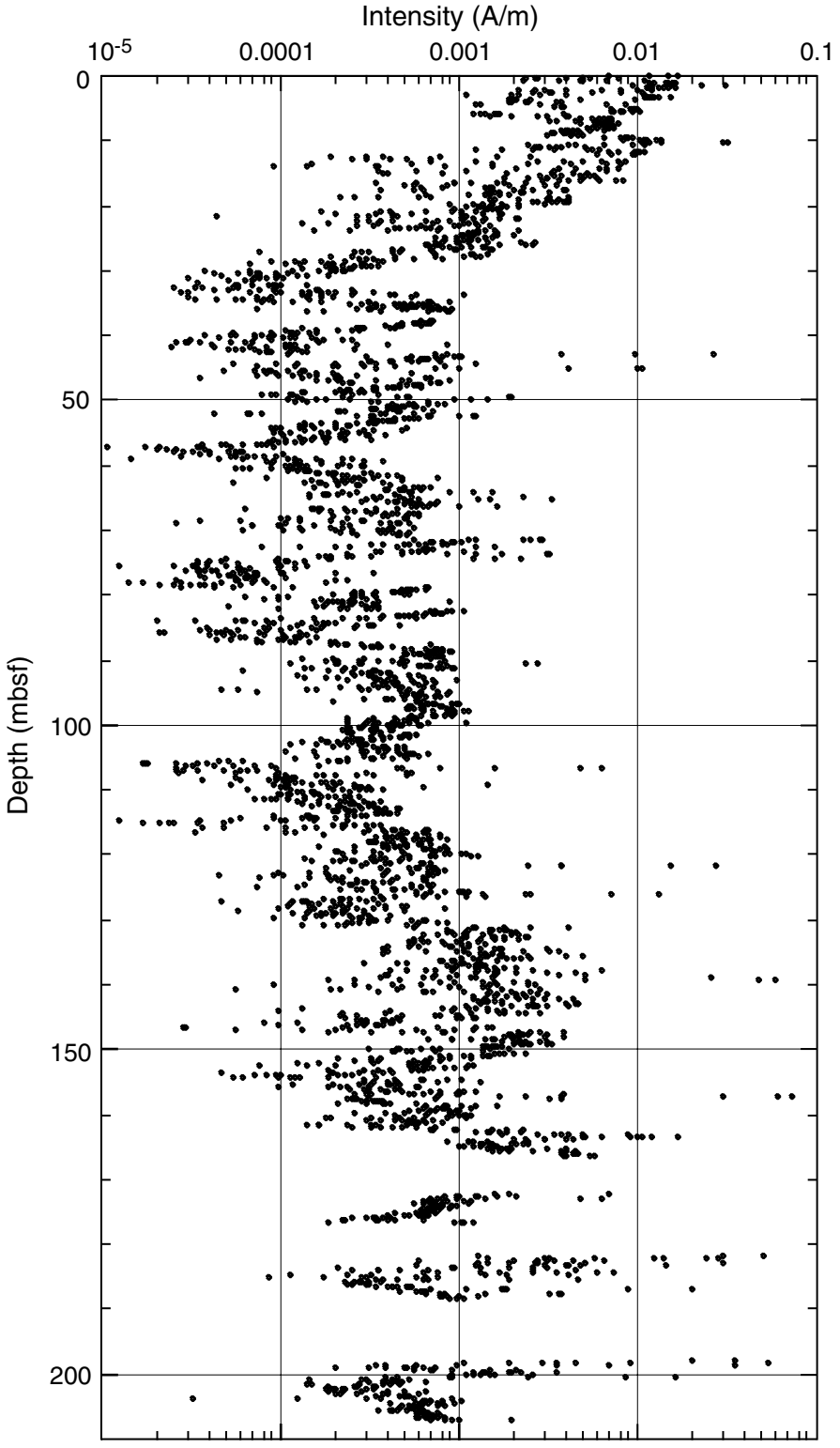

Figure F29. Inclination after AF demagnetization at peak fields of 20 mT as measured with the shipboard pass-through magnetometer at Hole 1207A. The column at the right of each plot shows interpreted zones of normal (black) and reversed (white) polarity. Gray intervals indicate zones in which no polarity interpretation is possible. Polarity zones at the top of the section and certain polarity zones farther downsection are tentatively correlated to polarity chrons.

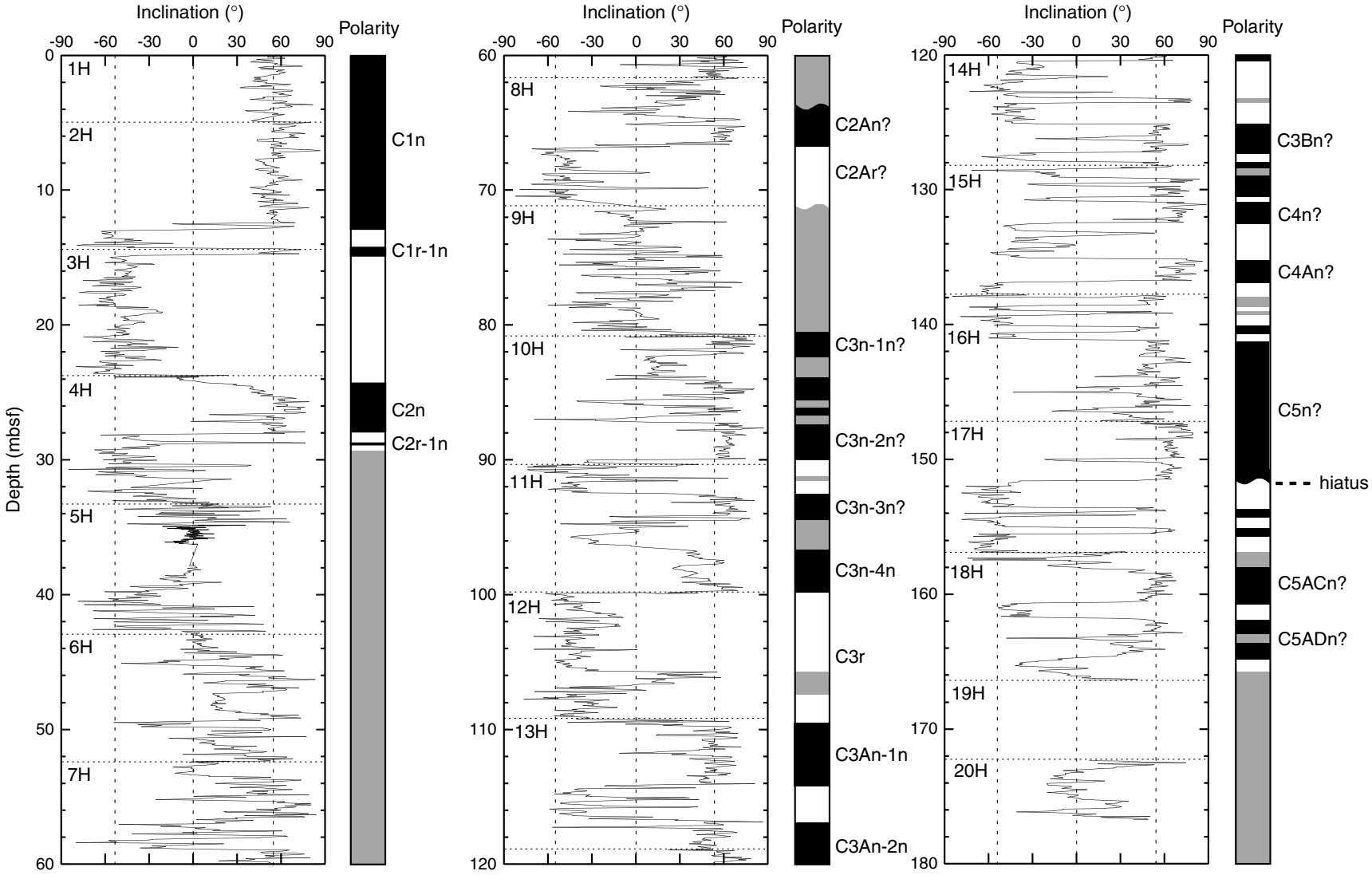

Figure F30. Age-depth curve for Site 1207 derived from magnetic stratigraphy, using the geomagnetic polarity time scale of Cande and Kent (1995) and showing the average sedimentation rates in meters per million years. Solid circles = more robust polarity chron interpretations, open circles = more tentative interpretations. Average sedimentation rates in meters per million years (m/m.y.) are also plotted. See Figure F20, p. 54 , in the "Site 1208" chapter for comparison.

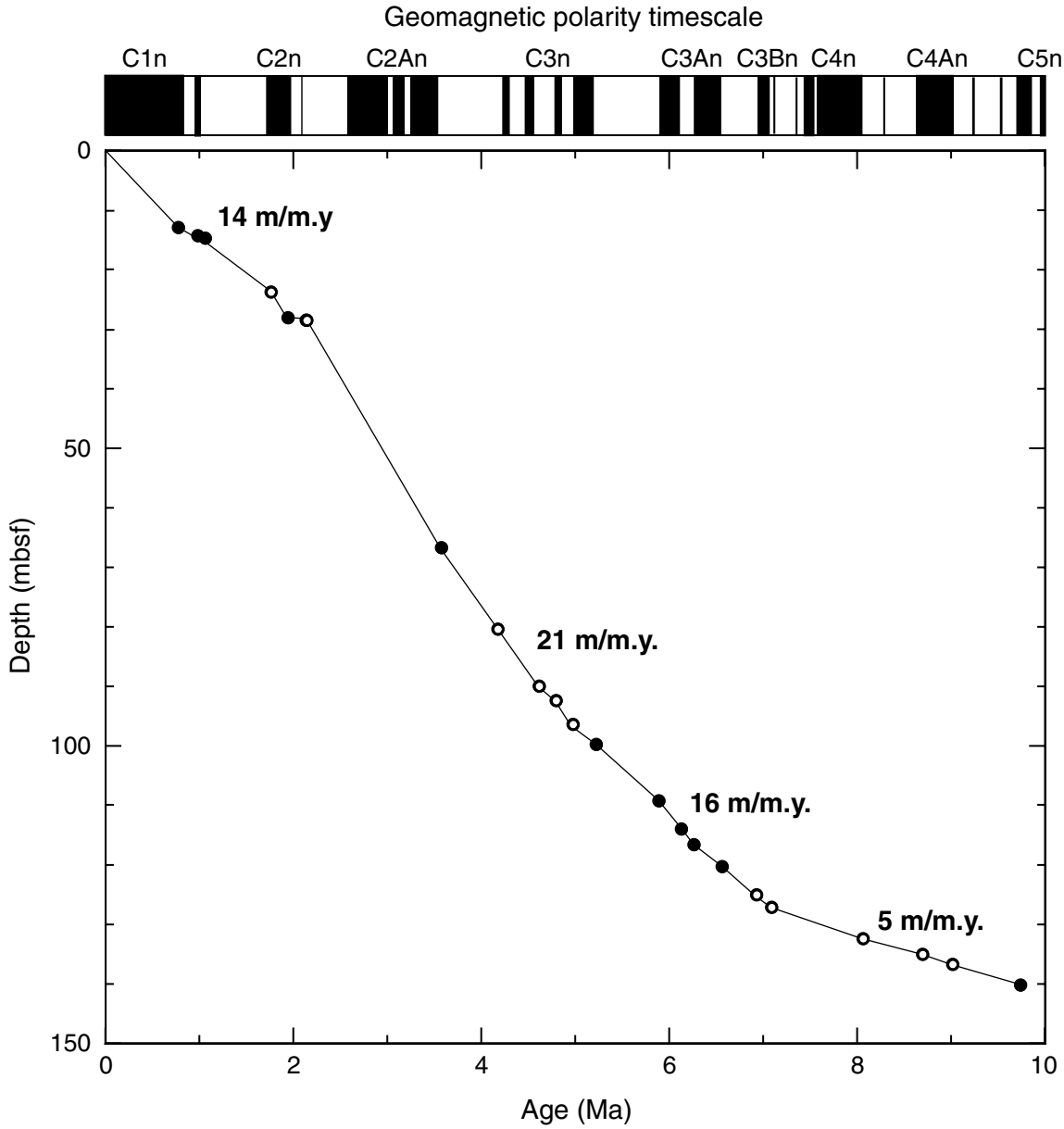

Figure F31. Age-depth plot of calcareous nannofossil (diamonds) and planktonic foraminiferal (crosses) datums at Site 1207. Datum ages and depths are presented in Tables T5, p. 121, and T6, p. 122.

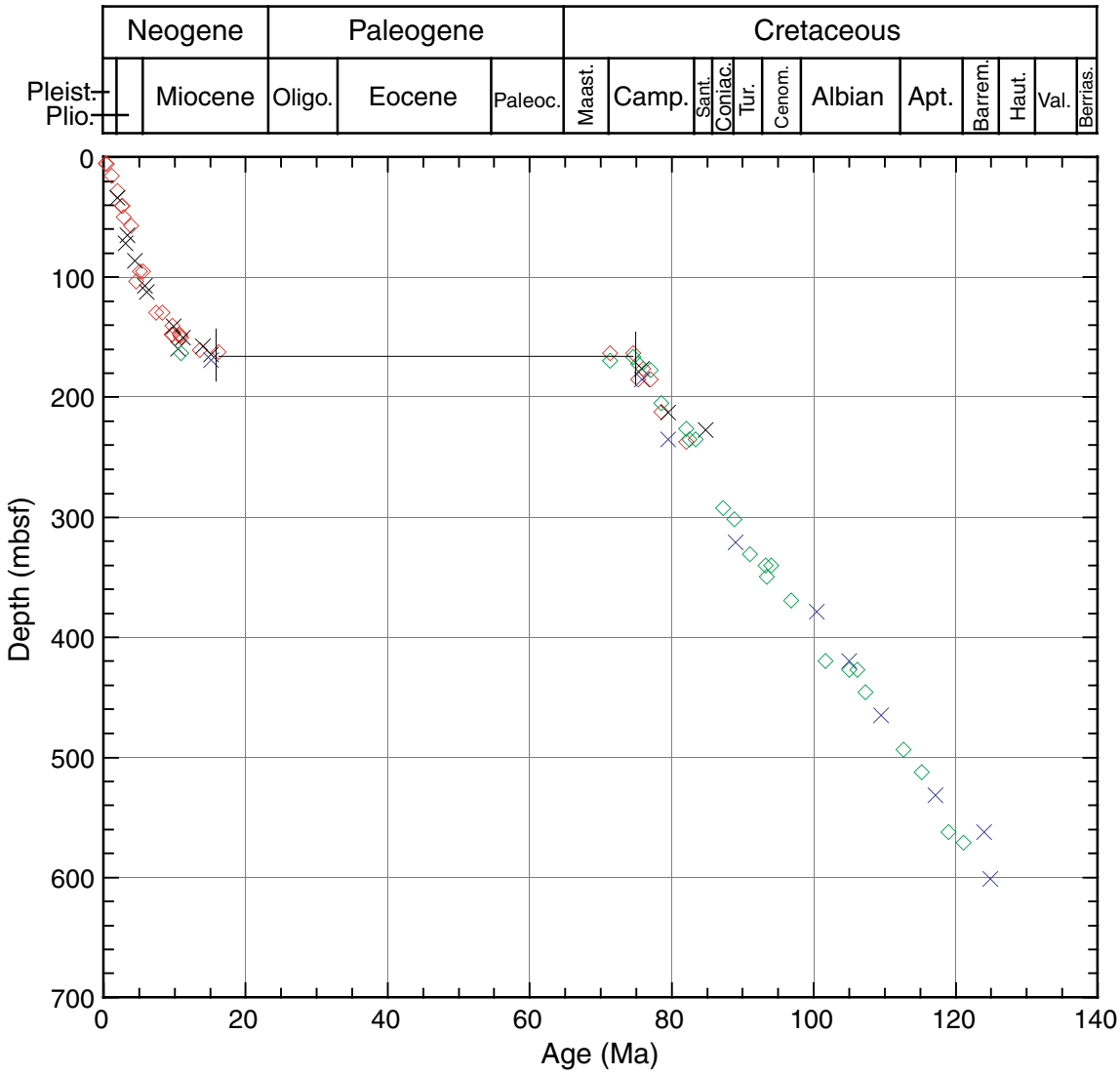

Figure F32. Age-depth plot of Neogene calcareous nannofossil (diamonds) and planktonic foraminiferal (crosses) datums in Hole 1207A. Datum ages and depths are presented in Tables T5, p. 121, and T6, p. 122. FO = first occurrence, LO = last occurrence.

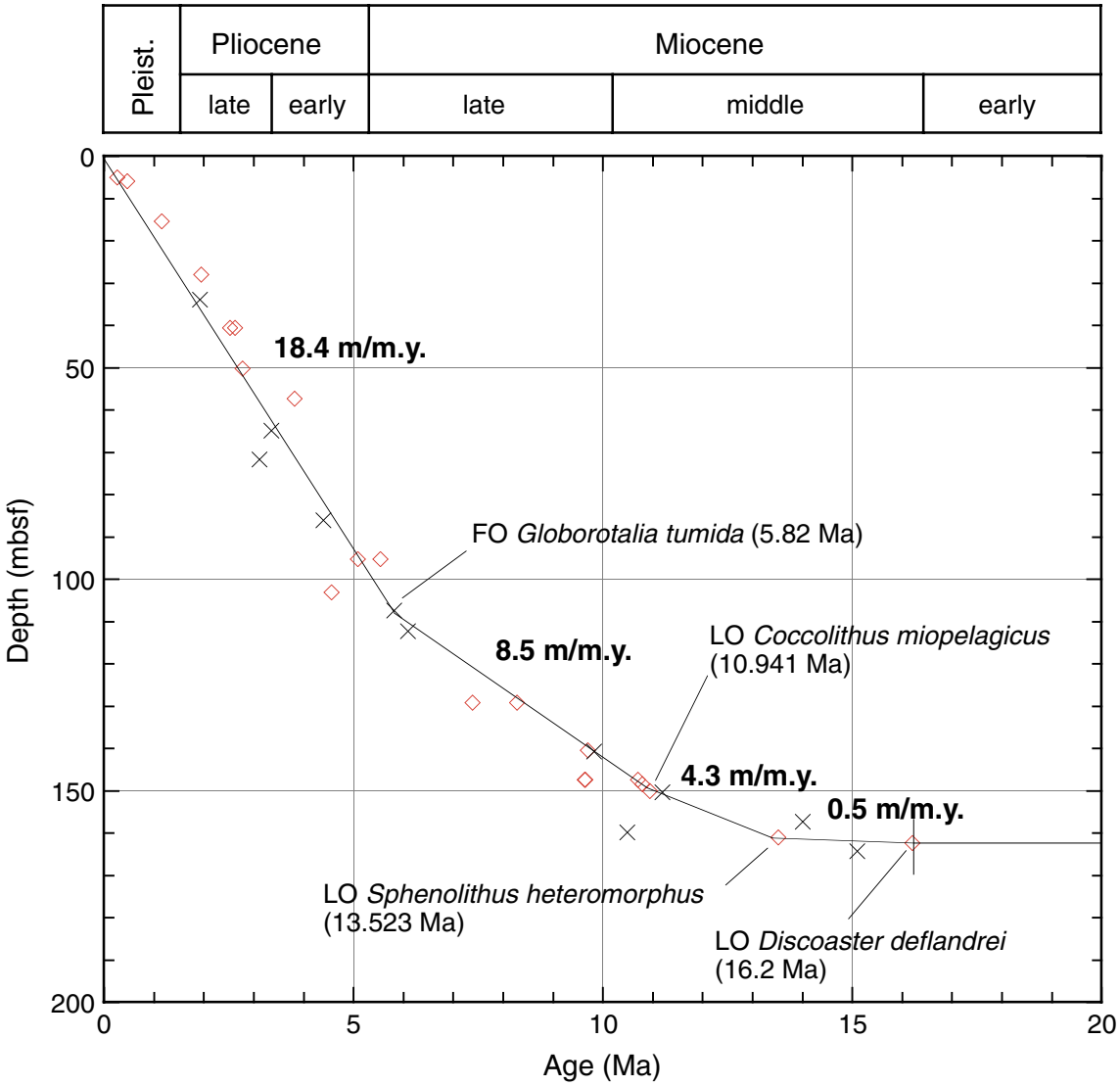

Figure F33. Age-depth plot of Cretaceous calcareous nannofossil (diamonds) and planktonic foraminiferal (crosses) datums at Site 1207. Datum ages and depths are presented in Tables T5, p. 121, and T6, p. 122. FO = first occurrence, LO = last occurrence.

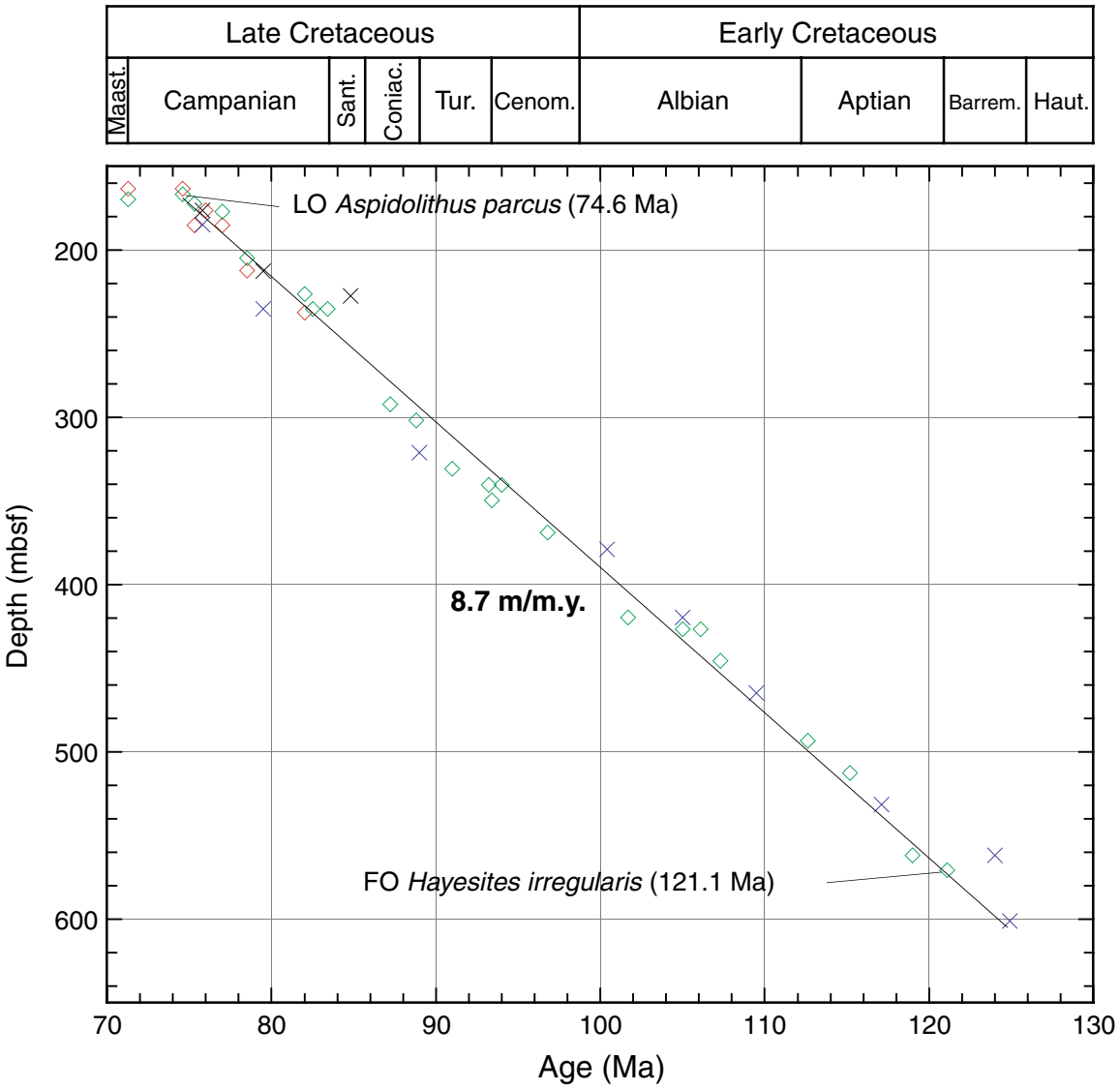

Figure F34. Mass accumulation rates for bulk sediment, carbonate fraction, and noncarbonate fraction vs. (**A**) depth and (**B**) age for the Neogene of Hole 1207A.

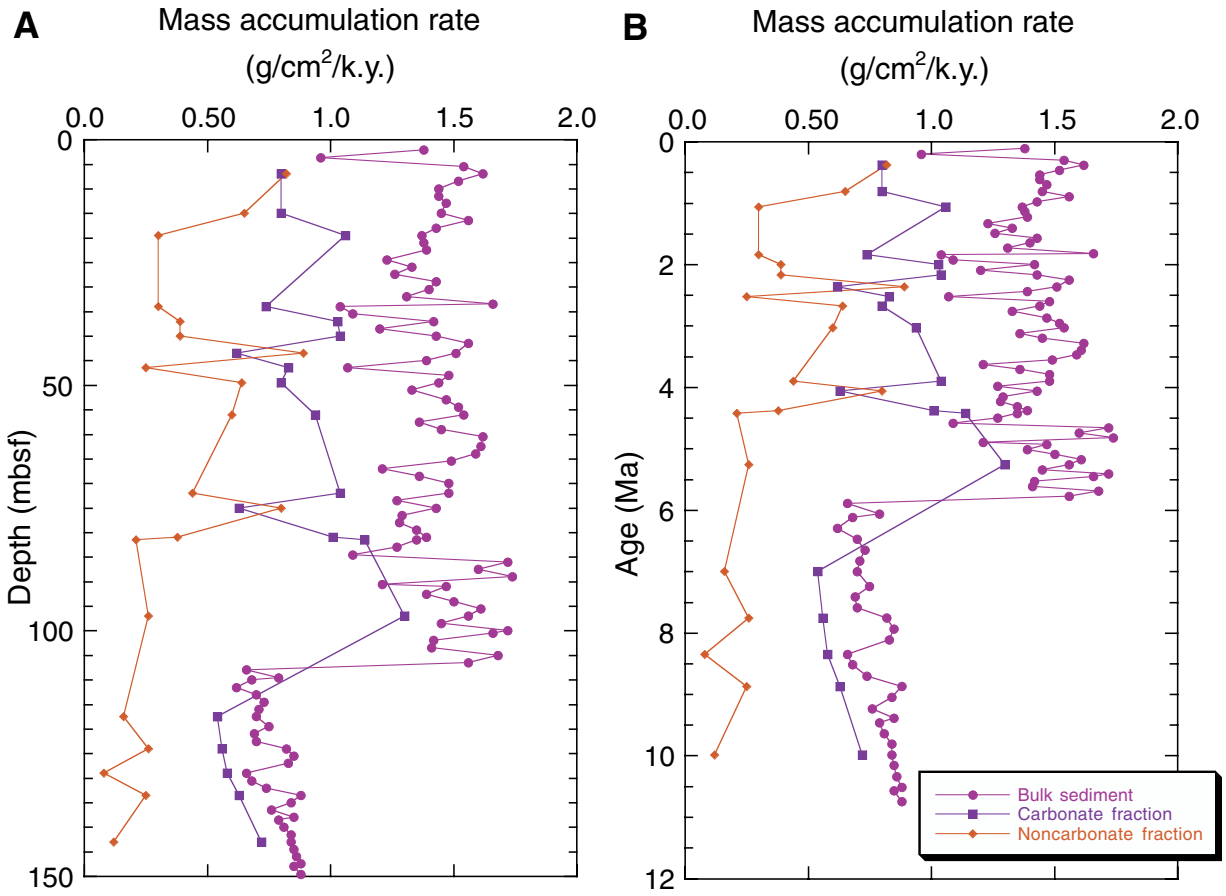

Figure F35. Downhole profiles of CH_4 and sulfate concentrations in Hole 1207A.

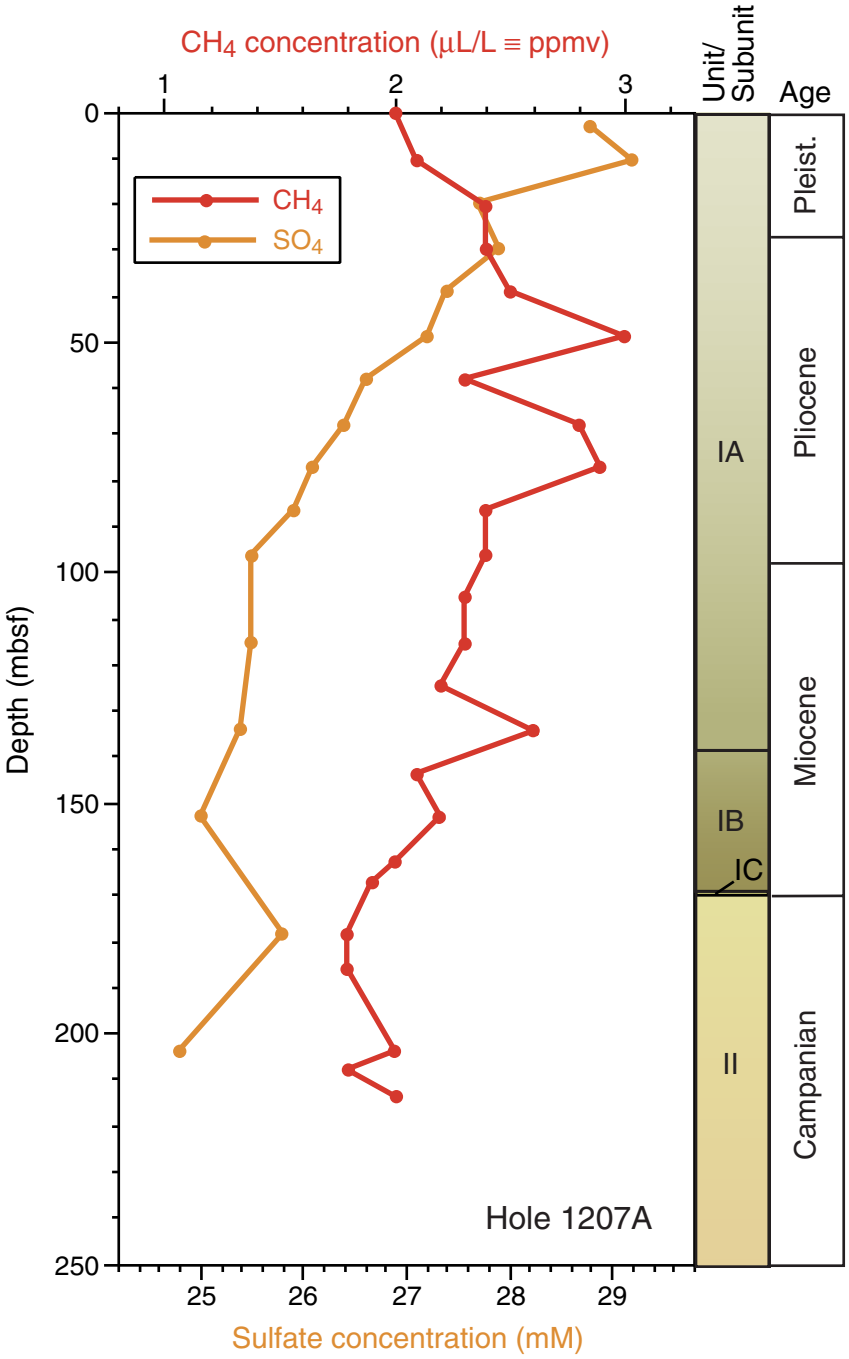

Figure F36. Downhole profiles of carbonate content in Holes 1207A and 1207B and organic carbon contents within samples from the upper, middle, and lower portions of the lower Aptian organic-rich horizon (OAE1a; Section 198-1207B-44R-1).

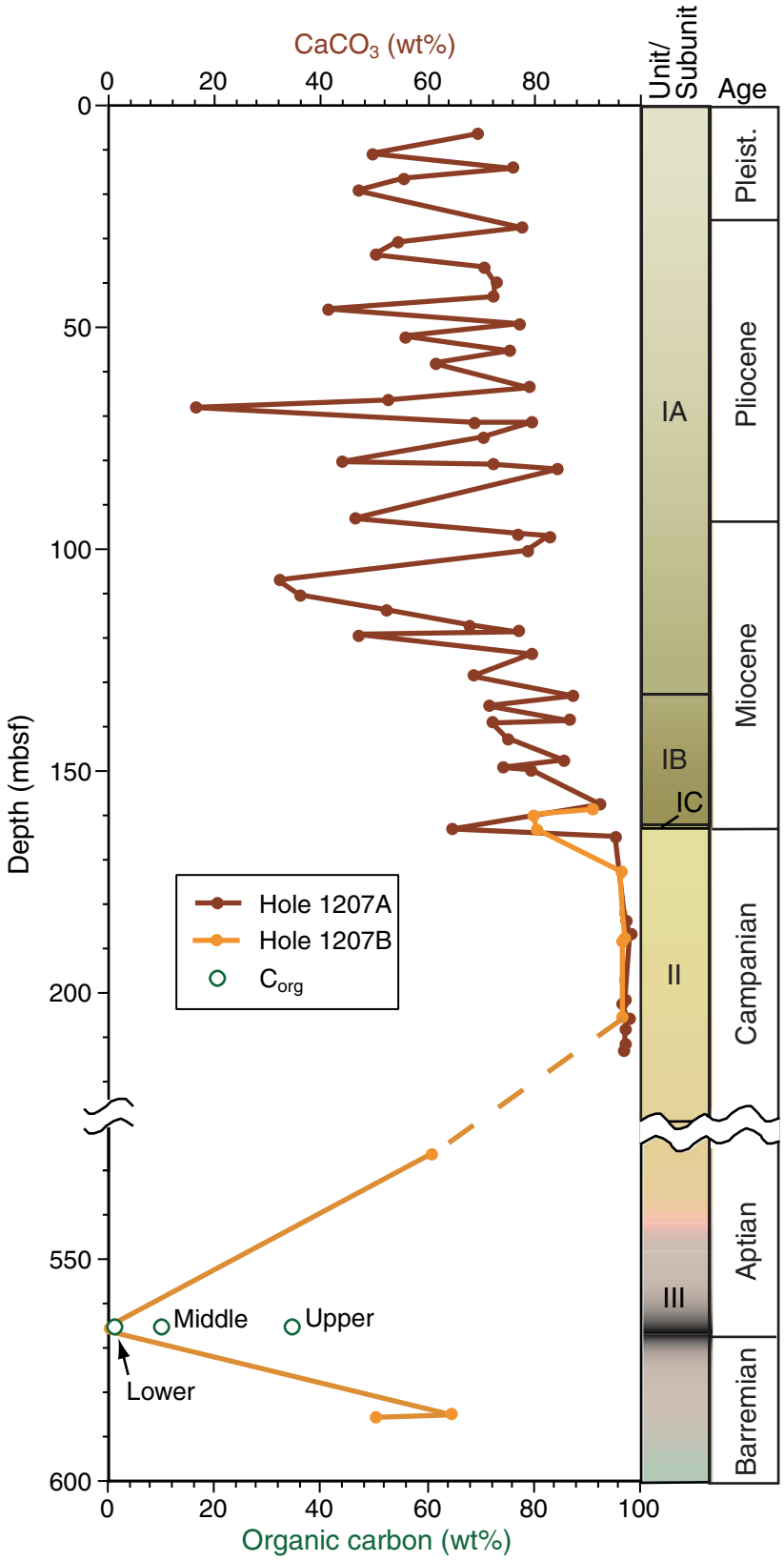

Figure F37. Oxygen and hydrogen indices for samples from the lower Aptian organic-rich horizon (OAE1a) (Table T13, p. 129)—labeled as upper, middle, and lower—plotted on a modified van Krevelen diagram. The characteristics of organic-rich samples from the Aptian at Sites 463 and 866 in the mid-Pacific are also shown. The size of the data points is proportional to organic carbon contents. The lines designated I, II, and III represent the evolutionary trends with thermal maturation of the three major kerogen types (Tissot et al., 1974).

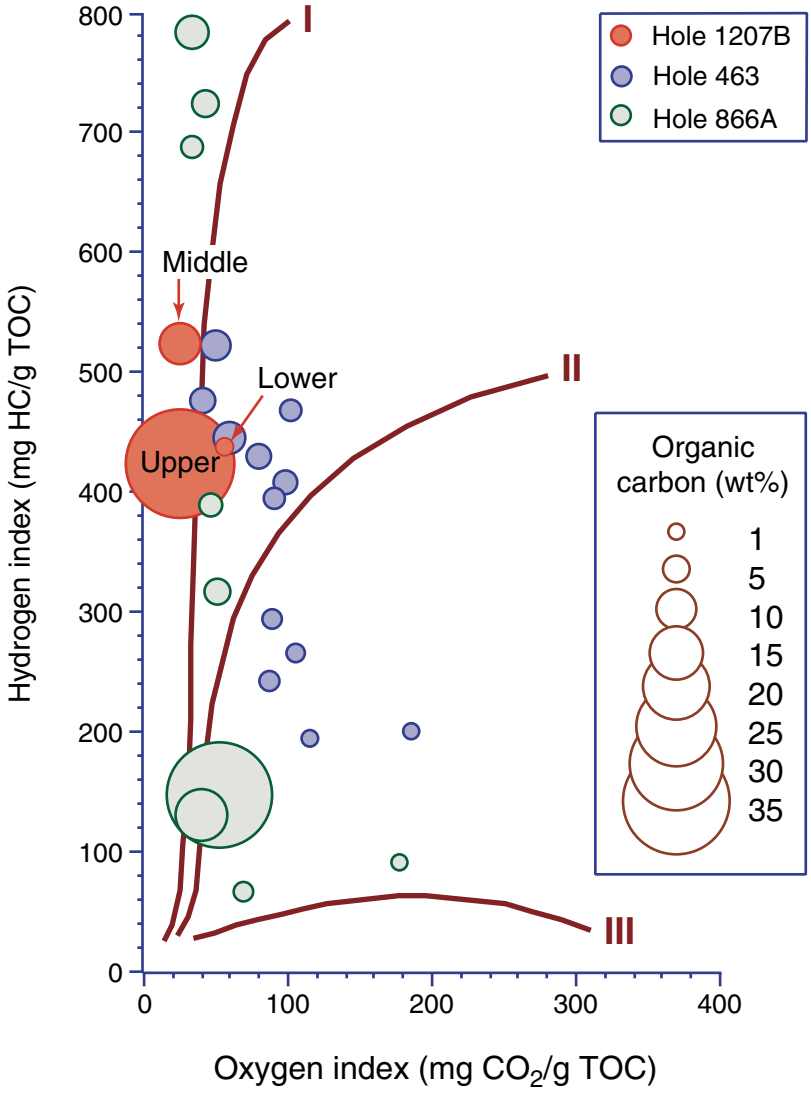

Figure F38. GC-MS trace of aliphatic hydrocarbons for Sample 198-1207B-44R-1, 103–104 cm, from the base of the lower Aptian organic-rich horizon. Peak identities are given in Table **T16,** p. 133.

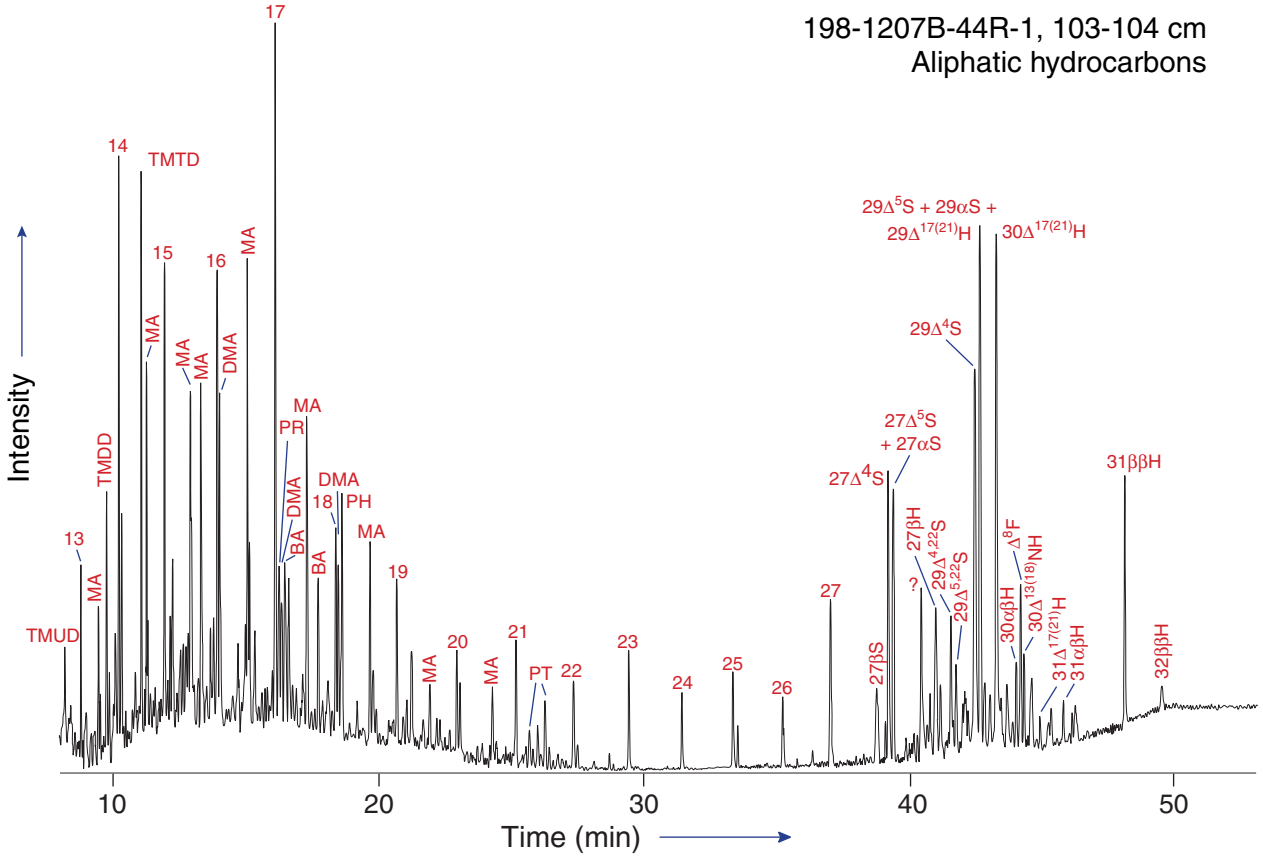

Figure F39. GC-MS trace of aliphatic hydrocarbons for Sample 198-1207B-44R-1, 60–61 cm, from the top of the lower Aptian organic-rich horizon. Peak identities are given in Table T16, p. 133.

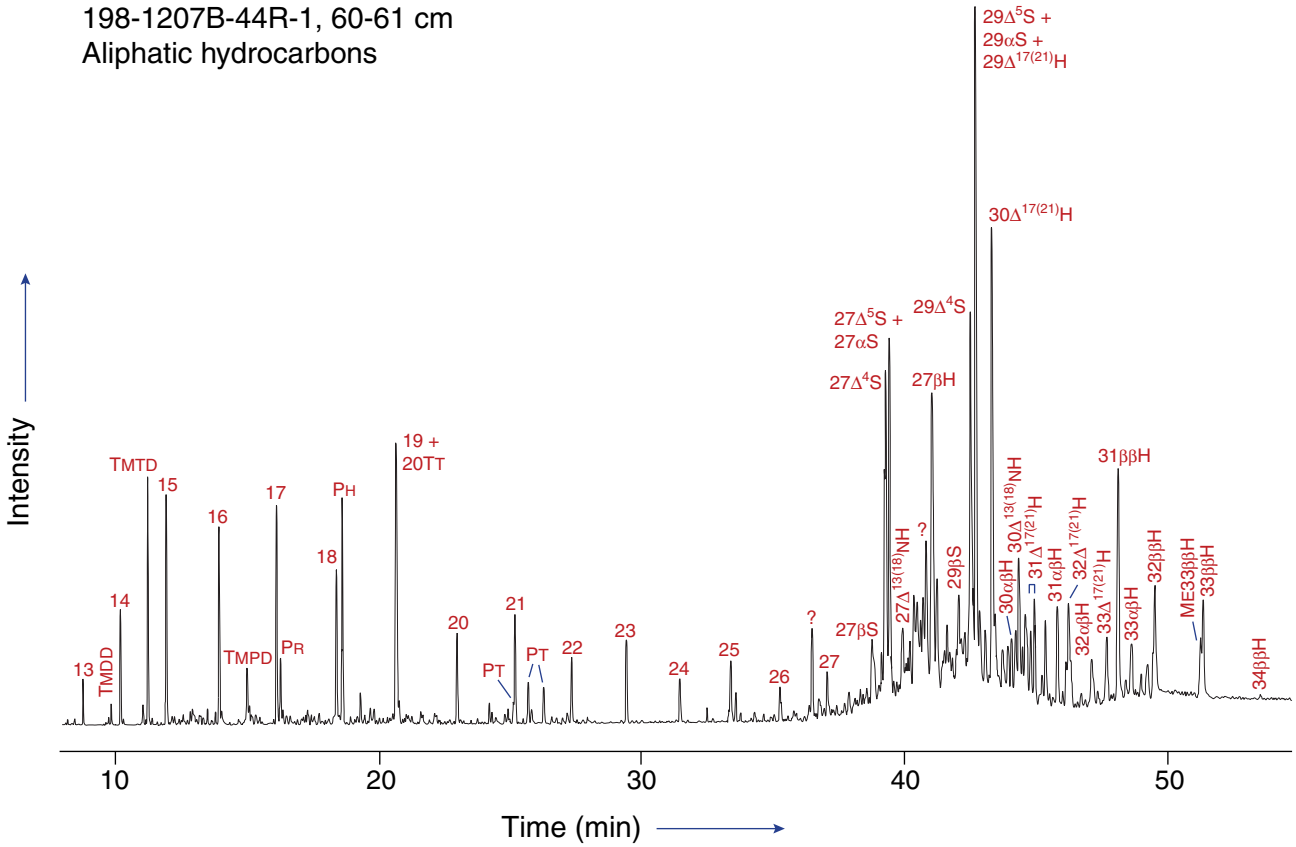

Figure F40. Interstitial water profiles for Hole 1207A. **A.** Sodium. **B.** Chloride.

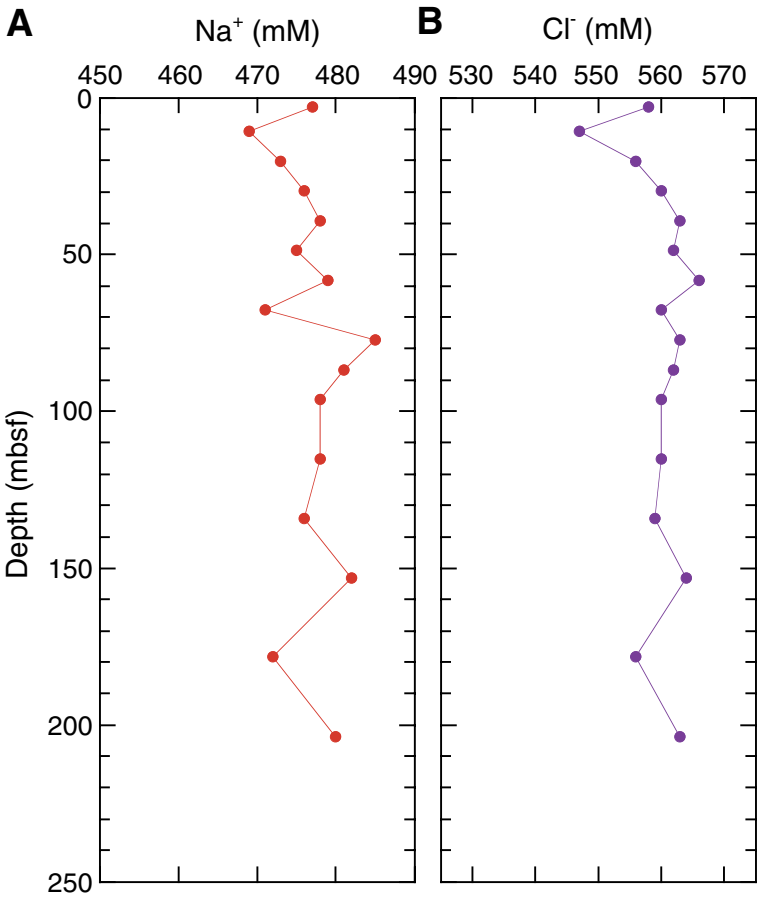

Figure F41. Interstitial water profiles for Hole 1207A. **A.** Alkalinity. **B.** Sulfate. **C.** Manganese. **D.** Iron. **E.** Phosphate. **F.** Ammonium.

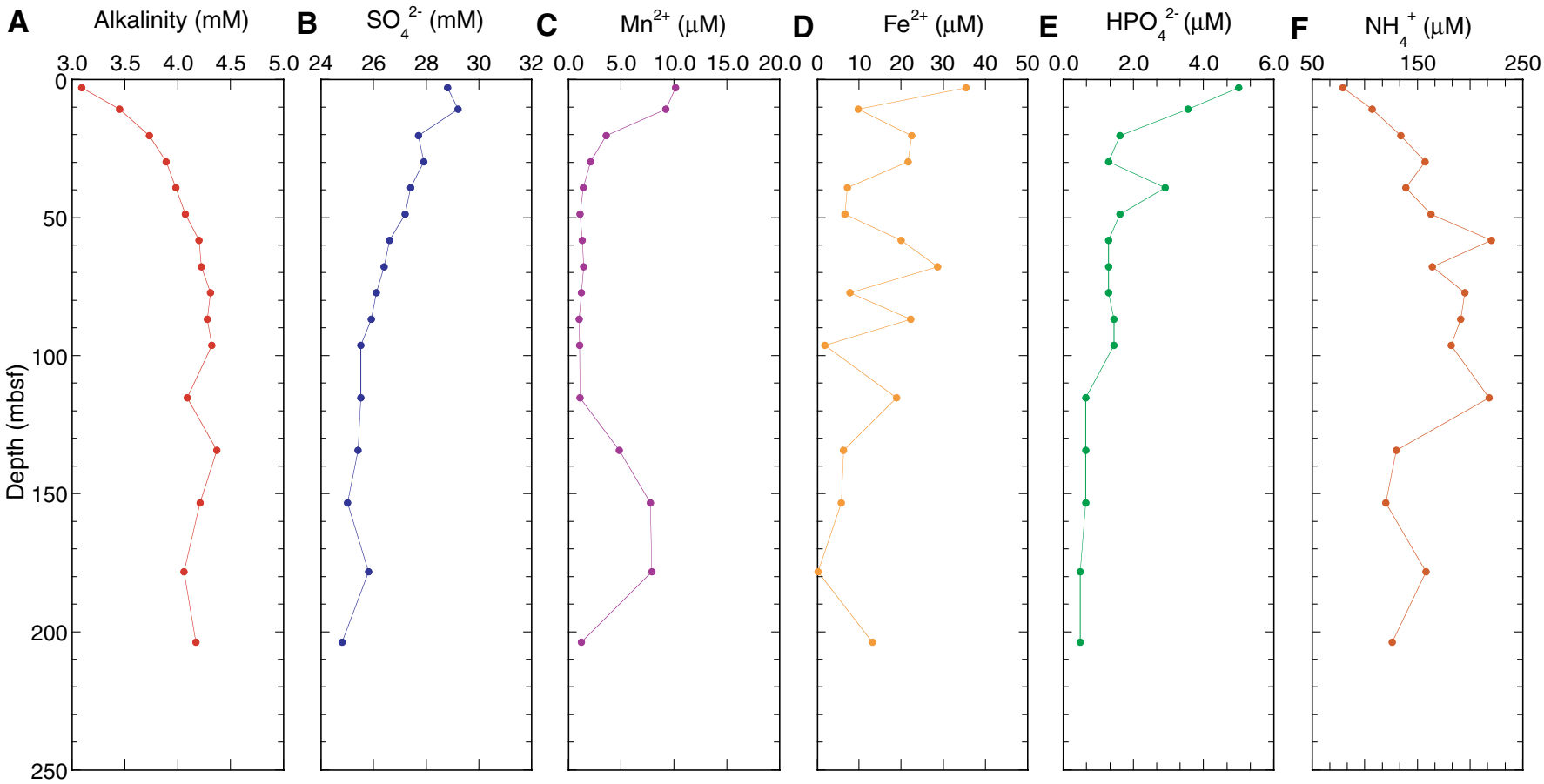

Figure F42. Interstitial water profiles for Hole 1207A. **A.** Potassium. **B.** Silica. **C.** Lithium.

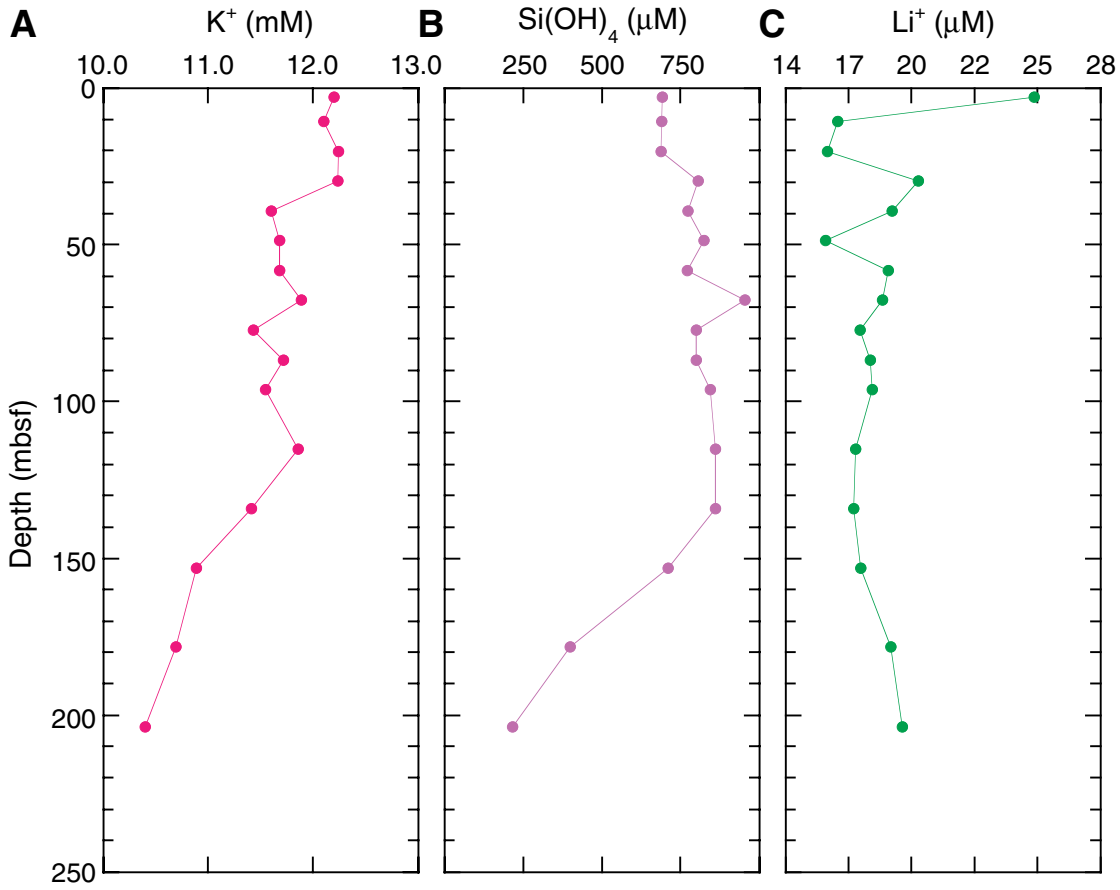

Figure F43. Interstitial water profiles for Hole 1207A. **A.** Calcium. **B.** Magnesium. **C.** Strontium and Sr/Ca. **D.** Boron. **E.** Barium.

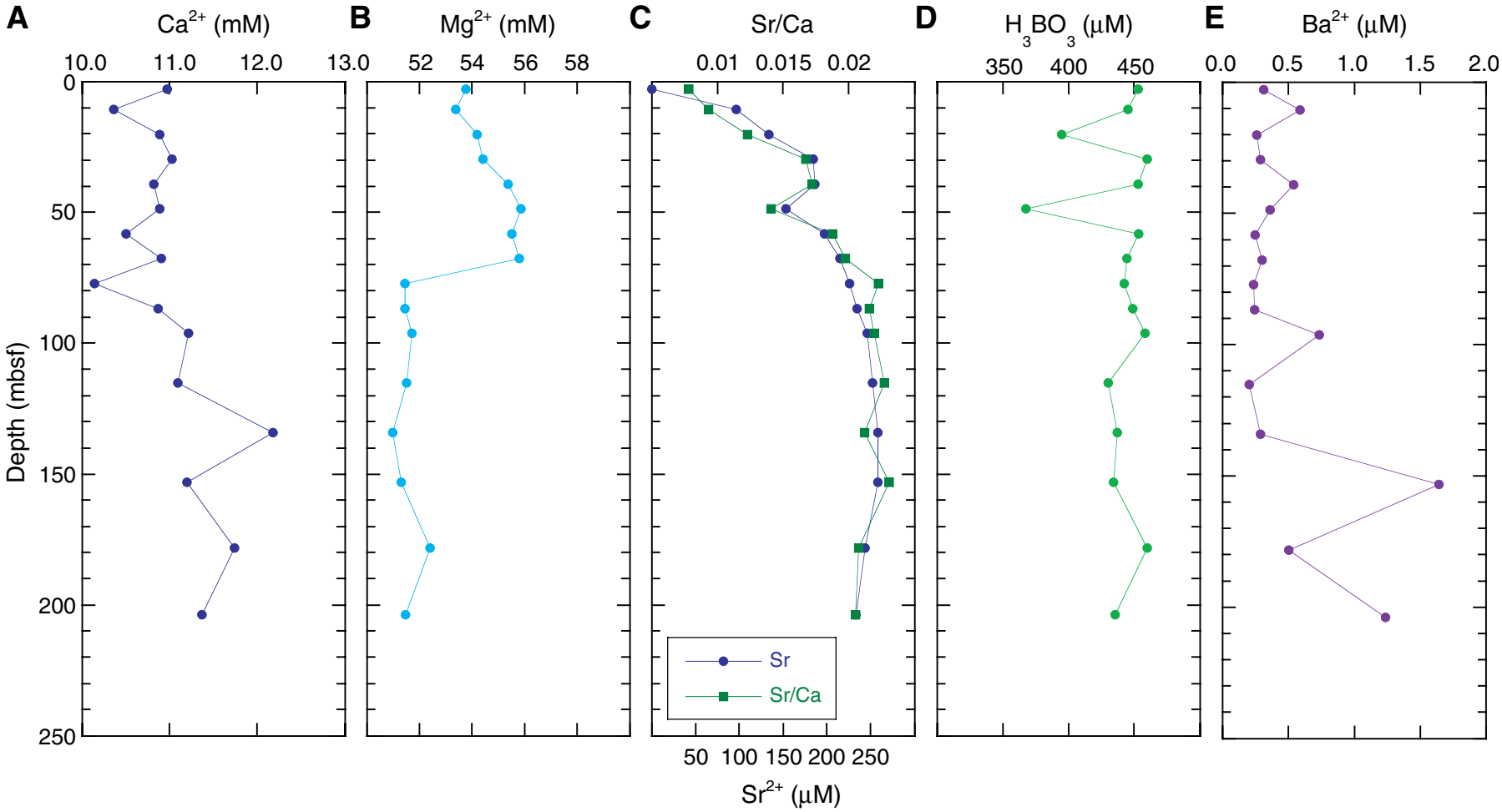

Figure F44. MST magnetic susceptibility measured in whole cores from Holes 1207A and 1207B vs. depth. The accurate correction factor for these raw instrument values is 0.68×10^{-5}.

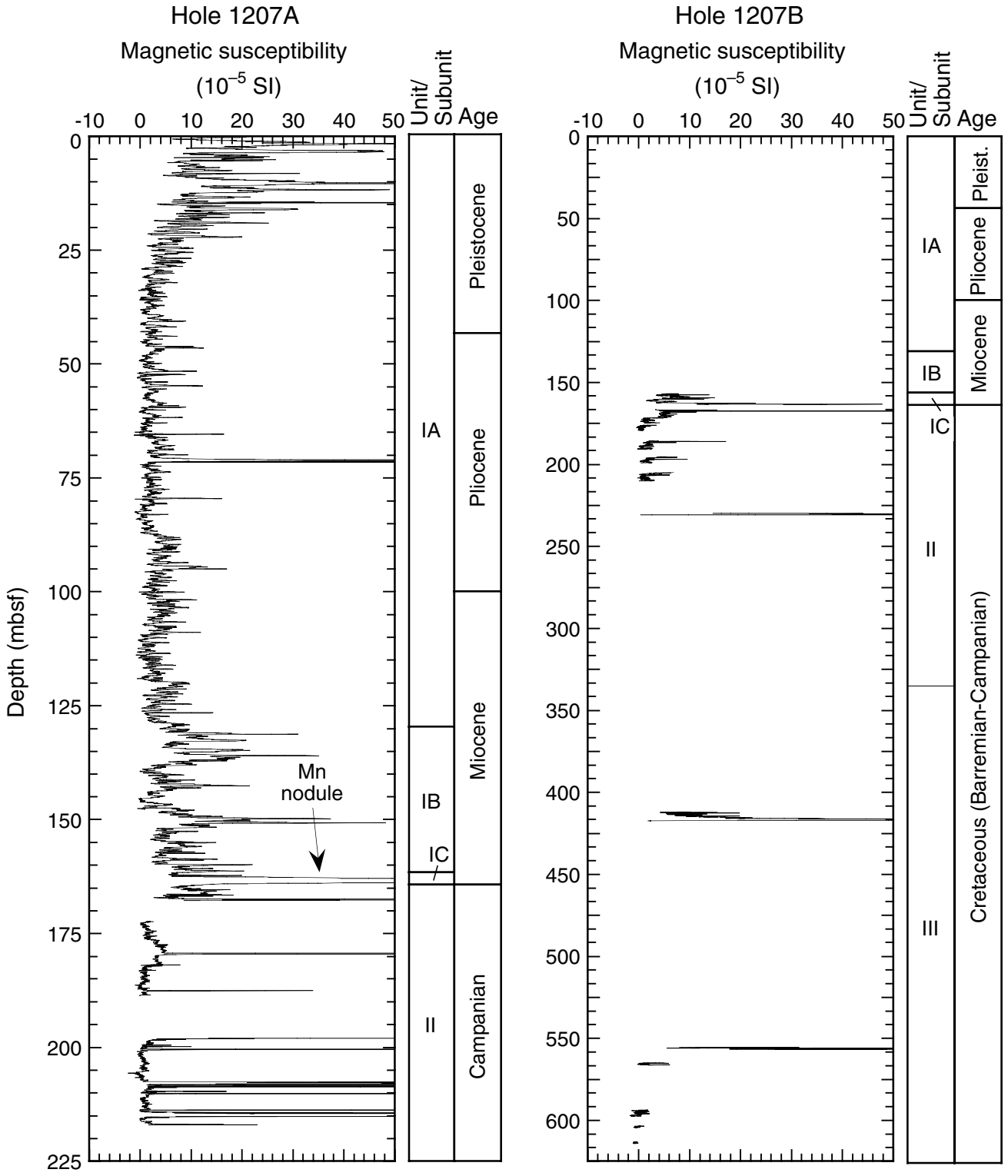

Figure F45. MST gamma ray attenuation (GRA) bulk density (lines) measured in whole cores from Holes 1207A and 1207B vs. depth. Discrete measurements of wet bulk density (Table T18, p. 135) from Holes 1207A (solid circles) and 1207B (open circles) are plotted for comparison with the MST GRA bulk density data from Hole 1207A.

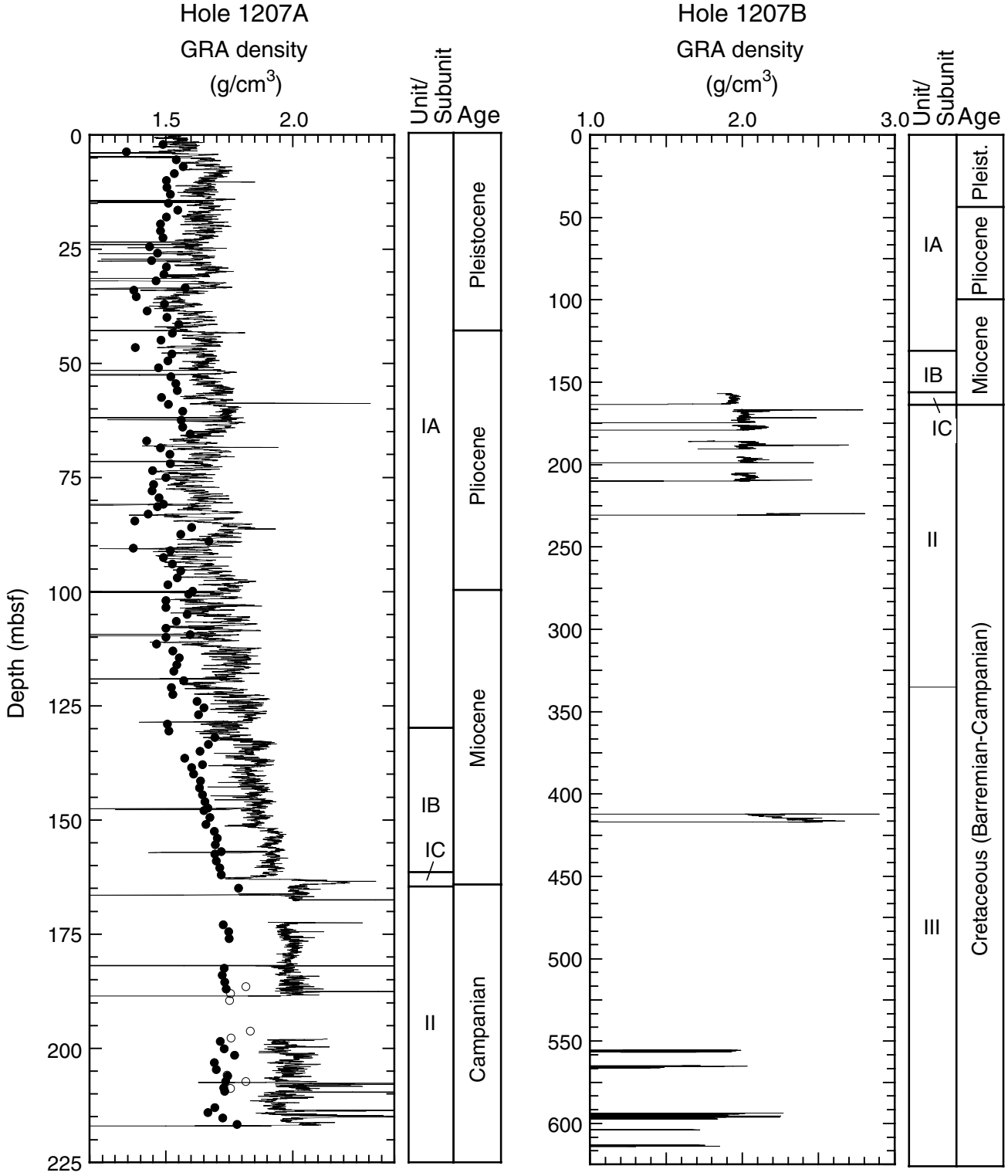

Figure F46. A. MST *P*-wave velocity measured in Hole 1207A whole cores vs. depth. Note that one of the MST PWL transducers was not working properly during the collection of Site 1207 data, so many data points are out of range (see **"MST Measurements,"** p. 37, in "Physical Properties" for further explanation). Solid circles and dots represent MST *P*-wave velocity data. **B.** Out of range MST data have been removed. For comparison, discrete Hamilton Frame (PWS3) velocity data (open circles) are also shown.

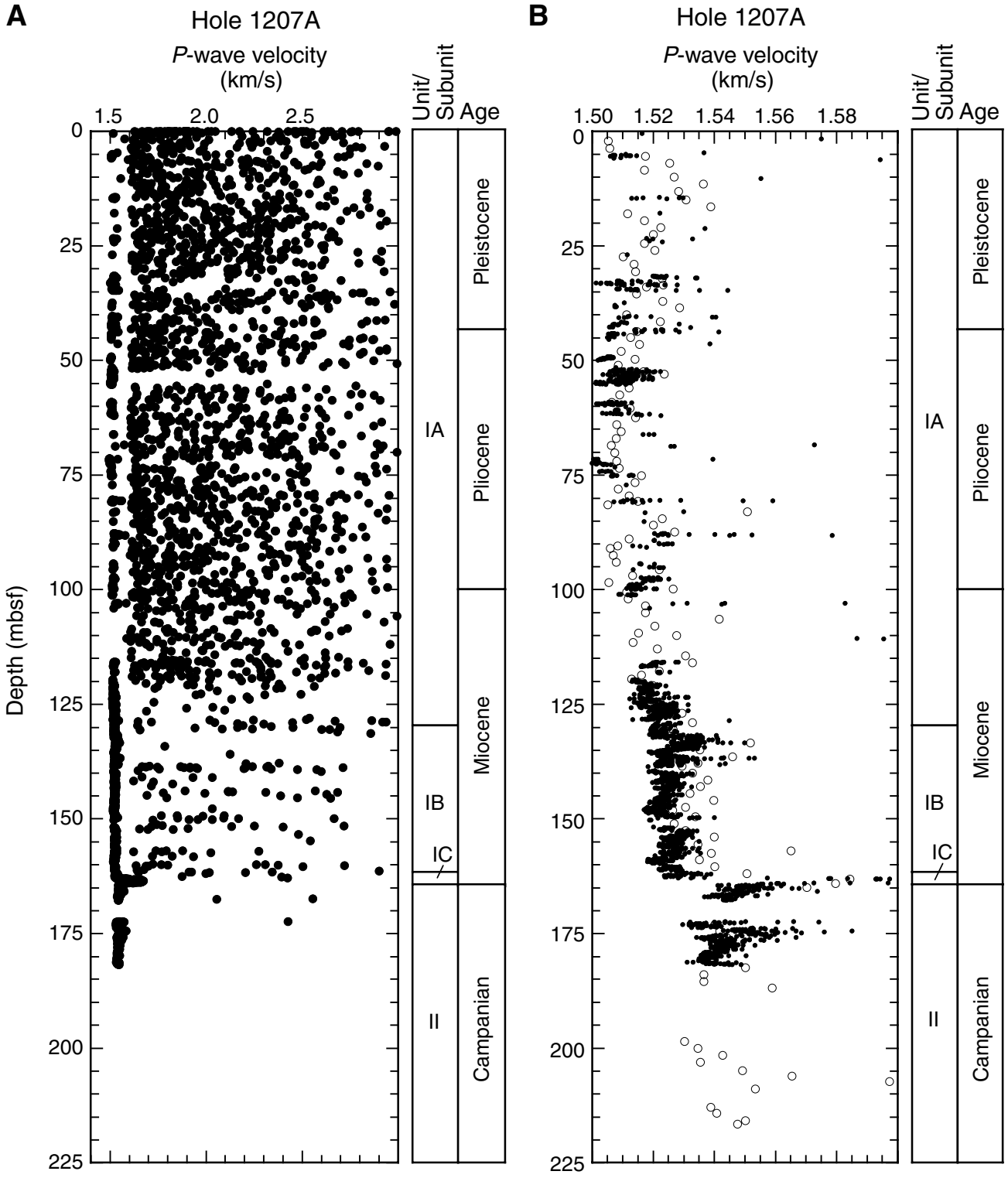

Figure F47. MST natural gamma radiation for Holes 1207A and 1207B vs. depth.

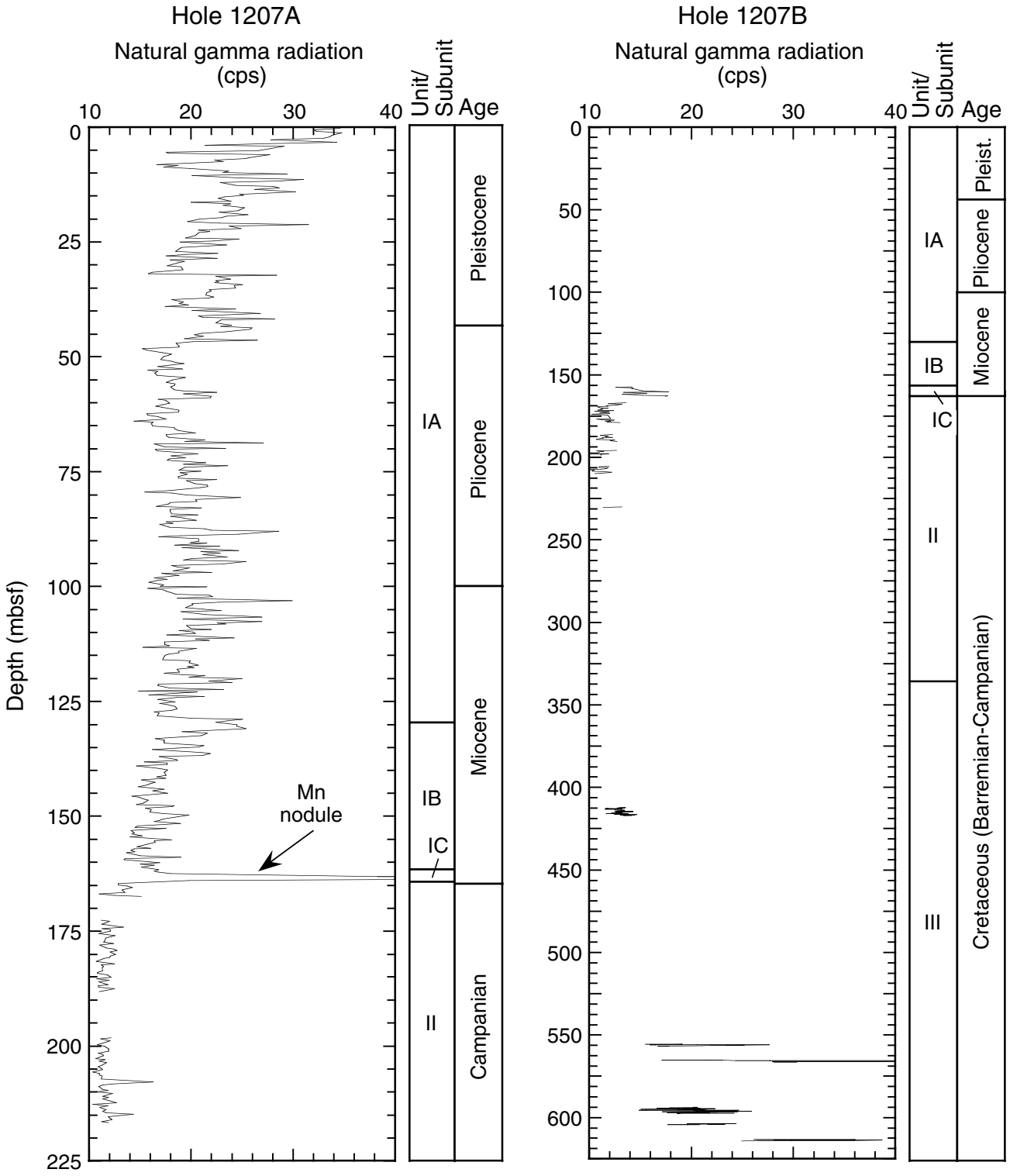

Figure F48. *P*-wave velocities for discrete samples from Holes 1207A (solid circles) and 1207B (open circles) vs. depth. **A.** Entire data set for Holes 1207A and 1207B. The very high *P*-wave velocities measured at chert horizons are not illustrated (see Table **T19,** p. 138, for these data). **B.** Close-up of data for the Pleistocene to Campanian time interval. The high *P*-wave velocity measured for the ferromanganese nodule situated near the Campanian–Miocene unconformity is not shown (see Table **T19,** p. 138, for this value).

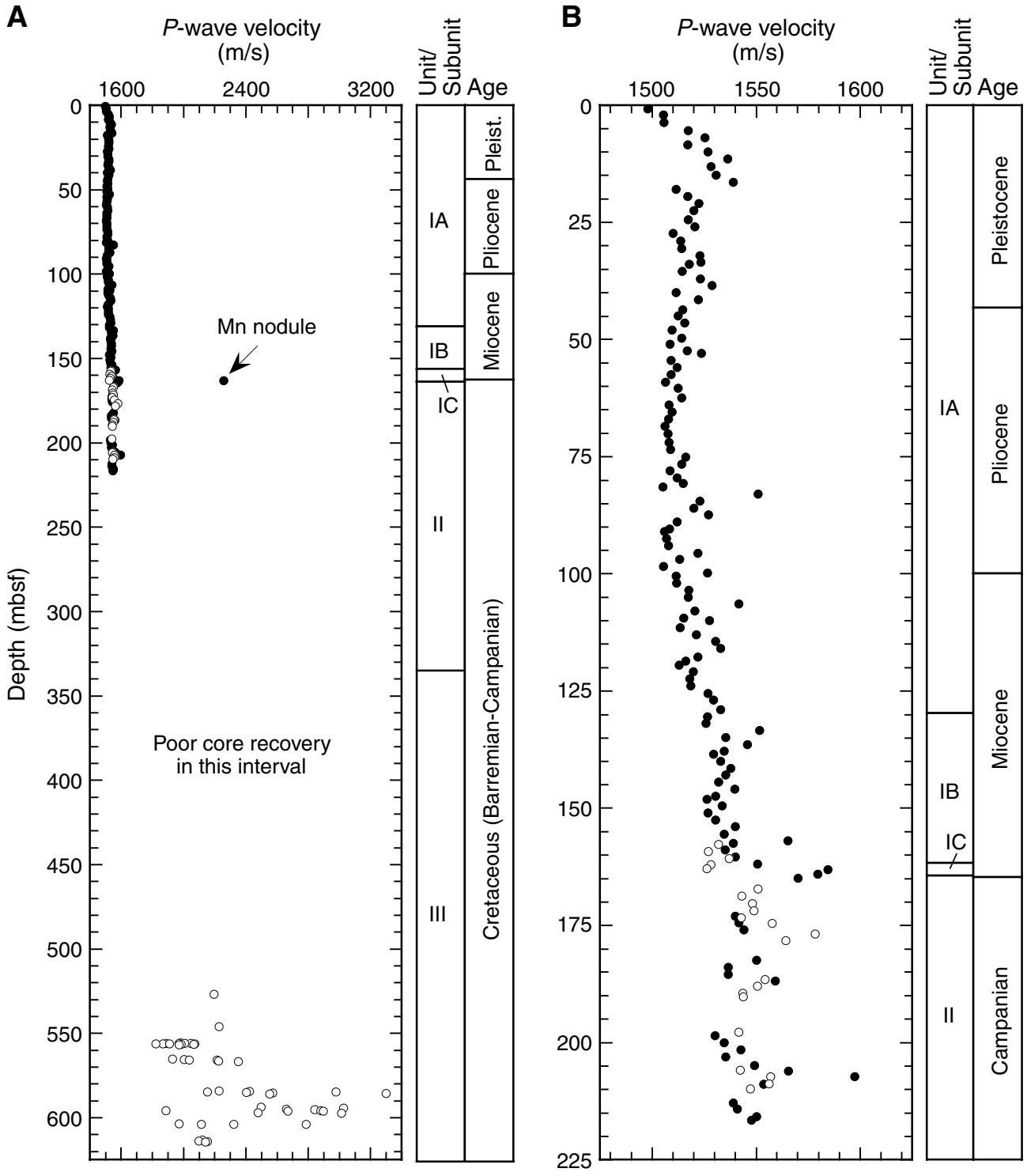

Figure F49. (**A**) Water content calculated relative to bulk sediment (circles) and solid phase (triangles), (**B**) porosity, and (**C**) void ratio determined for discrete samples from Hole 1207A (solid circles and triangles) and Hole 1207B (open circles and triangles) vs. depth.

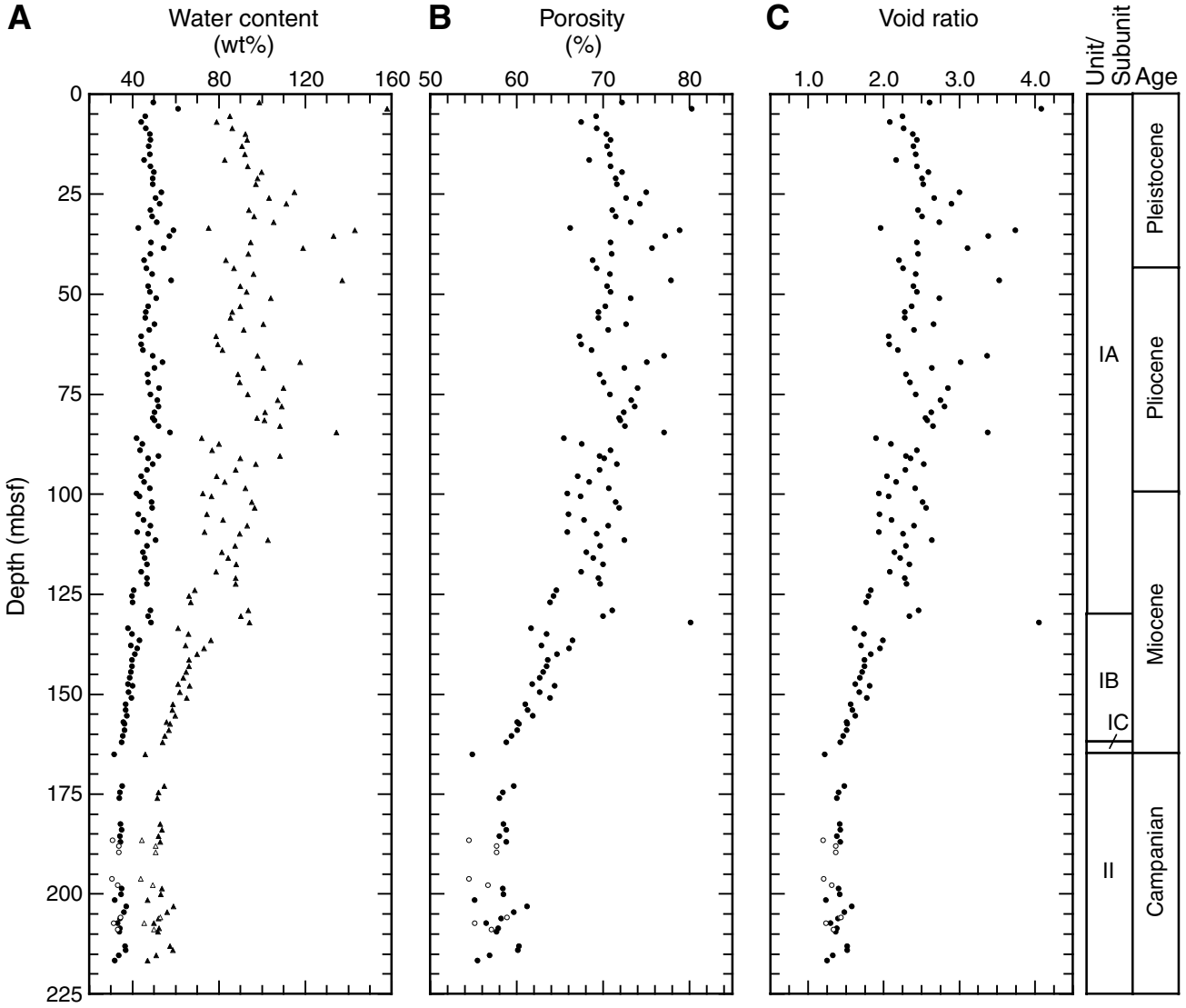

Figure F50. Discrete measurements of Hole 1207A *P*-wave velocities vs. discrete wet bulk density measurements at comparable stratigraphic horizons.

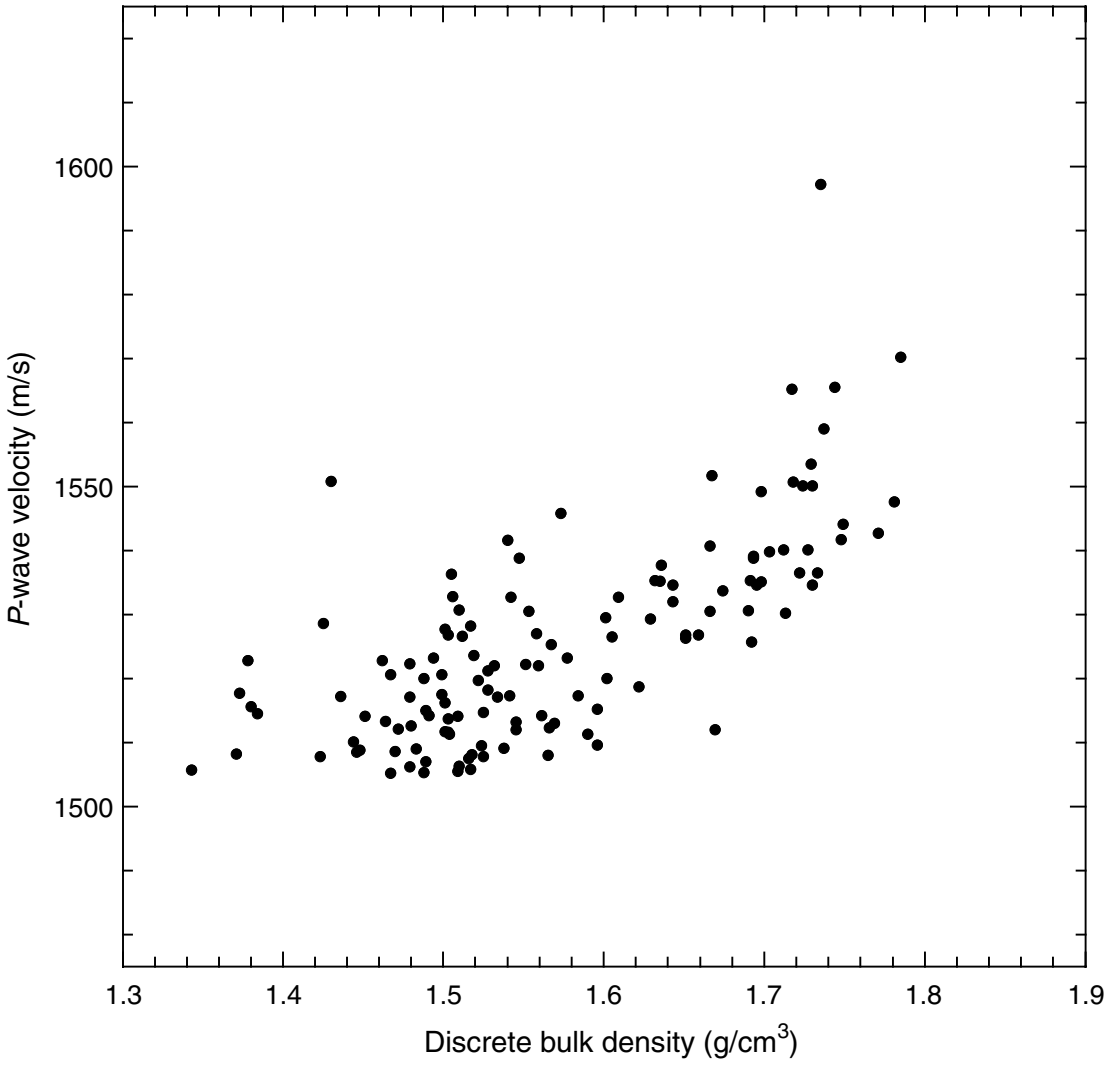

Figure F51. Whole-core thermal conductivity measured for Hole 1207A (solid circles) and Hole 1207B (open circles) vs. depth. Additional data acquired from Core 198-1207B-28R are not shown (see Table T20, p. 140, for these data).

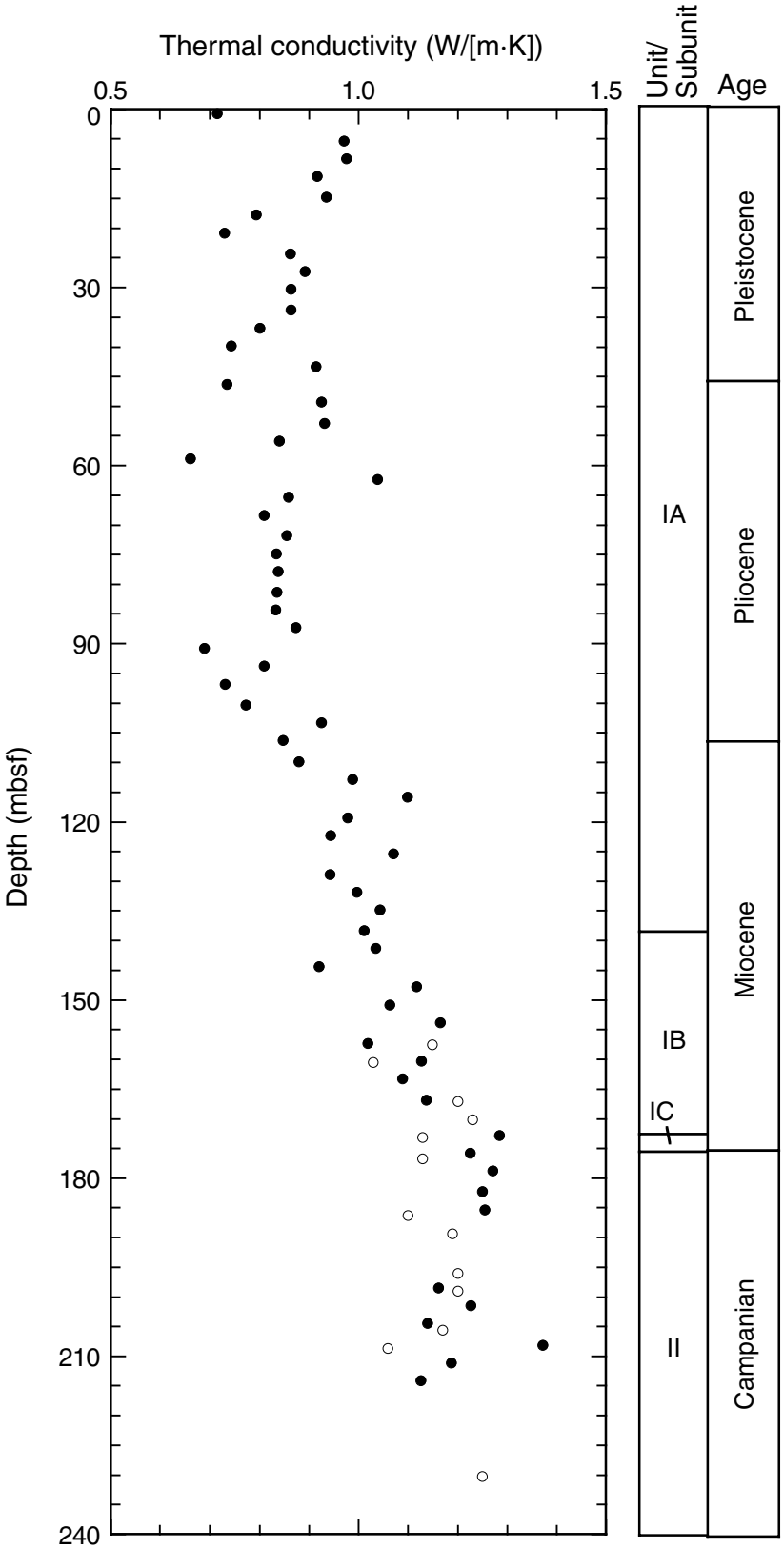

Figure F52. Hole 1207A whole-core thermal conductivity vs. discrete measurements of porosity.

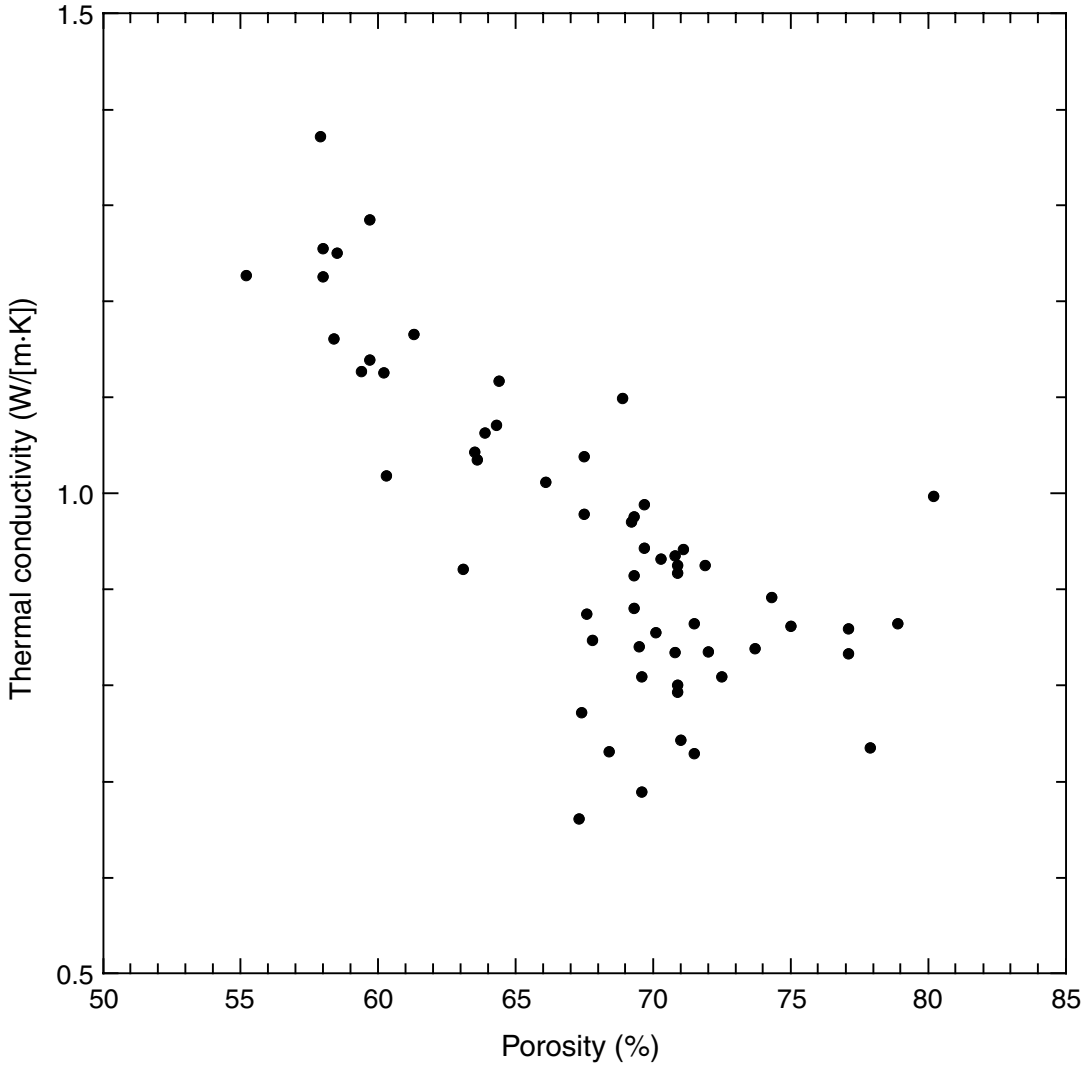

Figure F53. (A) Wet bulk density, (B) dry density, and (C) grain density determined for discrete samples from Hole 1207A (solid circles) and Hole 1207B (open circles) vs. depth.

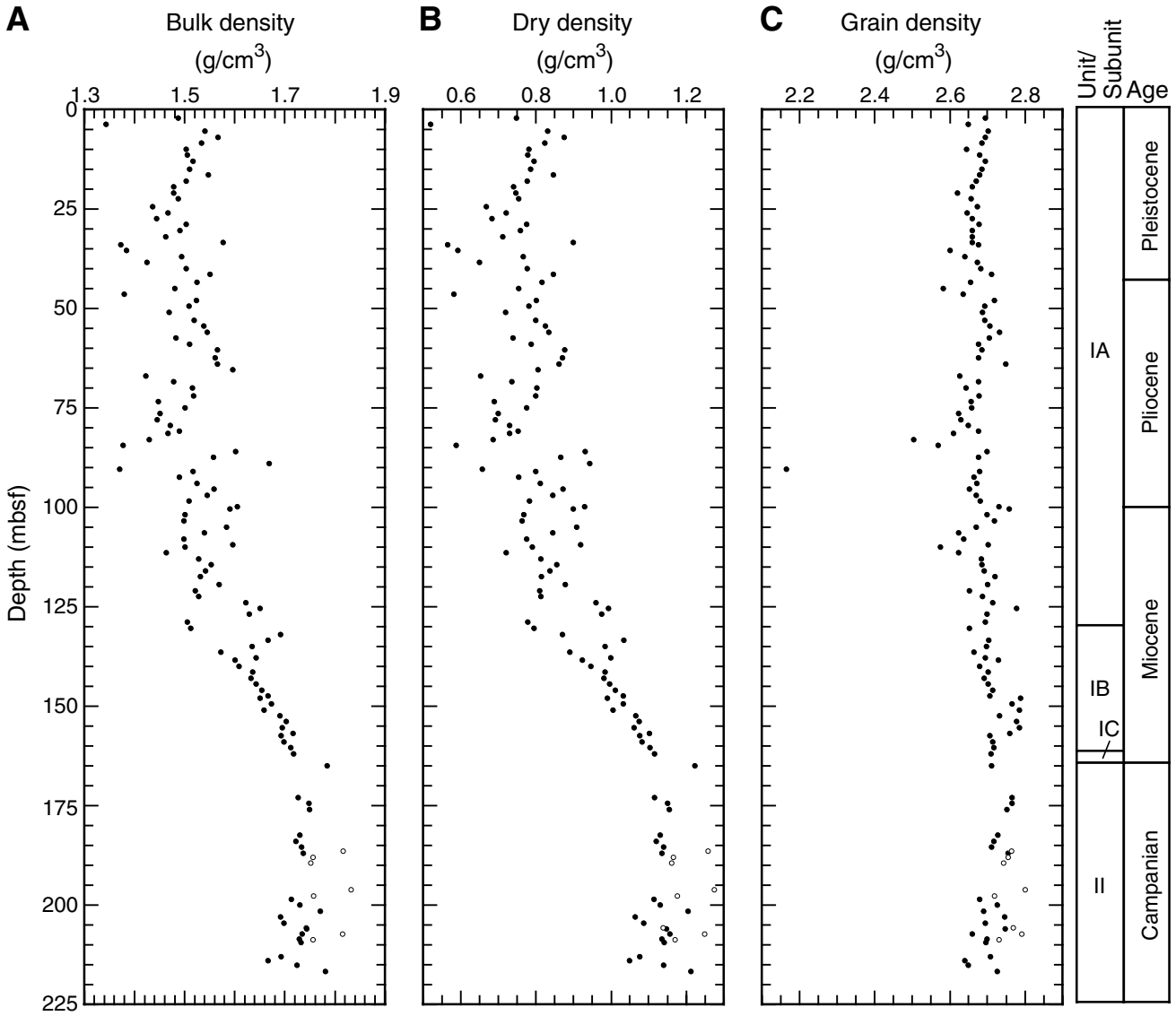

Figure F54. Summary of the logging runs at Hole 1207B. FMS = Formation MicroScanner, GHMT = geologic high-resolution magnetic tool, MGT = multisensor spectral gamma ray tool.

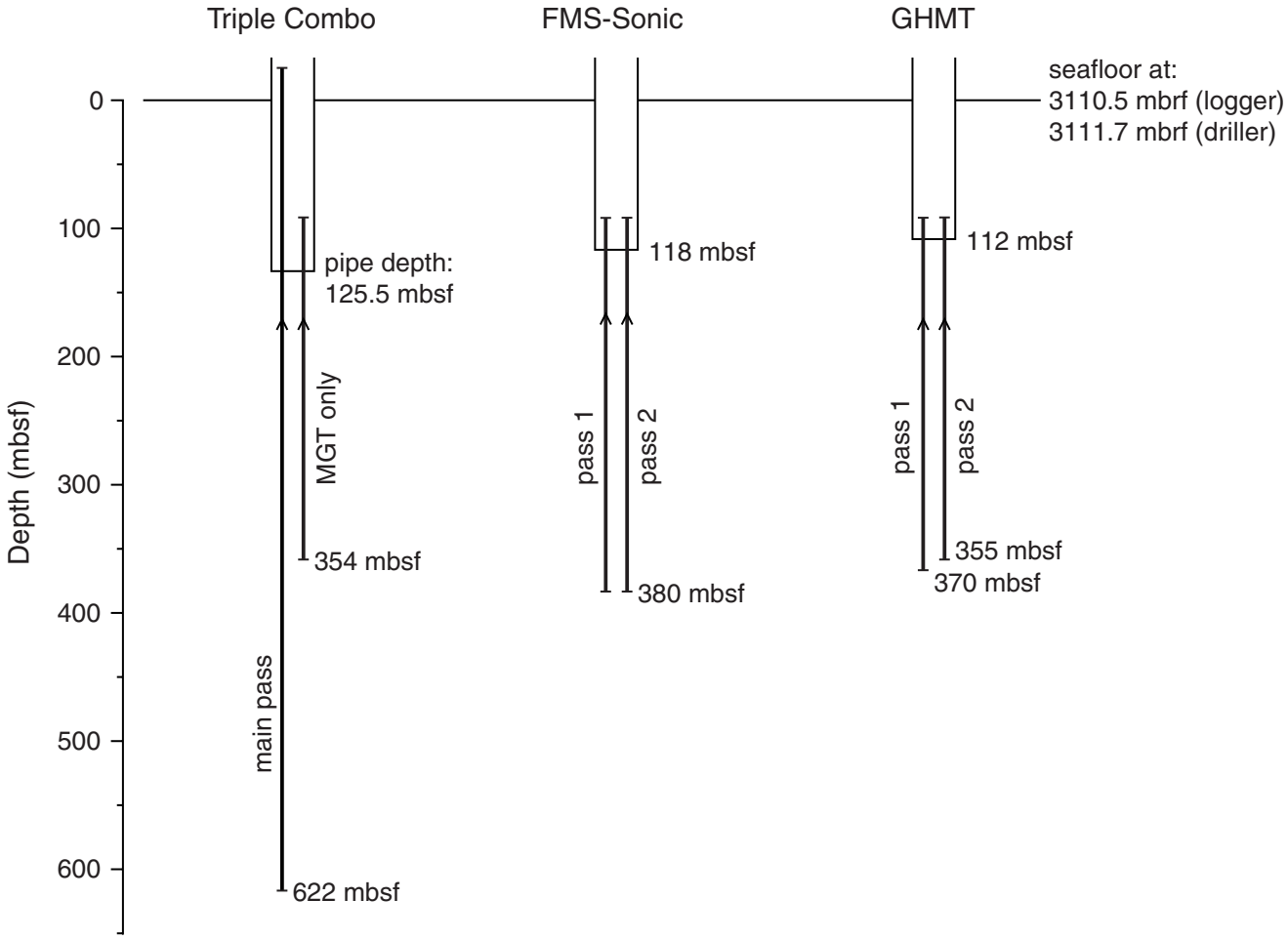

Figure F55. Geophysical logs and equivalent core physical properties measurements, Hole 1207B. Lith. = lithologic.

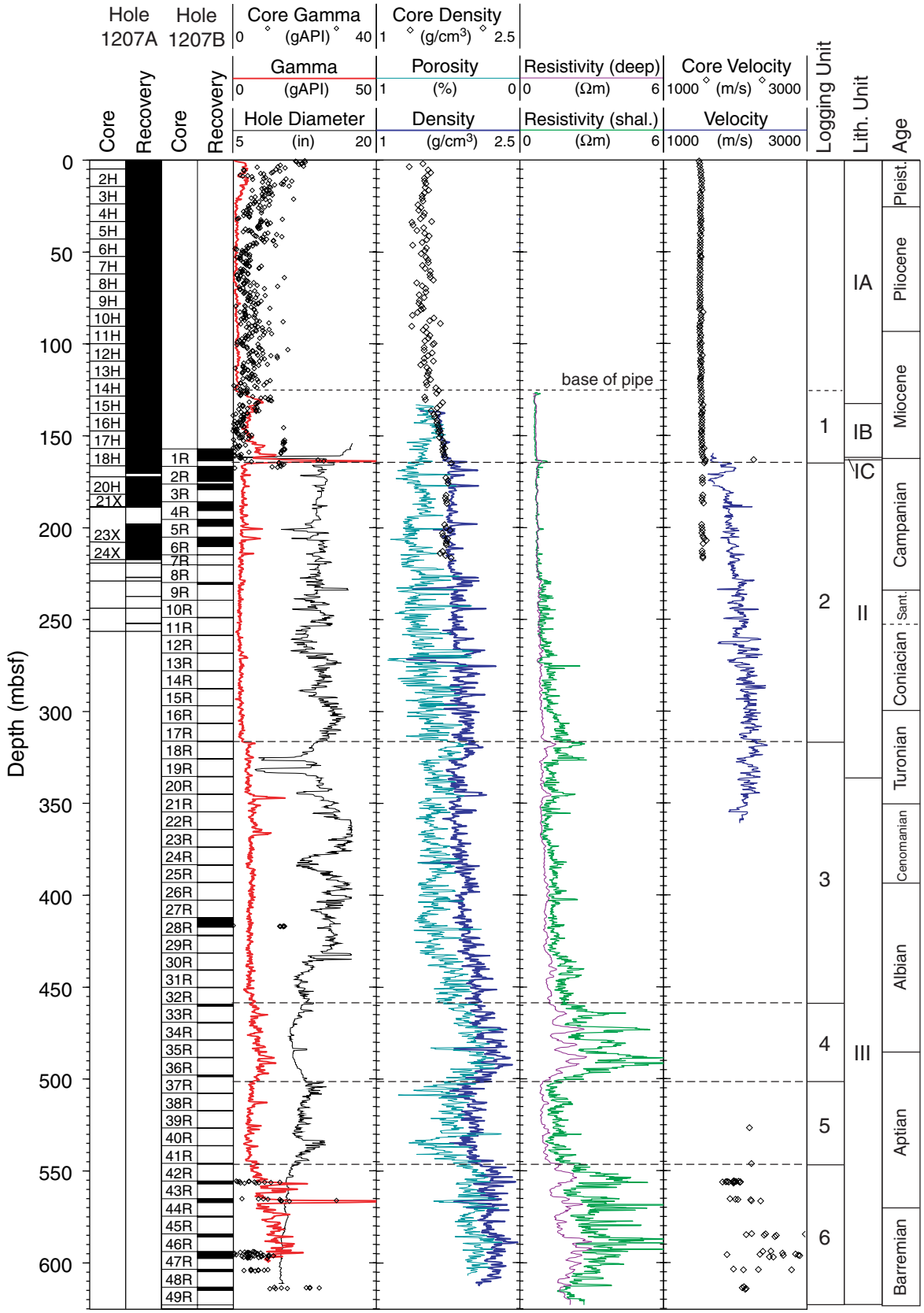

Figure F56. Geochemical logs at Hole 1207B. PEF = photoelectric effect, lith. = lithologic.

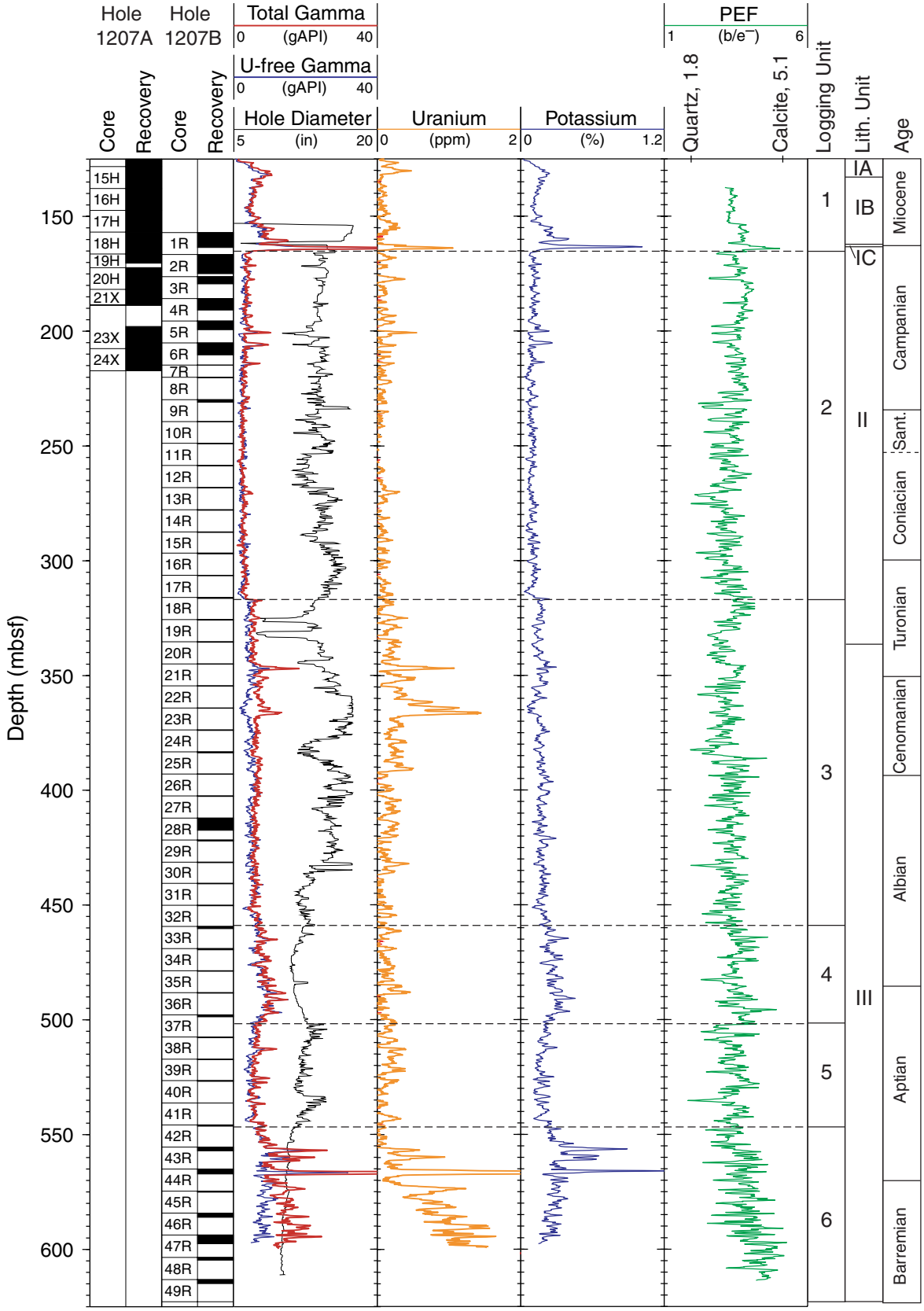

Figure F57. Gamma radiation, density, and porosity logs around the OAE1a black shale interval at 566 mbsf. HSGR = total spectral gamma ray, HCGR = computed gamma ray, HROM = high resolution bulk density, HALC = high resolution array porosity (limestone corrected).

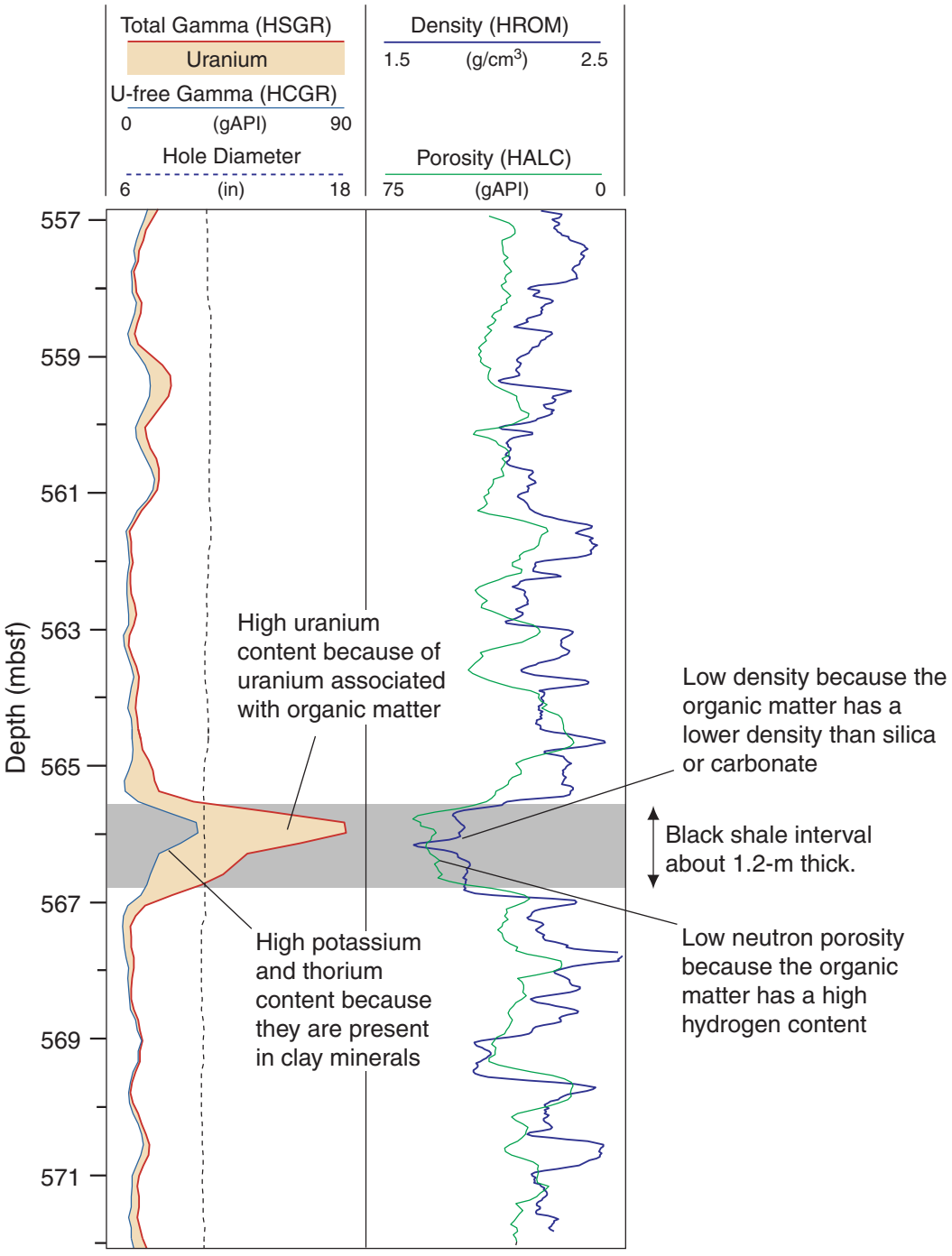

Figure F58. Comparison of the gamma radiation logs around the Cenomanian/Turonian boundary. HSGR = total spectral gamma ray, HCGR = computed gamma ray, MGT = multisensor spectral gamma ray tool.

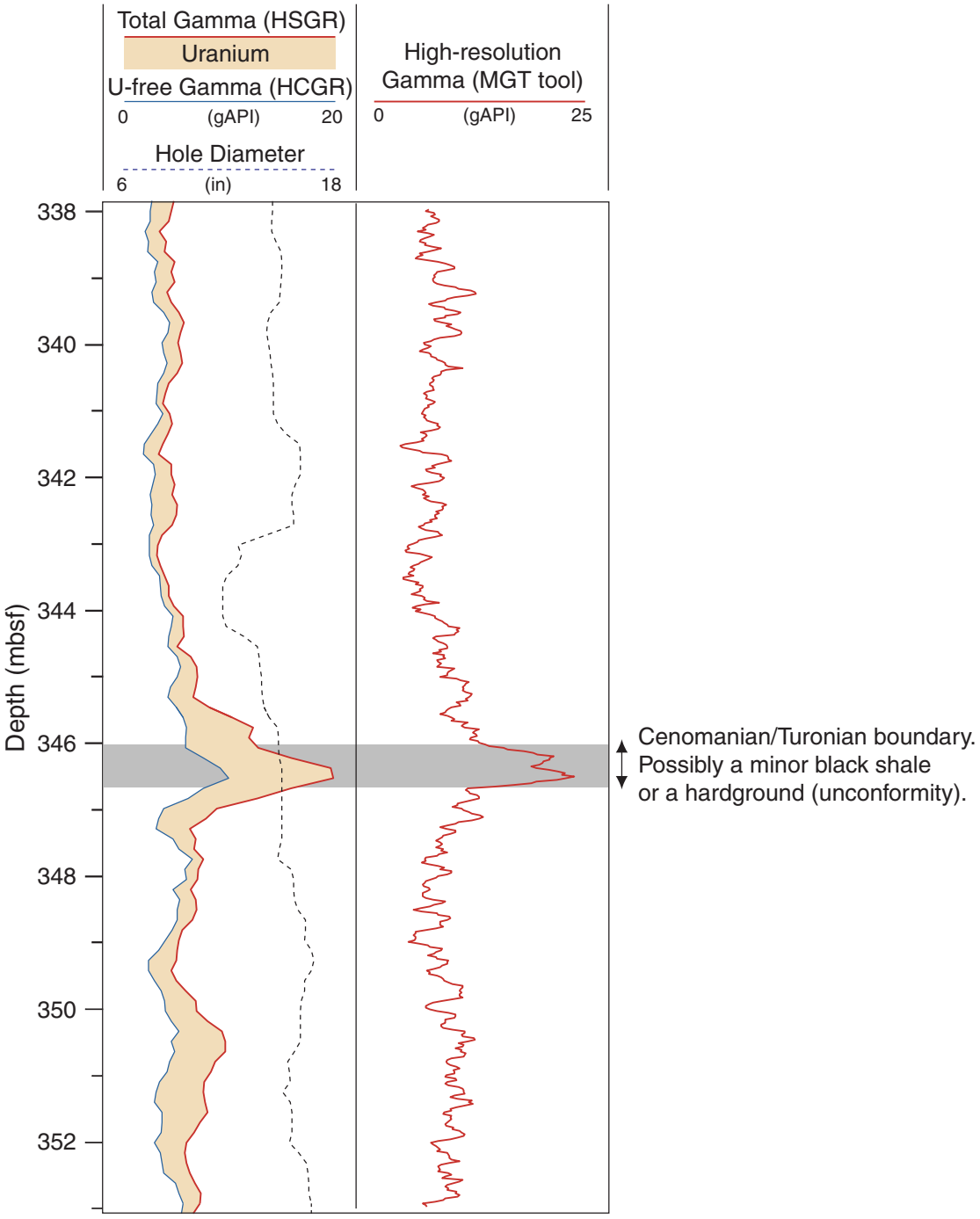

Figure F59. Example FMS image showing layered cherts as resistive (light colored) bands across the four pads.

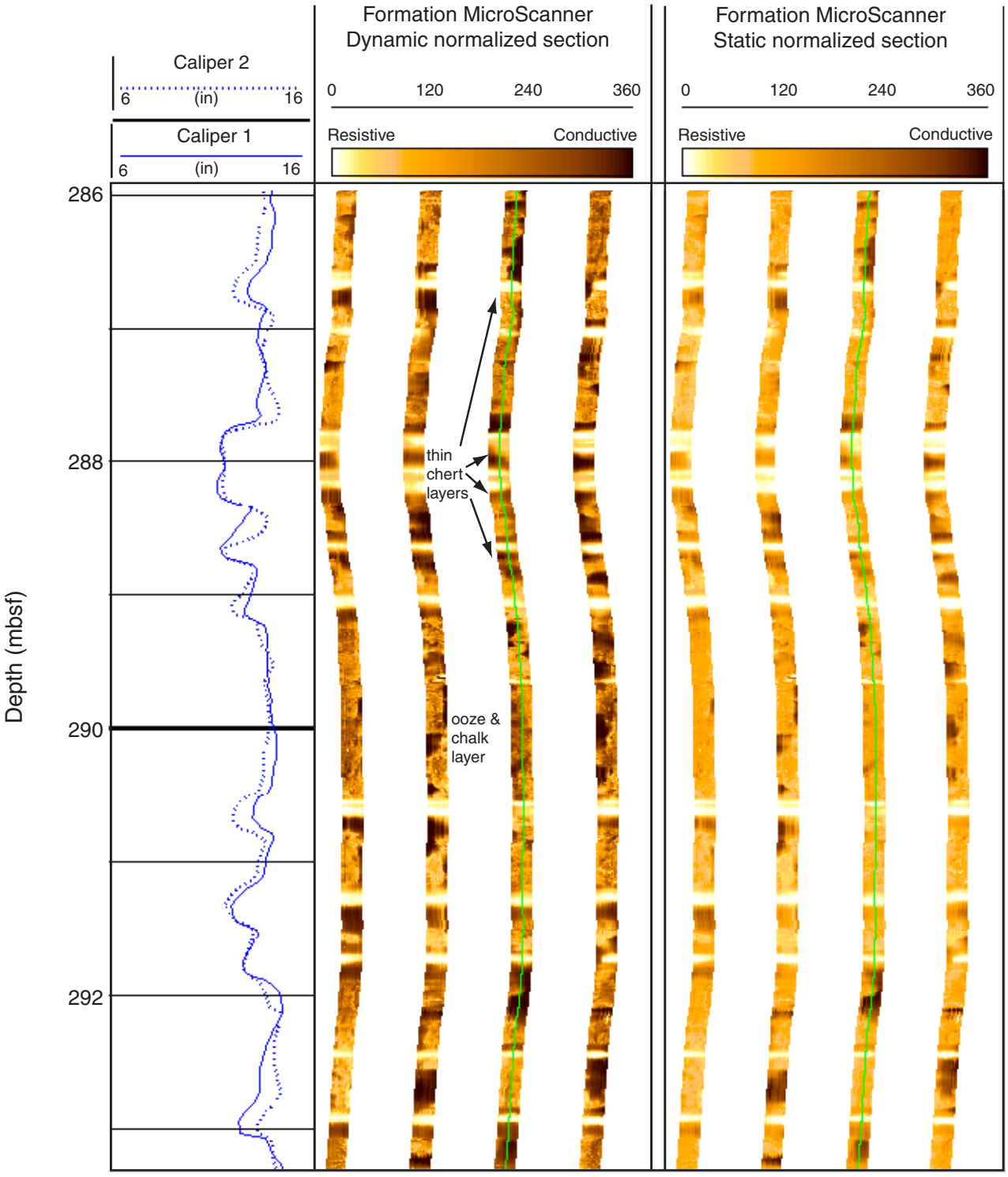

Figure F60. Chert distribution, thickness, and percentage from 200–380 mbsf in Hole 1207B. In the right-hand graph, the thin line is the percentage of chert in an ooze-chert couplet, and the thick line is a 5-point smoothing of the thin line.

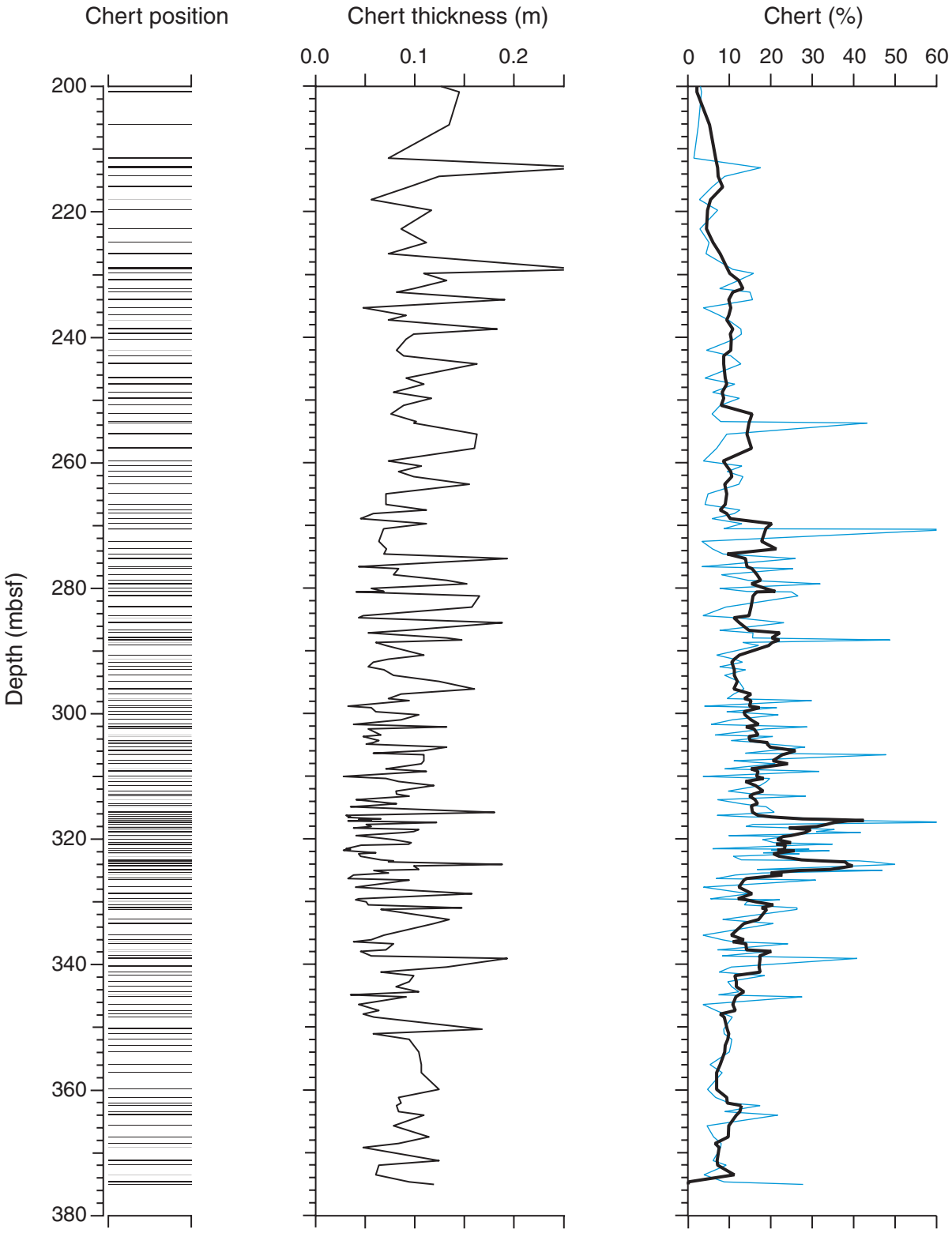

Figure F61. Synthetic seismogram for Hole 1207B. The input velocity and density data, reflection coefficients, and source wavelet are also shown. TWT = two-way traveltime.

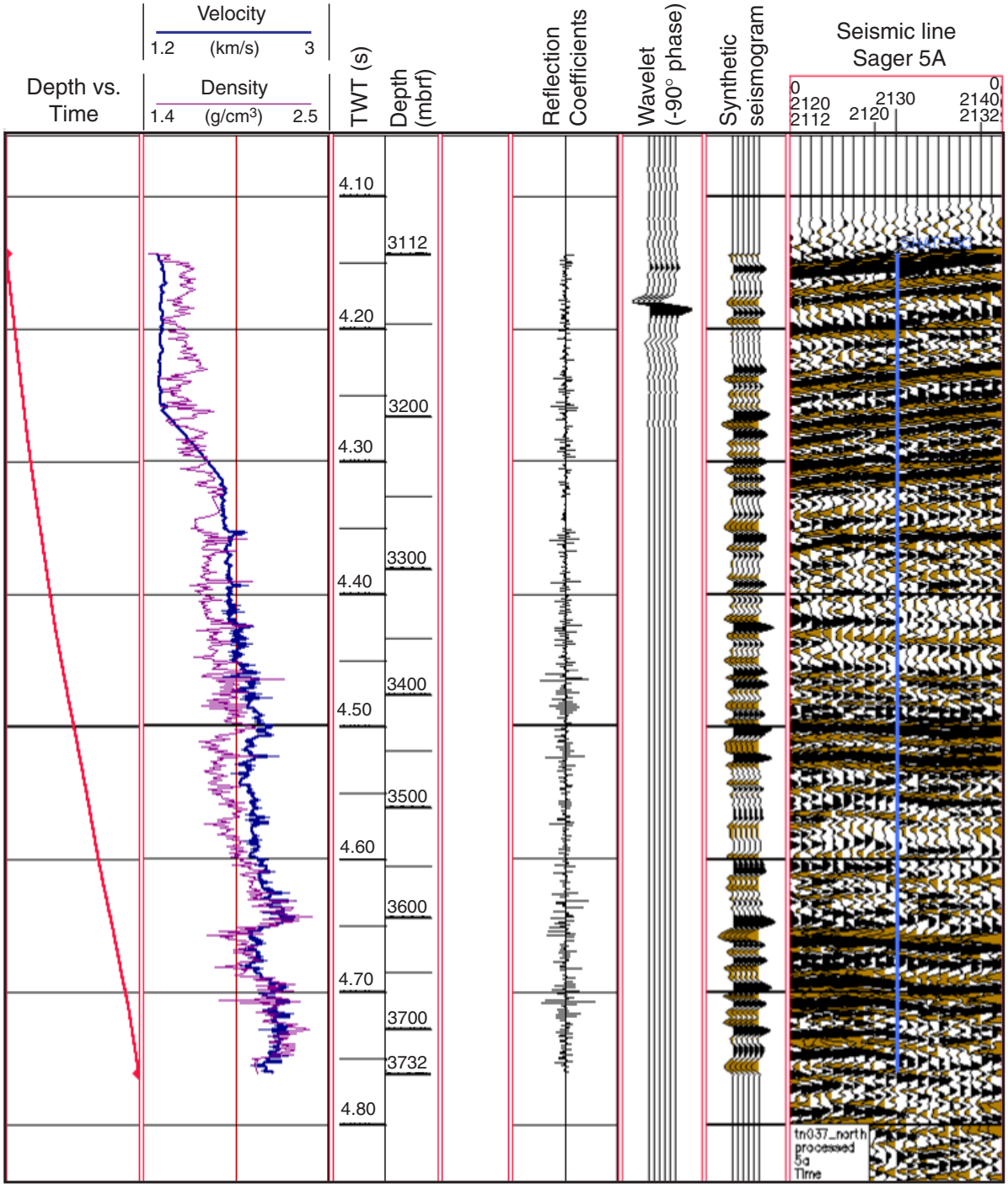

Figure F62. Synthetic seismogram plotted on seismic line Sager 5A. Geological boundaries observed in the core are plotted on the section. Black represents a positive reflection, white a negative reflection. 1207B = Hole 1207B, CDP =common depth point, SP = shotpoint.

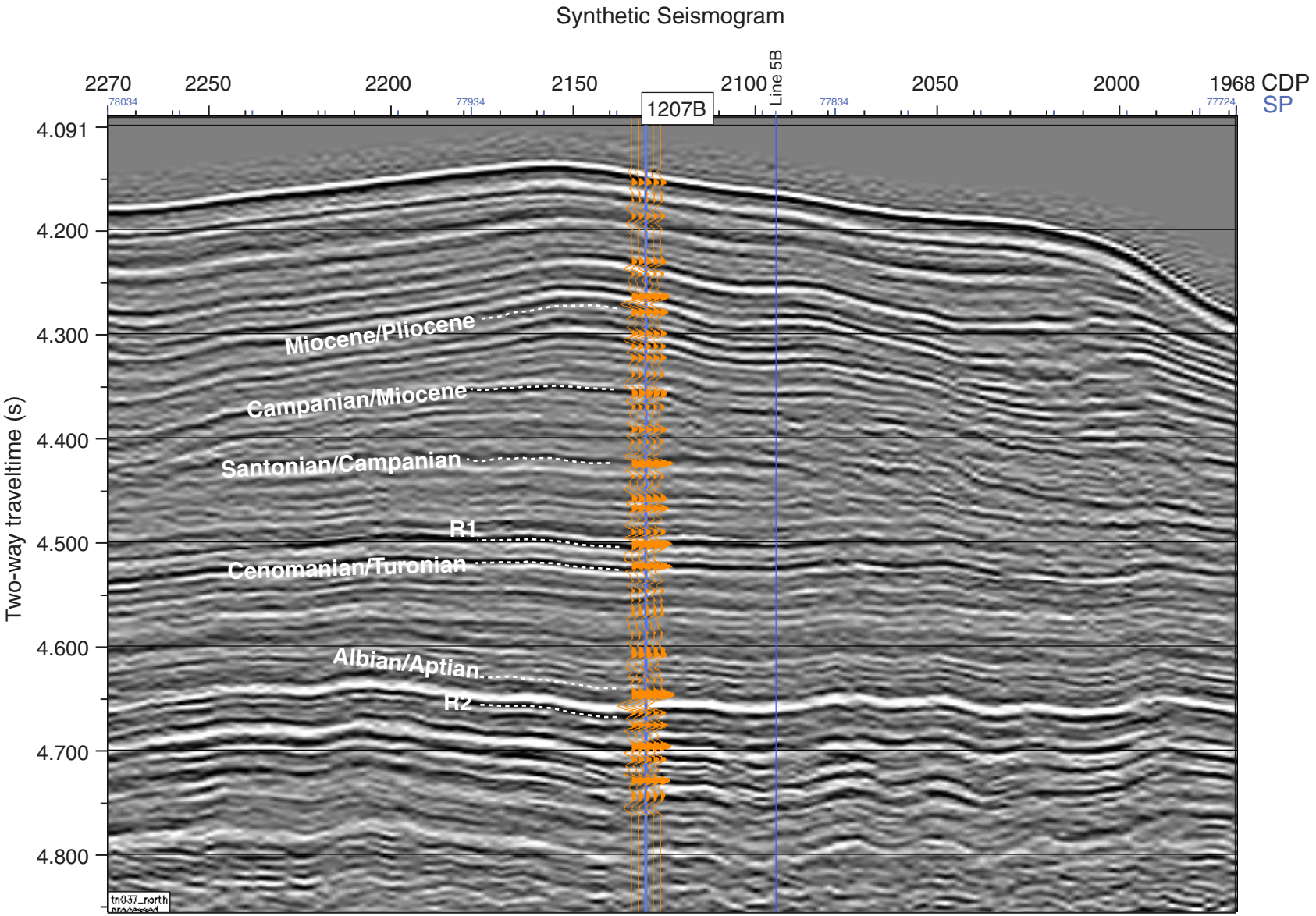

Table T1. Locations, depths, maximum ages, and ages of major unconformities at Shatsky Rise holes.

Site	Latitude	Longitude	Water depth (m)	Total penetration (mbsf)	Maximum age	Major unconformities
47	32°26.898′N	157°42.702′E	2689	129	Maastrichtian	Eocene/Miocene
48	32°24.498′N	158°1.302′E	2619	72	Maastrichtian	Miocene/Maastrichtian
49	32°24.102′N	156°36.000′E	4282	20	Tithonian	Pleistocene/Tithonian
50	32°24.198′N	156°34.302′E	4487	45	Tithonian	Pleistocene/Tithonian
305	32°0.132′N	157°51.000′E	2903	631	Valanginian	Miocene/Oligocene, Paleocene/Eocene
306	31°52.020′N	157°28.710′E	3399	381	Berriasian	Pleistocene/Albian
577	32°26.506′N	157°43.394′E	2675	123	Maastrichtian	Pliocene/Eocene
810	32°25.376′N	157°50.757′E	2634	136	Maastrichtian	Miocene/Eocene, Paleocene/Maastrichtian
1207	37°47.433′N	162°45.053′E	3123	623	Barremian	Miocene/mid-Campanian
1208	36°7.630′N	158°12.095′E	3346	392.3	Albian	late Eocene/early Eocene, late Paleocene/mid-Campanian, lower Campanian/mid-Albian
1209	32°39.102′N	158°30.359′E	2387	307.5	Maastrichtian	early Miocene/early Oligocene
1211	32°0.131′N	157°51.000′E	2907	169.9	Maastrichtian	late Miocene/middle Miocene, middle Miocene/late Oligocene
1212	32°26.903′N	157°42.701′E	2681	207.6	Albian	early Miocene/early middle Eocene, late Campanian/Santonian, late Coniacian/early Cenomanian
1213	31°34.649′N	157°17.861′E	3883	494.4	Berriasian	early Pliocene/Santonian, Coniacian/mid-Cenomanian, late Barremian/late Hauterivian
1214	31°52.025′N	157°28.717′E	3402	235.9	Hauterivian	Pleistocene/late Albian, late Barremian/ late Hauterivian

Table T2. Coring summary, Site 1207. (Continued on next page.)

Hole 1207A
Latitude: 37°47.4287′N
Longitude: 162°45.0530′E
Time on site (hr): 196.25 (1915 hr, 5 Sep–2330 hr, 13 Sep 2001)
Time on hole (hr): 77 (1915 hr, 5 Sep–0015 hr, 9 Sep 2001)
Seafloor (drill pipe measurement from rig floor, mbrf): 3111.7
Distance between rig floor and sea level (m): 11.1
Water depth (drill pipe measurement from sea level, m): 3100.6
Total depth (drill pipe measurement from rig floor, mbrf): 3368.3
Total penetration (mbsf): 256.6
Total length of cored section (m): 223.0
Total core recovered (m): 213.62
Core recovery (%): 95.8
Total number of cores: 29
Total number of drilled intervals: 4

Hole 1207B
Latitude: 37°47.4370′N
Longitude: 162°45.0534′E
Time on hole (hr): 119.25 (0015 hr, 9 Sep–2330 hr, 13 Sep 2001)
Seafloor (drill pipe measurement from rig floor, mbrf): 3111.7
Distance between rig floor and sea level (m): 10.9
Water depth (drill pipe measurement from sea level, m): 3100.8
Total depth (from rig floor, mbrf): 3734.5
Total penetration (mbsf): 622.8
Total length of cored section (m): 465.8
Total core recovered (m): 60.22
Core recovery (%): 12.9
Total number of cores: 49
Total number of drilled intervals: 1

Core	Date (Sep 2001)	Local time (hr)	Depth (mbsf) Top	Depth (mbsf) Bottom	Length (m) Cored	Length (m) Recovered	Recovery (%)
198-1207A-							
1H	6	1250	0.0	4.8	4.8	4.82	100.4
2H	6	1355	4.8	14.3	9.5	9.86	103.8
3H	6	1440	14.3	23.8	9.5	9.91	104.3
4H	6	1550	23.8	33.3	9.5	10.13	106.6
5H	6	1655	33.3	42.8	9.5	9.76	102.7
6H	6	1745	42.8	52.3	9.5	9.91	104.3
7H	6	1850	52.3	61.8	9.5	9.75	102.6
8H	6	2020	61.8	71.3	9.5	9.81	103.3
9H	6	2125	71.3	80.8	9.5	9.87	103.9
10H	6	2220	80.8	90.3	9.5	10.04	105.7
11H	6	2310	90.3	99.8	9.5	9.98	105.1
12H	7	0005	99.8	109.3	9.5	10.01	105.4
13H	7	0105	109.3	118.8	9.5	9.99	105.2
14H	7	0210	118.8	128.3	9.5	9.89	104.1
15H	7	0310	128.3	137.8	9.5	10.02	105.5
16H	7	0410	137.8	147.3	9.5	9.99	105.2
17H	7	0510	147.3	156.8	9.5	9.96	104.8
18H	7	0620	156.8	166.3	9.5	9.84	103.6
19H	7	0720	166.3	172.3	6.0	4.02	67.0
20H	7	0830	172.3	181.8	9.5	9.73	102.4
21X	7	1050	181.8	188.5	6.7	6.74	100.6
22X	7	1245	188.5	188.6	0.1	0.00	0.0
		*****Drilled from 188.6 to 197.9 mbsf*****					
23X	7	1525	197.9	207.6	9.7	9.67	99.7
24X	7	1640	207.6	217.2	9.6	9.51	99.1
25X	7	1830	217.2	219.2	2.0	0.00	0.0
		*****Drilled from 219.2 to 226.9 mbsf*****					
26X	7	2350	226.9	228.9	2.0	0.10	5.0
		*****Drilled from 228.9 to 251.9 mbsf*****					
27X	8	0800	237.3	243.7	6.4	0.08	1.2
		*****Drilled from 243.7 to 237.3 mbsf*****					
28N	8	1410	251.9	256.4	4.5	0.23	5.1
29X	8	1515	256.4	256.6	0.2	0.00	0.0
				Cored totals:	223.0	213.62	95.8
				Drilled total:	33.6		
				Total:	256.6		

Table T2 (continued).

Core	Date (Sep 2001)	Local time (hr)	Depth (mbsf) Top	Depth (mbsf) Bottom	Length (m) Cored	Length (m) Recovered	Recovery (%)
198-1207B-							
		*****Drilled from 0 to 157 mbsf*****					
1R	9	1610	157.0	166.6	9.6	6.55	68.2
2R	9	1655	166.6	176.2	9.6	8.29	86.4
3R	9	1745	176.2	185.8	9.6	3.13	32.6
4R	9	1835	185.8	195.5	9.7	4.92	50.7
5R	9	1920	195.5	205.1	9.6	3.79	39.5
6R	9	2015	205.1	214.7	9.6	5.20	54.2
7R	9	2105	214.7	220.1	5.4	0.00	0.0
8R	9	2155	220.1	229.8	9.7	0.12	1.2
9R	9	2345	229.8	239.4	9.6	1.11	11.6
10R	10	0045	239.4	248.8	9.4	0.05	0.5
11R	10	0145	248.8	258.5	9.7	0.19	2.0
12R	10	0250	258.5	268.1	9.6	0.15	1.6
13R	10	0400	268.1	277.8	9.7	0.17	1.8
14R	10	0515	277.8	287.4	9.6	0.21	2.2
15R	10	0615	287.4	296.7	9.3	0.26	2.8
16R	10	0710	296.7	306.3	9.6	0.26	2.7
17R	10	0815	306.3	316.0	9.7	0.20	2.1
18R	10	0910	316.0	325.6	9.6	0.39	4.1
19R	10	1000	325.6	335.3	9.7	0.17	1.8
20R	10	1125	335.3	344.9	9.6	0.21	2.2
21R	10	1235	344.9	354.5	9.6	0.20	2.1
22R	10	1340	354.5	364.1	9.6	0.05	0.5
23R	10	1440	364.1	373.7	9.6	0.18	1.9
24R	10	1610	373.7	383.3	9.6	0.23	2.4
25R	10	1727	383.3	392.9	9.6	0.34	3.5
26R	10	1900	392.9	402.5	9.6	0.16	1.7
27R	10	2010	402.5	412.1	9.6	0.13	1.4
28R	10	2125	412.1	421.7	9.6	5.29	55.1
29R	10	2240	421.7	431.3	9.6	0.43	4.5
30R	11	0005	431.3	440.5	9.2	0.20	2.2
31R	11	0110	440.5	450.1	9.6	0.28	2.9
32R	11	0215	450.1	459.3	9.2	0.23	2.5
33R	11	0320	459.3	469.0	9.7	1.04	10.7
34R	11	0445	469.0	478.6	9.6	0.50	5.2
35R	11	0620	478.6	488.2	9.6	0.28	2.9
36R	11	0730	488.2	497.8	9.6	0.17	1.8
37R	11	0845	497.8	507.5	9.7	0.90	9.3
38R	11	1002	507.5	517.1	9.6	0.27	2.8
39R	11	1110	517.1	526.5	9.4	0.22	2.3
40R	11	1245	526.5	536.2	9.7	0.35	3.6
41R	11	1430	536.2	545.8	9.6	0.06	0.6
42R	11	1635	545.8	555.4	9.6	0.52	5.4
43R	11	1755	555.4	565.0	9.6	1.63	17.0
44R	11	1945	565.0	574.6	9.6	2.18	22.7
45R	11	2135	574.6	584.2	9.6	0.50	5.2
46R	11	2355	584.2	593.8	9.6	1.80	18.7
47R	12	0155	593.8	603.5	9.7	3.74	38.6
48R	12	0340	603.5	613.2	9.7	1.23	12.7
49R	12	0525	613.2	622.8	9.6	1.74	18.1
				Cored totals:	465.8	60.22	12.9
				Drilled total:	157.0		
				Total:	622.8		

Table T3. Downhole variation in colors of recovered chert, Hole 1207B.

Core	Depth (mbsf) Top	Depth (mbsf) Bottom	Recovery (m)
198-1207B-			
1R	157.00	166.60	6.55
2R	166.60	176.20	8.29
3R	176.20	185.80	3.13
4R	185.80	195.50	4.92
5R	195.50	205.10	3.79
6R	205.10	214.70	5.20
7R	214.70	220.10	0.00
8R	220.10	229.80	0.12
9R	229.80	239.40	1.11
10R	239.40	248.80	0.05
11R	248.80	258.50	0.19
12R	258.50	268.10	0.15
13R	268.10	277.80	0.17
14R	277.80	287.40	0.21
15R	287.40	296.70	0.26
16R	296.70	306.30	0.26
17R	306.30	316.00	0.20
18R	316.00	325.60	0.39
19R	325.60	335.30	0.17
20R	335.30	344.90	0.21
21R	344.90	354.50	0.20
22R	354.50	364.10	0.05
23R	364.10	373.70	0.18
24R	373.70	383.30	0.23
25R	383.30	392.90	0.34
26R	392.90	402.50	0.16
27R	402.50	412.10	0.13
28R	412.10	421.70	5.29
29R	421.70	431.30	0.43
30R	431.30	440.50	0.20
31R	440.50	450.10	0.28
32R	450.10	459.30	0.23
33R	459.30	469.00	1.04
34R	469.00	478.60	0.50
35R	478.60	488.20	0.28
36R	488.20	497.80	0.17
37R	497.80	507.50	0.90
38R	507.50	517.10	0.27
39R	517.10	526.50	0.22
40R	526.50	536.20	0.35
41R	536.20	545.80	0.06
42R	545.80	555.40	0.52
43R	555.40	565.00	1.63
44R	565.00	574.60	2.18
45R	574.60	584.20	0.50
46R	584.20	593.80	1.80
47R	593.80	603.50	3.74
48R	603.50	613.20	1.23
49R	613.20	622.80	1.74

Table T4. Results of XRD analyses on sediments, Hole 1207A.

Core, section, interval (cm)	Primary mineral	Secondary mineral
198-1207A-		
2H-3, 100–101	Calcite	Qz
3H-1, 96–97	Calcite	Qz, illite, kaolinite/chlorite
4H-4, 69–70	Calcite	Qz
4H-6, 14–15	Calcite	Qz, illite, kaolinite/chlorite
6H-3, 60–61	Calcite	Qz, illite, kaolinite/chlorite
6H-4, 103–104	Calcite	Qz
8H-3, 117–118	Calcite	Pyrite, qz, (halite, hornblende)
9H-2, 53–54	Calcite	Qz, halite
13H-4, 41–42	Calcite	Qz, halite
18H-5, 46–47	Calcite	Qz, illite, kaolinite/chlorite, manganite, (halite)
18H-5, 51–52	Calcite	Qz, phillipsite, kaolinite/chlorite, pyrite, (halite)
18H-CC, 14–15	Calcite	Qz, phillipsite, manganite
21X-5, 9–10	Calcite	—

Notes: All identifiable materials listed. Qz = quartz. — = not identified.

Table T5. Calcareous nannofossil datums, ages, and depths, Site 1207.

Datum	Zone/Subzone (base)	Core, section, interval (cm) Top	Core, section, interval (cm) Bottom	Depth (mbsf) Top	Depth (mbsf) Bottom	Depth (mbsf) Mean	Age (Ma)
		198-1207A-	198-1207A-				
FO *Emiliania huxleyi*	CN15	1H-CC	2H-1, 45–46	4.72	5.25	5.0	0.26
LO *Pseudoemiliania lacunosa*	CN14b	2H-1, 45–46	2H-2, 45–46	5.25	6.75	6.0	0.46
FO *Reticulofenestra asanoi*		2H-CC	3H-2, 45–46	14.61	16.26	15.4	1.16
LO *Discoaster brouweri*	CN13a/NN19	4H-3, 45–46	4H-4, 45–46	27.25	28.75	28.0	1.95
LO *Discoaster pentaradiatus*	CN12d/NN18	5H-4, 45–46	5H-CC	38.25	42.85	40.6	2.52
LO *Discoaster surculus*	CN12c/NN17	5H-4, 45–46	5H-CC	38.25	42.85	40.6	2.63
LO *Discoaster tamalis*	CN12b	6H-4, 45–46	6H-CC	47.75	52.55	50.2	2.78
LO *Reticulofenestra pseudoumbilicus*	CN12a/NN16	7H-1, 45–46	7H-CC	52.75	62.00	57.4	3.82
LO *Amaurolithus* spp.	CN11	11H-CC	12H-5, 45–46	100.05	106.25	103.2	4.56
FO *Ceratolithus rugosus*	CN10c/NN13	10H-CC	11H-CC	90.62	100.05	95.3	5.089
LO *Discoaster quinqueramus*	CN10a/NN12	10H-CC	11H-CC	90.62	100.05	95.3	5.537
FO *Amaurolithus* spp.	CN9b	14H-CC	15H-1, 147–148	128.64	129.75	129.2	7.392
FO *Discoaster berggrenii*	CN9a/NN11a	14H-CC	15H-1, 147–148	128.64	129.75	129.2	8.281
LO *Discoaster hamatus*	CN8a/NN10	16H-7, 45–46	16H-CC	147.25	147.74	147.5	9.635
LO *Catinaster calyculus*		16H-7, 45–46	16H-CC	147.25	147.74	147.5	9.641
LO *Catinaster coalitus*		16H-1, 45–46	16H-4, 45–46	138.25	142.75	140.5	9.694
FO *Catinaster calyculus*		16H-7, 45–46	16H-CC	147.25	147.74	147.5	10.705
FO *Catinaster coalitus*	CN6/NN8	17H-1, 45–46	17H-2, 45–46	147.75	149.26	148.5	10.794
LO *Coccolithus miopelagicus*		17H-2, 45–46	17H-3, 45–46	149.26	150.75	150.0	10.941
LO *Sphenolithus heteromorphus*	CN5a/NN6	18H-3, 45–46	18H-4, 45–46	160.25	161.75	161.0	13.523
Acme *Discoaster deflandrei*		18H-4, 45–46	18H-5, 20–21	161.75	163.00	162.4	16.2
LO *Uniplanarius trifidum*		18H-5, 43–44	18H-5, 56–57	163.23	163.36	163.3	71.3
LO *Aspidolithus parcus constrictus*	UC17	18H-5, 43–44	18H-5, 48–49	163.23	163.36	163.3	74.6
LO *Eiffellithus eximius*	CC23/UC16	20H-CC	21X-CC	181.93	188.54	185.2	75.3
FO *Uniplanarius trifidum*	CC22	19H-CC	20H-CC	170.27	181.93	176.1	76.0
FO *Uniplanarius sissinghii*	CC21	20H-CC	21X-CC	181.93	188.54	185.2	77.0
FO *Ceratolithoides aculeus*	CC20	23X-CC	24X-CC	207.52	217.06	212.3	78.5
FO *Ceratolithoides verbeekii*		27X-CC	27X-CC	237.37	237.37	237.4	82.0
		198-1207B-	198-1207B-				
LO *Coccolithus miopelagicus*		1R-CC	1R-CC	163.50	163.50	163.5	10.941
LO *Uniplanarius trifidum*		2R-3, 0–1	2R-3, 0–1	169.60	169.60	169.6	71.3
LO *Aspidolithus parcus*	UC17	1R-CC	2R-3, 0–1	163.50	169.60	166.6	74.6
LO *Eiffellithus eximius*	CC23/UC16	2R-3, 0–1	2R-CC	169.60	174.84	172.2	75.3
FO *Uniplanarius sissinghii*	CC21	2R-CC	3R-CC	174.84	179.28	177.1	77.0
FO *Ceratolithoides aculeus*	CC20	5R-CC	6R-CC	199.24	210.25	204.7	78.5
FO *Ceratolithoides verbeekii*		8R-CC	9R-CC	221.36	230.86	226.1	82.0
FO *Aspidolithus parcus constrictus*		9R-CC	10R-CC	230.86	239.45	235.2	82.5
FO *Aspidolithus parcus*	CC18/UC14	9R-CC	10R-CC	230.86	239.45	235.2	83.4
FO *Micula decussata*	CC14/UC10	15R-CC	16R-CC	287.40	296.96	292.2	87.2
FO *Lithastrinus septenarius*	UC9	16R-CC	17R-CC	296.96	306.50	301.7	88.8
FO *Eiffellithus eximius*	CC12/UC8	19R-CC	20R-CC	325.77	335.51	330.6	91.0
FO *Quadrum gartneri*	CC11/UC7	20R-CC	21R-CC	335.51	344.90	340.2	93.2
LO *Helenea chiastia*	UC6	21R-CC	22R-CC	344.90	354.50	349.7	93.4
LO *Lithraphidites acutus*	UC5	20R-CC	21R-CC	335.51	344.90	340.2	94.0
FO *Lithraphidites acutus*	CC10/UC3	23R-CC	24R-CC	364.27	373.92	369.1	96.8
FO *Eiffellithus turriseiffelii*	NC10a	28R-CC	29R-CC	417.34	422.12	419.7	101.7
FO *Eiffellithus monechiae*	NC9b	29R-CC	30R-CC	422.12	431.49	426.8	105.0
FO *Axopodorhabus albianus*	NC9a	29R-CC	30R-CC	422.12	431.49	426.8	106.1
FO *Tranolithus orionatus*	NC8c	31R-CC	32R-CC	440.78	450.33	445.6	107.3
FO *Prediscosphaera columnata*	NC8a	36R-CC	37R-CC	488.37	498.70	493.5	112.6
FO *Rhagodiscus achlyostaurion*	NC7c	38R-CC	39R-CC	507.77	517.27	512.5	115.2
FO *Eprolithus floralis*	NC7a	43R-CC	44R-CC	557.02	566.90	562.0	119.0
FO *Hayesites irregularis*	NC6a	44R-CC	45R-CC	566.90	574.89	570.9	121.1

Notes: FO = first occurrence, LO = last occurrence. These data are presented in age vs. depth plots (see **"Sedimentation and Accumulation Rates,"** p. 26, and Figs. **F31,** p. 84, **F32,** p. 85, and **F33,** p. 86).

Table T6. Planktonic foraminiferal datums, ages, and depths, Site 1207.

Datum	Zone (base)	Core, section, interval (cm) Top	Core, section, interval (cm) Bottom	Depth (mbsf) Top	Depth (mbsf) Bottom	Depth (mbsf) Mean	Age (Ma)
		198-1207A-	198-1207A-				
FO *Truncorotalia truncatulinoides*	N22	4H-CC, 11–16	5-1, 80–82	33.79	34.10	33.95	1.92
FO *Truncorotalia tosaensis*	N21	8H-1, 77–79	8H-4, 77–79	62.57	67.07	64.82	3.35
LO *Sphaeroidinellopsis seminulina*		8H-CC, 8–13	9H-1, 77–79	71.48	72.07	71.78	3.11
LO *Globoturborotalita nepenthes*		10H-1, 78–80	10H-CC, 3–8	81.58	90.62	86.10	4.39
FO *Globorotalia tumida*	N18	12H-4, 78–80	12H-CC, 17–22	105.08	109.73	107.41	5.82
FO *Globorotalia margaritae*		13H-1, 78–80	13H-4, 78–80	110.08	114.58	112.33	6.09
FO *Neogloboquadrina acostaensis*	N16	16H-1, 77–79	16H-4, 78–80	138.57	143.08	140.83	9.82
LO *Paragloborotalia mayeri*	N15	18H-1, 79–81	18H-4, 78–80	157.59	162.08	159.84	10.49
FO *Globoturborotalita nepenthes*	N14	17H-1, 77–79	17H-4, 77–79	148.07	152.57	150.32	11.19
FO *Fohsella praefohsi*	N11	17H-CC, 20–25	18H-1, 79–81	157.21	157.59	157.40	14.0
FO *Orbulina universa*	N9	18H-4, 78–80	18H-CC, 12–17	162.08	166.59	164.34	15.1
LO *Globotruncanita atlantica*		19H-CC, 0–5	20H-CC, 8–18	170.27	181.93	176.10	75.8
FO *Globotruncanita atlantica*		23X-CC, 19–24	24X-CC, 23–28	207.52	217.06	212.56	79.5
FO *Globotruncanita elevata*		24X-CC, 23–28	27X-CC, 7–8	217.06	237.37	227.49	84.8
		198-1207B-	198-1207B-				
FO *Orbulina* spp.	N9	1R-CC, 17–19	2R-CC, 8–13	163.50	174.84	169.17	15.1
LO *Globotruncanita atlantica*		3R-CC, 11–16	4R-CC, 8–13	179.28	190.67	184.98	75.8
FO *Globotruncanita atlantica*		9R-CC, 16–21	10R-CC, 4.5–5	230.86	239.45	235.16	79.5
FO *Hedbergella holmdelensis*		18R-CC, 37–39	19R-CC, 16.5–17	316.37	325.77	321.07	89.0
FO *Rotalipora appenninica*	KS16	24R-CC, 22–23	25R-CC, 33–34	373.92	383.63	378.78	100.4
FO *Biticinella breggiensis*	KS14	28R-CC, 11–16	29R-CC, 42–43	417.34	422.12	419.73	105.0
FO *Ticinella primula*	KS13	33R-1, 103–104	34R-CC, 49.5–50	460.33	469.50	464.92	109.5
FO *Globigerinelloides barri*		40R-CC, 15–17	41R-CC, 5–6	526.65	536.25	531.45	117.1
FO *Globigerinelloides blowi*	KS6	43R-CC, 20–21	44R-2, 47–48	557.02	566.90	561.96	124.0
FO Clavihedbergellids		47R-3, 79–81	48R-1, 131–133	597.38	604.81	601.10	124.9

Notes: FO = first occurrence, LO = last occurrence. These data are presented in age vs. depth plots (see **"Sedimentation and Accumulation Rates,"** p. 26, and Figs. **F31,** p. 84, **F32,** p. 85, and **F33,** p. 86).

Table T7. Distribution of Cretaceous planktonic foraminifers in indurated lithologies identified in thin section, Site 1207.

Core, section, interval (cm)	Depth (mbsf)	Planktonic foraminifers	*Hedbergella* cf. *aptica*	*Globigerinelloides* sp.	*Leupoldina* sp.	*Hedbergella delrioensis*	*Hedbergella trocoidea*	*Globigerinelloides ferreolensis*	*Globigerinelloides aptiense*	*Gubkinella graysonensis*	*Planomalina cheniourensis*	*Ticinella bejaouaensis*	*Globigerinelloides barri*	*Hedbergella* sp.	*Hedbergella gorbachikae*	*Ticinella primula*	*Hedbergella planispira*	*Heterohelix* sp.	*Archaeoglobigerina cretacea*	*Whiteinella* sp.	*Whiteinella aprica*	*Whiteinella baltica*	*Heterohelix reussi*	*Globigerinelloides bollii*	*Globigerinelloides ultramicrus*	*Hedbergella flandrini*	*Marginotruncana tarfayaensis*	*Marginotruncana coronata*	*Marginotruncana sigali* gr.	*Dicarinella concavata*	*Pseudotextularia nuttalli*	*Archaeoglobigerina blowi*	*Dicarinella primitiva*	*Marginotruncana pseudolinneiana*	*Marginotruncana marginata*	*Marginotruncana renzi*
198-1207A-																																				
24X-5, 4–5	213.64	R																																		
26X-CC, 5–7	226.95	x																x																		
28N-1, 0–3	251.90	?																																		
28N-1, 3–4	251.93	F/C																x	x					x				F						x	x	
198-1207B-																																				
8R-CC, 3–5	220.13	R																																		
8R-CC, 9–12	220.19	F																	x																	
10R-CC, 1–3	239.41	C																	x														x			
12R-CC, 3–5	258.53	Abs																																		
12R-CC, 12–14	258.62	F/C																	x														x			
13R-CC, 4–7	268.14	C																F	x				x	R				x								
14R-CC, 1–3	277.81	Abs																																		
14R-CC, 15–21	277.95	C/A																R	x									F	x					R		
15R-CC, 12–15	287.52	F																	x					x				R	x	x		x		x		
15R-CC, 20–22	287.60	F/C																C					F					x		x			x	x	x	x
16R-CC, 14–16	296.84	F/C																											R	?	?	x	x				
16R-CC, 22–24	296.92	R												x				x																		
18R-CC, 10–11	316.10	x															x									x										
18R-CC, 14–15	316.14	C/A				x											x			C	x	R	R	x	x	x	x	x								
18R-CC, 21–22	316.21	R		?		x													x	x																
19R-CC, 9–11	325.69	R/F												R				x																		
33R-CC, 80–82	460.10	AA				x									x	A	x																			
37R-CC, 25–27	498.05	F/C					F					F			x																					
37R-CC, 53–55	498.33	C				x	F			x		F	x	F	x																					
37R-CC, 63–66	498.43	C					F				1?	F	cf																							
37R-CC, 68–73	498.48	F/C					C				1?	F																								
42R-CC, 40–41	546.20	F/C				x	R	x	x	x	?																									
46R-1, 96–98	585.16	R/F	x	x	x?																															

Note: x = presence, R = 2–3 specimens, F = 3–5 specimens, C = >5–10 specimens, A = >10 specimens, AA = >50 specimens, AAA = extremely abundant (only radiolarians), Abs = absent, fish = fish bones, ech = echinoid spines, org = organic matter.

Table T8. Distribution of Neogene benthic foraminifers, Site 1207.

Core, section	Depth (mbsf)	Age	Size fraction (µm)	Preservation	Benthic abundance	Bathymetry	Trochospiral and planispiral																		Other calcareous									*Stilostomella*			*Uvigerina*				Miliolids			Agglutinated			
							Oridorsalis umbonatus	*Nonion* spp.	*Pullenia bulloides*	*Anomalinoides globulosus*	*Cibicidoides subhaidingeri*	*Cibicidoides wuellerstorfi*	*Gyroidinoides girardanus*	*Cibicidoides renzi*	*Cibicidoides bradyi*	*Pullenia quinqueloba*	*Melonis pompilioides*	*Cibicidoides cicatricosus*	*Cibicidoides incrassatus*	*Gyroidinoides soldanii*	*Haplophragmoides* spp.	*Cibicidoides* spp.	*Melonis sphaeroides*	*Dentalina* spp.	*Fissurina* spp.	*Pleurostomella* spp.	*Lenticulina* spp.	*Nodosaria* spp.	*Bolivina* spp.	*Bulimina* spp.	*Stainforthia complanata*	*Stilostomella* spp.	*Stilostomella abyssorum*	*Stilostomella subspinosa*	*Uvigerina hispida*	*Uvigerina graciliformis*	*Uvigerina hispidocostata*	*Uvigerina* spp.	*Pyrgo lucernula*	*Pyrgo murrhina*	*Quinqueloculina* sp.	*Karreriella bradyi*	*Eggerella bradyi*	*Gaudryina* spp.	*Vulvulina spinosa*
198-1207A-																																															
1H-CC	4.72	late Pleistocene	>250	G	F	UA	R	R	R			R														R	T			R	R	R					R		C	R	R	R				R	
4H-CC	33.79	early Pleistocene	>250	VG	F	UA	R		T			R				R						T	C	R	T	T		R	T				T			R				F	F	T	T	R			
6H-CC	52.55	late Pliocene	>250	G	R	UA	R	T				C															T	R						F				R	F	T		R	R		
8H-CC	71.48	early Pliocene	>250	G	F	UA	F	R	R	T	T	C	R							R	R	T		R			T										R	F	T	T	R	R		
11H-CC	100.05	early Pliocene	>250	G	R	UA	F		R		R		R					R	R	R	R	T		T	T						R	F	T	R	R	R	R	F	T	R	R			
12H-CC	109.73	late Miocene	>250	M	R	UA	F	R	R		R		R			T						T		T	T	T							R	T			R	F		R	F	R		
15H-CC	138.27	late Miocene	>250	M	F	UA	F					T			R		R					R		R	R	T					T	C					T				R			
17H-CC	157.21	middle Miocene	>250	G	F	UA	R	R	R	F	F	F	R	R	T	T						R		R	R								F							R	T		R	
198-1207B-																																														
1R-CC	163.50	middle Miocene	>250	M	F	UA	T	T	F	F	T	T										T		T	T						T	F	F								T				

Notes: Preservation: VG = very good, G = good, M = moderate. Abundance: C = common, F = few, R = rare, T = trace. Bathymetry: UA = upper abyssal.

Table T9. Distribution of Cretaceous benthic foraminifers, Site 1207.

Core, section, interval (cm)	Depth (mbsf)	Nannofossil zone/ subzone	Size fraction (µm)	Preservation	Benthic abundance	Trochospiral															Other calcareous																		Agglutinated									
						Gyroidinoides infracretaceus	*Serovaina lobulata*	*Protosangularia cenomaniana*	*Protosangularia albiana*	*Hanzawaia ammophila*	*Protosangularia* sp.	*Gyroidinoides globosus*	*Gavelinella* sp.	*Osangularia plummerae*	*Nuttallides truempyi*	*Conorbinoides hillebrandti*	*Oridorsalis umbonatus*	*Nuttallinella michelinianus*	*Gyroidinoides* spp.	*Gyroidinoides quadratus*	*Pyrulina* spp.	*Oolina* spp.	*Lenticulina* spp.	*Dentalina* spp.	*Lagena* spp.	*Astacolus* spp.	*Nodosaria* spp.	*Fissurina* spp.	*Praebulimina reussi*	*Guttulina* sp.	*Pyramidina* sp.	*Saracenaria* spp.	*Ellipsodimorphina* spp.	*Buliminella carseyae*	*Aragonia velascoensis*	*Aragonia ouezzanensis*	*Pyramidina szajnochae*	*Pleurostomella* spp.	*Marssonella* sp.	*Gaudryina dividens*	*Dorothia* spp.	*Remesella* sp.	*Pseudoclavulina globulifera*	*Gaudryina pyramidata*	*Spiroplectinella excolata*	*Marssonella oxycona*	*Spiroplectammina spectabilis*	*Bathysiphon brosgeri*
198-1207A-																																																
18H-CC	166.59	UC16	>250	G	F									F	R	R	R			T			R	T											T			T		R				F				
21X-CC	188.54	CC20	>125	G	F							R		F	R	R	R		F	T			R	R							R		R				R							T				
23X-CC	207.52	CC20	>125	M	F	T						R		T	R	R	F		F				R	R					R		R		R	R	R	R								R			T	
198-1207B-																																																
2R-CC	174.84	CC21	>125	G	F	T								F		F	C			R			R	R			R									R				F			T			F		
3R-CC	179.28	CC20	>125	G	R									T	R	R	F			F																		R						C		R		T
5R-CC	199.24	CC20	>125	M	R									F	F		F		T					T					T					T	R												T	T
6R-CC	210.25	CC18	>125	G	F							R		F	R	R	C	R				R	T	R							T			T	R											T		
9R-CC	230.86	CC18/UC4	>125	M	T					T				C	R	R						T		T									R													R		
22R-CC	354.50	UC1	>125	M	R	R	R	F	R	R		R	R									T	T	R			R					R											R		F	R		
24R-CC	373.92	NC10a	>125	P	F	R	R	F	F	T		R	R										R	R			T		R	T	T	R								T			R	R	R			
28R-CC	417.34	NC10a	>125	M	F	R	R	R		R	F	F											R		T	R	T		T	R	T									R	R	R	R	T				
30R-CC	431.49	NC8c	>125	M	F	F	R	R	F	T	R												R	R	T			R												R	R	R						
33R-1, 103–104	460.33	NC7c	>125	P	F	F	T	R	F	T											T		R	F				R	R											F	R	R	F					
40R-CC	526.55	NC7a	>125																																													
42R-CC	545.93	NC7b	>125																																													
43R-CC	557.02	NC7a	>125	P	A	R															R	R	F	C	R	R	R													F	T							
46R-2, 37–39	586.07		>125																																													
47R-3, 79–81	597.38	NC5d–e	>125	M	F																T	R	C	R															A									
49R-2, 24–26	614.94		>125																																													

Notes: Preservation: VG = very good, G = good, M = moderate, P = poor. Abundance: A = abundant, C = common, F = few, R = rare, T = trace.

Table T10. Concentrations of CH_4 in headspace gas, Site 1207.

Core, section, interval (cm)	Depth (mbsf)	CH_4 (ppmv)
198-1207A-		
1H-1, 0–5	0.00	2.0
2H-5, 0–5	10.80	2.1
3H-5, 0–5	20.30	2.4
4H-5, 0–5	29.80	2.4
5H-5, 0–5	39.30	2.5
6H-5, 0–5	48.80	3.0
7H-5, 0–5	58.30	2.3
8H-5, 0–5	67.80	2.8
9H-5, 0–5	77.30	2.9
10H-5, 0–5	86.80	2.4
11H-5, 0–5	96.30	2.4
12H-5, 0–5	105.80	2.3
13H-5, 0–5	115.30	2.3
14H-5, 0–5	124.80	2.2
15H-5, 0–5	134.30	2.6
16H-5, 0–5	143.80	2.1
17H-5, 0–5	153.30	2.2
18H-5, 0–5	162.80	2.0
19H-2, 0–5	167.80	1.9
20H-5, 0–5	178.30	1.8
21X-4, 0–5	186.30	1.8
23X-5, 0–5	203.90	2.0
24X-5, 0–5	213.60	2.0
198-1207B-		
6R-3, 0–5	208.10	1.8
28R-3, 0–5	415.10	4.5

Table T11. Carbonate content, Site 1207.

Core, section, interval (cm)	Depth (mbsf)	Total carbon (wt%)	$CaCO_3$ (wt%)
198-1207A-			
2H-2, 65–66	6.95	8.4	69.6
2H-5, 33–34	11.13	5.9	49.3
3H-1, 66–67	14.96	9.1	76.0
3H-2, 126–127	17.06	6.7	55.5
3H-4, 70–71	19.50	5.6	47.0
4H-4, 70–71	29.00	9.4	78.0
4H-6, 13–14	31.43	6.5	54.0
5H-1, 72–73	34.02	6.0	50.0
5H-3, 72–73	37.02	8.5	71.0
5H-5, 72–73	40.02	8.7	72.8
6H-1, 68–69	43.48	8.7	72.6
6H-3, 68–69	46.48	4.9	41.1
6H-5, 68–69	49.48	9.3	77.2
7H-1, 8–9	52.38	6.7	55.6
7H-3, 73–74	56.03	9.0	75.3
7H-5, 31–32	58.61	7.4	61.3
8H-2, 95–96	64.25	9.5	79.0
8H-4, 37–38	66.67	6.3	52.4
8H-5, 94–95	68.74	1.9	16.2
9H-1, 48–49	71.78	8.2	68.3
9H-1, 83–84	72.13	9.6	79.8
9H-3, 73–74	75.03	8.5	70.5
10H-1, 16–17	80.96	5.3	44.2
10H-1, 72–73	81.52	8.7	72.3
10H-2, 35–36	82.65	10.2	84.6
11H-3, 23–24	93.53	5.6	46.4
11H-5, 71–72	97.01	9.2	76.7
11H-5, 98–99	97.28	10.0	83.1
12H-1, 93–94	100.73	9.4	78.6
12H-6, 28–29	107.58	3.8	31.7
13H-2, 30–31	111.10	4.4	36.3
13H-4, 44–45	114.24	6.3	52.4
13H-6, 72–73	117.52	8.1	67.7
14H-1, 37–38	119.17	9.2	77.0
14H-1, 107–108	119.87	5.6	46.9
14H-4, 67–68	123.97	9.5	79.5
15H-1, 110–111	129.40	8.2	68.6
15H-4, 72–73	133.52	10.5	87.3
15H-6, 30–31	136.10	8.6	71.2
16H-1, 119–120	138.99	10.4	86.4
16H-2, 23–24	139.53	8.7	72.4
16H-4, 68–69	142.98	9.0	75.2
17H-1, 85–86	148.15	10.3	85.8
17H-2, 95–96	149.75	8.9	74.0
17H-2, 124–125	150.04	9.6	79.6
18H-1, 137–138	158.17	11.1	92.5
18H-5, 90–91	163.70	7.8	65.0
18H-6, 73–74	165.03	11.5	95.4
21X-2, 86–87	184.16	11.7	97.3
21X-4, 88–89	187.18	11.8	98.2
23X-1, 89–90	198.79	11.7	97.2
23X-4, 89–90	203.29	11.6	97.0
23X-6, 89–90	206.29	11.8	97.9
24X-2, 34–35	209.44	11.7	97.5
24X-4, 87–88	212.97	11.7	97.3
24X-5, 46–47	214.06	11.6	96.7
198-1207B-			
1R-2, 56–57	159.06	11.0	91.3
1R-3, 13–14	160.13	9.6	80.1
1R-5, 63–64	163.63	9.7	80.5
2R-5, 26–27	172.86	11.6	96.4
2R-5, 80–81	173.40	11.6	96.4
3R-2, 50–51	178.20	11.6	96.7
4R-2, 53–54	187.83	11.7	97.4
4R-3, 53–54	189.33	11.6	96.7
5R-2, 74–75	197.74	11.6	96.9
6R-1, 65–66	205.75	11.6	96.6
40R-CC, 30–31	526.80	7.3	60.9
44R-1, 60–61	565.60	0.0	0.0
44R-1, 76–77	565.76	0.0	0.0
44R-1, 103–104	566.03	0.0	0.0
46R-1, 52–53	584.72	7.7	64.2
46R-1, 74–75	584.94	5.9	49.1

Table T12. Results from CNSH analysis of samples from OAE1a, Hole 1207B.

Core, section, interval (cm)	Depth (mbsf)	Organic carbon (wt%)	Nitrogen (wt%)	Sulfur (wt%)	Hydrogen (wt%)	C/N ratio (atomic)
198-1207B-						
44R-1, 60–61	565.60	34.7	1.2	10.6	4.0	25.0
44R-1, 76–77	565.76	10.4	0.4	1.9	1.7	22.3
44R-1, 103–104	566.03	1.7	0.1	1.3	0.6	16.2

Table T13. Organic carbon contents and results from Rock-Eval pyrolysis of Aptian organic-rich horizons in the mid-Pacific.

Core, section, interval (cm)	TOC (wt%)	S_1 (mg/g)	S_2 (mg/g)	S_3 (mg/g)	T_{max} (°C)	PI (S_1/S_2)	HI (mg HC/g TOC)	OI (mg CO_2/g TOC)
Shatsky Rise (Northern High):								
198-1207B-								
44R-1, 60–61	34.7	13.99	147.12	7.64	401	0.09	423	21
44R-1, 76–77	10.4	3.24	54.46	2.69	403	0.06	523	25
44R-1, 103–104	1.7	0.49	7.45	0.94	417	0.06	438	55
Shatsky Rise (Southern High):								
32-305-								
65-1, 100–103	9.3							
Manihiki Plateau:								
31-317A-								
16-2, 126	0.1							
16-2, 131–134	24.9							
16-2, 133	29.6							
16-2, 150	0.7							
Mid-Pacific Mountains:								
62-463-								
70-1, 92	1.7							
70-2, 53–54	1.0				430		210	190
70-2, 68–70	1.2				425		197	118
70-2, 77–78	6.2				417		521	51
70-2, 116	2.1							
70-3, 20–21	2.9				424		393	89
70-3, 21	3.7							
70-3, 30–31	1.9				430		265	105
70-3, 31–32	6.9				419		451	61
70-3, 32	4.4							
70-4, 112	2.3							
70-5, 100–101	2.3				411		294	93
70-5, 101	2.0							
70-5, 106–108	4.2				413		408	101
70-5, 110	4.4							
70-5, 115	3.0							
70-5, 120	5.1							
70-5, 125	4.6							
70-5, 129–130	3.0				416		469	103
70-5, 130	7.5							
70-5, 135	4.8							
70-5, 140	3.9				415		431	80
70-6, 39–42	4.4				429		478	40
70-6, 41	1.7							
70-6, 44–46	2.6				418		243	88
70-CC, 20	1.2							
Mid-Pacific Mountains (Resolution Guyot):								
143-866A-								
85R-3, 47–49	34.5	5.39	50.36		387	0.11	146	53
85R-3, 50–52	3.2	2.29	22.22		398	0.10	686	35
86R-1, 143–145	5.0	1.97	35.83		425	0.05	720	42
86R-2, 111–113	7.4	5.93	58.17		418	0.10	784	36
88R-1, 56–58	3.6	0.84	14.18		413	0.06	390	48
89R-1, 94–95	1.0	0.04	0.96		419	0.04	921	77
89R-1, 96–97	2.3	0.04	1.59		419	0.03	68	69
89R-1, 97–98	14.4	0.39	18.72		422	0.02	130	39
89R-1, 98–99	4.7	0.57	14.97		423	0.04	318	51

Notes: TOC = total organic carbon. S_1 and S_2 = peaks corresponding to free and kerogen-bound HC, respectively generated by Rock-Eval pyrolysis; S_3 = amount of CO_2 released by thermal cracking of kerogen. T_{max} = peak temperature of kerogen breakdown. PI = production index. HI = hydrogen index, HC = hydrocarbon. OI = oxygen index. Data compiled from Bode (1975); Shipboard Scientific Party, Leg 32 (1975); Cameron (1976); Jackson and Schlanger (1976); Dean (1981); Dean et al. (1981); Mélières et al. (1981); Simoneit and Stuermer (1982); Baudin et al. (1995). The TOC value for 31-317A-16-2, 133 cm, is the average of two measurements. The table includes all values for organic-rich intervals (>1.0 wt% TOC) reported in the literature.

Table T14. Dominant biomarkers and compound ratios in samples from OAE1a.

Biomarker feature	198-1207B-44R-1 Upper (60–61 cm)	Middle (76–77 cm)	Lower (103–104 cm)
Dominant components:			
n-alkane	C_{15}	C_{17}	C_{17}
Acyclic isoprenoid	C_{16}	C_{16}	C_{16}
Sterane	$C_{29}5\alpha(H)$	$C_{29}5\alpha(H)$	$C_{29}5\alpha(H)$
Sterene	$C_{29}\ \Delta^4$	$C_{29}\ \Delta^4$	$C_{29}\ \Delta^4$
Hopane	$C_{27}17\beta(H)$	$C_{31}17\beta(H),21\beta(H)$	$C_{31}17\beta(H),21\beta(H)$
Hopene	$C_{30}\ \Delta^{17(21)}$	$C_{30}\ \Delta^{17(21)}$	$C_{30}\ \Delta^{17(21)}$
Compound ratios:			
PR/PH	0.35	0.56	0.77
C_{27}:C_{28}:C_{29} in steroids	33:16:51	33:16:51	41:13:46

Notes: Compound codes are described in Table T16, p. 133. Steroid carbon number ratios are based on the distributions of steranes and Δ^4- and Δ^5-sterenes.

Table T15. Biomarker carbon number ranges and relative abundances in samples from Section 198-1207B-44R-1 and their putative biological source(s) and process of formation with references. (See table notes. Continued on next page.)

Biomarker class components (code)	Range	Relative abundance			Putative biological source(s)/process of formation	References
		Upper	Middle	Lower		
n-Alkyl compounds:						
Lower alkanes with OEP	C_{13}–C_{19}	+++	+++	+++	Algae, bacteria, cyanobacteria	Han et al., 1968; Gelpi et al., 1970; Brassell et al., 1978
Higher alkanes with OEP	C_{23}–C_{33}	ND	+	+	Vascular plants	Eglinton and Hamilton, 1963; Simoneit, 1978
Branched compounds:						
Monomethylalkanes (MA)	C_{14}–C_{21}	ND	+	+++	Bacteria, cyanobacteria	Shiea et al., 1990; Dachs et al., 1998; Köster et al., 1999
Dimethylalkanes (DMA)	C_{17}–C_{19}	ND	ND	+++	Cyanobacteria	Shiea et al., 1990; Kenig et al., 1995; Köster et al., 1999
Branched alkenes (BA)	C_{18}?	ND	ND	++	Cyanobacteria	Philp et al., 1978; Brassell et al., 1978
Acyclic and cyclic isoprenoids:						
TMUD, TMDD, TMTD, TMPD	C_{14}–C_{16}, C_{18}	+++	+++	+++	Photoautotrophs	Didyk et al., 1978; Volkman and Maxwell, 1986
Pristane (PR)	C_{19}	++	+	+	Photoautotrophs	Didyk et al., 1978; Goossens et al., 1984
Phytane (PH)	C_{20}	+++	++	++	Photoautotrophs, methanogens	Didyk et al., 1978; Brassell et al., 1981
C_{20} terpane	C_{20}	+++	++	ND	Bacteria?	Aquino Neto et al., 1982; Ourisson et al., 1987
Steroids:						
5α(H)- and 5β(H)-steranes	C_{27}–C_{29}	+++	+++	+++	Eukaryotes/sterol reduction	Mackenzie et al., 1982; Volkman, 1986
5α(H)- and 5β(H)-steranes	C_{30}	+	+	ND	Marine eukaryotes/sterol reduction	Moldowan et al., 1990
Δ^4- and Δ^5-sterenes	C_{27}–C_{29}	+++	+++	+++	Eukaryotes/sterol dehydration	Mackenzie et al., 1982; Peakman and Maxwell, 1988
Δ^4- and Δ^5-sterenes	C_{30}	+	+	ND	Marine eukaryotes/sterol dehydration	Moldowan et al., 1990; Peakman and Maxwell, 1988
$\Delta^{4,22}$- and $\Delta^{5,22}$-steradienes	C_{29}	ND	ND	+	Eukaryotes/sterol dehydration	Rullkötter et al., 1984; Farrimond et al., 1986
20S, 20R diasterenes	C_{27}–C_{29}	+	+	+	Eukaryotes/sterene rearrangment	Brassell et al., 1984; Peakman and Maxwell, 1988
A-ring monoaromatic	C_{27}–C_{29}	+	++	+	Eukaryotes/sterol aromatization	Hussler et al., 1981; Brassell et al., 1984
B-ring monoaromatic anthra-	C_{27}–C_{29}	+	++	+	Eukaryotes/sterol aromatization	Hussler and Albrecht, 1983; Rullkötter and Welte, 1983
A-nor, B-ring aromatic anthra-	C_{22}	NA	+	NA	Eukaryotes/sterol aromatization	Peakman et al., 1986
Triterpenoids:						
17β(H),21β(H)-hopanes	C_{27}, C_{29}–C_{31}	+++	+++	+++	Prokaryotes	Ourisson et al., 1979, 1987; Rohmer et al., 1992
17α(H),21β(H)-hopanes	C_{27}, C_{29}–C_{31}	++	++	++	Prokaryotes	Ourisson et al., 1979, 1987; Rohmer et al., 1992
17β(H),21β(H)-methylhopanes	C_{34}	++	+	ND	Cyanobacteria, methylotrophs	Ourisson et al., 1987; Summons and Jahnke, 1990
Hopanes ≥ C_{32}	C_{32}, C_{33}	+++	+	+	Bacteria, methylotrophs	Ourisson et al., 1979, 1987; Rohmer et al., 1992
Hop-17(21)-enes	C_{27}, C_{29}–C_{31}	+++	++	++	Bacteria, anaerobic phototrophs	Brassell and Eglinton, 1983; Rohmer et al., 1984
Aromatic hopanoids	C_{24}, C_{27}	NA	++	NA	Bacteria/aromatization	Greiner et al., 1976, 1977
Neohop-13(18)-enes	C_{27}, C_{29}, C_{30}	++	+++	++	Bacteria, anaerobic phototrophs	Brassell and Eglinton, 1983; Howard et al., 1984
Fernenes	C_{30}	+	++	+++	Bacteria, anaerobic phototrophs	Brassell and Eglinton, 1983; Howard et al., 1984
Dammarenes	C_{30}	++	ND	ND	Bacteria?	Meunier-Christmann et al., 1991
Triterpene (dammaradiene?)	C_{30}	ND	++	+++	Bacteria?	Brassell, 1984; Rullkötter et al., 1984
Triterpene (nordammaradiene?)	C_{29}	++	++	+++	Bacteria?	
Ketones:						
Alkan-2-ones	C_{13}–C_{25}	NA	+	NA	Algae, bacteria/oxidation	Brassell et al., 1980
TMTD-2-one	C_{18}	NA	++	NA	Photoautotrophs; oxidation	Simoneit, 1973
5α(H)- and 5β(H)-stanones	C_{27}–C_{29}	NA	++	NA	eukaryotes/sterol oxidation	Gagosian and Smith, 1979; Robinson et al., 1984
Δ^4-stenones	C_{27}–C_{29}	NA	++	NA	Eukaryotes/sterol oxidation	Edmunds et al., 1980; Brassell et al., 1987
Hopanones	C_{27}, C_{29}–C_{31}	NA	++	NA	Bacteria, algae/predation, oxidation	Dastillung et al., 1980
Other biomarkers:						
5-methyl-2-undecylthiophene	C_{20}	NA	+	NA	Sulfurization	Sinninghe-Damsté et al., 1988, 1989

Table T15 (continued).

Biomarker class components (code)	Range	Relative abundance			Putative biological source(s)/process of formation	References
		Upper	Middle	Lower		
Phytenyl thiophenes (PT)	C_{20}	++	++	++	Photoautotrophs; sulfurization	Rullkötter et al., 1984; Brassell et al., 1986
α-, β-, γ-, δ-tocopherols	C_{27}–C_{29}	NA	+++	NA	Photoautotrophs	Brassell et al., 1983; Goossens et al., 1984

Notes: Upper, middle, and lower refer to samples at 60–61 cm, 76–77 cm, and 103–104 cm of Section 198-1207B-44R-1, respectively. OEP = odd/even preference. +, ++, +++ = approximate relative abundances corresponding to major, minor, and trace amounts. ND = not detected. NA = not analyzed. See Table **T16,** p. 133, for definitions of biomarker class components (codes).

Table T16. Identities of biomarker components labeled with codes in Figures F38, p. 91, and F39, p. 92.

Code	Identification
TMUD	2,6,10-trimethyltundecane
TMDD	2,6,10-trimethyldodecane
TMTD	2,6,10-trimethyltridecane
TMPD	2,6,10-trimethylpentadecane
MA	Methylalkanes
DMA	Dimethylalkanes
BA	Branched alkenes
PR	Pristane
PH	Phytane
20TT	$C_{20}H_{36}$ tricyclic terpane
PT	Phytenyl thiophenes
27β S	5β(H)-cholestane
27Δ^4S	Cholest-4-ene
27Δ^5S	Cholest-5-ene
27αS	5α(H)-cholestane
27$\Delta^{13(18)}$NH	22,29,30-trisnorneohop-13(18)-ene
27βH	22,29,30-trisnor-17β(H)-hopane
29$\Delta^{4,22}$S	24-ethylcholesta-4,22-diene
29$\Delta^{5,22}$S	24-ethylcholesta-5,22-diene
29βS	24-ethyl-5β(H)-cholestane
29Δ^4S	24-ethylcholest-4-ene
29Δ^5S	24-ethylcholest-5-ene
29αS	24-ethyl-5α(H)-cholestane
29$\Delta^{17(21)}$H	30-norhop-17(21)-ene
30$\Delta^{17(21)}$H	Hop-17(21)-ene
30αβH	17α(H),21β(H)-hopane
Δ^8F	Fern-8-ene
30$\Delta^{13(18)}$NH	Neohop-13(18)-ene
31$\Delta^{17(21)}$H	22S and 22R homohop-17(21)-ene
31αβH	17α(H),21β(H)-homohopane
32$\Delta^{17(21)}$H	Bishomohop-17(21)-ene
32αβH	17α(H),21β(H)-bishomohopane
33$\Delta^{17(21)}$H	Trishomohop-17(21)-ene
31ββH	17β(H),21β(H)-homohopane
33αβH	17α(H),21β(H)-trishomohopane
32ββH	17β(H),21β(H)-bishomohopane
ME34ββH	17β(H),21β(H)-methylbishomohopane
33ββH	17β(H),21β(H)-trishomohopane
34ββH	17β(H),21β(H)-tetrakishomohopane

Note: Pristane = 2,6,10,14-tetramethylpentadecane; Phytane = 2,6,10,14-tetramethylhexadecane; Phytenyl thiophenes = 2-(2,6,10-trimethylundecyl), 4-methylthiophene, 2-(3,7,11-trimethyldodecyl), 3-methylthiophene, and 3-(4,8,12-trimethyltridecyl)-thiophene.

Table T17. Results of geochemical analyses, Hole 1207A.

Core, section, interval (cm)	Depth (mbsf)	pH	Alkalinity (mM)	Salinity	Cl^- (mM)	SO_4^{2-} (mM)	Na^+ (mM)	Mg^{2+} (mM)	Ca^{2+} (mM)	K^+ (mM)	H_4SiO_4 (μM)	NH_4^+ (μM)	HPO_4^{2-} (μM)	Sr^{2+} (μM)	Fe^{2+} (μM)	Mn^{2+} (μM)	Li^+ (μM)	Ba^{2+} (μM)	H_3BO_3 (μM)
198-1207A-																			
1H-2, 145–150	2.95	7.34	3.09	35.0	558	28.8	477	53.8	11.0	12.2	692	79	5.0	86	35.4	10.1	25	0.3	453
2H-4, 145–150	10.75	7.42	3.45	35.0	547	29.2	469	53.4	10.4	12.1	690	107	3.6	97	9.7	9.2	16	0.6	445
3H-4, 145–150	20.25	7.43	3.73	35.0	556	27.7	473	54.2	10.9	12.2	688	134	1.6	134	22.5	3.6	16	0.3	395
4H-4, 145–150	29.75	7.41	3.89	35.0	560	27.9	476	54.4	11.0	12.2	807	157	1.3	185	21.6	2.1	20	0.3	460
5H-4, 145–150	39.25	7.17	3.98	35.0	563	27.4	478	55.4	10.8	11.6	774	139	2.9	186	7.1	1.4	19	0.5	453
6H-4, 145–150	48.75	7.37	4.07	34.0	562	27.2	475	55.9	10.9	11.7	824	163	1.6	154	6.6	1.1	16	0.4	368
7H-4, 145–150	58.25	7.34	4.21	35.0	566	26.6	479	55.5	10.5	11.7	772	220	1.3	197	19.9	1.3	19	0.3	453
8H-4, 145–150	67.75	7.35	4.23	35.0	560	26.4	471	55.8	10.9	11.9	954	164	1.3	215	28.6	1.5	18	0.3	444
9H-4, 145–150	77.25	7.31	4.31	35.0	563	26.1	485	51.5	10.1	11.4	799	195	1.3	226	7.8	1.2	17	0.2	443
10H-4, 145–150	86.75	7.29	4.28	35.0	562	25.9	481	51.5	10.9	11.7	801	191	1.5	235	22.2	1.0	18	0.3	449
11H-4, 145–150	96.25	7.29	4.32	35.0	560	25.5	478	51.7	11.2	11.5	845	182	1.5	246	1.8	1.1	18	0.7	458
13H-4, 145–150	115.25	7.32	4.09	35.0	560	25.5	478	51.5	11.1	11.9	860	218	0.6	252	18.9	1.1	17	0.2	430
15H-4, 145–150	134.25	7.29	4.37	35.0	559	25.4	476	51.0	12.2	11.4	862	130	0.6	258	6.2	4.8	17	0.3	437
17H-4, 145–150	153.25	7.29	4.21	35.0	564	25.0	482	51.3	11.2	10.9	711	120	0.6	258	5.7	7.8	17	1.7	434
20H-4, 145–150	178.25	7.39	4.06	35.0	556	25.8	472	52.4	11.7	10.7	400	158	0.5	243	0.1	7.9	19	0.5	460
23X-4, 140–150	203.80	7.31	4.18	35.0	563	24.8	480	51.5	11.4	10.4	216	126	0.5	233	13.1	1.2	19	1.2	436

Table T18. Discrete index properties measurements, Site 1207. (Continued on next two pages.)

Core, section, interval (cm)	Depth (mbsf)	Water content (wt%)		Density (g/cm^3)			Porosity (%)	Void ratio
		Bulk mass	Dry mass	Bulk	Dry	Grain		
198-1207A-								
1H-2, 62–64	2.12	49.7	98.8	1.49	0.75	2.70	72.2	2.60
1H-3, 70–72	3.70	61.2	158.0	1.34	0.52	2.65	80.3	4.09
2H-1, 70–72	5.50	46.0	85.1	1.54	0.83	2.70	69.2	2.25
2H-2, 70–72	7.00	44.1	78.9	1.57	0.88	2.70	67.5	2.08
2H-3, 70–72	8.50	46.3	86.2	1.53	0.82	2.69	69.3	2.26
2H-4, 70–72	10.00	48.0	92.3	1.50	0.78	2.65	70.4	2.38
2H-5, 70–72	11.50	48.2	93.2	1.51	0.78	2.68	70.9	2.44
2H-6, 70–72	13.00	47.6	90.7	1.52	0.80	2.70	70.5	2.39
3H-1, 70–72	15.00	48.0	92.2	1.51	0.79	2.69	70.8	2.42
3H-2, 70–72	16.50	45.3	82.7	1.55	0.85	2.68	68.4	2.16
3H-3, 70–72	18.00	48.3	93.4	1.50	0.78	2.67	70.9	2.43
3H-4, 70–72	19.50	50.0	99.8	1.48	0.74	2.66	72.2	2.59
3H-5, 70–72	21.00	49.5	98.0	1.48	0.75	2.62	71.5	2.51
3H-6, 70–72	22.50	49.3	97.1	1.49	0.76	2.66	71.6	2.52
4H-1, 68–70	24.48	53.5	114.9	1.44	0.67	2.67	75.0	3.00
4H-2, 68–70	25.98	50.8	103.2	1.47	0.72	2.65	72.7	2.67
4H-3, 67–69	27.47	52.7	111.4	1.44	0.68	2.66	74.3	2.90
4H-4, 67–69	28.97	48.4	93.9	1.50	0.78	2.68	71.1	2.46
4H-5, 71–73	30.51	49.1	96.4	1.49	0.76	2.66	71.5	2.50
4H-6, 71–73	32.01	51.3	105.4	1.46	0.71	2.66	73.2	2.74
4H-7, 70–72	33.50	42.9	75.3	1.58	0.90	2.66	66.2	1.96
5H-1, 70–72	34.00	58.9	143.1	1.37	0.57	2.68	78.9	3.74
5H-2, 70–72	35.50	57.1	133.2	1.38	0.59	2.60	77.2	3.38
5H-3, 70–72	37.00	48.6	94.7	1.49	0.77	2.64	70.9	2.44
5H-4, 70–72	38.50	54.4	119.1	1.43	0.65	2.67	75.7	3.11
5H-5, 70–72	40.00	48.4	93.7	1.50	0.78	2.68	71.0	2.45
5H-6, 70–72	41.50	45.4	83.2	1.55	0.85	2.71	68.8	2.20
6H-1, 70–72	43.50	46.5	87.0	1.53	0.82	2.66	69.3	2.26
6H-2, 70–72	45.00	49.0	96.0	1.48	0.76	2.58	70.8	2.42
6H-3, 70–72	46.50	57.8	137.1	1.38	0.58	2.64	77.9	3.53
6H-4, 70–72	48.00	47.4	90.0	1.52	0.80	2.72	70.5	2.39
6H-5, 70–72	49.50	48.1	92.8	1.51	0.78	2.69	70.9	2.44
6H-6, 70–72	51.00	51.0	104.1	1.47	0.72	2.69	73.2	2.73
7H-1, 70–72	53.00	47.4	90.1	1.52	0.80	2.69	70.3	2.37
7H-2, 70–72	54.50	46.3	86.1	1.54	0.83	2.71	69.5	2.28
7H-3, 71–73	56.01	46.0	85.3	1.55	0.83	2.73	69.5	2.28
7H-4, 70–72	57.50	50.2	100.7	1.48	0.74	2.71	72.7	2.66
7H-5, 70–72	59.00	47.8	91.7	1.51	0.79	2.68	70.6	2.40
7H-6, 70–72	60.50	44.0	78.7	1.57	0.88	2.69	67.3	2.06
8H-1, 70–72	62.50	44.2	79.4	1.56	0.87	2.68	67.5	2.07
8H-2, 70–72	64.00	44.9	81.6	1.57	0.86	2.75	68.7	2.19
8H-3, 70–72	65.50	49.5	97.9	1.60	0.81	3.52	77.1	3.37
8H-4, 70–72	67.00	54.1	117.7	1.42	0.65	2.63	75.1	3.02
8H-5, 70–72	68.50	50.2	100.8	1.48	0.74	2.68	72.5	2.63
8H-6, 70–72	70.00	47.0	88.8	1.52	0.80	2.64	69.6	2.29
9H-1, 70–72	72.00	47.3	89.7	1.52	0.80	2.68	70.1	2.35
9H-2, 70–72	73.50	52.4	109.9	1.45	0.69	2.66	74.0	2.85
9H-3, 70–72	75.00	48.3	93.4	1.50	0.78	2.66	70.8	2.43
9H-4, 70–72	76.50	51.7	107.2	1.45	0.70	2.62	73.3	2.75
9H-5, 70–72	78.00	52.2	109.1	1.45	0.69	2.63	73.7	2.80
9H-6, 70–72	79.50	50.4	101.5	1.47	0.73	2.65	72.4	2.63
9H-7, 60–62	80.90	49.4	97.7	1.49	0.75	2.68	71.9	2.55
10H-1, 70–72	81.50	50.3	101.1	1.47	0.73	2.61	72.0	2.58
10H-2, 71–73	83.01	52.0	108.3	1.43	0.69	2.50	72.6	2.65
10H-3, 70–72	84.50	57.3	134.4	1.38	0.59	2.57	77.1	3.37
10H-4, 70–72	86.00	41.9	72.0	1.60	0.93	2.70	65.5	1.90
10H-5, 70–72	87.50	44.5	80.0	1.56	0.87	2.68	67.6	2.09
10H-6, 70–72	89.00	43.5	77.0	1.67	0.94	3.24	70.9	2.44
10H-7, 70–72	90.50	52.0	108.4	1.37	0.66	2.17	69.6	2.29
11H-1, 70–72	91.00	47.4	90.0	1.52	0.80	2.68	70.2	2.36
11H-2, 70–72	92.50	49.3	97.1	1.49	0.76	2.66	71.6	2.53
11H-3, 70–72	94.00	46.7	87.7	1.53	0.81	2.67	69.6	2.29
11H-4, 70–72	95.50	44.1	78.9	1.56	0.87	2.65	67.1	2.04
11H-5, 70–72	97.00	45.3	82.9	1.55	0.85	2.67	68.4	2.16
11H-6, 70–72	98.50	48.0	92.4	1.51	0.78	2.68	70.7	2.42
11H-7, 62–64	99.92	42.1	72.6	1.61	0.93	2.73	65.9	1.94

Table T18 (continued).

Core, section, interval (cm)	Depth (mbsf)	Water content (wt%)		Density (g/cm³)			Porosity (%)	Void ratio
		Bulk mass	Dry mass	Bulk	Dry	Grain		
12H-1, 70–72	100.50	43.4	76.7	1.59	0.90	2.76	67.4	2.07
12H-2, 70–72	102.00	48.8	95.4	1.50	0.77	2.70	71.5	2.51
12H-3, 69–71	103.49	49.1	96.5	1.50	0.76	2.72	71.9	2.56
12H-4, 70–72	105.00	42.7	74.5	1.58	0.91	2.67	66.0	1.94
12H-5, 70–72	106.50	45.1	82.1	1.54	0.85	2.62	67.8	2.10
12H-6, 70–72	108.00	48.2	93.1	1.50	0.78	2.64	70.6	2.40
12H-7, 70–72	109.50	42.3	73.4	1.60	0.92	2.70	65.9	1.94
13H-1, 70–72	110.00	47.3	89.6	1.50	0.79	2.58	69.3	2.26
13H-2, 70–72	111.50	50.7	102.8	1.46	0.72	2.62	72.5	2.63
13H-3, 70–72	113.00	46.7	87.6	1.53	0.81	2.68	69.7	2.30
13H-4, 70–72	114.50	44.9	81.5	1.55	0.86	2.69	68.1	2.14
13H-5, 70–72	116.00	45.7	84.3	1.54	0.84	2.69	68.9	2.22
13H-6, 70–72	117.50	46.8	88.0	1.53	0.82	2.72	70.0	2.34
14H-1, 70–72	119.50	44.0	78.7	1.57	0.88	2.70	67.5	2.08
14H-2, 70–72	121.00	46.8	87.8	1.52	0.81	2.65	69.5	2.28
14H-3, 70–72	122.50	46.7	87.7	1.53	0.81	2.69	69.7	2.30
14H-4, 70–72	124.00	40.8	68.9	1.62	0.96	2.71	64.6	1.83
14H-5, 70–72	125.50	39.9	66.3	1.65	0.99	2.78	64.3	1.80
14H-6, 70–72	127.00	40.2	67.1	1.63	0.98	2.70	63.9	1.77
15H-1, 70–72	129.00	48.4	93.7	1.51	0.78	2.70	71.1	2.47
15H-2, 70–72	130.50	47.4	90.3	1.51	0.80	2.65	70.0	2.34
15H-3, 70–72	132.00	48.5	94.3	1.69	0.87	4.40	80.2	4.05
15H-4, 70–72	133.50	37.9	61.1	1.67	1.03	2.70	61.7	1.61
15H-5, 70–72	135.00	39.7	66.0	1.64	0.99	2.70	63.5	1.74
15H-6, 70–72	136.50	43.3	76.4	1.57	0.89	2.66	66.5	1.99
15H-7, 62–64	137.92	39.2	64.5	1.64	1.00	2.69	62.9	1.70
16H-1, 70–72	138.50	42.3	73.3	1.60	0.92	2.73	66.1	1.95
16H-2, 70–72	140.00	41.1	69.9	1.61	0.95	2.68	64.7	1.83
16H-3, 70–72	141.50	39.8	66.1	1.64	0.99	2.70	63.6	1.75
16H-4, 70–72	143.00	39.9	66.3	1.63	0.98	2.69	63.5	1.74
16H-5, 70–72	144.50	39.3	64.8	1.64	1.00	2.70	63.1	1.71
16H-6, 70–72	146.00	38.8	63.5	1.65	1.01	2.71	62.7	1.68
16H-7, 68–70	147.48	38.0	61.3	1.67	1.03	2.71	61.8	1.62
17H-1, 70–72	148.00	40.0	66.6	1.65	0.99	2.79	64.4	1.81
17H-2, 70–72	149.50	38.3	62.1	1.67	1.03	2.77	62.7	1.68
17H-3, 70–72	151.00	39.4	65.1	1.66	1.01	2.79	63.9	1.77
17H-4, 70–72	152.50	37.0	58.6	1.69	1.07	2.73	61.0	1.56
17H-5, 70–72	154.00	36.9	58.4	1.70	1.08	2.78	61.3	1.58
17H-6, 70–72	155.50	37.4	59.8	1.70	1.06	2.79	61.9	1.63
17H-7, 66–68	156.96	35.8	55.8	1.72	1.10	2.76	60.1	1.51
18H-1, 70–72	157.50	36.4	57.4	1.69	1.08	2.71	60.3	1.52
18H-2, 70–72	159.00	36.3	56.9	1.70	1.08	2.71	60.1	1.51
18H-3, 70–72	160.50	35.5	55.0	1.71	1.10	2.72	59.4	1.46
18H-4, 70–72	162.00	35.0	54.0	1.72	1.12	2.71	58.8	1.43
18H-6, 70–72	165.00	31.5	46.0	1.79	1.22	2.71	54.9	1.22
20H-1, 70–72	173.00	35.4	54.8	1.73	1.12	2.77	59.7	1.48
20H-2, 70–72	174.50	34.2	52.0	1.75	1.15	2.77	58.4	1.41
20H-3, 70–72	176.00	34.0	51.5	1.75	1.16	2.75	58.0	1.38
21X-1, 70–72	182.50	34.6	53.0	1.73	1.13	2.73	58.5	1.41
21X-2, 70–72	184.00	34.9	53.7	1.72	1.12	2.72	58.8	1.43
21X-3, 70–72	185.50	34.2	52.1	1.73	1.14	2.71	58.0	1.38
21X-4, 70–72	187.00	34.6	53.0	1.74	1.14	2.76	58.8	1.43
23X-1, 65–67	198.55	34.9	53.6	1.71	1.12	2.68	58.4	1.40
23X-2, 70–72	200.10	34.7	53.1	1.73	1.13	2.73	58.5	1.41
23X-3, 70–72	201.60	31.9	46.9	1.77	1.21	2.69	55.2	1.23
23X-4, 70–72	203.10	37.1	58.9	1.69	1.06	2.75	61.2	1.58
23X-5, 70–72	204.60	36.0	56.2	1.70	1.09	2.70	59.7	1.48
23X-6, 70–72	206.10	34.2	52.0	1.74	1.15	2.75	58.2	1.39
23X-7, 36–38	207.26	33.3	50.0	1.74	1.16	2.66	56.5	1.30
24X-1, 100–102	208.60	34.3	52.3	1.73	1.14	2.70	57.9	1.38
24X-2, 34–36	209.44	34.1	51.8	1.73	1.14	2.70	57.7	1.36
24X-4, 90–92	213.00	36.5	57.4	1.69	1.08	2.71	60.3	1.52
24X-5, 48–50	214.08	37.0	58.8	1.67	1.05	2.64	60.2	1.52
24X-6, 15–17	215.25	33.8	51.1	1.72	1.14	2.65	56.9	1.32
24X-7, 58–60	216.68	31.9	46.9	1.78	1.21	2.73	55.5	1.25
198-1207B-								
4R-1, 70–72	186.50	30.7	44.3	1.82	1.26	2.76	54.5	1.20
4R-2, 70–72	188.00	33.6	50.7	1.76	1.17	2.76	57.7	1.37

Table T18 (continued).

Core, section, interval (cm)	Depth (mbsf)	Water content (wt%)		Density (g/cm³)			Porosity (%)	Void ratio
		Bulk mass	Dry mass	Bulk	Dry	Grain		
4R-3, 70–72	189.50	33.7	50.9	1.75	1.16	2.74	57.7	1.36
5R-1, 70–72	196.20	30.5	43.8	1.83	1.27	2.80	54.5	1.20
5R-2, 70–72	197.70	33.1	49.4	1.76	1.18	2.72	56.7	1.31
6R-1, 70–72	205.80	34.6	52.9	1.74	1.14	2.77	58.9	1.43
6R-2, 70–72	207.30	31.2	45.3	1.82	1.25	2.79	55.2	1.23
6R-3, 70–72	208.80	33.3	49.9	1.76	1.17	2.73	57.1	1.33

Table T19. Discrete measurements of *P*-wave velocity, Site 1207. (See table note. Continued on next page.)

Core, section, interval (cm)	Depth (mbsf)	Velocity (m/s)
198-1207A-		
1H-1, 74	0.74	1498.0
1H-2, 58	2.08	1505.4
1H-3, 67	3.66	1505.7
2H-1, 68	5.48	1517.4
2H-2, 66	6.96	1525.4
2H-3, 65	8.45	1517.1
2H-4, 66	9.96	1526.9
2H-5, 67	11.47	1536.4
2H-6, 81	13.11	1528.3
3H-1, 66	14.96	1530.8
3H-2, 66	16.46	1538.9
3H-3, 65	17.95	1511.6
3H-4, 64	19.44	1517.1
3H-5, 66	20.96	1522.4
3H-6, 66	22.46	1520.0
4H-1, 65	24.45	1517.2
4H-2, 68	25.98	1520.6
4H-3, 59	27.39	1510.1
4H-4, 64	28.94	1513.7
4H-5, 77	30.57	1514.2
4H-6, 82	32.12	1522.9
4H-7, 67	33.47	1523.3
5H-1, 66	33.96	1517.8
5H-2, 67	35.47	1514.5
5H-3, 75	37.05	1523.2
5H-4, 67	38.47	1528.6
5H-5, 72	40.02	1511.4
5H-6, 66	41.46	1522.3
6H-1, 82	43.62	1514.7
6H-2, 67	44.97	1512.6
6H-3, 68	46.48	1515.6
6H-4, 68	47.97	1509.5
6H-5, 94	49.74	1514.1
6H-6, 67	50.97	1508.6
6H-7, 63	52.43	1516.8
7H-1, 65	52.95	1523.6
7H-2, 66	54.46	1509.1
7H-3, 66	55.96	1512.0
7H-4, 66	57.46	1509.0
7H-5, 83	59.13	1506.4
7H-6, 66	60.46	1512.4
8H-1, 66	62.46	1514.2
8H-2, 66	63.96	1508.0
8H-3, 67	65.47	1509.6
8H-4, 67	66.96	1507.9
8H-5, 67	68.47	1506.2
8H-6, 80	70.10	1507.5
9H-1, 67	71.97	1508.1
9H-2, 67	73.47	1508.9
9H-3, 80	75.10	1516.2
9H-4, 80	76.60	1514.1
9H-5, 67	77.97	1508.5
9H-6, 75	79.55	1512.1
9H-7, 46	80.76	1515.0
10H-1, 67	81.47	1505.2
10H-2, 69	82.99	1550.9
10H-3, 68	84.47	1522.9
10H-4, 65	85.95	1520.0
10H-5, 66	87.46	1527.0
10H-6, 64	88.94	1512.0
10H-7, 67	90.47	1508.3
11H-1, 66	90.96	1505.9
11H-2, 67	92.47	1507.0
11H-3, 73	94.03	1507.9
11H-4, 77	95.57	1522.0
11H-5, 66	96.96	1513.3
11H-6, 67	98.47	1505.5
11H-7, 59	99.89	1526.5
12H-1, 67	100.47	1511.4
12H-2, 67	101.97	1511.8
12H-3, 66	103.46	1517.5
12H-4, 68	104.98	1517.4
12H-5, 65	106.45	1541.6
12H-6, 67	107.97	1520.6
12H-7, 67	109.47	1515.2
13H-1, 67	109.97	1527.7
13H-2, 65	111.45	1513.4
13H-3, 65	112.95	1521.3
13H-4, 65	114.45	1530.5
13H-5, 67	115.96	1532.8
13H-6, 94	117.74	1522.0
13H-7, 38	118.68	1516.1
14H-1, 66	119.46	1513.0
14H-2, 53	120.83	1519.8
14H-3, 64	122.43	1518.2
14H-4, 65	123.95	1518.7
14H-5, 77	125.57	1526.9
14H-6, 61	126.91	1529.4
15H-1, 65	128.95	1532.9
15H-2, 66	130.46	1526.6
15H-3, 63	131.93	1525.7
15H-4, 66	133.46	1551.7
15H-5, 65	134.95	1535.3
15H-6, 66	136.46	1545.9
15H-7, 57	137.87	1534.6
16H-1, 67	138.47	1529.5
16H-2, 67	139.97	1532.8
16H-3, 67	141.47	1537.8
16H-4, 68	142.98	1535.4
16H-5, 67	144.47	1532.0
16H-6, 67	145.97	1539.8
16H-7, 66	147.46	1530.5
17H-1, 77	148.07	1526.4
17H-2, 66	149.46	1533.7
17H-3, 75	151.05	1526.9
17H-4, 76	152.56	1530.6
17H-5, 65	153.95	1539.9
17H-6, 75	155.55	1534.6
17H-7, 67	156.97	1565.2
18H-1, 66	157.46	1539.1
18H-2, 66	158.96	1535.1
18H-3, 66	160.46	1540.1
18H-4, 66	161.96	1550.7
18H-5, 37	163.17	1584.4
18H-5, 45	163.25	2257.5*
18H-5, 128	164.08	1579.6
18H-6, 67	164.96	1570.2
20H-1, 67	172.97	1540.1
20H-2, 61	174.40	1541.7
20H-3, 67	175.97	1544.1
21X-1, 65	182.45	1550.1
21X-2, 65	183.95	1536.5
21X-3, 66	185.46	1536.5
21X-4, 54	186.84	1559.0
23X-1, 61	198.51	1530.3
23X-2, 66	200.06	1534.6
23X-3, 66	201.56	1542.7
23X-4, 68	203.08	1535.4
23X-5, 101	204.91	1549.2
23X-6, 67	206.07	1565.5
23X-7, 34	207.24	1597.3
24X-1, 133	208.93	1553.5
24X-4, 82	212.92	1538.9

Table T19 (continued).

Core, section, interval (cm)	Depth (mbsf)	Velocity (m/s)
24X-5, 58	214.18	1540.8
24X-6, 71	215.81	1550.1
24X-7, 51	216.61	1547.6
27X-CC, 6	237.36	4322.4†
198-1207B-		
1R-1, 76	157.76	1531.8
1R-2, 76	159.26	1527.1
1R-3, 76	160.76	1537.0
1R-4, 52	162.02	1528.4
1R-5, 44	162.94	1526.2
2R-1, 58	167.18	1551.0
2R-2, 70	168.80	1543.1
2R-3, 72	170.32	1548.2
2R-4, 75	171.85	1549.1
2R-5, 73	173.33	1543.0
2R-6, 47	174.57	1557.8
3R-1, 60	176.80	1578.3
3R-2, 58	178.28	1564.2
4R-1, 67	186.47	1554.3
4R-2, 66	187.96	1550.6
4R-3, 66	189.46	1543.6
4R-4, 44	190.24	1543.8
5R-2, 77	197.77	1541.7
5R-3, 33	198.83	1563.8
6R-1, 2	205.12	5842.5†
6R-1, 76	205.86	1542.3
6R-2, 67	207.27	1556.9
6R-3, 75	208.85	1556.2
6R-4, 23	209.83	1547.2
11R-CC, 11	248.91	4909.7†
40R-CC, 28	526.78	2197.2
42R-CC, 42	546.22	2226.9
43R-1, 23	555.63	1981.4
43R-1, 51	555.91	2045.3
43R-1, 59	555.99	1889.3
43R-1, 64	556.04	2009.3
43R-1, 68	556.08	1971.0
43R-1, 79	556.19	2072.9
43R-1, 84	556.23	1867.7
43R-1, 87	556.27	1909.6
43R-1, 94	556.34	1821.4
43R-1, 104	556.44	2064.8
43R-1, 108	556.48	1985.3
43R-CC, 7	556.89	1974.1
44R-1, 38	565.38	1928.8
44R-1, 64	565.64	2003.3‡
44R-1, 80	565.80	2038.1‡
44R-1, 100	565.99	2216.4†
44R-1, 142	566.41	2225.5
44R-2, 16	566.59	2352.5
44R-2, 23	566.66	4786.4†
45R-1, 2	574.62	5076.2**
45R-1, 24	574.84	4869.0†
45R-1, 28	574.88	4583.6†
46R-1, 16	584.35	2229.2
46R-1, 32	584.52	2422.7
46R-1, 36	584.56	4998.2†
46R-1, 51	584.71	2976.6
46R-1, 72	584.92	2154.4
46R-1, 100	585.20	2402.3
46R-1, 115	585.35	2572.8
46R-1, 135	585.55	4817.0†
46R-1, 147	585.67	3297.8
46R-2, 9	585.79	5316.0†
46R-2, 34	586.03	2552.1
47R-1, 3	593.83	2496.4
47R-1, 46	594.26	3027.0
47R-1, 97	594.77	4696.3†
47R-1, 111	594.91	2660.6
47R-2, 24	595.44	2839.7
47R-2, 63	595.83	1886.6
47R-2, 85	596.04	2878.5
47R-2, 100	596.20	2670.1
47R-2, 113	596.33	2897.7
47R-3, 36	596.95	2477.1
47R-3, 76	597.34	3013.2
48R-1, 14	603.64	1974.2
48R-1, 45	603.95	2321.8
48R-1, 52	604.02	2115.5
48R-1, 56	604.06	2786.2
48R-1, 112	604.62	4807.5†
48R-1, 122	604.72	4632.7†
49R-1, 13	613.33	2120.3
49R-1, 61	613.80	2098.2
49R-1, 97	614.16	2151.9
49R-1, 136	614.56	2140.4
49R-2, 19	614.89	4665.2†
49R-2, 38	615.08	4789.3†

Note: * = Mn nodule, † = chert, ‡ = black shale, ** = siliceous limestone.

Table T20. Discrete measurements of thermal conductivity, Site 1207.

Core, section, interval (cm)	Depth (mbsf)	Thermal conductivity (W/[m·K])
198-1207A-		
1H-1, 75	0.75	0.72
2H-1, 55	5.35	0.97
2H-3, 55	8.35	0.98
2H-5, 55	11.35	0.92
3H-1, 55	14.85	0.94
3H-3, 55	17.85	0.79
3H-5, 55	20.85	0.73
4H-1, 55	24.35	0.86
4H-3, 55	27.35	0.89
4H-5, 55	30.35	0.86
5H-1, 55	33.85	0.86
5H-3, 55	36.85	0.80
5H-5, 55	39.85	0.74
6H-1, 55	43.35	0.91
6H-3, 55	46.35	0.74
6H-5, 55	49.35	0.93
7H-1, 55	52.85	0.93
7H-3, 55	55.85	0.84
7H-5, 55	58.85	0.66
8H-1, 55	62.35	1.04
8H-3, 55	65.35	0.86
8H-5, 55	68.35	0.81
9H-1, 55	71.85	0.86
9H-3, 55	74.85	0.83
9H-5, 55	77.85	0.84
10H-1, 55	81.35	0.84
10H-3, 55	84.35	0.83
10H-5, 55	87.35	0.87
11H-1, 55	90.85	0.69
11H-3, 55	93.85	0.81
11H-5, 55	96.85	0.73
12H-1, 55	100.35	0.77
12H-3, 55	103.35	0.93
12H-5, 55	106.35	0.85
13H-1, 55	109.85	0.88
13H-3, 55	112.85	0.99
13H-5, 55	115.85	1.10
14H-1, 55	119.35	0.98
14H-3, 55	122.35	0.94
14H-5, 55	125.35	1.07
15H-1, 55	128.85	0.94
15H-3, 55	131.85	1.00
15H-5, 55	134.85	1.04
16H-1, 55	138.35	1.01
16H-3, 55	141.35	1.04
16H-5, 55	144.35	0.92
17H-1, 55	147.85	1.12
17H-3, 55	150.85	1.06
17H-5, 55	153.85	1.17
18H-1, 55	157.35	1.02
18H-3, 55	160.35	1.13
18H-5, 55	163.35	1.09
19H-1, 55	166.85	1.14
20H-1, 55	172.85	1.29
20H-3, 55	175.85	1.23
20H-5, 55	178.85	1.27
21X-1, 55	182.35	1.25
21X-3, 55	185.35	1.26
23X-1, 55	198.45	1.16
23X-3, 55	201.45	1.23
23X-5, 55	204.45	1.14
24X-1, 55	208.15	1.37
24X-3, 55	211.15	1.19
24X-5, 55	214.15	1.13
198-1207B-		
1R-1, 55	157.55	1.15
1R-3, 55	160.55	1.03
2R-1, 55	167.15	1.20
2R-3, 55	170.15	1.23
2R-5, 55	173.15	1.13
3R-1, 55	176.75	1.13
4R-1, 55	186.35	1.10
4R-3, 55	189.35	1.19
5R-1, 55	196.05	1.20
5R-3, 55	199.05	1.20
6R-1, 55	205.65	1.17
6R-3, 55	208.65	1.06
9R-1, 50	230.30	1.25
28R-1, 55	412.65	1.26
28R-3, 55	415.65	1.35